UNIVERSITÄT HAMBURG
DEPARTMENT PHYSIK

Time-resolved studies at PETRA III with a highly repetitive synchronized laser system

Dissertation
zur Erlangung des Doktorgrades
des Department Physik
der Universität Hamburg

vorgelegt von

Moritz Schlie

aus
Sigmaringen

Hamburg

2013

Gutachter der Dissertation:	Prof. Dr. Markus Drescher
	Dr. Jens Viefhaus
Gutachter der Disputation:	Prof. Dr. Markus Drescher
	Prof. Dr. Henning Moritz
Datum der Disputation:	26. August .2013
Vorsitzender des Prüfungsausschusses:	PD Dr. Michael Martins
Vorsitzender des Promotionsausschusses:	Prof. Dr. Peter Hauschildt
Dekan der Fakultät für Mathematik, Informatik und Naturwissenschaften:	Prof. Dr. Heinrich Graener

No synchrotrons were harmed in the making of this thesis.

Abstract

Atomic and molecular processes can nowadays be directly followed in the time domain. This is a core technique for a better understanding of the involved fundamental physics, thus auguring new applications in the future as well. Usually the so-called pump-probe technique making use of two synchronized ultrashort light pulses is utilized to obtain this time-resolved data. In this work, the development and characterization of a synchronization system enabling such pump-probe studies at the storage ring PETRA III in combination with an external, then synchronized fs-laser system is described. The synchronization is based on an extended PLL approach with three interconnected feedback loops allowing to monitor short-time losses of the lock and thus prevent them. This way, the jitter between the laser PHAROS and the PETRA III reference signal is reduced to $\sigma < 5$ ps. Thus the system allows to conduct experiments at a repetition rate of 130 kHz with a temporal resolution limited only by the X-ray pulse length.

A major emphasis in the fundamental introductory chapters is an intuitive explanation of the basic principles of phase locked loops and the different aspects of phase noise to allow a deeper understanding of the synchronization.

Furthermore, first pump-probe experiments conducted at different beamlines at PETRA III are presented, demonstrating the usability of the laser system in a scientific environment as well. In first characterizing experiments the pulse duration of PETRA III X-ray pulses has been measured to be 90 ps FWHM.

In particular, there have been time resolved X-ray absorption spectroscopy experiments on Gaq3 and Znq2 conducted at beamline P11. First results show dynamics of the electronic excitation on the timescale of a few hundred pico seconds up to a few nano seconds and provide a basic understanding for further research on those molecules. For Gaq3 this data is analyzed in detail and compared with visible fluorescence measurements suggesting at least two excited and probed states with different decay constants.

Time resolved electron-ion coincidence spectroscopy conducted at P04 shows the flexibility of the system to be usable at different beamlines and to obtain spatial and temporal overlap in vacuum as well.

Zusammenfassung

Atomare und molekulare Prozesse können heute direkt in der Zeit-Domäne untersucht werden. Dies stellt eine wesentliche Methode dar um ein besseres Verständnis der zugrundeliegenden Physik zu erlangen und stellen somit auch deren zukünftige Anwendung in Aussicht. Üblicherweise wird hierfür die sogenannte Pump-Probe Methode (Anrege-Abfrage Methode) angewandt, welche mittels zweier ultrakurzer Lichtpulse zeitaufgelöste Datenaufnahme ermöglicht. In dieser Arbeit wird die Entwicklung und Charakterisierung eines Synchronisationssystems beschrieben, welches derartige Pump-Probe Experimente am Speicherring PETRA III in Kombination mit einem hiermit synchronisierten fs-Lasersystem ermöglicht. Die Synchronisierung basiert auf einem erweiterten PLL Ansatz mit drei verknüpften Regelkreisen, was es ermöglicht den kurzfristigen Verlust der Synchronisation festzustellen, und somit zu verhindern.

Somit reduziert sich der Jitter zwischen dem Laser PHAROS und dem PETRA III Referenz Signal auf $\sigma < 5$ ps. Deshalb erlaubt das System Experimente mit einer Wiederholrate von 130 kHz durchzuführen, deren zeitliche Auflösung nur durch die Röntgenpulslänge limitiert wird.

Ein Schwerpunkt in den grundlegenden Kapiteln liegt bei einer intuitiven Beschreibung der Grundlagen von Phasenregelschleifen und verschiedener Aspekte von Phasenrauschen um ein tiefgreifendes Verständnis der Synchronisierung zu ermöglichen.

Weiterhin werden erste Pump-Probe Experimente, welche an unterschiedlichen Beamlines an PETRA III durchgeführt wurden, präsentiert. Sie belegen die Tauglichkeit des Systems im wissenschaftlichen Alltag. In ersten characterisierenden Experimenten wurde die PETRA III Röntgenpulslänge mit 90 ps FWHM gemessen.

Insbesondere wurden zeitaufgelöste Röntgenabsorptionsspektroskopie Experimente mit Gaq3 und Znq2 an Beamline P11 durchgeführt. Erste Ergebnisse zeigen Dynamik der elektronischen Anregung in der Größenordnung von einigen hundert pico Sekunden bis zu einigen nano Sekunden und erlauben grundlegende Einblicke für weitere Experimente mit diesen Proben. Die Gaq3 Daten werden ausführlich diskutiert und mit Messungen optischer Fluoreszenz verglichen, welche nahelegen, dass zumindest zwei unterschiedliche angeregte Zustände mit unterschiedlicher Zeitkonstante vermessen wurden.

Zeitaufgelösten Elektronen-Ionen Koinzidenz-Spektroskopie - durchgeführt an Beamline P04 - zeigt die Flexibilität und vielfältige Einsetzbarkeit des Systems an unterschiedlichen Messplätzen sowie die Möglichkeit räumlichen sowie zeitlichen Überlapp der Pulse ebenfalls im Vakuum zu erreichen.

Contents

1. Introduction

Time resolved studies at synchrotron radiation sources can be conducted in pump probe setups utilizing synchronized laser systems. Such studies enable temporal resolutions limited by the pulse length of the synchrotron radiation and the laser.

Pump-probe experiments using laser and synchrotron radiation sources are a common approach nowadays [87], [19]. Time-resolved experiments at synchrotron radiation facilities are an important field, thus they are mentioned for several scientific fields as a trend in [16] for example. The importance of time-resolved experiments at synchrotron radiation sources is based on the unique properties of the third-generation synchrotron storage rings. These are namely [19]: A broad and continuous energy range, (ultra) short pulses, high photon flux, high timing stability and the possibility to synchronize a laser source. In order to utilize the high repetition rate of 3rd generation synchrotron radiation sources, the data acquisition rate as well as the laser repetition rate ideally need to be high as well. To this end - besides the presented approach in this work - further approaches exist, for example [56] or [60].

Further evidence for the relevance of time-resolved experiments at synchrotron radiation sources is the development of slicing techniques to achieve ultrashort synchrotron pulses [89], [75]. For this purpose, the electron bunch is modulated with synchronized laser pulses, thus also fortifying the significance of synchronized laser systems. Also the advent of free-electron lasers as synchrotron radiation sources - offering even better temporal resolution - confirms the scientific relevance of time resolved experiments at synchrotron radiation sources.

Synchronized laser systems are common at synchrotron radiation facilities. There are for example such systems described at the ALS[1] by [46] or at the SLS[2] described in [36]. They have been used for pump-probe experiments like time resolved X-ray absorption spectroscopy (XAS) for many years now - a detailed overview on time-resolved XAS including X-ray absorption near-edge structure (XANES) and extended X-ray absorption fine structure (EXAFS) is given in [19]. However those systems often operate at low repetition rates thus allowing to pump only a very small fraction of the X-ray pulses. The aforementioned systems are described to be operating at only 1 kHz while synchrotron radiation sources reach several MHz. Unlike other synchrotron facilities, a synchronized laser system for pump-probe studies had not been foreseen for PETRA III from the start.

Even though shorter pulse length than those of PETRA III - and thus better temporal resolution - are meanwhile available at free electron lasers or synchrotron sources with slicing ability, a synchronized laser at PETRA III is a useful scientific tool. Various

[1] Advanced Light Source at Lawrence Berkeley National Laboratory in Berkeley, California
[2] Swiss Light Source at Paul Scherrer Institut (PSI) in Villigen, Switzerland.

processes in molecules as well as in solids, liquids, and biological systems do take place on different timescales (see [24] for a general overview) and thus the available temporal resolution is sufficient for many relevant dynamical processes.

The comparably high repetition rate of the presented PHAROS system of 130 kHz allows to use a higher share of the synchrotron pulses to be combined with laser pulses thus improving the efficiency and make use of the generally high average flux at synchrotrons. Furthermore, the higher repetition rate does allow experiments with higher statistical requirements. The PHAROS laser system reaches 130 kHz corresponding to PETRA III single bunch mode, PETRA III in multi bunch mode reaches even between 5.2 and 31.2 MHz while the upcoming XFEL is limited to 27 kHz according to [10] which will still be unique for X-ray lasers.

A synchronized laser system can not only be used to pump or probe with its light but can also be used as a synchronized switch for other physical variables (see [82] for the presented PHAROS system being used to switch magnetic fields for example).

Providing such a laser system was the necessary first step to be able to perform that kind of time resolved experiments at PETRA III. The presented system is equipped with an optical parametric amplifier (OPA) and a harmonics module to deliver laser pulses from the ultraviolet (UV) to the infrared (IR) region.

The focus of this work is on the synchronization including characterization and the necessary background explained to allow a deeper understanding thereof. Within the introductory chapter “Fundamental Preconditions” (chapter 2), the necessary physical principles and engineering basics of the used instruments and methods are explained to ease to follow the later chapters of this experimental work. A major focus is on the explanation of phase locked loops within the time domain to offer an uncommon but intuitive approach. The following chapter “Experimental environment” (chapter 3) describes the actual facilities and devices of major importance within this work. The synchronization itself is presented (chapter 4) and characterized (chapter 5) before the conducted time resolved experiments are shown (chapter 6).

An advanced setup of three interconnected loops has been used to allow full control of the bucket jumps. A major emphasis is on the different aspects of phase noise to allow a deeper understanding of the synchronization. Within those chapters the temporal resolution is deduced and analyzed. First time resolved dynamics of tris(8-hydroxyquinolinato)gallium (Gaq3), namely lifetime measurements of laser induced fluorescence, are shown and discussed.

As this work touches various disciplines the explained basics are chosen in a way that less experienced readers in some of the fields should be able to follow as well.

2. Fundamental Preconditions

In this chapter, the theoretical background is explained that is necessary to follow the later chapters. It covers topics in the field of physics but as well in control engineering. Further references for deeper understanding are provided.

2.1. Pump-Probe Method

The observable timescale in an experimental setup is often limited by electronic devices such as cameras or oscilloscopes and the timescale they are working on. In order to be able to perform measurements beyond the temporal resolution of typical electronic devices the pump-probe method can be applied. In a pump-probe setup the considered process is started via a so-called pump and measured (probed) with a second step with a defined and known time-delay. This has to be repeated with varying time delays to get the temporal evolution of the pumped process, in this work typically an electronic excitation. Therefore, the considered process needs to be repeatable, i.e it needs to be completely reversible or the target of the pump has to be renewed at the rate of the experiment.

In figure 2.1 the pump-probe method is explained by a simple example demonstrating how one would "tape" a movie of a sprint using a pump-probe setup.

The starting shot is then the pump starting the dynamic process. The probe would be the camera to take a picture of the athletes. To perform a pump-probe measurement one has to repeat the sprint several times with varied time between pump an probe Δt (i.e. the time between starting signal and taking the picture). Finally all pictures taken have to be put in an order according to their particular Δt to get a movie of the dynamics (here the sprint). In this scenario it is quite obvious, that a meaningful video can only be achieved if the athlete runs exactly the same every time. This illustrates that the pump-probe method is depending on the process to be observed being reproducible. The example also shows that the quality of the movie and especially its temporal accuracy is highly dependent on a precise determination of Δt so typically an advanced synchronization between pump and probe with an adjustable but still precisely known delay (i.e. Δt) is used. Usually, this method is applied when temporal resolution is necessary that cannot be achieved otherwise, of course.

For example, a laser pulse can be used as a pump exciting a target which changes a certain property when excited. This property - i.e. reflectivity, absorbance, possible ionization channels - can then be probed, for example, with a second pulse. As the delay between pump- and probe-pulse is very well known, the achievable temporal resolution exceeds that of the used instruments to measure the probed property (i.e. cameras,

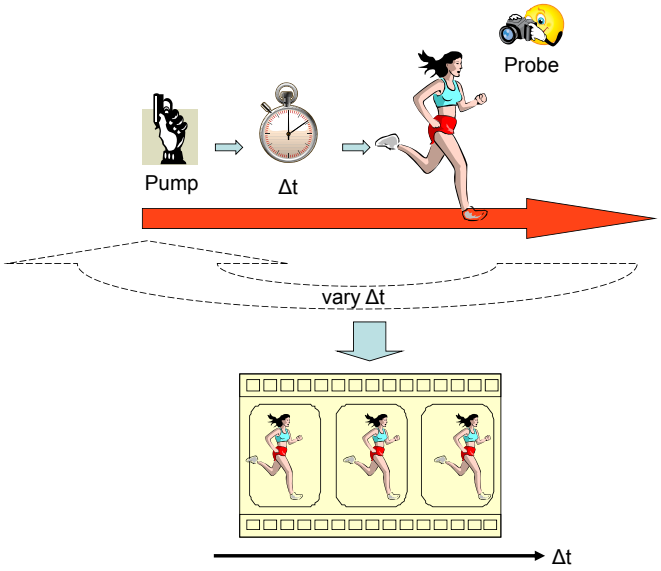

Figure 2.1.: Pump-Probe Method - explained in a simple example

power meter, spectrometer) as the integrated[1] value can be assigned to the very precisely known time delay. The temporal resolution of such pump-probe-experiments is, therefore, limited by the pulse length of pump and probe as well as by the relative jitter between them.

To perform pump-probe experiments at a synchrotron (such as PETRA III in this work), a synchronized laser system is necessary. Providing such a system is, therefore, a major part of this work.

The pump-probe technique has been widely used for many years now. It got broader attention beyond the scientific community when in 1999 Ahmed Zewail received the Nobel Price in Chemistry "'for his studies of the transition states of chemical reactions using femtosecond spectroscopy"' using pump-probe techniques [7].

The group of Markus Drescher where this work has been carried out is experienced in various pump probe experiments (see, for example, [50] where the pump probe principle is used on a gas target as well as on a surface used as timing tool).

A more educational description with further examples can be found in [28].

[1] the process of measuring itself takes longer (due to the speed of the instruments) than the temporal resolution of the examined process, thus the given values are integrated values

2.2. Phase Locked Loop (PLL)

Synchronization problems are typical control engineering problems. A well known task is locking a variable or physical property to a certain value. This property could be anything like temperature, fill level, flow capacity, voltage,... in any field where keeping a property stable is needed. In this work, it was necessary to synchronize laser pulses with synchrotron pulses and, therefore, to synchronize the repetition rate of the laser system's oscillator to the PETRA III master clock. The basic terms and ideas are described in this chapter. Further information on control design are given, for example, in [58].

Phase locked loops (PLL) are circuits to lock an adjustable oscillator to an external frequency by stabilizing their relative phase (and, therefore, their frequency as well).

PLLs are composed of three major components, shown in figure 2.2:

- A voltage controlled oscillator (VCO), allowing its frequency to be adjusted using a voltage input.
- A phase detector, giving an error signal proportional to the phase difference of two signals.
- A controller, generating a control signal out of the error signal. This control signal is fed into the VCOs voltage input.

Furthermore, a reference frequency is necessary to synchronize the VCO to it. This is fed into the phase detector input (the PLLs principle function can be seen in figure 2.2).

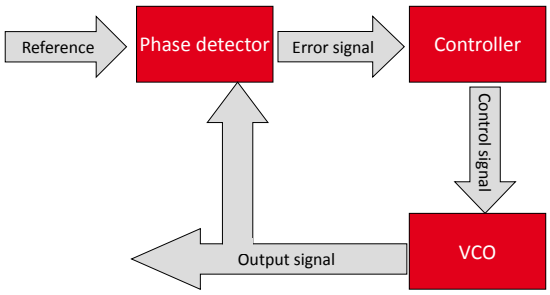

Figure 2.2.: General description of a PLL

The reference frequency and the VCO frequency are compared by the phase detector, the phase detector returns a signal that is (in linear approximation or in ideal case) proportional to the phase difference of the two signals. This so-called error signal is fed into the controller which generates a control signal depending on the error signal. For this purpose the controller could also take into account the error signals history and its speed of change as well. This control signal is put into the VCO to adjust its phase. Therefore, a locked loop will lead to a constant phase difference between both signals.

To understand PLL better, it can be advantageous to consider frequency to be a linear time dependent phase. This can be illustrated mathematically, starting with an

arbitrary sinusoidal signal $A(t)$ with frequency ω and phase ϕ:

$$A(t) = sin(\omega t + \phi(t))$$

In this equation it can be seen, that a linear time dependence in $\phi(t)$, for example

$$\phi_{var1}(t) = \phi(t) + at$$

can not be distinguished from an identical contribution to ω (in the same example:

$$\omega_{var2} = \omega + a$$

). Both variations of ω as well as of $\phi(t)$ would lead to the same result:

$$\begin{aligned} A_{var2}(t) &= sin(\omega_{var2} t + \phi(t)) \\ &= sin((\omega + a)t + \phi(t)) \\ &= sin(\omega t + at + \phi(t)) \\ &= sin(\omega t + (\phi(t) + at)) \\ &= sin(\omega t + \phi_{var1}(t)) \qquad\qquad = A_{var1}(t) \end{aligned} \tag{2.1}$$

This allows to consider reference frequency and VCO frequency to be identical by definition, and all differences are considered to be changes in phase.

A further consideration closely connected to this is that a constant phase difference over time is only possible for identical frequencies. Having a PLL keeping the phase difference stable at every time t automatically means having identical frequencies. This point of view will be helpful within the next subsections going deeper into the three major parts of the PLL.

In control engineering science, control circuits are usually designed and described in the complex frequency domain, connected to the time domain by Laplace transformations. As the target audience of this work are physicists, the principles are explained in the - less common - time domain. While it does not offer the same amount of tools to design circuits, however, the approach is more intuitive and allows direct identification of parameters of the model within the device. Furthermore the system in this work consists of three interconnected loops, several ADC-DAC operations[2] and a freely programmable FPGA (Field Programmable Gate Array) making a meaningful simulation with linearized models rather hard if not impossible. Therefore the chosen way has been the systematic variation and adjustment of parameters. It is also not favorable to use the impulse response method to measure the transfer function of the PLL, since the probing impulse would open the loop at once by causing the loss of mode-locking.

The following theoretical considerations will be helpful to understand the described synchronization in chapter 4.1.

[2] ADC: analog-to-digital converter
DAC: digital-to-analog converter

2.2.1. Phase Detector

The phase detector is - as the name indicates - the part that compares two signals of assumed identical frequencies and returns a value proportional to the phase difference (in linear approximation). A typical phase detector as used in this work consists of a mixer and a low-pass filter.

A mixer is an electronic element that multiplies signals. The product of two sine or cosine signals will lead to a sum or difference of two sine or cosine signals with sum frequency and sum phase and with frequency difference and phase difference (for the elementary math see for example [21] chapter 2.7.2.6). This is illustrated in equation 2.2 where the typical electronic symbol ($\otimes$) is shown with abstract input and output signal representations of sinusoidal signals.

Mixer as first part of a phase detector:

$$\begin{gathered} \sin\left(\omega_1 t + \phi_1(t)\right) \quad \Rightarrow \otimes \Leftarrow \quad \sin\left(\omega_2 t + \phi_2(t)\right) \\ \Downarrow \\ \frac{1}{2}\left(\cos\left((\omega_1 - \omega_2)t + \phi_1(t) - \phi_2(t)\right) - \cos\left((\omega_1 + \omega_2)t + \phi_1(t) + \phi_2(t)\right)\right) \end{gathered} \tag{2.2}$$

A low-pass filter (symbol: $\approx\!\!\!\!\!\!\diagdown$) attenuates all frequency components above a certain threshold thus letting only low frequencies pass. Applying a low-pass filter after the mixer will lead to the desired error signal (see equation 2.3).

Low-pass as second part of a phase detector:

$$\begin{gathered} \frac{1}{2}\left(\cos\left((\omega_1 - \omega_2)t + \phi_1(t) - \phi_2(t)\right) - \cos\left((\omega_1 + \omega_2)t + \phi_1(t) + \phi_2(t)\right)\right) \\ \Downarrow \\ \approx\!\!\!\!\!\!\diagdown \\ \Downarrow \\ \cos\left(\Delta\omega t + \Delta\phi(t)\right) \end{gathered} \tag{2.3}$$

Applying the phase considerations resulting from equation 2.1 (so $\omega_1 = \omega_2 =: \omega$ and, therefore, $\Delta\omega = 0$) illustrates the error signal as a mere phase error:

$$\begin{gathered} \sin\left(\omega t + \phi_1(t)\right) \quad \Rightarrow \otimes \Leftarrow \quad \sin\left(\omega t + \phi_2(t)\right) \\ \Downarrow \\ \approx\!\!\!\!\!\!\diagdown \\ \Downarrow \\ \cos\left(\Delta\phi(t)\right) \end{gathered} \tag{2.4}$$

However, this error is not proportional to the phase error as desired in ideal case (see above). Thus the consideration of the phase error signal to be linear is only valid around the cosines zero-crossing where it can be approximated linearly rather well. This is commonly referred to as the *small-angle approximation*. This means the error signal is only useful and, therefore, the whole loop is only able to synchronize properly as long as the phase jumps are not too big! The whole consideration hardly changes if one describes one or both of the input signals as cosines instead of sines, which is for real signals not distinguishable and makes only a difference in phase difference of $\frac{\pi}{2}$. This fixed offset is irrelevant for the goal of synchronization, as the only thing that is important is, that the phase difference needs to be held constant. Hence the phase detector finally gets described mathematically (with all discussed limitations) as a device, where two phases $\phi_1(t)$ and $\phi_2(t)$ are the input signals and a sufficiently small phase difference $\Delta\phi(t)$ is the output:

$$\begin{array}{ccc} \phi_1(t) & \Rightarrow \otimes \Leftarrow & \phi_2(t) \\ & \Downarrow & \\ & \approx & \\ & \Downarrow & \\ & \Delta\phi(t) & \end{array} \tag{2.5}$$

2.2.2. Controller

The controller is responsible to translate the phase error signal into a signal to control the VCO. Typical controllers are PID based (PID = proportional-integral-derivative). PIDs consist out of three parts operating parallel.

P-term the proportional term reacts linearly on the error signal: It contributes stronger the stronger the error signal is.

I-term the integral term reacts on the history of the error signal: It is reacting stronger the longer the error signal keeps its mathematical sign.

D-term the derivative term reacts on the change of the error signal: It is reacting stronger the bigger the change of the error signal is.

Therefore, the output of the controller is mathematically described as the sum of three weighted functions of the input (see equation 2.6). The input voltage $V(t)$ is actually a voltage $V(\Delta\phi(t))$ proportional to the phase difference $\Delta\phi(t)$ in linear approximation (see 2.5). The three constants K_P, K_I, and K_D are the characteristic parameters of a PID controller for the components described above.

$$V(t) \quad \Rightarrow \quad PID \quad \Rightarrow \quad V_{PIDout}(t) = K_P \cdot V(t) + K_I \cdot \int V(t)dt + K_D \cdot \frac{d}{dt}V(t) \tag{2.6}$$

2.2.3. VCO

The voltage controlled oscillator (VCO) is the frequency generator that can be adjusted by an external voltage to change its frequency (or phase, depending on the point of view). In the described system the VCO is the laser oscillator which is equipped with a piezo movable mirror. Thus the cavity length and, therefore, the repetition rate can be adjusted via an external voltage. More information on lasers in principle will be given in chapter 2.3.1, more on the particular laser system used in this work in chapter 3.2.1. A general laser oscillator is described in figure 2.10. In that principle one mirror needs to be put on a piezo table being able to move it parallel to the beam path. Then the resonator length is adjustable and, therefore, the repetition rate of the laser pulses can be slightly adjusted. See chapter 2.3.1 for more insights into mode-locked pulsed lasers. The piezo changes its position depending on a voltage applied, that directly changes the cavity length and, therefore, the repetition rate as well. This is obvious if one considers one pulse traveling through the oscillator, and it can only be released once per roundtrip when reaching the pockels cell. Therefore, the repetition rate f_{rep} is directly depending on the cavity length or more general the length of the optical path for one roundtrip l as

$$f_{rep} = \frac{c}{l}$$

where c is the speed of light. Of course one would need to consider different c for air and gain media. However, that would be only an offset Δl contributing to l as the thickness of the gain media is not changed. The piezo controller has an input transferring the voltage input linearly into a piezo position. Hence the varied repetition rate $f_{rep-var}$ gets:

$$f_{rep-var} = \frac{c}{l + \Delta l}$$

leading to the frequency difference Δf_{rep} of:

$$\Delta f_{rep} = f_{rep} - f_{rep-var} = \frac{c}{l} - \frac{c}{l + \Delta l} = \frac{c\Delta l}{l(l + \Delta l)}$$

The voltage frequency dependence is strictly speaking not linear, but for $\Delta l << l$ the denominator can be considered constant and, therefore, the approximation

$$\Delta f_{rep} \approx \frac{c\Delta l}{l^2} \propto \Delta l \tag{2.7}$$

is valid. This consideration is rather general as l is the length of the beampath for one roundtrip independent of the cavity design. The length of actual cavities differs from the optical path for one roundtrip, depending on the actual construction. In the most simple case by a factor of $\frac{1}{2}$ if the beampath is leading once back and forth. Thus, the distance the piezo mirror has to be moved is also dependent on the the cavity design. In the simplest setup the piezo moves the mirror $\frac{\Delta l}{2}$ along the beampath. This is the case if the mirror is passed once per roundtrip. If the mirror is passed n times it only needs to be moved $\frac{\Delta l}{2n}$ to change the beampath by Δl (provided the mirror is mounted in a way so the incidence on other mirrors is not affected). As here everything is considered

from a phase point of view, further considerations are necessary to include the VCO:

Starting again with the consideration from equation 2.1 above, one can identify the frequency variation a there with $2\pi\Delta f$ here and thus the phase variation $a \cdot t$ corresponds here to the phase difference $\Delta\phi$:

$$\Delta\phi = 2\pi t \Delta f_{rep} \tag{2.8}$$

This gets more comprehensible if one substitutes $\frac{c}{l} = f_{rep}$ in equation 2.7 by the roundtrip time $T_{rep} = \frac{1}{f_{rep}}$.

$$\Delta f_{rep} \approx \frac{c\Delta l}{l^2} = f_{ref}\frac{\Delta l}{l} = \frac{1}{T_{rep}}\frac{\Delta l}{l} \tag{2.9}$$

Especially interesting now is to interpret the included equation (with all the above approximations being valid):

$$\Delta f_{rep} = f_{rep}\frac{\Delta l}{l} \tag{2.10}$$

and from equation 2.9 inserted in 2.8

$$\Delta\phi = 2\pi\frac{t}{T_{rep}}\frac{\Delta l}{l} \tag{2.11}$$

Here equation 2.10 states, that Δf_{rep} scales with the ratio of Δl to l. Equation 2.11, however, means that for every roundtrip (i.e. $t = T_{rep}$) one $\frac{\Delta l}{l}$th phase is accumulated. Therefore a phase offset accumulates with the time, it sums up or - as of course in general Δl is time dependent - integrates.

$$\Delta\phi = \frac{2\pi}{T_{rep}l}\int \Delta l(t)dt \tag{2.12}$$

The piezo is equipped with a controller to translate applied voltage linearly into a change in Δl. The constant of proportionality is called k_{piezo} in the following equations. Hence the overall behavior of the VCO in terms of phase is that an input voltage $V(t)$ is translated into a change in phase of the output.

$$V(t) \quad \Rightarrow \quad VCO \quad \Rightarrow \quad \Delta\phi = \frac{2\pi}{T_{rep}l}\int k_{piezo}V(t)dt \tag{2.13}$$

This is a mathematical representation of a laser oscillator as an VCO showing the effect of an applied voltage on the phase.

2.2.4. Discrete Example

Having now all necessary parts for the PLL modeled mathematically, the process of synchronizing a VCO via PLL to an external source is illustrated best with an example. The first part to consider is again the phase detector. In the following $\phi_1(t)$ is the phase of the reference, while $\phi_2(t)$ is the phase of the signal from the VCO. In the real setup

as described in chapter 3.2, a photodiode is mounted inside the cavity delivering the VCO repetition rate as an electronic signal. Physically the inputs and outputs of the phase detector are voltages, however, only their parameters relevant as a signal carrying information are stated in equation 2.5. To avoid confusion the phase detector output can be given as a voltage

$$V_{pd}(t) = k_{pd}\Delta\phi(t) \tag{2.14}$$

with the constant of proportionality k_{pd}. The control loop here is discrete, as the PID controller is implemented on a field-programmable gate array (FPGA). It is reading out the ADCs once per control period. In the discrete case equation 2.6 becomes:

$$V_{PIDout}(t) = K_P \cdot V(t-1) + K_I \cdot \sum_{n=1}^{N} V(t-n) + K_D \cdot (V(t-1) - V(t-2)) \tag{2.15}$$

Here the discrete case is modeled by assuming t to be an integer thus $V(t-n)$ is the value of V observed n discrete steps before t. Hence the differentiation becomes the difference between the two last values, the integration turns into a sum over the last N values. Then N corresponds to the integration limit and defines the number of values summed up.

V being the input of the PID now is, as can be seen in figure 2.2, the output of the phase detector and, therefore, a voltage proportional to the phase difference called V_{pd} in equation 2.14. Putting equation 2.14 in equation 2.15 leads to

$$V_{PIDout}(t) = k_{pd}\left(K_P \cdot \Delta\phi(t-1) + K_I \cdot \sum_{n=1}^{N} \Delta\phi(t-n) + K_D \cdot (\Delta\phi(t-1) - \Delta\phi(t-2))\right) \tag{2.16}$$

Finally one has to consider the VCO as well. It is not obvious to treat it discrete as well, as the repetition rate of the oscillator is much higher than the control frequency and, therefore, changes in Δl might occur during one control period[3] T_{loop} that have the possibility to contribute to the phase. However, to ease things in this example we assume that the changes Δl performed by the loop are so small that they are quick and so the varied $V(t)$ as well as the proportional $\Delta l(t)$ are basically constant during the period. Real discrepancies towards this can be interpreted to be part of a general noise or disturbance term ϕ_{noise} which will be introduced later. The VCO then can be modeled by taking equation 2.13 and assuming $V(t)$ being discrete again for the discussed reason. $V(t)$ is substituted by the actual input of the VCO, the output of the PID controller $V_{PIDout}(t)$:

$$\Delta\phi(t) = \frac{2\pi k_{piezo}}{T_{repl}} \sum_{m=0}^{t} V_{PIDout}(m) T_{loop} \tag{2.17}$$

[3] In the considered system typically 1.4 ms, see chapter 4 for more details

Before inserting equation 2.16 into equation 2.17 the constants are combined:

$$A = \frac{2\pi k_{piezo} k_{pd} T_{loop}}{l T_{rep}} \tag{2.18}$$

leading to

$$\Delta\phi(t) = A \sum_{m=0}^{t} \left(K_P \cdot \Delta\phi(m-1) + K_I \cdot \sum_{n=1}^{N} \Delta\phi(m-n) + K_D \cdot (\Delta\phi(m-1) - \Delta\phi(m-2)) \right) \tag{2.19}$$

This recursive definition offers insights into the control loop and feedback behavior with simple tools as any spreadsheet program or can be implemented in any typical programming environment in a straight forward way. Note that the amplitude A needs to be adjusted depending on the PID parameter, as they contribute to the loop gain. The first thing to consider is what happens if one activates the loop. For all the examples, N is set to a fixed value of $N = 10$. This is the length of the memory[4] the I-term reacts on. To consider the PLL systematically, the effect of each of the three PID parameter is shown independently. K_I and K_D are set 0 leaving only a P-controller. The first example in figure 2.3 shows what happens if one switches on the feedback loop at $t = 0$ with an initial offset of 1 (i.e. $\forall n \in \{-11, -10, ..., -1, 0\} : \Delta\phi(n) = 1$) for various values of K_P. A small absolute value leads to slower controlling behavior while a larger absolute value can lead to oscillations and even to overshoot the setpoint stronger with every regulation step. P-controllers can be used alone but have as a major disadvantage that they can lead to an offset.

To overcome this disadvantage, often PI-controllers are used. To illustrate how the I-term influences the controller, figure 2.4 shows the behavior of the loop if K_P and K_D are both set to 0. For larger absolute values of K_I, the loop gets instable and the output starts to oscillate while for smaller absolute values the setpoint is reached. It is important to note that this reacts slower than the P-controller. The same scenario with combined P and I terms is illustrated in figure 2.5. The reason for still adding an I-term is, however, that its 'memory' can compensate the P-terms offset property. This property is not directly intuitive in this case but can be understood the following way: As a P-controller only reacts proportional on the actual error signal it does not control if this error signal is zero. That is usually desired, however, it can occur that a constant control value is needed to stay at the setpoint. This is, for example, when a constant drift occurs where the P-term will always be one step behind, while an I-term will based on the former offsets over regulate to reduce the offset (but lead to overshooting as well if the direction of the drift changes). This is illustrated in figure 2.6 after introducing

[4] The integral part can be realized in discrete case by adding the last N values thus representing a memory of length N. In case of the locked loop the deviations of the controlled parameter should be randomly distributed above and below the setpoint thus its integral should be vanishing. Therefore a non-infinite memory as an Integral is no limitation.

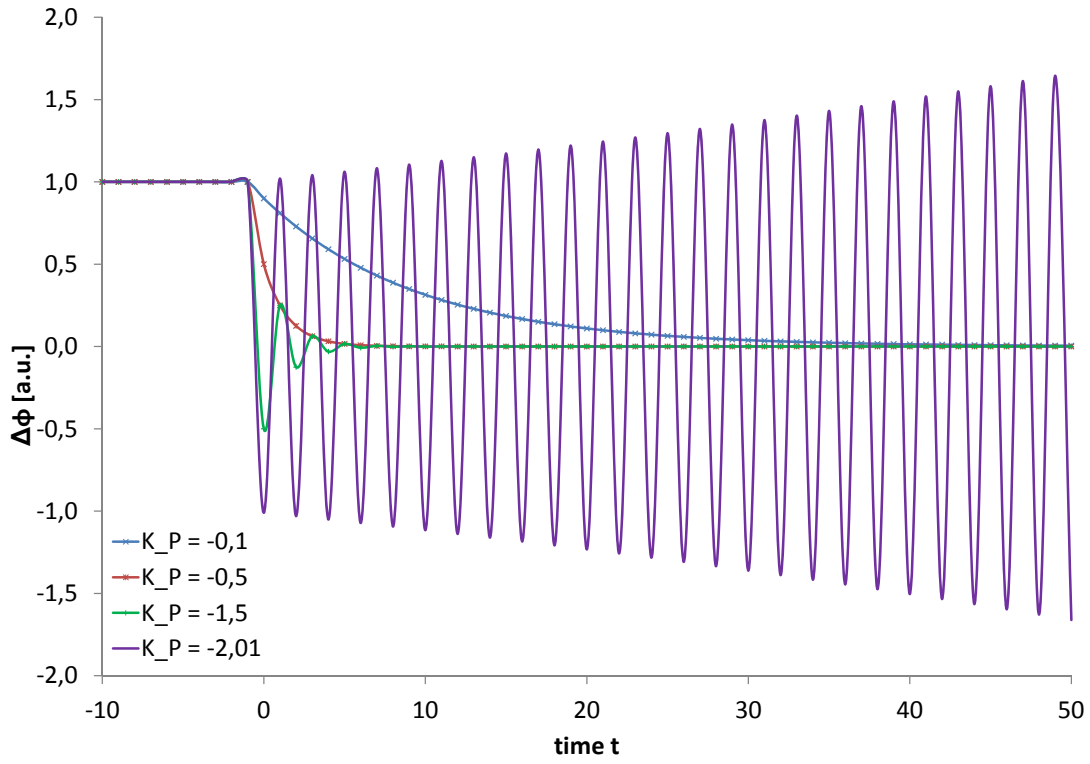

Figure 2.3.: Simulation of the start-up of discrete PLL with only a P controller based on equation 2.19. K_I and K_D are both set to 0 to demonstrate the effect of the P term.

the setpoint in equation 2.20.

The common effect of the P- and I-terms (so called *PI-controller*) are shown in figure 2.6. To simulate drifts of the VCO, the loop output is set to be $\Delta\phi \neq 0$, the setpoint is following a ramp function. An I-term can reduce the offset but leads to overshooting if the drift changes direction.

The D-term can not be used as a controller alone. As it only reacts on changes it cannot lead away from a incorrect value that is constant. It also would not lead to the desired setpoint when the incorrect value is not constant but only works against the change of that value.

To be able to look at the response of the loop to noise, drifts or also a desired change of the reference it is necessary to add this to the equation 2.19:

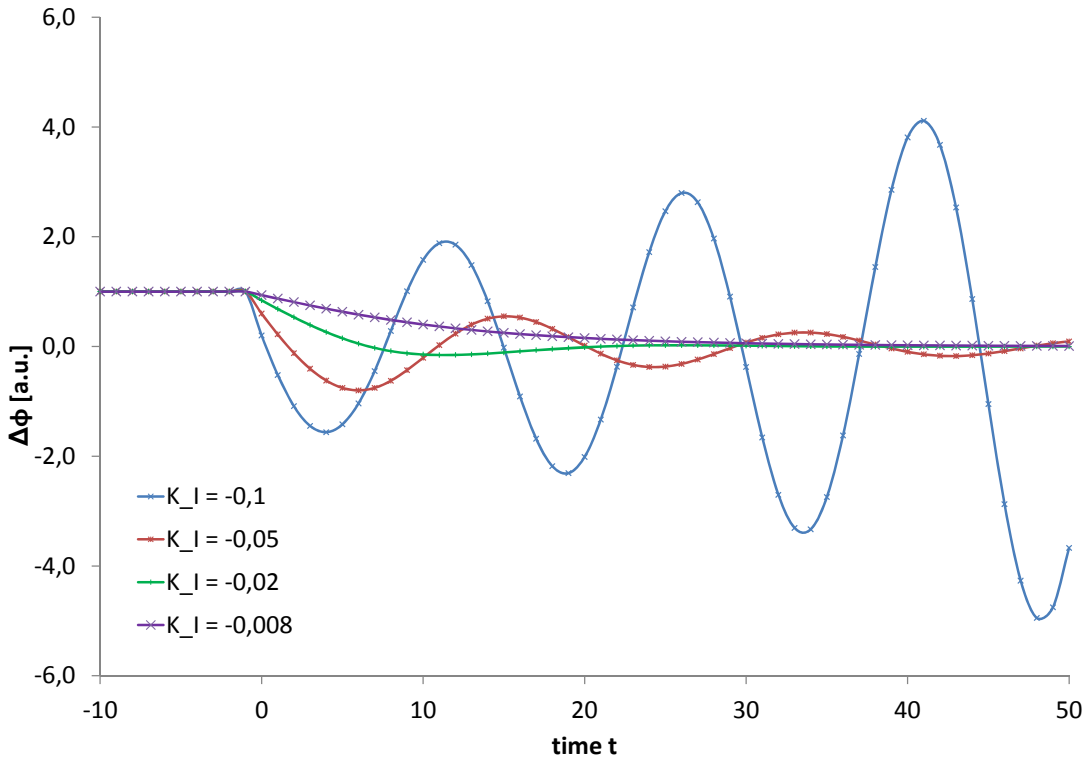

Figure 2.4.: Simulation of the start-up of the discrete PLL with only an I-controller based on equation 2.19. K_P and K_D are both set to 0 to demonstrate the effect of the I term.

$$\Delta\phi(t) = A \sum_{m=0}^{t} \left(K_P \cdot \Delta\phi(m-1) + K_I \cdot \sum_{n=1}^{N} \Delta\phi(m-n) + K_D \cdot (\Delta\phi(m-1) - \Delta\phi(m-2)) \right) + \dot{\phi}_{noise}(t) \quad (2.20)$$

The additional $\dot{\phi}_{noise}(t)$ is added to be able to model disturbances and noise as the rest of the term is simulating the complete synchronization as an ideal case. It would also have been possible to add this at an earlier stage, for example, as a time dependent part of l or of ϕ_2 or other variables that might be seeing temporal drifts, for example, due to temperature changes. Also $\dot{\phi}_{noise}(t)$ allows to consider changes in the setpoint. The temporal evolution of $\dot{\phi}_{noise}(t)$ is $\phi_{noise}(t)$ and will also be called *setpoint* now. There is no difference in the loops behavior if it has to follow a desired change of setpoint or an undesired change due to noise. It is more intuitive to consider the setpoint $\phi_{noise}(t)$ and the position of the controlled variable $\phi(t) = \phi_{noise}(t) - \Delta\phi(t)$ instead of $\Delta\phi(t)$ which

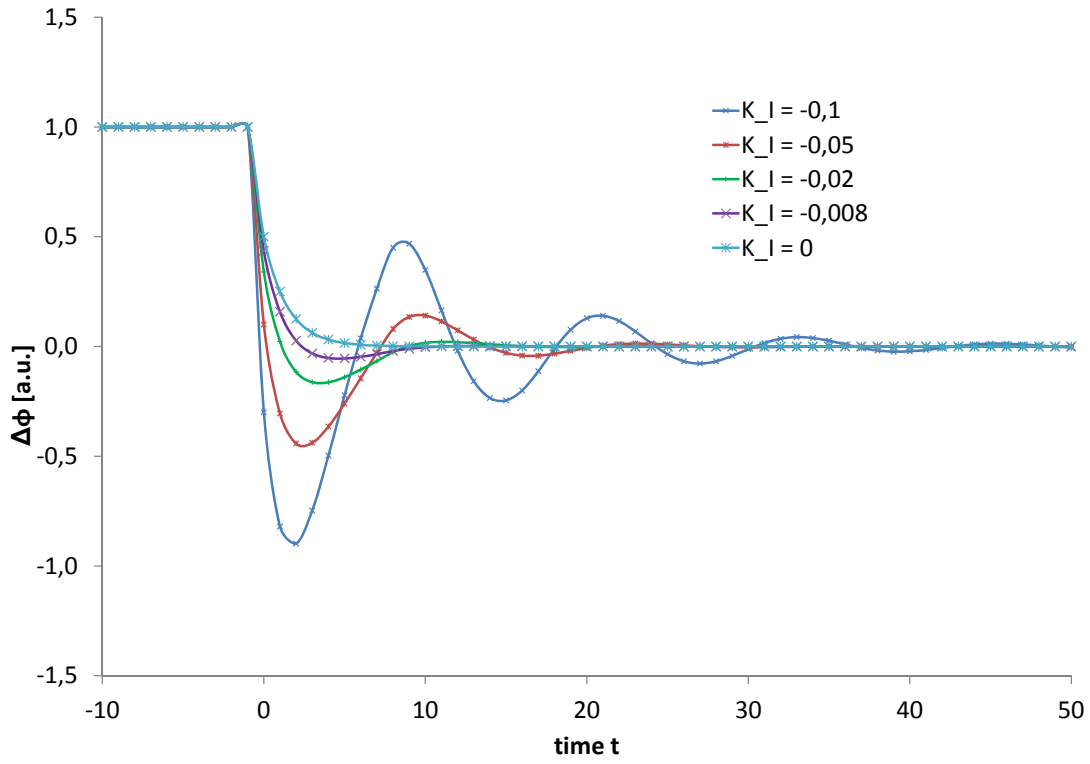

Figure 2.5.: Simulation of the start-up of the discrete PLL with P- and I-controller based on equation 2.19. K_D is still set to 0 to demonstrate the effect of the P and I term together. For all curves here $K_P = -0,5$.

is a measure how far the locked variable is off the setpoint - and, therefore, the value to minimize. In the discrete world $\dot{\phi}_{noise}(t)$ is $\phi_{noise}(t) - \phi_{noise}(t-1)$.

This allows to consider the effect of the I-term again in figure 2.6.

To consider the effect of a D-term, in figure 2.7 the phase error as well as the phase are shown for the start-up process with an offset of 1 when closing the loop at $t = 0$ and additionally the same ramp which illustrated the effect of the I-term in figure 2.6. The D-term can compensate for the overshoot while preserving the possibilities of the I-term. As can be seen for too large absolute values it can lead to instabilities as well. It also can be seen that, for example, the red curve for $K_D = -0.2$ at the ramp leads to a smaller phase error $\Delta\phi$ than the PI-controller as well as the P-controller while it can only compensate partly for the overshoot of the PI-controller at the step at the beginning. Therefore, the reasonable choice of the PID parameters is also depending highly on the expected types of changes in $\phi(t)$.

Having all the PID parameters examined in examples, one can finally have a look at the loops behavior on different possible drifts or types of noise (see figure 2.8). This is simulated here with the setpoint. In the mathematical model it makes no difference whether the actual reference is changed or the VCO drifted away - in both cases the

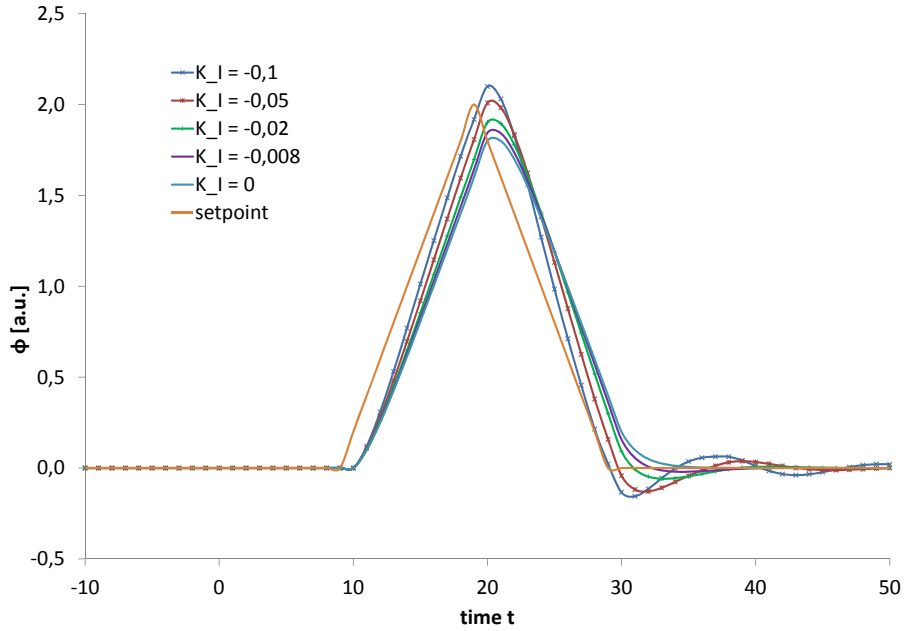

(a) $\phi(t)$ for a PI-controller with various values for K_I

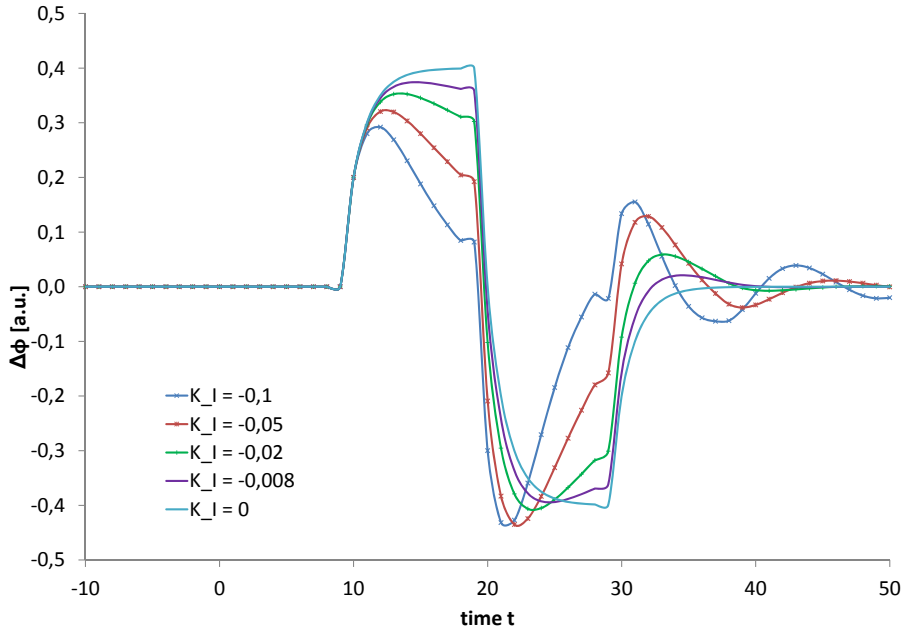

(b) $\Delta\phi(t)$ instead of $\phi(t)$ as in figure 2.6a.

Figure 2.6.: In cases of drifts in constant direction I-terms consider the history of the error signal and reduce the difference to the reference while the single P-term keeps an offset. However, this leads as well to overshooting if the drift changes direction. Figure 2.6b illustrates even better that the I-terms reduce the offset which in P-term case stays. It also shows the behavior if the direction of the drift changes. See 2.6a as well to view the exact type of drift by looking at setpoint. For all curves here again $K_P = -0.5$.

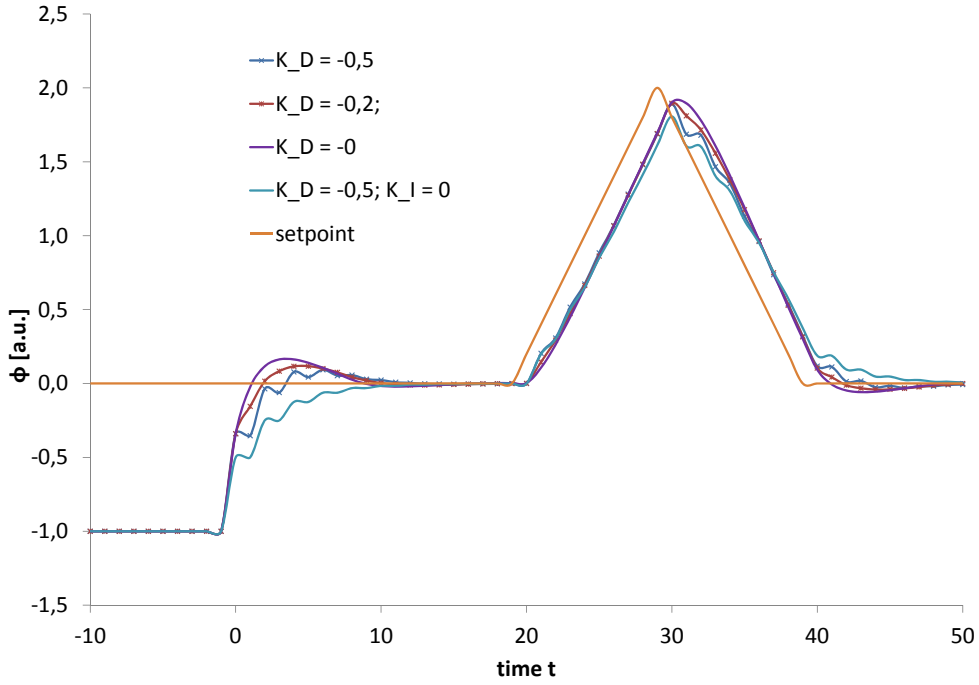

(a) $\phi(t)$ for different K_D

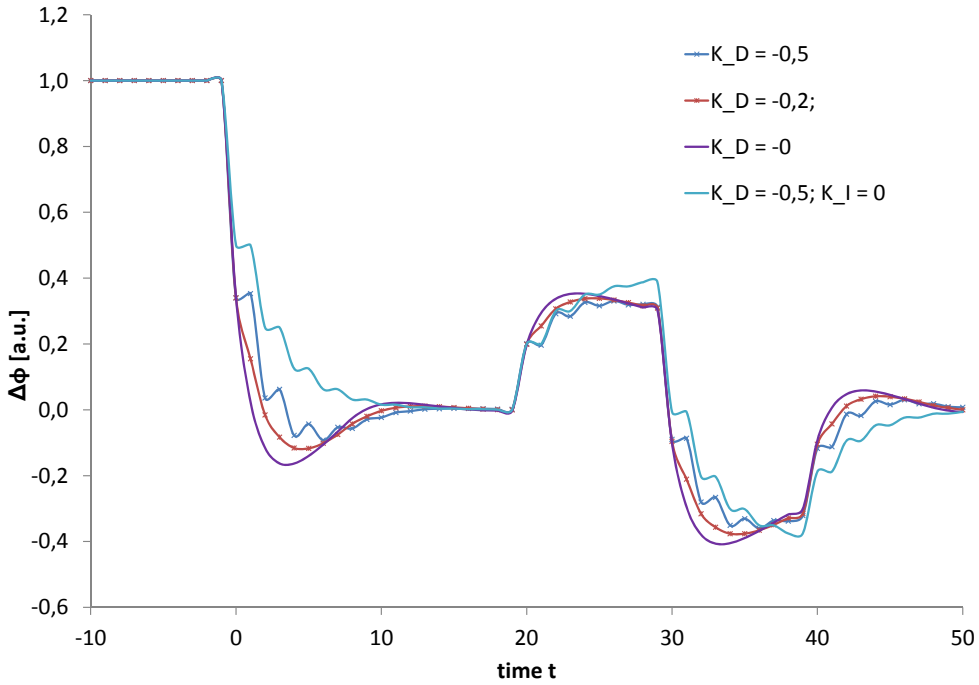

(b) $\Delta\phi(t)$ for different K_D

Figure 2.7.: The D-terms impact is illustrated for various values of K_D here. If not stated otherwise in the graph $K_I = -0,02$ and $K_P = -0,5$.

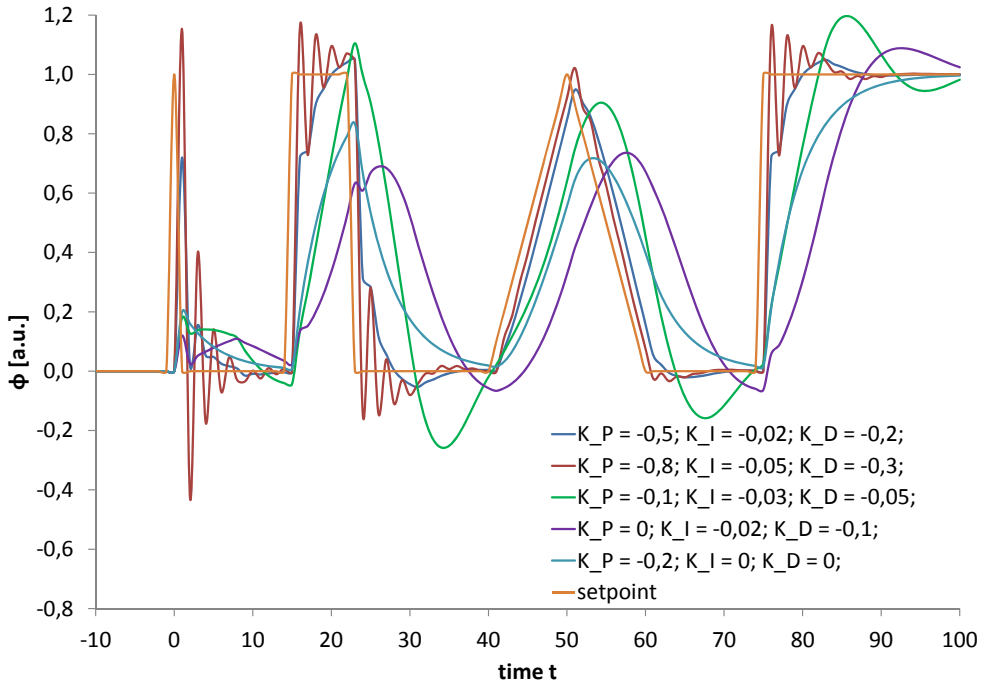

(a) $\phi(t)$ for different PID values

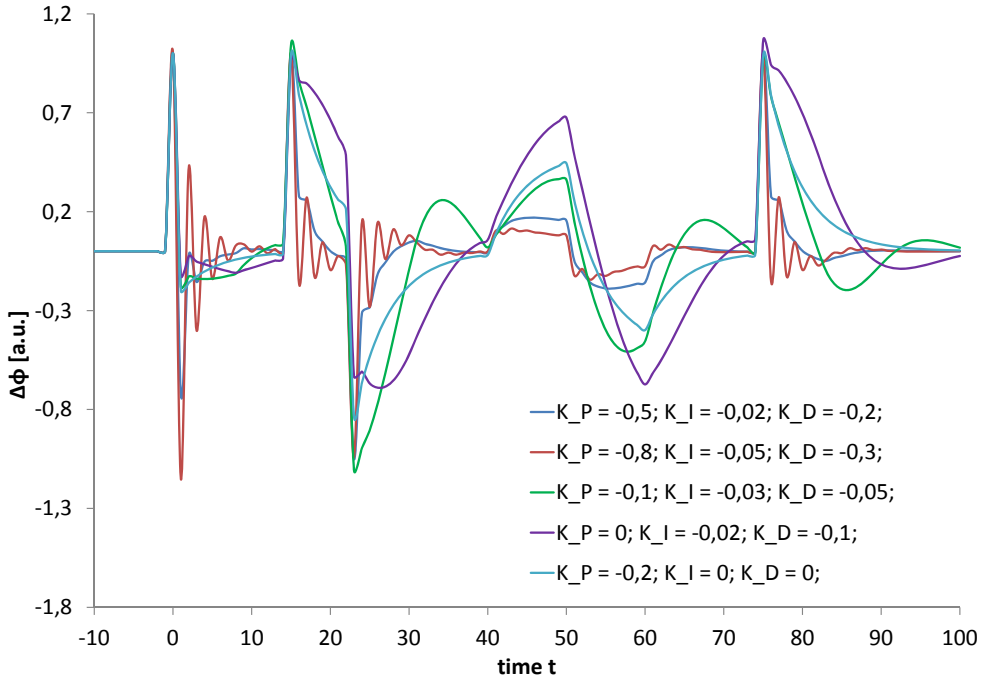

(b) $\Delta\phi(t)$ for different PID values

Figure 2.8.: Response of the PLL for various PID values when confronted with impulse, rectangular, ramp and step function

phase difference increases and, therefore, the loop will react the same way. To illustrate various possible changes of the reference the setpoint undergoes a series of different kinds of variations: Starting locked the setpoint describes an impulse, followed by a rectangular function, then a ramp up and back to zero again and finally a step function. The combination of P, I and D from the examples before is used and there are further examples of sets of parameters illustrating once more that a fast and strong response on errors is paid for by increased overshot, oscillations and also a strong response on short-time changes in error that then relaxed faster than the response of the loop. On the other hand smoother setting can lead to being far off the setpoint for a longer time and in cases where the direction of the noise changes often it can even mislead instead of compensating.

2.3. Visible Light Source

2.3.1. Laser

Laser (Light Amplification by Stimulated Emission of Radiation) describes a principle (or a device based on that principle) where the interaction between electromagnetic waves and matter allows to create light sources with high coherence, narrow spectral width and also highly parallel beams. It was first experimentally demonstrated in 1960 by T. H. Maiman [59] while the concept was known for *masers* (Microwave Amplification by Stimulated Emission of Radiation) before and it was expected to be transferable to light as well (see, for example, [74], note that lasers were called *optical masers* back then).

Lasers are nowadays powerful tools in science but as well widely established in everyday life as well as various other disciplines beginning with laser pointers, optical drives (CD, DVD, Blu-ray), lasers as lightsources in spectroscopic or tomographic measurements, lasers used for material processing in industries as well as in medicine and many many more.

The phenomenon that lasers are based on is *stimulated emission*. It was predicted by Einstein (as "Zustandsänderungen durch Einstrahlung") in 1916 - see [32][5] - already (for a brief historical synopsis on the evolution of the fundamental theoretical considerations see introductory chapters of [73]) It is the effect, that besides absorption and spontaneous emission there is a third type of interaction between matter and electromagnetic radiation: A photon passing a suitable excited state can lead to a decay of this state, not spontaneously but *stimulated*, meaning that the new photon figuratively speaking accompanies the original photon i.e. it has the same direction, frequency, polarization and phase being like a "clone" of the original one. Stimulated emission thus can be considered the complement of absorption.

This effect is used in lasers to produce continuous or pulsed light beams. All lasers have in common that they use a laser active media where stimulated emission can occur[6]. Nowadays there are a huge variety of possible laser active media and lasers are often classified according to its state of matter (solid-state lasers, gas lasers, dye laser (usually in liquid solution)). Furthermore, one can categorize, for example, the solid-state lasers by their setup (for example fiber lasers, disk lasers, semiconductor lasers, ...).

To amplify a signal within a laser active media it is necessary to obtain and maintain a so called *population inversion*. It describes the situation where more atoms are in the excited state E_2 than in the ground state E_1, thus more stimulated emission than absorption occurs. To reach this the media needs to be pumped (often optically). Only if this is true a gain can be achieved.

If only these two levels - illustrated in figure 2.9a - exist population inversion can never be achieved: Pump beam as well as the desired beam (seeded by spontaneous emission)

[5] [73] quotes 1917 as the paper has been reprinted in Physikalische Zeitschrift 18/1917

[6] There might be devices called "laser" that do not in a strict sense fulfill this criteria - like free electron lasers, for example - however, this is due to related or similar properties but is out of scope for this work.

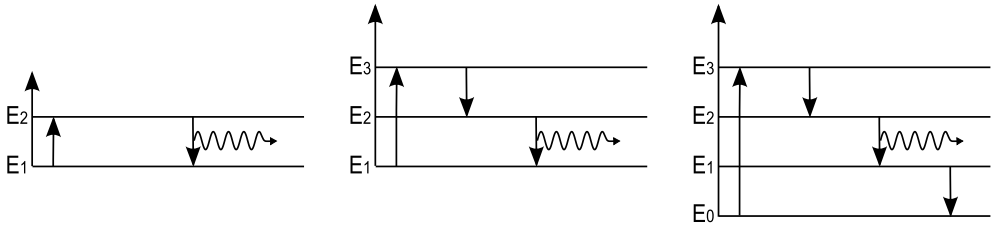

(a) Hypothetical 2 level gain media (b) 3 level gain media (c) 4 level gain media

Figure 2.9.: Easy 2,3 and 4 level models supporting the explanations on population inversion

needed to have the same frequency and thus both would cause absorption and stimulated emission alike. As the occurrence of absorption is proportional to the number of ground states and that of stimulated emission to that of the excited state there will be always be more absorption (thus no amplification) unless population inversion is reached which cannot be reached as from the moment that both states are as often there will be no further change any more. As additionally spontaneous emission occurs this upper limit is even lower.

Thus to be able to reach population inversion at least a third energy level is necessary. A higher excited state E_3 with $E_1 < E_2 < E_3$ decaying fast (compared to the lifetime of E_2) into E_2 solves the problem that the pump photons can also cause stimulated emission and thus annihilate their work. Thus pumping to E_2 can be done much more efficient. This is illustrated in figure 2.9b. In this scenario population inversion can be reached, however, the laser beam to be amplified still can be absorbed putting atoms on the level E_1 to E_2.

Introducing a fourth energy level E_0 with $E_0 < E_1 < E_2 < E_3$ (as illustrated in figure 2.9c) can avoid this loss: Provided that the lifetime of electrons on E_1 decaying into E_0 is again fast, it is assured that there are approximately no electrons in the states E_1 and E_3, thus pumping from E_0 to E_3 occurs only in this direction and then E_3 electrons "immediately" populate E_2. Photons with $\Delta E = E_2 - E_1$ originating from spontaneous emission can then stimulate electrons on E_2 to emit an identical photon, thus amplifying the beam. As E_1 is immediately depopulated towards E_0, the opposite effect of absorption does not occur. Thus a population inversion between E_1 and E_2 is ensured. It should be noted that in real gain media further intermediate levels might occur.

For this work the focus is on solid state lasers with a traditional setup. It is shown in figure 2.10:
Two mirrors are set up around the active medium to have an optical path passing various times through the active media. This setup is called *cavity* or *oscillator*. Photons from spontaneous emission that have by chance that direction will pass the active medium often thus causing many further photons by stimulated emission to go the same optical path. The optical path may be folded by further mirrors (or other optical devices like

i.e. prisms). This, however, does not change the principle operation.
For pumping other lightsources or diode lasers can be used[7].

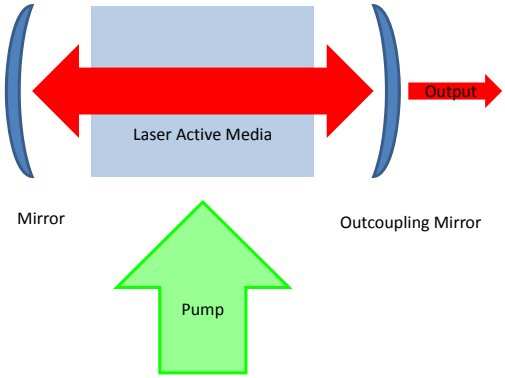

Figure 2.10.: Scheme of the optical resonator (or cavity or oscillator)

The optical path length - and therefore in pulsed operation also the repetition rate - can be subject to drifts caused by various quantities such as air pressure, temperature or humidity. Studies on the effect of temperature, pressure, humidity and CO_2 concentration on the refractive index of air have already been combined and discussed in 1966 [31] and since then been updated and adapted (see for example [66], [25], [17]). From the simplified formulas as suggested in [66] for typical laboratory conditions in the ideal case (dry air at 20 °C, 100 kPa and 0.04 % CO_2) the refractive index would be n = 1.0002659583212 for a wavelength of $\lambda = 1000$ nm. As those formulas suggest for the refractive index n to be dependent on the pressure p as $(n-1) \propto p$ this would cause an optical path of 3.6 m in an oscillator[8] to change roughly by 1 μm for a change in air pressure by 1 hPa. Furthermore, those formulas suggest that the considered optical path would decrease by 0.4 μm for each increase of the relative humidity by 10 percentage points (all other parameters kept stable). For a temperature drift of 1 °C the optical path decreases around 3.4 μm. This does not consider possible thermal elongations of the laser components, yet. Thus also in air conditioned labs with rather stable conditions laser systems are subject to drifts. Compensating them as described in chapter 4 therefore demands the possibility to manipulate the optical path in the order of several μm.

(Passive Kerr Lens) Mode Locking

Mode locking is a technique to generate ultrashort pulses from laser oscillators. The fundamental principle is based on the fact that enforcing the possible modes[9] in the oscillator to be in phase leads to the generation of pulses where the modes interfere

[7] This is not circular logic as laser diodes are not pumped optically but by electric current.
[8] A round trip length of 3.6 m is corresponding roughly to 83 MHz repetition rate as used in later chapters.
[9] i.e. the different possible standing waves

constructively. The existence of different modes is caused by the cavity length and the spectral width of the emission of the active media.

This chapter is mainly based on [73] and [72], but also inspired by [86] to allow a description covering the necessary information for the following chapters.

With an optical path length l, longitudal modes with wavelength λ are possible that fulfill the condition

$$N \cdot \lambda = 2 \cdot l \tag{2.21}$$

with N being an integer and $2 \cdot l$ being the optical path l back and forth. Additionally, relevant modes need to be within the bandwidth of the gain media.

The possible modes are equidistant in frequency (with $f = \frac{c}{\lambda}$ and equation 2.21):

$$\Delta f = f_{N+1} - f_N = \frac{c}{\lambda_{N+1}} - \frac{c}{\lambda_N} = \frac{c}{\frac{2l}{N+1}} - \frac{c}{\frac{2l}{N}} = \frac{c}{2l} \tag{2.22}$$

The superposition of various modes forming pulses is illustrated in figures 2.11 and 2.12 where the intensity (squared amplitude) of $2 \cdot K$ different modes with

$$I(t) = \left(\sum_{k=-K}^{K} cos((\omega + K \cdot \Delta\omega)t) \right)^2 \tag{2.23}$$

are calculated for various K. It can be seen that the more modes are combined (with

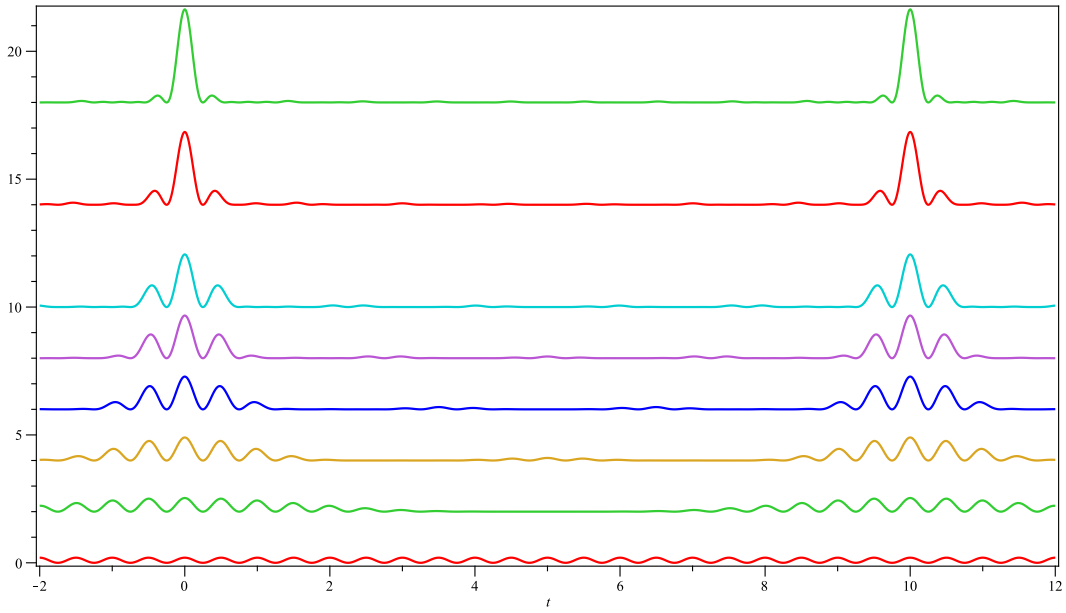

Figure 2.11.: Intensity of the superposition of various modes according to equation 2.23 for $K = \{0; 1; 2; 3; 4; 5; 7; 9\}$; normalized to average intensity; offset of $2K$ for better perceptibility. Small K allow to study the formation of the pulse.

fixed phase) the more a pulse is shaped getting higher and more narrow with every mode

contributing. To illustrate the formation of the pulse in figure 2.11, only few combined modes are shown. The narrowing of the pulse can better be seen when more modes are combined, which is shown in figure 2.12. In both cases, parameters of equation 2.23 have been chosen with a focus on the illustration of the formation of pulses.

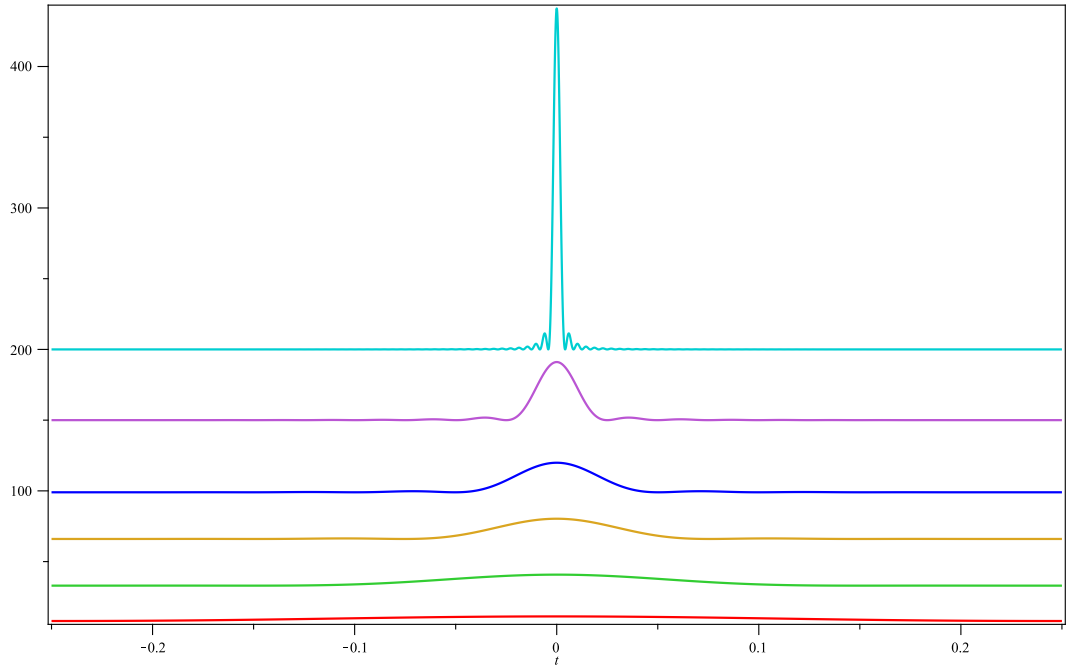

Figure 2.12.: Intensity of the superposition of various modes according to equation 2.23 for $K = \{8; 33; 66; 99; 200; 1200\}$; normalized to average intensity; offsets of $\{8; 33; 66; 99; 150; 200\}$ for better perceptibility. Larger K allow to study the narrowing of the pulse.

The mode-locking can technically be achieved in different ways, however, they all do have in common that within the oscillator a modulation of the cavity losses or the gain synchronized to the roundtrip time are necessary. This can be achieved by an active device synchronized with the roundtrip time modulating the resonator losses or gain (active mode locking) or passively by intensity depending processes inside the cavity supporting stronger fluctuations while repressing weaker ones. Here, the focus is on passive mode locking which allows even shorter pulses as the speed of the involved processes can be faster than actively controlled devices. A typical way to implement passive mode-locking is to use a saturable absorber or a mechanism leading to saturable absorption. A saturable absorber will - as the name suggests - attenuate small intensities but - if being saturated - not effect large intensities any more. Thus, in the cavity modes with decreasing intensities then also only get less and less amplified and, therefore, vanish while strong intensities take unresisted part in the gain process further on. Thus modes get locked the way that only those contributing to the strongest peak survive while all others get attenuated.

In case of Kerr lens mode-locking the saturable absorber is based on the effect, that for an intensity dependent refractive index an intensity dependent focusing (or defocusing) occurs. This is called a *Kerr lens*. In a media where focusing occurs for higher energies the saturable absorber can be completed by adding an aperture thus the unfocused lower intensities get clipped. As a consequence, they lose energy and are also subject to smaller gain. The aperture can also be induced by other concepts such as for example the gain media being pumped only in the focus [18].

As the intensity dependence of Kerr lensing is not only spatial but also temporal, the rising edges of the intense pulse get attenuated as well thus the pulse also becomes shorter.

Mode-locking can be started from intensity fluctuations occurring within the oscillator. A strong fluctuation is subject to the described Kerr lens effect and will start mode locked operation by seeding an intensity that then is amplified and shaped as described above. Such a fluctuation can be caused by deploying a shock on a part of the beam path. In the used PHAROS system (see chapter 3.2.1) mode-locking is started with a (motorized) hit on a prism within the oscillators beampath.

CPA

Chirped pulse amplification (CPA) is a technique to achieve laser pulses with high peak power avoiding the limitations of the damage threshold of the lasers gain media. It was demonstrated by Strickland and Mourou in 1985 [79] and is an established technology meanwhile and widely used to produce short pulses with high power. Also the commercial PHAROS laser includes an amplifier based on CPA.

Illustration 2.13 shows an abstract representation of an amplified pulse by CPA.

CPA allows increased peak power by stretching the pulse in time, amplifying the pulse which is then longer but with smaller peak intensity in a gain media and afterwards recompressing it. Thus the damage threshold of the gain media is not the limiting factor any more. The stretch can be reached in different ways such as gratings or prisms where the path for different colors varies and, therefore, the pulse gets chirped.

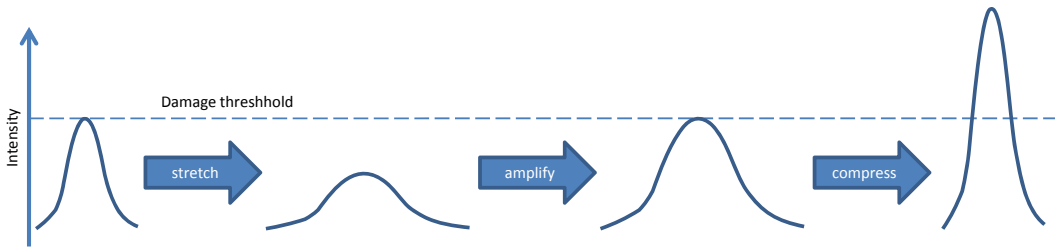

Figure 2.13.: Basic idea of CPA: The first step is to stretch the pulse with a peak intensity already at the destruction limit (symbolised as line here) of a gain media in time. The longer pulse can then be amplified again and be compressed afterwards leading to an amplified pulse with a possible peak energy above the destruction limit of the gain media.

The amplification process itself is in principle the same as lasing, however, instead of spontaneous emission the stretched pulse seeded into the gain media is subject to gain.

2.3.2. Non-Linear Optics

To be able to follow the description of the laser system and its frequency conversion units some basics of non-linear optics are necessary. In strong lightfields, well known linear optics are not sufficient to describe nature any more. Since lasers are available to produce the necessary high intensities also the non-linear optics became accessible experimentally and in technological applications as well. The fundamental effect can be illustrated by considering a spring pendulum (or any other comparable system typically described as harmonic oscillator) where for small amplitudes the force is proportional to the amplitude. However, if the spring gets overstretched this is not valid any more. This picture might help to motivate why for huge electromagnetic fields the polarization of a material also can show non-linear properties (i.e. electrons being "pulled back" non-linearly).

For this work mainly non-linear phenomena with an intensity dependent so called *second order susceptibility* $\chi^{(2)}$ are important. The description here follows [72] and more loosely [73], both are suggested as further readings to obtain a broader overview.

The susceptibility states the property of a material to be polarized within an electric field[10] and thus in linear case is the constant of proportionality. In materials where it is dependent on the amplitude of the electric field as well it has typically been shown as series expansion:

$$\boldsymbol{\chi}(\mathbf{E}) = \boldsymbol{\chi}^{(1)} + \boldsymbol{\chi}^{(2)}\mathbf{E} + \boldsymbol{\chi}^{(3)}\mathbf{E}\mathbf{E} + \ldots \tag{2.24}$$

where $\boldsymbol{\chi}$ in anisotropic media becomes a tensor.

Thus the polarization becomes:

$$\mathbf{P} = \sum_m \mathbf{P}^{(m)} \tag{2.25}$$

$$= \sum_m \epsilon_0 \boldsymbol{\chi}^{(m)} \mathbf{E}^m \tag{2.26}$$

$$= \epsilon_0 \boldsymbol{\chi}^{(1)}\mathbf{E} + \epsilon_0 \boldsymbol{\chi}^{(2)}\mathbf{E}\mathbf{E} + \ldots \tag{2.27}$$

To illustrate various non-linear phenomena the superposition of two plane waves is assumed[11]:

[10] i.e. the light field

[11] plane waves are not just an example but also a typical approximation when only considering small parts of other kinds of waves

$$\mathbf{E}(\mathbf{x},t) = \Re\left[\mathbf{E}_1 e^{-i(\mathbf{k}_1\cdot\mathbf{x}-\omega_1 t)} + \mathbf{E}_2 e^{-i(\mathbf{k}_2\cdot\mathbf{x}-\omega_2 t)}\right] \tag{2.28}$$

$$= \frac{1}{2}\left[\mathbf{E}_1 e^{-i(\mathbf{k}_1\cdot\mathbf{x}-\omega_1 t)} + \mathbf{E}_2 e^{-i(\mathbf{k}_2\cdot\mathbf{x}-\omega_2 t)} + \mathbf{E}_1^* e^{i(\mathbf{k}_1\cdot\mathbf{x}-\omega_1 t)} + \mathbf{E}_2^* e^{i(\mathbf{k}_2\cdot\mathbf{x}-\omega_2 t)}\right] \tag{2.29}$$

with $\mathbf{E}_1$ and $\mathbf{E}_2$ being the complex amplitude. Then the second order polarization $\mathbf{P}^{(2)}(\mathbf{x},t)$ can be expressed as:

$$\mathbf{P}^{(2)}(\mathbf{x},t) = \epsilon_0 \boldsymbol{\chi}^{(2)} \quad \mathbf{E}(\mathbf{x},t)\mathbf{E}(\mathbf{x},t) \tag{2.30}$$

$$= \epsilon_0 \boldsymbol{\chi}^{(2)} \left(\frac{1}{4}\Big[\quad \mathbf{E}_1 e^{-i(\mathbf{k}_1\cdot\mathbf{x}-\omega_1 t)} \quad + \mathbf{E}_1^* e^{i(\mathbf{k}_1\cdot\mathbf{x}-\omega_1 t)} \right.$$
$$\left. + \mathbf{E}_2 e^{-i(\mathbf{k}_2\cdot\mathbf{x}-\omega_2 t)} \quad + \mathbf{E}_2^* e^{i(\mathbf{k}_2\cdot\mathbf{x}-\omega_2 t)} \Big]^2\right) \tag{2.31}$$

$$= \epsilon_0 \boldsymbol{\chi}^{(2)} \left(\frac{1}{4}\Big[\right.$$
$$\mathbf{E}_1^2 e^{-i2(\mathbf{k}_1\cdot\mathbf{x}-\omega_1 t)} \quad + \mathbf{E}_1^{*2} e^{i2(\mathbf{k}_1\cdot\mathbf{x}-\omega_1 t)}$$
$$+ \mathbf{E}_2^2 e^{-i2(\mathbf{k}_2\cdot\mathbf{x}-\omega_2 t)} \quad + \mathbf{E}_2^{*2} e^{i2(\mathbf{k}_2\cdot\mathbf{x}-\omega_2 t)}$$
$$+ 2\mathbf{E}_1\mathbf{E}_2 e^{-i((\mathbf{k}_1+\mathbf{k}_2)\cdot\mathbf{x}-(\omega_1+\omega_2)t)} \quad + 2\mathbf{E}_1^*\mathbf{E}_2^* e^{i((\mathbf{k}_1+\mathbf{k}_2)\cdot\mathbf{x}-(\omega_1+\omega_2)t)}$$
$$+ 2\mathbf{E}_1\mathbf{E}_2^* e^{-i((\mathbf{k}_1-\mathbf{k}_2)\cdot\mathbf{x}-(\omega_1-\omega_2)t)} \quad + 2\mathbf{E}_1^*\mathbf{E}_2 e^{i((\mathbf{k}_1-\mathbf{k}_2)\cdot\mathbf{x}-(\omega_1-\omega_2)t)}$$
$$+ \mathbf{E}_1\mathbf{E}_1^* + \mathbf{E}_2\mathbf{E}_2^* \quad + \mathbf{E}_1^*\mathbf{E}_1 + \mathbf{E}_2^*\mathbf{E}_2$$
$$\left.\Big]\right) \tag{2.32}$$

showing the appearance of different frequency components. Every line in equation 2.32 names a certain frequency component consisting of an expression and its complex conjugate (in the second "column"). To keep this structure the last line has not been combined.

Within the polarization components appear with frequencies two times the original frequencies respectively, with sum and difference of the frequencies as well as non oscillating static field. These polarization components also show the mathematical properties of a plane wave. Hence the assumed electromagnetic plane waves cause a plane polarization wave releasing a new electromagnetic wave:

$$\mathbf{E}_3(\mathbf{x},t) = \Re\left[\mathbf{E}_3 e^{-i(\mathbf{k}_3\cdot\mathbf{x}-\omega_3 t)}\right] \tag{2.33}$$

where for ω_3 and $\mathbf{k}_3$ apply different relations for the different frequency components. These so called *phase matching conditions* for this example are stated in table 2.1.

The phase matching conditions ensure that the polarization wave keeps a constant phase to the electromagnetic wave it serves as a source (this is directly visible from the

$\omega_3 = 2\omega_1$	$\mathbf{k}_3 = 2\mathbf{k}_1$
$\omega_3 = 2\omega_2$	$\mathbf{k}_3 = 2\mathbf{k}_2$
$\omega_3 = \omega_1 + \omega_2$	$\mathbf{k}_3 = \mathbf{k}_1 + \mathbf{k}_2$
$\omega_3 = \omega_1 - \omega_2$	$\mathbf{k}_3 = \mathbf{k}_1 - \mathbf{k}_2$

Table 2.1.: The different frequency components and their respective phase matching condition.

definition[12] of the **k**-vector which is a) perpendicular to the plane of constant phase[13] and b) has the length of the phase difference per unit length - thus a closed trail of the involved **k**-vectors is indispensable to obtain a constant phase ratio). Otherwise the contributions along the beam path would not be phase stable and thus interfere destructively.

To fulfill the phasematching condition is not trivial as the refractive index and thus the **k**-vector are frequency dependent. In an anisotropic media like, for example, a birefringent crystal the refractive index is different for different directions and orientations. Thus it is possible to find a beampath and polarization where the condition is fulfilled. Further possible ways to achieve phasematching include an adjustment of the temperature or the direction of the incoming beam(s).

It has to be mentioned that the generation of doubled, difference and sum frequency can also be considered in the photon model:

In this consideration the relation between the frequencies ω states energy conservation where either two photons disappear to generate one with higher frequency (energy) or the other way round. The phase matching condition would then correspond to conservation of momentum. This interpretation leads to the same results, however, it is not as easy to motivate why frequency changes occur at all and to explain the generation of certain harmonics..

Now it is possible to consider the non-linear effects that the frequency conversion units in the laser system as presented in chapter 3.2 are based on:

SHG

Second harmonic generation (SHG) as used in the HIRO setup (see chapter 3.2.2) can be understood by simplifying the incoming plane wave to just one monochromatic wave (i.e. $\mathbf{E}_2 = \mathbf{E}_1$, $\omega_2 = \omega_1$ and $\mathbf{k}_2 = \mathbf{k}_1$). Then equation 2.32 becomes:

$$\mathbf{P}^{(2)}(\mathbf{x},t) = \epsilon_0 \boldsymbol{\chi}^{(2)} \Big(\mathbf{E}_1^2 e^{-i2(\mathbf{k}_1\cdot\mathbf{x}-\omega_1 t)} + \mathbf{E}_1^{*2} e^{i2(\mathbf{k}_1\cdot\mathbf{x}-\omega_1 t)} + \mathbf{E}_1\mathbf{E}_1^* + \mathbf{E}_1^*\mathbf{E}_1 \Big) \tag{2.34}$$

[12] as can be found in many textbooks such as [49](equation 6.66 with explanations) or in [67] (chapter K.12) and of course as well in http://en.wikipedia.org/wiki/Wavevector (May 13, 2013)

[13] a.k.a. wavefront

The first case in table 2.1 is valid here and for SHG the phase matching condition in the plane wave example is $\mathbf{k}_3 = 2\mathbf{k}_1$.

As in real setups the phase matching conditions can never be fulfilled perfectly along the path, periodic modulations of the intensity occur so the length of the non-linear media needs to be adapted as well.

THG

Third harmonic generation (THG) could now be expected to be a process of third order susceptibility $\chi^{(3)}$ in accordance with the described way of SHG. Indeed this is a possible way [65], however, neither the way the harmonics module in the described laser system works nor the typical one [9].

Hence THG based on second order susceptibility $\chi^{(2)}$ is applied and explained: In this case two non-linear $\chi^{(2)}$ processes are applied sequentially. At first SHG as described is performed. The obtained second harmonic together with the remaining fundamental are brought together in a second non linear crystal, thus for the second stage the incoming waves from equation 2.29 are modified according to the findings of equation 2.34 $\mathbf{E}_2 = \mathbf{E}_1^2$, $\omega_2 = 2\omega_1$ and $\mathbf{k}_2 = 2\mathbf{k}_1$) and equation 2.32 becomes (reduced to the components relevant for $3\omega_1$ considerations):

$$\mathbf{P}^{(2)}(\mathbf{x},t) = \frac{1}{4}\epsilon_0\boldsymbol{\chi}^{(2)}\Big(\ldots \quad +2\mathbf{E}_1^3 e^{-i(3\mathbf{k}_1\cdot\mathbf{x}-3\omega_1 t)} \quad +2\mathbf{E}_1^{*3} e^{i(3\mathbf{k}_1\cdot\mathbf{x}-3\omega_1 t)} + \ldots \Big) \tag{2.35}$$

and thus the THG phase matching condition in the plane wave example is $\mathbf{k}_3 = 3\mathbf{k}_1$.

OPA

Optical parametric amplification or amplifier (OPA) describes a process or device based on frequency difference generation (typically) within a second order susceptibility $\chi^{(2)}$ non-linear process. Here, a laserpulse of low intensity, the so called *signal*, can be amplified by energy transfer from a strong pump pulse.

In equation 2.32, the fourth line of frequency contributions takes place in a way that a strong pump wave with the frequency ω_1 is combined inside the nonlinear medium with a so called *signal wave* of ω_2 (with $\omega_2 < \omega_1$). Then for fullfilled phasematching condition $\mathbf{k}_3 = \mathbf{k}_1 - \mathbf{k}_2$ a so called *idler wave* with $\omega_3 = \omega_1 - \omega_2$ is generated. This idler also interacts with the pump wave and thus amplifies the signal wave $\omega_2 = \omega_1 - \omega_3$ as the phasematching condition $\mathbf{k}_2 = \mathbf{k}_1 - \mathbf{k}_3$ is mathematical identical to the one for idler generation.

It might be more intuitive to consider this using the photon picture: A pump photon ω_1 is substituted by two photons signal and idler (ω_2 and ω_3 with $\omega_1 = \omega_2 + \omega_3$).

The length of the media also needs to be adjusted as with increased signal and idler intensities also the backwards process occurs i.e. $\omega_2 + \omega_3 = \omega_1$ which corresponds to two photons combining to one photon of sum frequency (and thus energy as well). In

equation 2.32 the sum frequency generation can be found in the third line. For this case, however, signal (ω_2) and idler (ω_3) are the waves to be considered thus leading to a reamplification of the original pump wave with ω_1.

White Light Generation

Another non-linear effect occurring in transparent media is *white light generation* (also: *continuum generation*). This is closely related to non-linear effects such as self-focusing[14] and self-phase modulation[73]. Some general considerations on different mechanisms and generally used models are illustrated in [20].

Important here is, that self-focusing and self-phase-modulation are based on the effect that strong lightfields can change the refractive index of the medium they travel through and thus effecting themselves (Kerr effect).

The phase Φ of a light wave having propagated the distance L through a medium of refractive index n is given by:

$$\Phi = \omega_0 t - \frac{2\pi}{\lambda_0} n \cdot L \tag{2.36}$$

with ω_0 being the original frequency and λ_0 the wavelength (in vacuum). If refractive index n is depending on the intensity $I(t)$ this causes a change in the instantaneous frequency $\omega(t)$:

$$\omega(t) = \frac{d\Phi}{dt} = \omega_0 \underbrace{- \frac{2\pi}{\lambda_0} \cdot L \frac{dn(I(t))}{dt}}_{\Delta\omega(t)} \tag{2.37}$$

Introducing a series expansion of $n = n_0 + n_1 \cdot I(t) + ...$ the first order for the change of the instantaneous frequency $\Delta\omega(t)$ shows a proportionality to the change of intensity:

$$\Delta\omega(t) \propto -\frac{dI(t)}{dt} \tag{2.38}$$

For light pulses equation 2.38 illustrates a shift to smaller frequencies (red shift) at the rising edge and to larger frequencies (blue shift) at the declining edge. Thus the pulse does not only show a broader spectrum but a chirp as well.

[14] Self-focusing has been mentioned in chapter 2.3.1 when discussing the Kerr lens. There it has the effect of pulse shortening and thus also spectral broadening.

2.4. Synchrotron Radiation Source

The time resolved experiments were carried out at the PETRA III synchrotron radiation source (or storage ring), therefore, the basics of the generation of synchrotron radiation are explained here.

A synchrotron is a long established scientific facility originating from the field of particle physics and is nowadays widely used as radiation source - even the research center this work was carried out has it in its name DESY (Deutsches Elektronen Synchrotron). The history of DESY and the applications of its huge experimental facilities also reproduces this change. The basic idea goes back to the mid of the last century. Some textbooks (like [63]) cite V.I. Veksler (or Weksler) as the inventor while others (like [83]) mention the McMillan paper [62] as well[15] (as this is not a thesis on history and the author is not able to read Russian publications no position is adopted here).

Within a synchrotron charged particle orbit in a vacuum and are kept on orbit by magnetic structures and are accelerated by electric fields.

Originally used for particle collision experiments, those circular particle accelerators have soon become interesting to scientists from many different professions. The reason is the emission of synchrotron radiation which originally was an undesired side effect of the circular path. Charged particles that are accelerated radiate[16]. This is known and described for various very different scenarios such as the dipole antenna or Bremsstrahlung.

While originally an unavoidable side product at the bending magnets used to force the particles on their circular path, nowadays synchrotron radiation is intendedly produced within so-called *undulators* being more complex magnetic structures optimized for the generation of synchrotron radiation (see chapter 2.4.1). A full overview of the historic evolution towards this kind of particle accelerator and the physical basics are shown on the timetable within the introductory chapter in [83]. The evolution of synchrotron sources itself is nicely presented in the introductory chapter of [14]. For this work the actual state of the art applied at PETRA III is of major interest with a focus on the aspects relevant for the synchronization (i.e. the "Masterclock") as well as those important for the experimental work (i.e. the properties of the undulator).

Synchrotron radiation has characteristic properties[14], therefore, being interesting for many disciplines:

- Tunable **energy** (wavelength or frequency)
- Controllable **polarization**
- Strong **collimation**
- High **average power**
- **Pulsed**

[15] so does wikipedia in the English as well as in the German version.

[16] A circular path needs an acceleration towards its center thus charged particles on a circular path radiate even if their angular velocity is constant.

An often stated property highly connected to collimation, intensity and energy is *brilliance*. Brilliance is defined as number of photons per source size and per solid angle and per time and per relative spectral bandwidth[17]. If the pulsed nature is included as well peak brightness is considered.

All circular accelerators are based on magnetic fields perpendicular to the orbit forcing the charged particle on its way. Thus Lorentz force F_L acts as centripetal force F_C:

$$F_L = q \cdot v \cdot B \tag{2.39}$$

$$F_C = \frac{m \cdot v^2}{r} \tag{2.40}$$

$$q \cdot v \cdot B = \frac{m \cdot v^2}{r} \tag{2.41}$$

$$r \cdot B = \frac{m \cdot v}{q} \tag{2.42}$$

with q being the particles charge, v its speed in the orbit plane, B the magnetic field perpendicular to it, r the radius of the orbit. Of course for higher energies relativistic effects on the mass need to be considered. However, equation 2.42 indicates that for increased momentum either the radius r or the magnetic field B needs to grow as well.

Synchrotrons as accelerators have a fixed radius thus the magnetic field in the bending magnets needs to be increased synchronized to the particles velocity. All the aforementioned considerations do not change in principle if taking into account that real synchrotrons are not perfectly circular but composed from circular sectors and straight segments.

The "synchrotron" as source of synchrotron radiation typically is not accelerating anymore and thus is considered a storage ring using its gain just to compensate for losses due to synchrotron radiation. It is then optimized to keep the beam propagating for a long time (thus "storage ring"). Therefore [83] calls it a "synchrotron frozen in time". Nevertheless, PETRA III might - in agreement with less strict lab-jargon - be called synchrotron instead of source of synchrotron radiation or storage ring in further chapters without imposing any confusion as no other synchrotrons are treated in this work.

The gain of velocity (and thus energy) of the charged particles is realized by electric fields. As orbiting particles in synchrotrons are pulsed no huge static field needs to be applied but strong alternating fields can be used. In case of PETRA III (and its ancestors) they are realized by cavities fed by klystrons. Hence those klystrons need to be synchronized with the revolution time of the storage ring. Thus a fundamental RF or "Masterclock" is necessarily distributed. This reference is of major importance for the synchronization of the laser system.

Synchrotrons are equipped with a lot of further devices such as multipoles to recollimate the beam, injectors to get the fast particles into it, the vacuum system, and many

[17] It is sometimes called *spectral brightness* or just *brightness* depending on the background. This discussion has even been published - see [64] for more details.

more that have no direct influence onto this work and thus stay unmentioned. For a much more detailed description of the involved parts in PETRA III see [14], information on all relevant parameters for this work as well as a description of the involved beamlines and pictures of the experimental hall for a true-to-life impression of the synchrotron can be found in chapter 3.1

2.4.1. Undulator

An undulator is a periodic magnetic structure where a beam of charged particles is forced on a sinusoidal path thus radiating. Undulators cause small deflection thus the radiations from various periods can interfere and narrow bandwidth and radiation cone can be achieved [12].

This chapter is based on [12] where everything is derived nicely. Its a highly recommended source for further information on undulators (not only) even though this is not its main topic.

A good start to understand undulators is the "Undulator equation":

$$\lambda = \frac{\lambda_u}{2\gamma^2}\left(1 + \frac{K^2}{2} + \gamma^2\theta^2\right) \tag{2.43}$$

With λ being the output wavelength, λ_u being the undulators "wavelength" i.e. the length of a pair of alternating magnetic structures, $\gamma = \frac{1}{\sqrt{1-(\frac{v}{c})^2}}$ is the Lorentz factor, and θ is the angle towards the direction of motion (of the charged particles through the undulator).

K is called *deflection parameter* or *undulator parameter* in different publications and is defined as:

$$K = \frac{eB\lambda_u}{2\pi mc} \tag{2.44}$$

The undulator equation can be interpreted vividly the following way: The factor in the beginning shrinks the emitted radiations wavelength compared with the undulator period twice. Once for the relativistic length contraction of the undulator period from the point of view of the particle, a second time for the relativistic doppler effect on the radiation. As this doppler effect is depending on the direction, a correction factor for angle dependence is added (last term of the sum). The second correction added is the undulator parameter. It can be motivated as the magnetic structure does not change the particles absolute velocity but its direction, the velocity component along the original axis is slightly smaller. This effect of course depends on the magnetic field and as well its oscillations. Therefore, K shows a dependence on B and λ_u. As B can be tuned by opening or closing the gap of the undulator (where the beam passes the periodic magnetic structure), an undulator allows to tune the photon energy independent, without applying changes to the charged particles inside the synchrotron ring. This enables many independent undulators for different kinds of photons to be installed and used at the same synchrotron at a time.

Synchrotron radiation from the electrons point of view is radiated in a torus-like way

This is the dipole radiation pattern: In the frame of reference where the electron was in rest before entering the undulator it will only oscillate along the magnetic field. However, due to the relativistic effect of length contraction in the lab frame this turns into a narrow cone. This cone gets narrower the bigger γ gets.

The whole derivations in detail are given in the mentioned source [12].

Because of the relative doppler effect on off-axis radiation monochromators are often used.

Using more advanced periodic magnetic structures than simply alternating also makes circular polarized emission possible instead[18].

2.4.2. Typical Values

Typical values of relevance for time resolved experiments at synchrotron radiation sources are presented here:

A compilation of the achievable energy and brilliance of various X-ray sources can be found in figure 2.14. The possible photon energy of synchrotron radiation from storage rings ranges from a few eV up to several hundreds of keV, highly depending on the undulator.

The revolution frequency (and thus revolution time) inside the storage rings is for example for PETRA III 130.1 kHz (7.685 μs), for ESRF 355 kHz (2.82 μs) and for SPring8 208.8 kHz (4.79 μs). As a huge variety of filling patterns (bunch modes) can be realized, the possible bunch intervals also cover a broad range. For the single bunch mode they are identical with the revolution time but much shorter intervals occur in higher bunch modes (for example PETRA III offers up to 960 bunches, ESRF up to 992 bunches, thus the interval also gets reduced by this factor). Also combinations of bunch trains and single bunches can be realized (for example at SPring-8), thus the actual time windows for time-resolved experiments need to be considered in advance. At PETRA III, 40 and 60 and 240 bunchmodes have been experienced during this work (corresponding to 192 ns, 128 ns and 32 ns time window between successive bunches).

The bunch duration - highly dominating the X-ray pulse length - is depending on bunchmode, beam current and further parameters. For ESRF given values are between 20 and 73 ps RMS, for PETRA III the design value is 44 ps RMS.

All values are taken from the respective homepages [4], [1], [6].

[18] This can be motivated in the electron frame of reference again if not a simple dipole oscillation is performed.

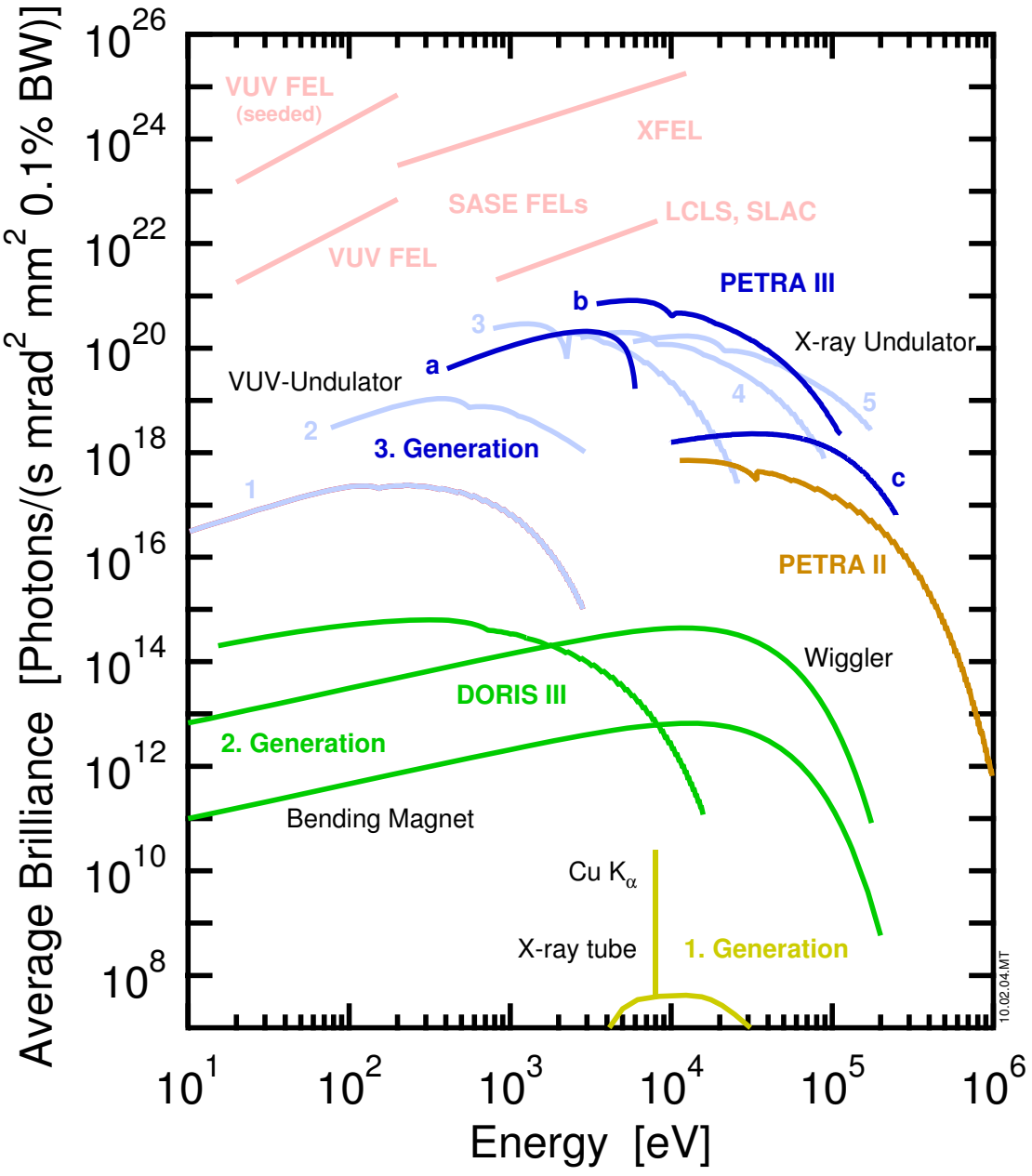

Figure 2.14.: Brilliance of various synchrotron radiation sources adapted from [14]. The numbers are standing for selected undulators of the storage rings (1) BESSY II ; (2) ALS; (3) DIAMOND; (4) ESRF; (5) SPring8.

2.5. Time Resolved X-Ray Absorption Spectroscopy

In this work first steps towards time-resolved X-Ray Absorption Spectroscopy (XAS) at PETRA III are presented. The focus is on the temporal information while the obtainable structural information is the focus of the attending work [30] by Benjamin Dicke. As molecular physics is a very broad field this section merely focuses on the necessary fundamentals to follow the later sections. For this purpose molecular physics basics are concentrated mainly based on [41] if not stated otherwise (and also inspired by [69]) while the time-resolved XAS basics are compiled according to [19].

2.5.1. Absorption, Fluorescence, and the Spectrum of Molecules

Molecules just as atoms can absorb photons. The energy is transferred then to an electron which is thus put into a higher electronic level or even into the continuum, i.e. it is unbound. Further processes in refilling the remaining hole in the electron shell (or also orbital in molecular cases) can lead to the emission of photons (fluorescence, phosphorescence) or Auger electrons. Absorption cross sections are typically larger if the incoming photons energy is suitable to the energy gap between two involved states.

The spectrum measuring the absorption of X-rays as a function of X-ray energy shows three general features (nicely summarized in [71]) being

- sharp rises (called *edge*) at the excitation energies of inner shell electrons
- a decrease with increasing energy
- oscillating structures above the edges called X-ray absorption fine structure (XAFS)

This is illustrated in figure 2.15. The position of the edges can be subject to so called

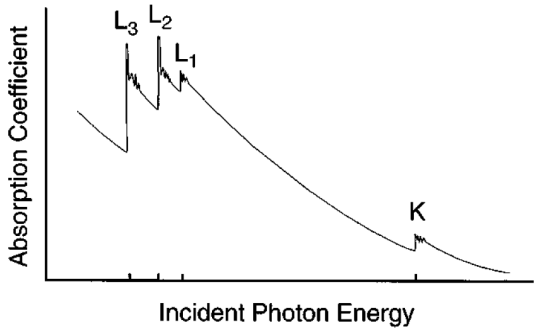

Figure 2.15.: General representation of the absorption coefficient as a function of X-ray energy. Figure taken from [71].

chemical shifts depending on the chemical environment or modification (summarized in [57]). Thus chemical and structural information can be obtained by measuring those primarily atomic parameters. Further structural information can be obtained from the

XAFS region. It originates from scattering of photoelectrons and is an important part in the attending work [30].

As with atoms the spectroscopic properties of molecules in the near-infrared (NIR), visible and UV regime are governed by electronic excitation. However, molecules offer additional vibrational levels and the electronic levels of electrons involved in the binding of the molecule are affected as well.

As the quantum mechanical description of larger atoms is already a difficult task demanding various approximations and advanced models, it is of little wonder that obtaining theoretical descriptions of those molecular orbitals is also a non-trivial task. To obtain suitable wave functions for molecules various further approximations and methods have to be used going beyond the scope of this work. For the interested reader wanting to inform himself on these methods a good start would be popular concepts as the Born-Oppenheimer approximation[19], the Franck-Condon principle[20], and molecular orbital theories based on linear combination of atomic orbitals[21].

For this work the existence of molecular orbitals with similar spectroscopic properties as those of atomic shells is of importance. They do show additional vibrational energy levels on electronic states. These orbitals can be categorized by symmetry (similar as the atomic shells s, p,... then named σ or π for example - many orbital illustrations are given in [29]).

For the spectroscopic considerations in this work the Jablonski diagram is the most important illustration of electronic states within the molecule.

The photo excitation of molecular orbitals can also cause inner shell electrons to be subject to a changed potential thus laser pumped XAS can measure a transient signal.

Jablonski Diagram

A Jablonski diagram[22] is the typical illustration of electronic excitation states in molecules of relevance for emission spectra. In figure 2.16 a typical diagram is presented. It illustrates the various possible channels of excitation.

For the spectrum only those involving a photon can be detected directly. This is absorption and fluorescence (marked with vertical straight arrows) and absorption and phosphorescence (marked with vertical dashed arrows to indicate that they are forbidden transitions due to the multiplicity, i.e. from singlet to triplet states or vice versa). A photon corresponding to the energy difference between the two involved states is emitted or absorbed respectively.

Furthermore, there exist two kinds of radiation free isoenergetic processes being internal conversion (horizontal arrow) and intersystem crossing (horizontal dashed arrow). Both are processes between levels of the same energy and thus no energy is released.

[19] roughly said splitting the wave function into separate terms for electrons and nucleus

[20] the probability of a transition depends on the overlap of the corresponding wave-functions, for a compact description see [80]

[21] discussed in detail in [69]

[22] named after Aleksander Jabłoński who used such a representation of electronic states within the molecule already in 1933[45]

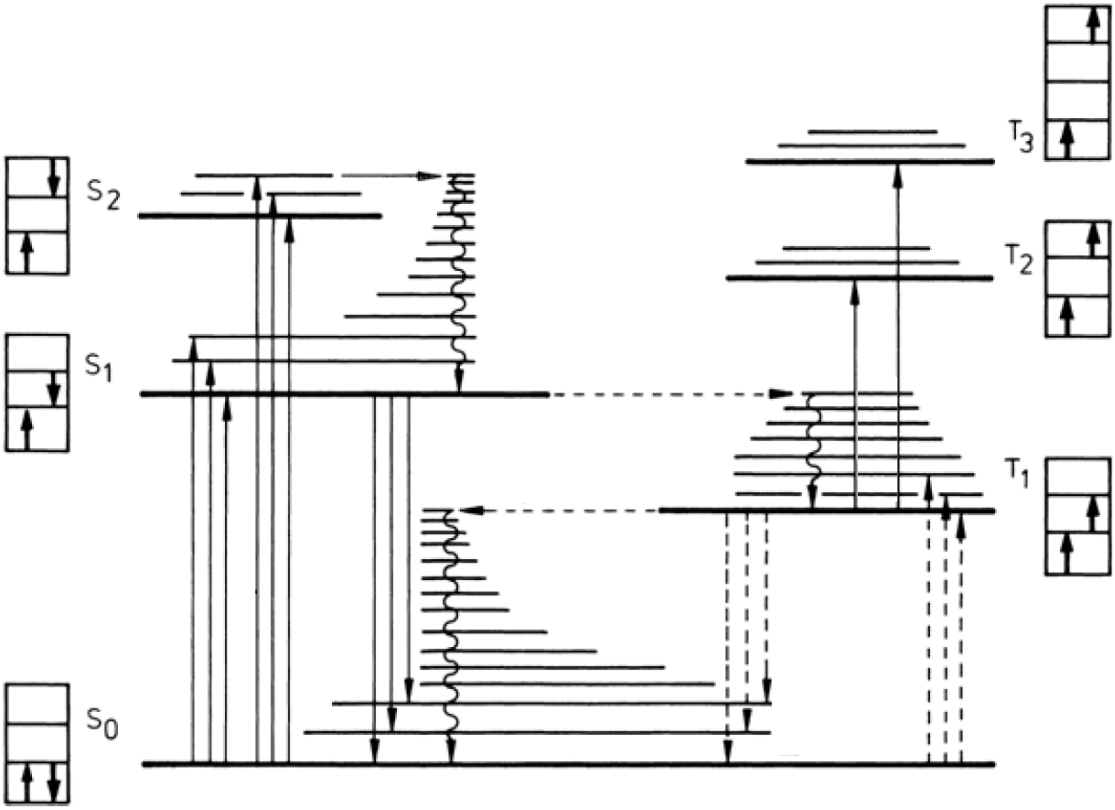

Figure 2.16.: Typical Jablonski diagram taken from [41]

However, some textbooks include following non-radiative relaxations (see below) into these terms (for example [41]).

Finally non radiative de-excitation can occur from higher vibrational levels to lower ones of the same electronic state (vertical sinusoidal arrows). The energy is transferred as heat to the surrounding.

As lifetimes are inversely proportional to the probability for relaxation the less likely processes (i.e. those that are considered forbidden) typically show longer lifetimes.

2.5.2. X-Ray Absorption Spectroscopy (XAS)

X-Ray Absorption Spectroscopy (XAS) describes a widely established method to analyze molecules, crystals and further assemblies of atoms. Therefore, it can meanwhile be found in textbooks like [11] and [35].

The X-ray fluorescence of a sample is examined depending on the X-ray energy in the region of an absorption edge of the target. Such an energy scan is presented in figure 6.7. XAS is typically divided into EXAFS (*extended X-ray absorption fine structure*) and XANES (*X-ray absorption near-edge structure*, sometimes also called NEXAFS - *near-edge X-ray absorption fine structure*) depending on the considered energy region

relative to the X-ray absorption edge. Both regions within the spectrum contain different information about the target. The XANES region around the edge contains information on electronic transitions and states just below the free electron state and multiply scattered electrons just above the edge while the EXAFS region starting ca. 50 eV above the edge contains information on the scattering of freed electrons at the nearest neighbor atoms [11]. Thus EXAFS contains further structural information.

XAS spectra are long known and a complex theory has been developed to analyze such spectra. First theoretical considerations on EXAFS can be found already more than 80 years ago [52]. Yet, according to [88], it was not before the 1980s or 90s that XAFS was developed "into a highly reliable and highly useful tool".

Time Resolved XAS

To be part of this work the described method still lacks the possibility to obtain temporal information as well. This has been introduced by pump probe methods (see chapter 2.1 for more details on the pump-probe method) typically using a synchronized laser system to pump the sample. An overview on methods of ultrafast structural dynamics classifying time-resolved XAS among other methods based on X-ray or electron diffraction and microscopy is given in [24]. A recent review on XAS to obtain molecular structural dynamics has been published by C. Bressler and M. Chergui [19] and is the foundation for this section.

A minimalistic scheme for time-resolved XAS is illustrated in figure 2.17. Laser and X-ray pulses are overlapped in space and time on the target. Detector D1 is used to normalize the measured data to the flux, detector D2 is measuring the actual X-ray fluorescence. It is necessary to control the temporal overlap or delay between laser and X-ray pulses to obtain temporal information.

Using a pump laser allows to measure structural information of the excited sample - after deducting the remaining unpumped contributions. This might need further examinations. Thus a pumped as well as an unpumped structure can be examined. In combination with a delay scan the lifetime of this structural change caused by the excitation can be observed.

Experimental Challenges

While being based on a rather simple principle occur nevertheless experimental challenges when performing such experiments. The transient between pumped and unpumped signal can be relatively small compared to the overall signal. Thus even smallest fluctuations of the overall signal can lead to large noise on the transient. Therefore, precautions have to be taken to ensure stable conditions. The spatial overlap of laser pulses, X-ray pulses and the sample might be subject to drifts, thus effort has to be made to stabilize the performance of the involved devices and to monitor meanderings, ideally allowing to compensate for or correct them. As at synchrotron facilities often the repetition rate of the synchrotron exceeds that of the laser system, also the data acquisition needs to account for the unpumped signals between the pumped ones. Furthermore,

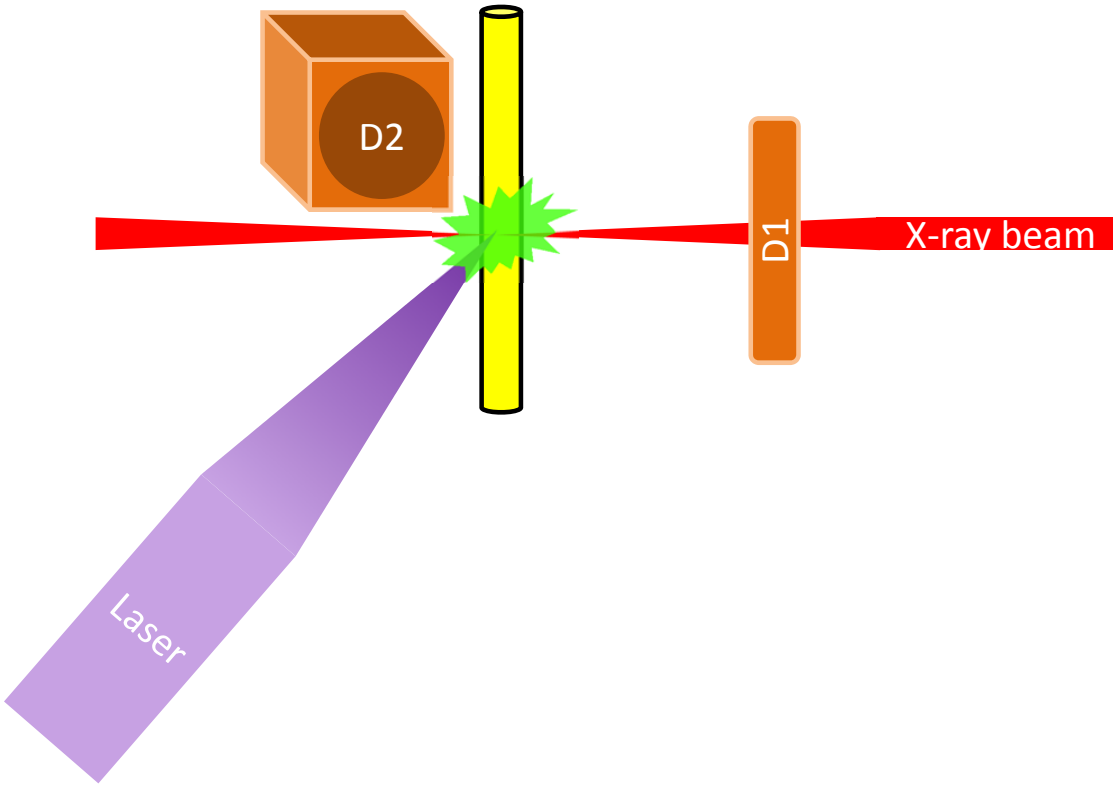

Figure 2.17.: Minimalistic scheme for time-resolved XAS

reaching temporal and spatial overlap of laser and X-ray pulses is a non-trivial task as the detection of both kinds of radiation can not always be carried out in the same way.

2.5.3. Expectable Characteristics of Delay Scans

Delay scans (see, for example, figure 6.8) contain two types of information. On the one hand, information on the temporal resolution. The rise time when the delay crosses the relative zero between pump and probe and, therefore, the change from probe-pump (no effect) to pump-probe with no delay (maximum effect) is examined. If the process is fast enough this rise contains information on the overall temporal resolution of the experiment and the synchrotron facility as well. This is discussed in chapter 6.1.2. On the other hand, the decay of the transient signal for longer pump-probe delays contains information about the examined sample and the pumped state in particular. As the pump has occurred earlier its effect - i.e. the excitation - has partly decayed depending on the lifetime of the pumped state (typically called excited state). In principle it can also be possible that the decay is a combination of different decay channels. An example of such a case can be found in [37], the different possible decay channels are illustrated in chapter 2.5.1 and illustrated in the general Jablonski diagram 2.16. Assuming the probed state is the pumped one or at least decayed from it faster than the temporal

resolution (as it would be the case in the mentioned example) there are a few possible interpretations of the data. It has to be considered in this case what can be read out of the data and what needs other ways of examination. In a system of different decay levels it needs to be considered which state(s) is or are the probed ones.

Figure 2.18 shows the possible interpretations of observed exponential decays in the data[23]: The representation of the models are highly simplified versions of Jablonski diagrams limited to only the probed state and decay channels. This way they are limited to and illustrate the in principle obtainable information from such delay scans. The simplest model is a single probed state A with a lifetime τ_1 as described in figure 2.18a.

In figure 2.18b the model has been extended to a single probed state A with two decay channels with lifetimes τ_1 and τ_2. In this case an exponential decay with the combined lifetime τ_c will be observed. It is connected to the two decay channels lifetimes in the following way: $\frac{1}{\tau_c} = \frac{1}{\tau_1} + \frac{1}{\tau_2}$. It can be seen that for big differences the combined lifetime is basically governed by the smaller lifetime. This is obvious as those decays occur correspondingly more often. As the larger lifetime still contributes a little the combined lifetime is smaller than both contributors. This would be valid also for more than two decay channels.

A further possible case is that two excited states with independent decay channels exist, but both are probed. This scenario - illustrated in figure 2.18c - leads to the linear combination of exponential decays as both excited states decay independently. This possibility could be observed within the delay scan as $A_A \cdot \exp^{-\frac{t}{\tau_1}} + A_B \cdot \exp^{-\frac{t}{\tau_2}}$. It cannot be combined to a single exponential decay.

Finally, also the possibility exists that the probed state is reached by one channel and further decaying via another. This is illustrated in figure 2.18d. This is described mathematically as the difference of two exponentials $\exp^{-\frac{t}{\tau_1}} - \exp^{-\frac{t}{\tau_2}}$.

Even though in principle combinations of all these possibilities could occur the observed overall delay scan will show only linear combinations (with positive sign in case c) and negative in case d)) of exponentials, possibly with combined lifetimes.

Especially linear combinations of exponential decays can be studied in logarithmic scale as well, where a straight line with change in slope will be observed.

Therefore, the physical information to be gained from the delay scan strongly depends on the fitted curves and their statistical relevance.

[23] The math behind those combined exponential decays is always based on a differential equation putting the change of a variable (number of excited samples) in relation to its value (possibly depending on time or other values) and a constant of proportionality (one over lifetime or often the reciprocal decayrate). This kind of math is also used in other fields of physics and, therefore, to be found in many textbooks, however, the nicest version I consider the description in Wikipedia about radioactive decay[24] also offering nice examples.

[24] http://en.wikipedia.org/wiki/Radioactive_decay#Mathematics_of_radioactive_decay (May 13, 2013)

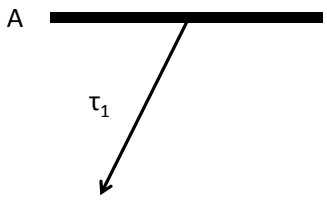

(a) Deacy from state A with one decay channel with lifetime τ_1 shows a $\exp^{-\frac{t}{\tau_1}}$ behavior.

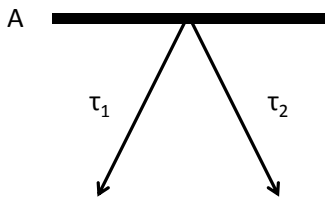

(b) Deacy from state A with two decay channel lifetimes τ_1 and τ_2 shows a $\exp^{-\left(\frac{1}{\tau_1}+\frac{1}{\tau_2}\right)t}$ behavior.

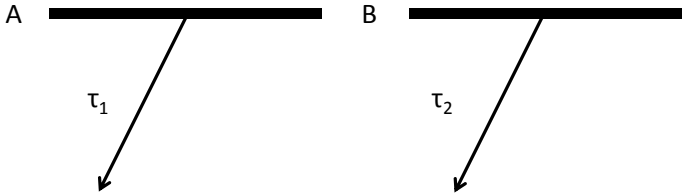

(c) Deacy of two probed states A and B with one decay channel each. Lifetimes are called τ_1 and τ_2 and the model shows a $A_A \cdot \exp^{-\frac{t}{\tau_1}} + A_B \cdot \exp^{-\frac{t}{\tau_2}}$ behavior.

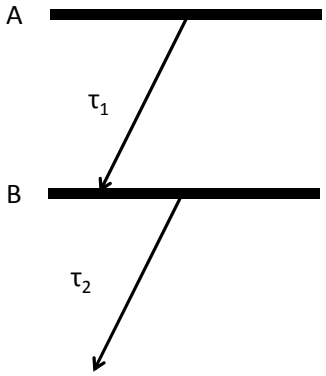

(d) Deacy of one probed state B reached by a decay with lifetime τ_1 and further decaying via τ_2 shows a $\exp^{-\frac{t}{\tau_1}} - \exp^{-\frac{t}{\tau_2}}$ behavior.

Figure 2.18.: Possible decays behind the observed data

3. Experimental Environment

3.1. PETRA III

PETRA III[1] is the latest synchrotron radiation source on the DESY site in Hamburg. The more than 2 km long electron/positron storage ring with the experimental hall with a length of about 300 m are dominant features on the DESY site. Pictures taken inside the experimental hall are shown in figure 3.1 illustrating the curvature and dimensions of the facility.

The physical basics and principles to understand synchrotron radiation and the devices described in this chapter have been explained in chapter 2.4.

Fundamental numbers and parameters relevant for this work are given in the following table 3.1. Most values are design values taken from the PETRA III and DESY Photon Science homepages [4], thus not all parameters might have been reached during the experiments. Values added to those from the stated references are marked with an * and are based on own observations during the experiments:

Length	2304	m
Positron energy	6.0	GeV
Number of positrons	4.8 10^{12}	
Positron beam current	100	mA (top-up mode)[2]
Available bunchmodes	40	
	60	*
	960	
Bunch separation	192	ns
	128	ns*
	8	ns
Bunch length (rms)	13.2	mm
Bunch duration (rms)	44	ps
RF[3]	499.564	MHz
Revolution time	7.685	μs
Revolution frequency	130.1	kHz
Harmonic number	3840	

Table 3.1.: PETRA III parameters

[1] PETRA is an acronym for "Positron-Electron Tandem Ring Accelerator", the number states that there were two earlier stages as particle collider and accelerator for HERA since the late seventieth

[2] In 40 bunch mode occasionally stable operation only with a reduction to 80 mA * has been possible.

[3] The actual RF distributed and used as reference might be slightly off (or the available ways to measure),

(a) View along the storage ring: On the right runs the storage ring, on the left beamlines are attached tangentially.

(b) View versus the direction of the beam at beamline P04

Figure 3.1.: Images of the PETRA III storage ring inside the experimental hall illustrating structure and dimensions of the facility.

A few comments on the RF value (radio-frequency) have to be made. This frequency is also distributed for synchronization purposes to the beamlines. For most applications reference signals are distributed to the experiments via the bunch-clock (called *Bunchuhr*). It is the device providing timing information and references for typical less time-critical experiments. The bunch-clock allows to shift its outputs temporally in ns steps. There is one standard downconverted reference signal used to feed the bunch-clock based on 40 MHz and having additional information modulated onto it. Further references can be recreated by the bunch-clock. The bunch-clock is in principle remotely controllable.

For timing sensitive experiments, however, the original 500 MHz signal is distributed with more effort to have a highly phase-noise reduced reference. This signal is called *Masterclock* or *Reference* within the description of the laser synchronization. The design value is not the value experienced during the setup of the laser synchronization. For the Masterclock there are four different values:

499.564 MHz according to design parameters

499.6655 MHz according to MKS conference proceeding [48].

499.662 MHz according to HP 8657B Signal Generator (no exact measurement, setting it to fit the PETRA III adjusted cavity)

499.6645 MHz according to Agilent E5052B Signal Source Analyzer

This is of major importance for synchronization issues of course as the PHAROS cavity needs to be designed to be oscillating at an integer (sub)harmonic of the reference. The first two values are numbers from DESY while the other two are own measurements. For the third value it needs to be mentioned that it was observed as a side product when the PHAROS cavity needed to be adjusted when visiting PETRA III for the first time or after servicing. After this adjustments the lab reference was adjusted to the newly aligned cavity leading to this value. It can be an important value to be able to pre-calibrate everything in the lab. The last measurement has been performed with the signal source analyzer which is described in chapter 5.2.4.

The last three values are all much closer to each other than to the design value thus a discrepancy of roughly 100 kHz between design value and realization is existent and can be taken into account for further synchronization efforts.

At PETRA III 14 different beamlines exist. Two are of relevance for this work and described in the next chapters:

3.1.1. Variable Polarization XUV Beamline P04

The variable polarization XUV beamline P04 offers - as the name already states - two markable features: It offers the smallest photon energies and additionally the possibility to switch between linear and circular polarized radiation.

see discussion below the table.

The details are taken from [81] and again the DESY Photon Science homepages [4]. The layout of P04 is illustrated in figure 3.2.

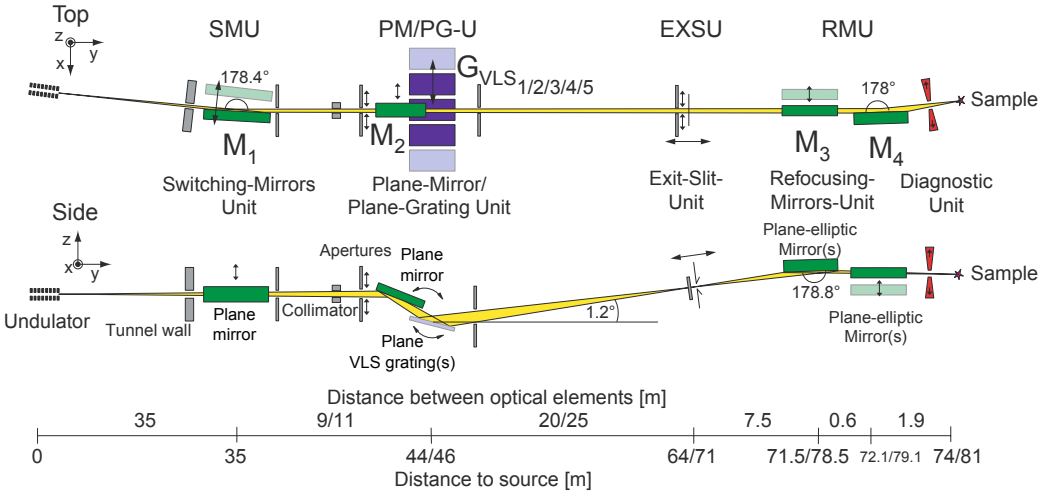

Figure 3.2.: P04 Schematic layout taken from [81]

After the undulator the switching-mirrors unit (SMU) allows to switch between two possible branches[4] of P04. It is followed by the monochromator consisting of plane mirrors and gratings (PM/PG-U) to select the desired wavelength (photon energy). The exit-slit-unit (EXSU, an adjustable aperture) also can have further influence on the bandwidth (remember the spatial frequency dependence as mentioned in chapter 2.4.1). Finally the beam is refocused by the refocusing-mirror-unit (RMU) into the experiment.

During the course of this work, P04 was still in the commissioning phase, thus, the specifications were not yet reached for some parameters. For example focusing has not been available and energy resolution design value was not reached. Therefore, the photon flux on sample necessarily became dramatically decreased.

Nominal specification according to [2]:

source brilliance	10^{20}	ph/s/mm^2/mrad^2/0.1% bw/100 mA
energy range	250 - 3000	eV
energy resolution	100	meV at 1 keV
max flux on sample	10^{13}	ph/s at 1 keV
spot size on sample	5000 x 2000 to 10 x 10	μm

Table 3.2.: P04 parameters

Beamline P04 is unique even for a scientifically uninformed visitor as it does not have an experimental hutch (see figure 3.1b). This is necessary at the other beamlines for

[4] Two branches allow to effectively use the beamline as experiments can be set up or removed while another experiment uses the beam at the other branch and vice versa.

radiation protection reasons but the soft X-ray or XUV radiation is absorbed even in air thus all experiments need to take place in vacuum. The vacuum system is at the same time a more than sufficient radiation protection. Working in vacuum, however, causes further experimental challenges as automatization is needed and tuning is hindered due to narrow vacuum pipes and hardly visible parts.

Furthermore, the lack of an experimental hutch creates the need of an extended laser safety concept. Relevant information to adapt the safety concept for future experiments are given in the appendix A.6

3.1.2. Bio-Imaging and Diffraction Beamline P11

P11 is the second beamline offering the necessary reference signals for laser synchronization. It is working in the X-ray regime thus being equipped with a different undulator and different optics. However, the principle is similar: A monochromator - here a Si crystal operates as grating - is used to select the desired photon energy. In the X-ray regime grazing incidence mirrors are used, being dynamically bendable to generate an intermediate focus.

Nominal specification according to [3]:

source brilliance	10^{18}	ph/s/0.1% bw/100 mA
energy range	2.4 - 30	keV
energy resolution	1	eV
max flux on sample	1.3 x 10^{13}	ph/s at 12 keV
spot size on sample	2 x 2 to 5000 x 1200	μm

Table 3.3.: P11 parameters

P11 operates at higher photon energies in the X-ray regime. Thus an experimental hutch shields the experiment during operation. The laser safety strategy can involve the experimental hutch and is installed permanently.

3.2. Laser System

The laser system used in this work is a commercial Yb:KGW laser by Lightconversion[5] called PHAROS. All details given were taken from the manual [54] or the service report if not stated otherwise. It is extended with a harmonics module HIRO and an optical parametric amplifier (OPA) called ORPHEUS from Lightconversion as a tunable frequency converter module. The stated properties are taken from the corresponding service reports and manuals as well [53] [55]. Everything is mounted on a movable optical table with a footprint of only 0,9 x 1,2 m, thus allowing the whole system to be used flexible at different beamlines and laboratories as well. The physical basics and principles to understand the devices described in this chapter have been explained in chapter 2.3. The power spectrum of the whole system including the frequency conversion modules is shown in figure 3.3.

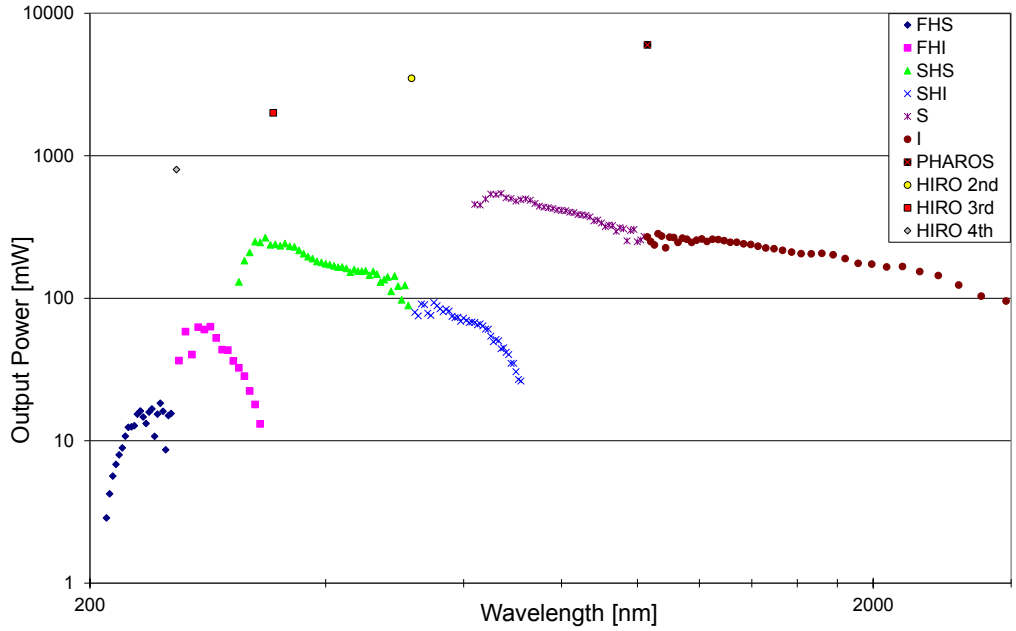

Figure 3.3.: Output power of the whole laser system including PHAROS, ORPHEUS and HIRO at 130,1 kHz

[5] www.lightcon.com

3.2.1. PHAROS

PHAROS is built in the traditional chirped pulse amplification (CPA) technique - see chapter 2.3.1. It is based on Yb:KGW (also Yb^{3+}:$KGd(WO_4)_2$ or ytterbium-doped potassium gadolinium tungstate) as gain media within the oscillator as well as the amplifier. The stretcher / compressor is based on a grating. The main laser system output parameters are provided in table 3.4, however, in principle PHAROS can be tuned so repetition rates between some kHz and up to 200 kHz can be achieved. The output power, however, can never exceed 6 W, therefore, pulse energy decreases with increased repetition rate and vice versa. For repetition rates below 100 kHz pulse energies become the limiting factor and 6 W cannot be reached any more. The stated values are based on a repetition rate of 130.1 kHz and are thus the values for our intended work synchronized to PETRA III. 130.1 kHz is the 3840th subharmonic of the PETRA III masterclock, usually referred to as 500 MHz (actually being slightly less, see chapter 3.1). The value of 130.1 kHz corresponds to (non-existent) single-bunch mode meaning no matter which bunch pattern PETRA III is running at one can always be in time with the same bunch.

Pulse duration:	<300 fs
Repetition rate:	130,1 kHz
Wavelength:	1030 nm
Power:	6 W

Table 3.4.: PHAROS parameters as stated in the service report

The used PHAROS oscillator has following special features:

- the roundtrip frequency is 83.26 MHz (being the 6th subharmonic of the PETRA III masterclock)
- the cavity can be slightly adjusted by one of the mirrors being mounted on a piezo (with a range of 12 μm). This is used for synchronization purpose, making the laser oscillator the VCO of the PLL to synchronize laser and synchrotron pulses (see chapter 2.2 for synchronization basics).
- the prism inside the cavity can also be used to adjust the roundtrip frequency to ensure the range of the piezo includes the reference to lock to.

PHAROS is equipped with various indicators on the internal operational status. Of major importance for this work are especially the two photo diodes called *PD OUT* and *PD OSC*. PD OUT is mounted in the last stage of the PHAROS setup thus delivering a signal representing the output pulse train. PD OSC is placed inside the oscillator hence delivering the oscillator pulses as necessary inputs for the synchronization (see chapter 4).

3.2.2. HIRO

HIRO is a harmonics module for PHAROS being able to generate the 2nd, 3rd and 4th harmonic. Its maximum output parameters for 103.1 kHz are given in table 3.5.

2nd harmoinc:	515 nm	3.5 W
3rd harmoinc:	343 nm	1.9 W
4th harmoinc:	257 nm	0.7 W

Table 3.5.: HIRO parameters as stated in the service report. HIRO is optimized to work at 130.1 kHz.

HIRO is based on non linear effects - namely SHG and THG - as described in chapter 2.3.2 (section SHG) and 2.3.2 (THG). The used nonlinear crystals are beta-barium borate (BBO). HIROs optical layout is illustrated in figure 3.4. Here A marks an aperture, L stands for lens (so does CL for collimation lens), HC is harmonics crystal, M mirror, BRM is beam routing mirror, RP is a half-wave-plate (standing for retardation plate, however, rotate polarization is the better memory hook for everyday use), TD is a bi-refrigerant crystal, and RS a reflection shield.

The fundamental from PHAROS is sent into HIRO through aperture A1 via the beam routing mirrors BRM1 and BRM2 that are the accessible tuning parameters outside HIRO.

For a general understanding accepting that reflection shields, apertures, lenses and mirrors have been pre-aligned to ensure the right beams with the necessary spotsize (to enable necessary non-linear processes while not destroying the optical elements) at the desired position (in space and time) eases the overview:

For the generation of the second harmonic the crystal HC2 is used. As the second harmonic is also needed for the generation of third and fourth harmonic HC2 is always involved. If the second harmonic is needed, the mirror toggle wheel containing M2 and M4 is turned to route the second harmonic to exit via port F. The tuning always starts at this point optimizing for maximum output power. Parameters used to adjust are basically BRM1 and BRM2. For fourth harmonic M2 is toggled out of the beam allowing the (optimized) second harmonic to propagate via M7 and RS5 into HC4 where the second harmonic of the second harmonic thus the fourth harmonic is generated. Both processes thus are based on the principle of SHG (as explained in chapter 2.3.2).

The generation of the third harmonic is slightly more complex. As described for THG in 2.3.2 the fundamental and the second harmonic are mixed for this purpose. Thus both need to be available at the same time and space inside the non-linear crystal for THG, here HC3. After second harmonic has been optimized the optimization for THG can take place. While for the second and fourth harmonic the maximum conversion efficiency in HC2 is desired, for THG an optimized ratio between the second harmonic and the fundamental is necessary. This can be tuned by RP1 which can be rotated around the optical axis thus allowing to adjust the polarization of the incoming fundamental pump beam. Only one direction of polarization fulfills all conditions necessary to obtain second harmonics thus the amount of fundamental available for SHG is adjusted by RP1.

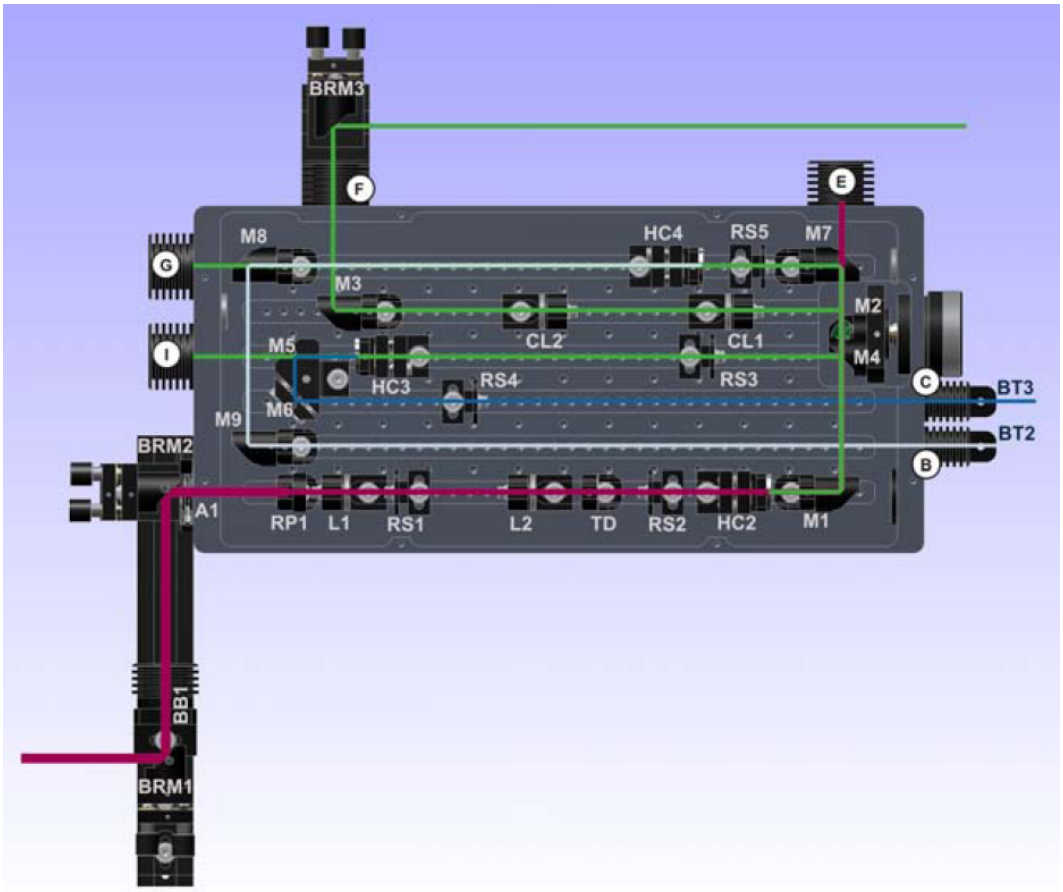

Figure 3.4.: Optical layout of HIRO. Taken from [53]

Therefore, fine tuning RP1 might also be necessary for second or fourth harmonic optimization in case THG has been applied previously.

3.2.3. ORPHEUS

ORPHEUS is a so called *collinear optical parametric amplifier* by Light Conversion extending the accessible wavelength range of the laser system to cover from 210 nm up to 2600 nm (UV to IR). While ORPHEUS has not been used experimentally within this work it is part of the mobile and synchronizable lasersystem presented here and contributes to its flexibility by enhancing the range of provided wavelengths. ORPHEUS has been used within Diploma theses in the past and thus proven to be a working and reliable part of the system [39][38].

The optical design of ORPHEUS as well as the explanation of the included abbreviations are given in figure 3.5. ORPHEUS is much more complex than HIRO but is motorized thus none or little adjustments within need to be done. It is delivered with software to control the desired output wavelength. Two further SHG stages behind the

shown layout further broaden the spectrum of the available output wavelength.

ORPHEUS again includes a huge amount of mirrors and other optics to ensure the optimal intensities to be at the necessary time and space. These are necessary for operation but can be ignored to understand the way ORPHEUS works.

After incoupling the PHAROS pump beam through aperture A1 the half wave plate RP1 is used to adjust the amount of pump beam to be reflected by polarizer P1 into the pump branch (later split into two further sub-branches, see below) or pass P1 into the white light branch.

The white light is generated from a small amount of fundamental only in a suitable substrate (a sapphire disc, WLG). It is used to select the wavelength to be amplified in the later process. As described in chapter 2.3.2 for the OPA process two incoming wavelength are needed. One pump wavelength (here the second harmonic) and one so called *signal* to be amplified. The OPA process transforms pump photons into signal and idler photons according to the condition: $\omega_{pump} = \omega_{signal} + \omega_{idler}$. The white light is used to select the signal: White light contains a broad frequency range, i.e. it has a broad spectrum. A chirp and temporal broadening is induced in WLG and TD thus the pulse is chirped. Thus by changing its arrival time at the OPA crystals changes the signal wavelength for the pump pulse. This delay is done software controlled by the delay stage (M1 and M2 are mounted on). In NC1 the first OPA process occurs when the chirped white light with adjusted delay gets to overlap with the firs pump sub-branch. Here the first amplification occurs non-collinearly. Signal as well as pump thus take separate paths after NC1 but are both reflected to pass NC1 a second time together leading to further amplification. These steps are harder to identify in figure 3.5 as the reflected beams follow a similar path only slightly adjusted in heights. The software controlled delay plate DP1 ensures that pump and signal have ideal temporal overlap within the second pass of the first amplification stage NC1. Afterwards the residual of this pump branch is blocked while the signal is led via another software controlled delay stage (DP2, M7, M8, DP3) towards the second amplification stage. This consists of the dichroic mirror DM2 used to get the signal collinear with the second sub-branch of the pump beam and th crystal NC2. Here the collinear second stage of amplification takes place. The pump beam before has been delayed by traveling an as long path as the signal via mirrors M19-M24.

While the pump branch was mentioned to be coupled out in P1 and its two branches were overlapped with the signal in NC1 and NC2 its fate in between needs to be supplied: The pump branch after P1 is used to generate the second harmonic - similar as in HIRO - which is used to pump the OPA process. To this end HC2 is used and the generated second harmonic propagates via M10 (where the pump residual is coupled out) and M11 towards RP3. This half wave plate is again used to select the ratio of intensity that is reflected by the following polarizer P2 thus determining the ratio of intensities in the two pump sub-branches for the different amplification stages.

Further reflection shields and dichroic mirrors basically filter out undesired residuals or reflections, lenses and half way plates as well as delay plates and mirrors are pre-aligned to ensure that for the whole described process the pulses reach the non-linear crystals with the desired timing, phase, and intensity.

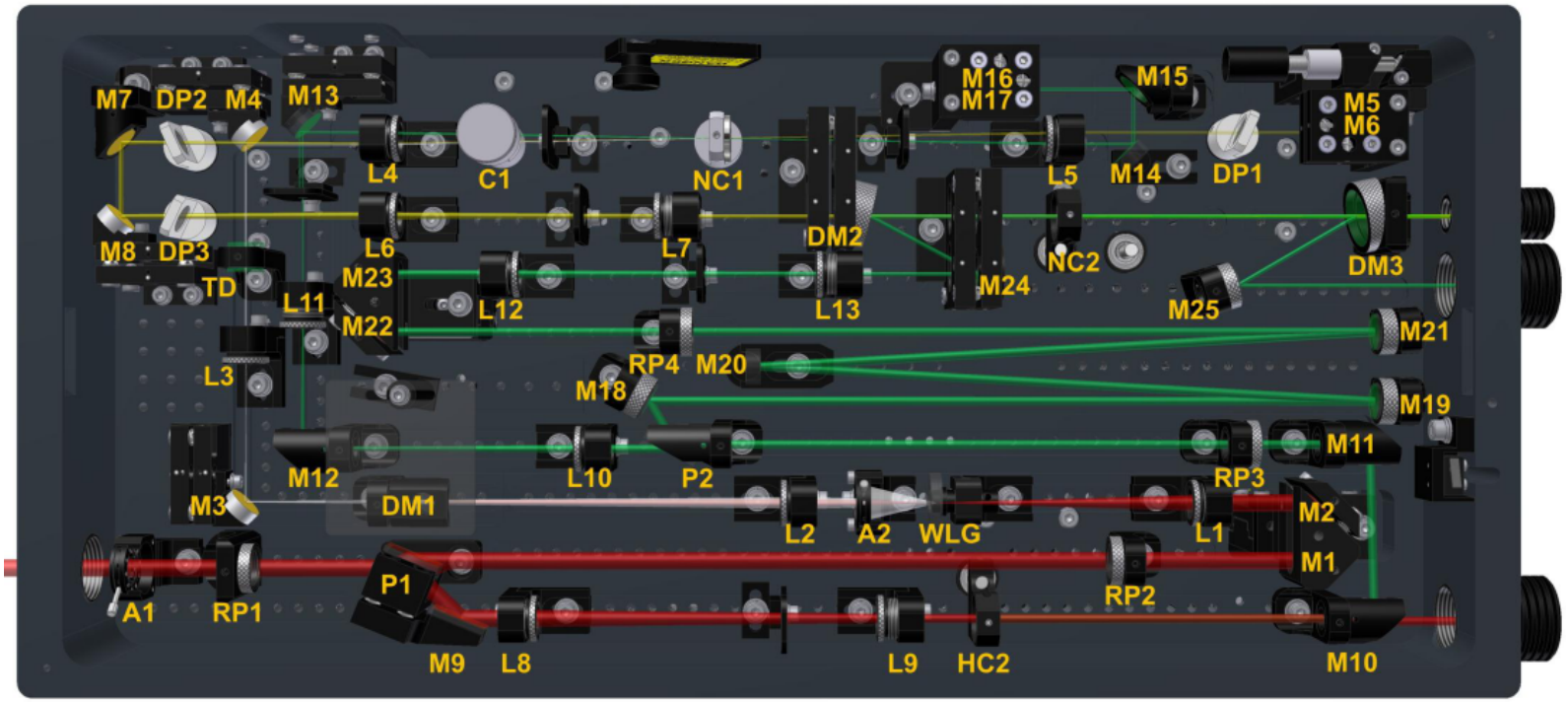

Figure 3.5.: Optical layout of the OPA ORPHEUS. Taken from [55]. A: Apperture; C: Compensator; DM: Dichroic mirror; DP: Delay plate; HC: Harmonic generation crystal; L: Lens; M: Mirror; NC: Nonlinear crystal; P: Polarizer; RP: Rotator of polarization (half wave plate); RS: Reflection shield; TD: Time dispersion medium; WLG: White light generation medium

.

The OPA setup is followed by two further SHG stages giving access to down to the fourth harmonic of the achievable spectrum of signal and idler. They are marked in figure 3.3 with SH (second harmonic) or FH (fourth harmonic) followed by S for signal or I for idler.

4. Laser Synchronization

To be able to perform pump-probe-experiments, the laser system has been equipped with a synchronization unit based on an extended PLL approach with an FPGA-based PID controller. It allows setting a desired delay between the laser pulses and an external reference (i.e. synchrotron pulses).

4.1. Synchronization Unit

The synchronization is based on the PLL principle as described in chapter 2.2. The master clock of PETRA III is running at 499.564 MHz (referred to as 500 MHz, furthermore) while the PHAROS oscillator is running at 83.26 MHz (referred to as 83 MHz) which is the sixth subharmonic. Therefore, the reference signal and the signal from the photo diode inside the oscillator are not directly compared in the mixer. Instead, a bandpass filters the sixth harmonic from the oscillator signal[1] to obtain 500 MHz.

Mathematically speaking this means while the Fourier transformation of a sinusoidal signal gives a delta peak of exactly the sines frequency, any other signal is - according to Fourier's theorem - composed of the sum of various sinusoidal signals. For periodic signals - like pulse trains - these sinusoidal contributions need to have periods that are integer multiples of the pulse trains period. This ensures that each summand of the Fourier series contributes in the same way to any pulse. A Gaussian pulse train is illustrated in figure 4.1a, the Fourier analysis in figure 4.1b.

Furthermore, two additional loops based on 83 MHz are implemented. To this end the 500 MHz reference is fed into a prescaler followed by a lowpass filter.

This two further loops play an important role to ensure locking without so-called *bucket jumps*[2] and for delay issues as discussed in chapter 4.2. The synchronization scheme (Fig. 4.2) gives an overview of the principle of the synchronization. It is based on mostly commercially available analogue parts connected via coaxial SMA connectors and with the nominal wave impedance of 50 Ω. One can see the three described loops and their phase detectors with their corresponding error signals all fed into the controller. A more detailed version including parts list is presented in appendix A.2. The controller processes these inputs depending on the task it is given. Usually, it just uses the 500 MHz loop to synchronize the oscillator to the reference. The error signal of the 500 MHz loop

[1] The pulse train trace as measured by a fast photo diode.

[2] Bucket is the term for the different positions that fulfill the constant phase condition the PLL ensures. The term is used as in [13]. In chapter 4.2 the buckets are of major importance.

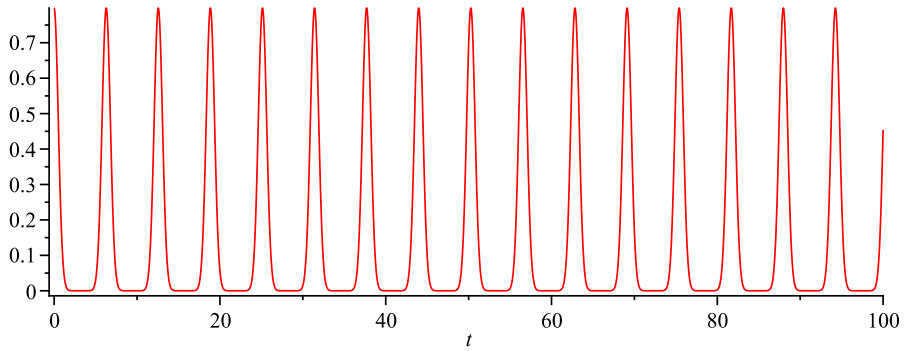

(a) Gaussian pulse train

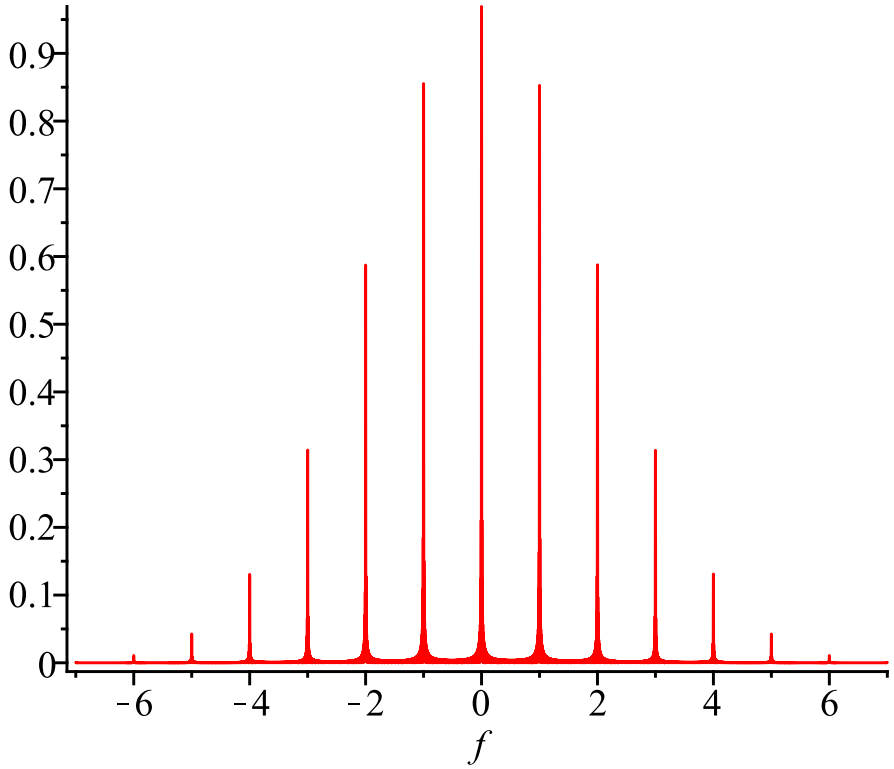

(b) Fourier transform of the Gaussian pulse train from figure 4.1a showing harmonics of the fundamental frequency $f = 1$

Figure 4.1.: Illustration of the occurrence of harmonics for periodic, non-sinusoidal signals.

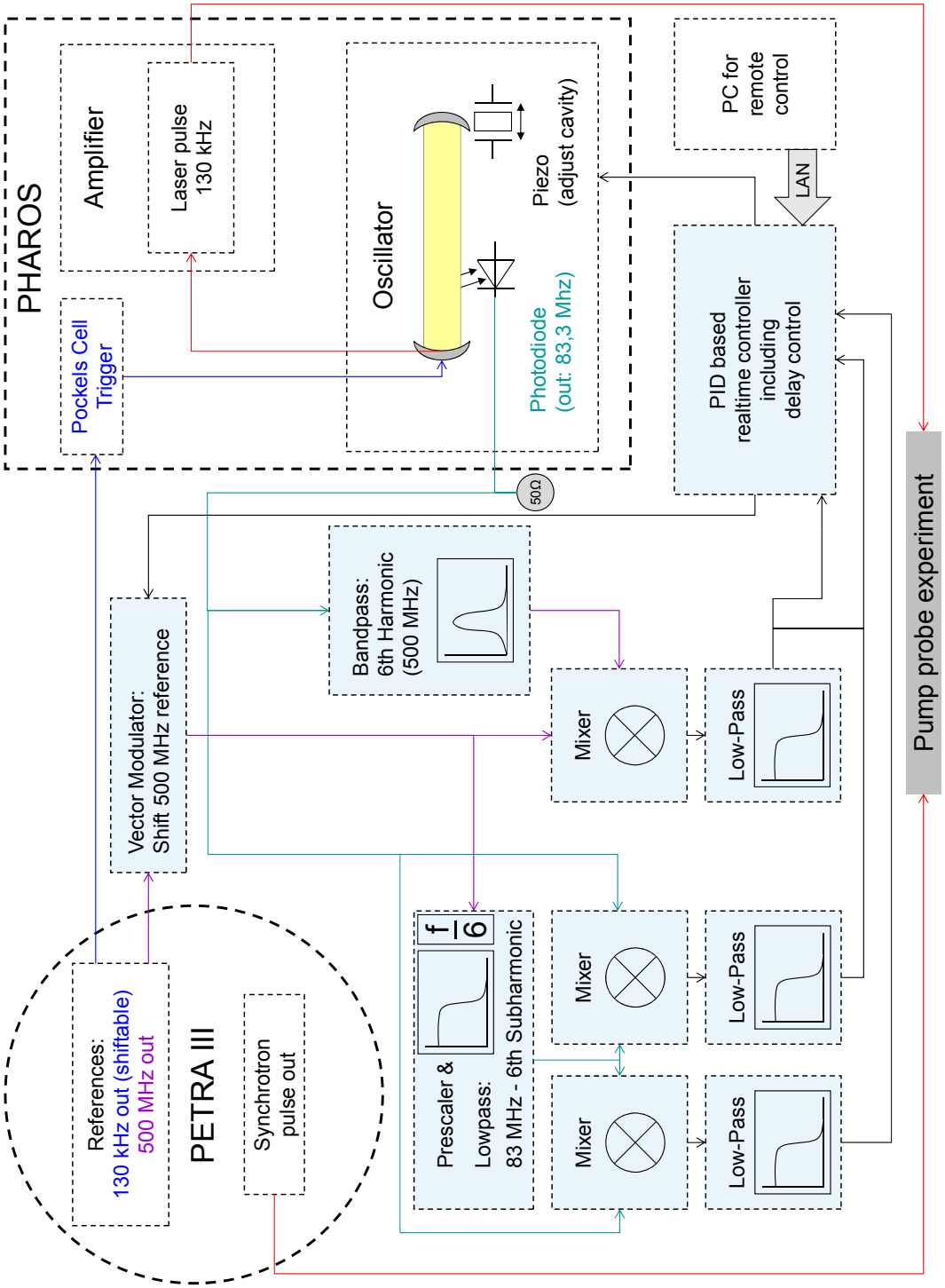

Figure 4.2.: Scheme of the Timing Box. A more detailed version including parts list is presented in appendix A.2.

leads to a better synchronization than the 83 MHz loop would, as the absolute value of the error signal for the same absolute time difference is larger. The two 83 MHz loops, however, get involved to monitor stable locking of the 500 MHz loop. Furthermore, it can be used to set the delay in 2 ns steps (however, using the vector modulator as phase shifter for the reference is preferable to set any delay in most cases - for more information on the vector modulator see appendix A.3).

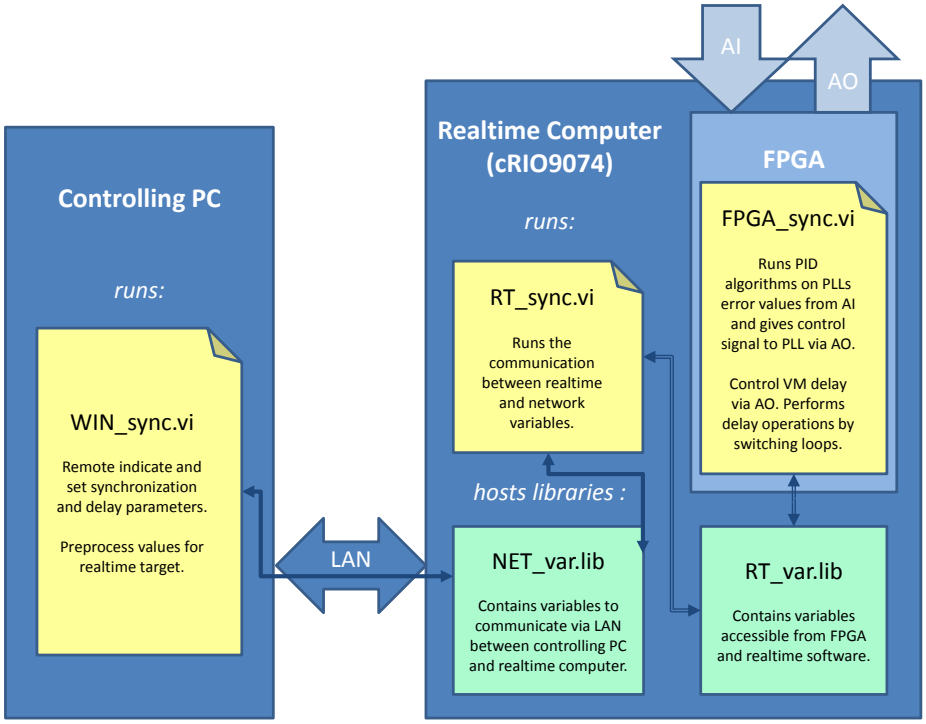

Figure 4.3.: Scheme of the Controller

The architecture of the software controlling the synchronization is illustrated in figure 4.3. The core of the synchronization unit is the field-programmable gate array (FPGA)[3] running the PID and the communications with the analog-to-digital converter (ADC) and digital-to-analog converter (DAC) modules to the analogue parts of the loop (FPGA_sync.vi). It communicates via a real-time variables library (RT_var.lib) with the communication software (RT_sync.vi) running on the real-time computer. This concept allows communication without any interrupts being necessary thus real-time operation of the FPGA code. The same is valid for the communication of RT_sync.vi with the remote software (WIN_sync.vi) running on the controlling PC. They communicate via a second library (NET_var.lib) on the real-time computer accessible via network and locally. All settings and parameters are accessible via the controlling PC's user interface. They are processed and, if necessary, converted and transferred to the real-time system.

[3] a programmable integrated circuit allowing real-time implementations

The communication with TANGO[4] is also performed within WIN_sync.vi. Important parts of the code of the mentioned VIs can be found in A.5.

Compared to analog PLLs the digital PID controller offers some interesting additional features. The setpoint can be adjusted to a value different to zero simply by adding (or subtracting) an offset to the input values. This can be used for intended switching between the loops without loosing the lock (see chapter 4.2.2). Also this switching is possible from one clock to the other. Note that the jitter is larger the further the setpoint is off the original value. This is caused by the linear approximation being less valid there.

These features are used in chapter 4.2.2 for delay opportunities and in chapters 4.3.3 and 4.3.4 it is explained how they are used to ensure stable operation.

The clock of the FPGA and thus of the whole loop can be set. However, the bottleneck of control rate is not the FPGA but the piezo within the PHAROS cavity. Figure 4.4 shows a graph of the piezos resonances that can be measured with the software of the piezo controller. To avoid the risk of resonance effects that might cause destruction, the cycle clock is set to be below the first resonance (marked with red arrow, here above 700 Hz). While the FPGA could operate at much faster cycles within the MHz regime its power in this setup is the real-time capability i.e. that every cycle takes the same amount of time thus minimizing timing errors in the sampling of the error signals as well as for the digital PID calculations that are based on precise discrete steps as well. The ADC are read out once per cycle and the DAC output to the piezo is adjusted once per cycle as well.

[4]TANGO (TAco Next Generation Objects) is an object oriented distributed control system developed by various facilities (ALBA, DESY, Elettra, ESRF, FRM II, MAX-IV, Solaris and SOLEIL) - see official homepage: http://www.tango-controls.org
TANGO is used for automatization and remote control of experiments and beamline devices at PETRA III

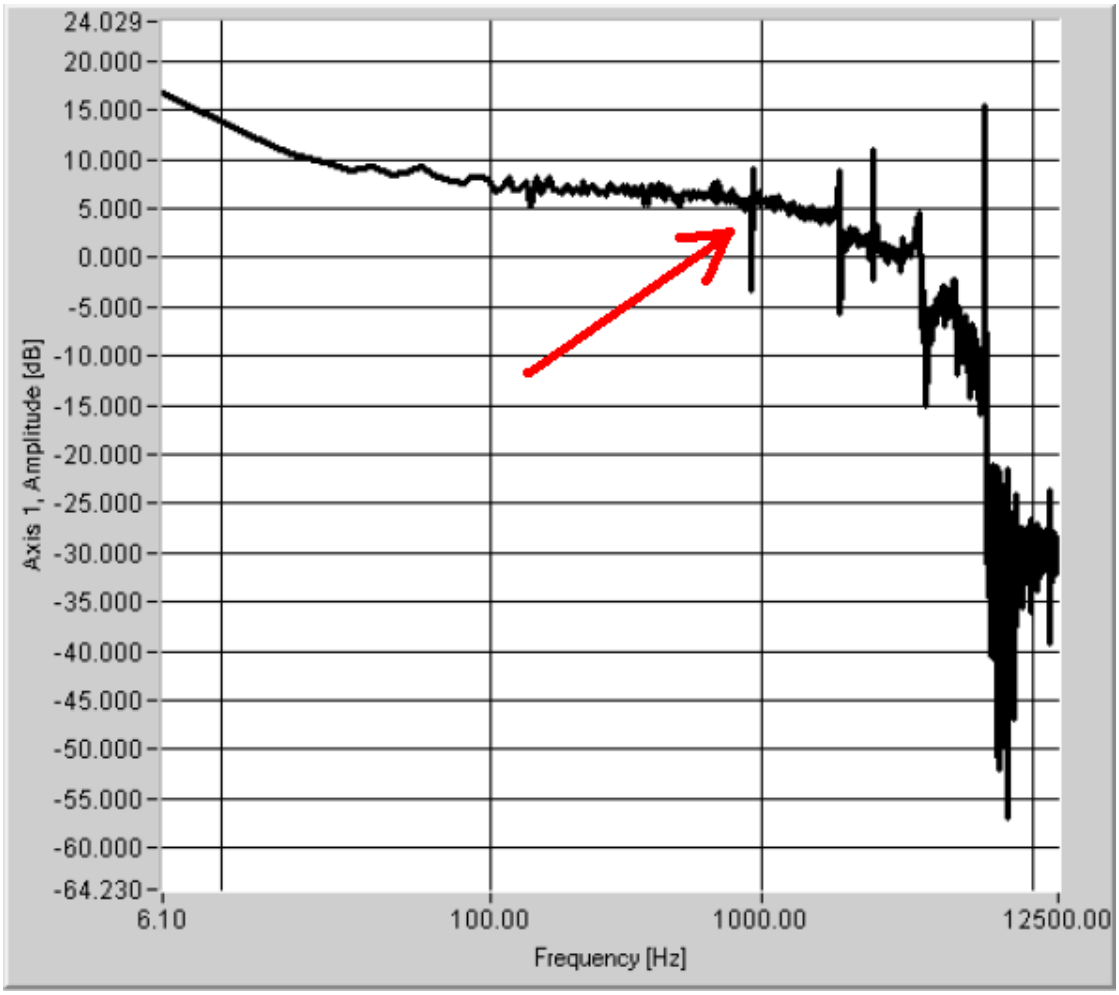

Figure 4.4.: Frequency response (impulse) of the piezo P-753.11C - measured with internal sensor and PI software of the piezo controller PI E-753.1CD. First resonance marked with a red arrow.

4.2. Delay

The delay opportunities offered have to be distinguished in three in principal different levels. A coarse pre-alignment in 12 ns steps is possible and necessary by shifting the pockels cell trigger, a smooth delay setting is offered by shifting the 500 MHz reference with a vector modulator, and setting the temporal position in 2 ns steps is possible based on systematic bucket jumps. The latter is more important to avoid undesired bucket jumps and ensure proper locking and stability. All three options are discussed in detail in the following.

4.2.1. 12 ns Grid

The first level with the broadest range is the 12 ns grid which is offered by the pockels cells that uncouple oscillator pulses into the regenerative amplifier of PHAROS. As the oscillator is running at 83 MHz if it is mode-locked, every 12 ns the pulse returns to the same position. Hence at every position in the beam path a pulse train with 12 ns pulse distance is observed. Therefore, the pockels cell as well is also reached only every 12 ns. An illustration can be found in figure 4.5.

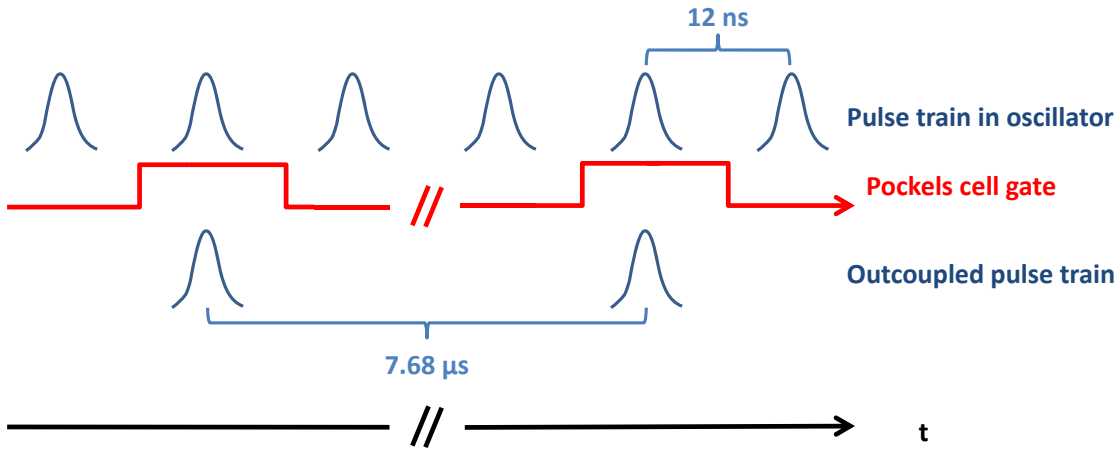

Figure 4.5.: Origination of the 12 ns grid from the 83 MHz oscillator repetition rate.

Shifting the pockels cell gate allows jumps of 12 ns. The 130 kHz reference for the pockels cells is delivered by the bunch-clock[5] and can be shifted with this device as well. As the bunch-clock is in principle remotely controllable as well an implementation in TANGO is possible and could be a useful tool if delays larger than 12 ns are needed.

4.2.2. 2 ns Grid

The 2 ns grid is given by the 500 MHz loop. While delay steps of 2 ns can also be conducted with the vector modulator (see chapter 4.2.3) the presented architecture allows

[5] as described in 3.1

to reach proper locking, optimized input signals for the synchronization and especially ensure long-term stability by monitoring the utilized bucket to synchronize to.

The PLL locks the 500 MHz reference and the 83 MHz oscillator signal to have a stable phase relation. Within one period of the 83 MHz signal there exist 6 different possible settings for the 500 MHz that lead to the same phase relation, typically called buckets. Thus the PLL can in principle lock to any of those buckets. This is illustrated in figure 4.6.

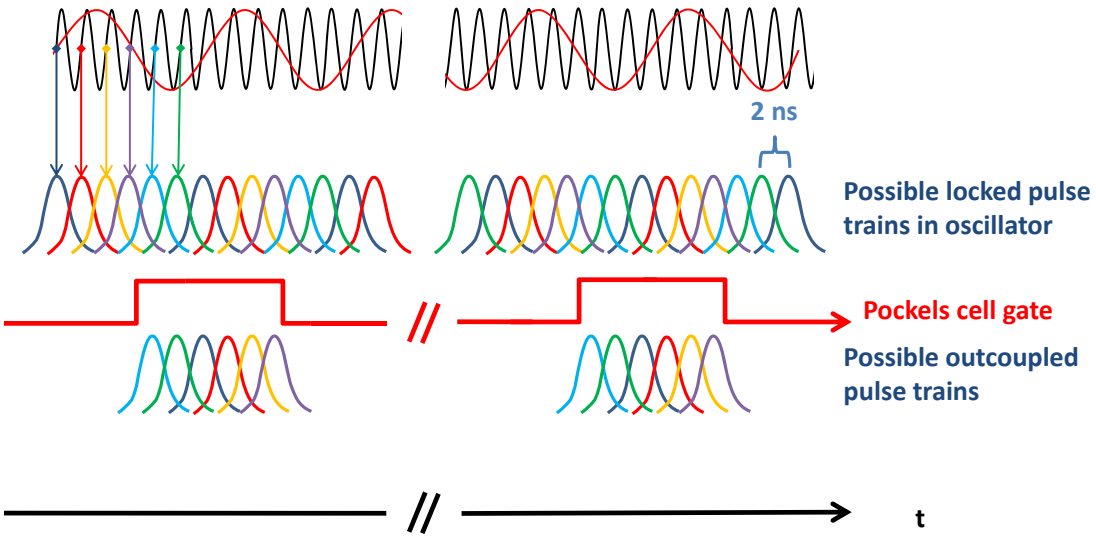

Figure 4.6.: Illustration of the buckets and the caused 2 ns grid of possible locking situations.

As poor calibrated PLLs can be subject to undesired bucket-jumps the described three loop setup is a tool to ensure long-term stability of the synchronization.

In this work the buckets are sometimes also referred to as "zero" or "positive zero" as the loop locks usually at the zero crossing of the signal where the slope is the biggest (and thus the sensitivity of the loop as well). This allows to discuss also the second zero crossings within a period with the exactly inverted slope: It is not sufficient to lock the loop in a stable way. Those crossings will be referred to as "negative zero" further on as the slope has an additional negative pre-sign compared to those zeros that allow locking. Why it cannot be locked at negative zeros can be depicted by comparing both zero crossings. Remembering the output of the phasedetector in chapter 2.2.1 which is a cosine, it is obvious that an additional phase difference of π would lead to the same result with a changed pre-sign, however. Therefore, the error signal and its processing in the controller would lead the loop away from those zero crossings instead of towards it.

To be able to distinguish between the buckets (or zeros) two additional 83 MHz loops have been implemented: They differ by an additional phase shift inserted by a fine-tuned difference in cable length. Therefore, the errorsignal is shifted on the phase axis as well.

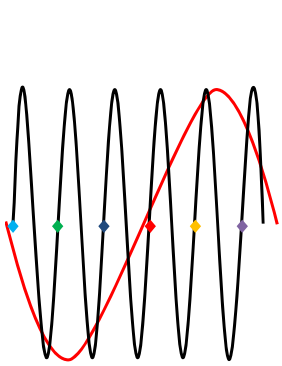

(a) Starting point: 500 MHz phase error signal (black) locked to dark blue zero crossing.

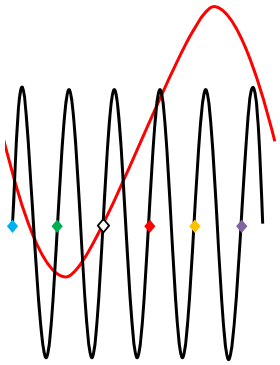

(b) Step 1: Adjusting the offset of the 83 MHz phase error signal (red) to have a zero crossing at the locked phase. Switching from the 500 MHz loop to the 83 MHz loop.

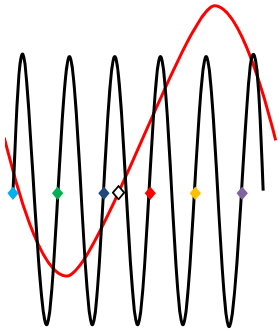

(c) Step 2: Slowly varying the offset (and thus the locked phase, marked white) towards the next bucket.

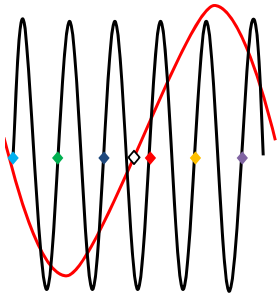

(d) Step 2 continued

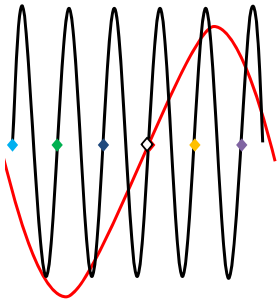

(e) Step 3: Reaching the next bucket.

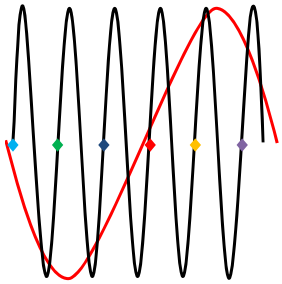

(f) Step 4: Switching back to the 500 MHz loop now locking one bucket further (red marker).

Figure 4.7.: Switching the bucket by switching between loops and adjusting the setpoint.

Within the 12 ns window given through the pockels cell trigger there are 6 possible zero crossings of the 500 MHz loop to lock to, that can be distinguished by the pairs of values of the two 83 MHz loops (see figure 4.8). Their values change sinusoidal over those 12 ns, and the value of one of them is not unique within this 12 ns period, however, as one of the two branches is shifted the pair of values is non-ambiguous.

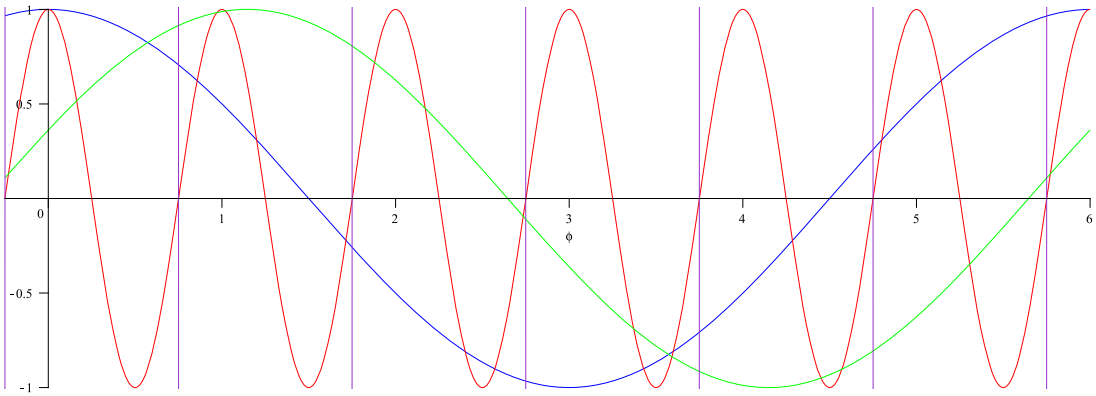

Figure 4.8.: Tunig overview of the 2 ns delay grid. In this example there is the errorsignal of the 500 MHz loop (red) and two 83 MHz loops (green and blue) depending on the phase error ϕ. The algorithm how to chose the correct loop to make a 2 ns step depending on the actual position is illustrated in in table 4.1. The vertical purple lines indicate the lockable zeros of the 500 MHz loop and the corresponding pair of values for the other two loops. They, furthermore, are the start or stop position for the delay steps, and are referred to as zero crossing in table 4.1

jump from zero crossing	0 to 1	1 to 2	2 to 3	3 to 4	4 to 5	5 to 6
using which loop signal?	green	blue	green (or blue)	green	blue	green (or blue)
inverted?	no	yes	yes	yes	no	no

Table 4.1.: Example: How to jump 2 ns steps. This is the algorithm for the example in figure 4.8. If the desired steps are performed by switching the loops according to those values, the setpoint will always be adjusted only in a region where the phase error is linear and has a positive slope being necessary to keep the loop locked and to perform predefined steps. Numbered zero crossings are marked with the vertical pink line and labeled with the number following on the phase error axis.

Hence it is possible do distinguish between those six different temporal positions, and switching between them targeted gets possible.

It is possible to select them by switching between the loops and varying the setpoints.

Usually, the setpoint is the zero crossing, as that is the position where the linear approximations of typical PLL design are most valid. Therefore, the most stable locking with smallest noise is possible here. However, it is possible to lock to a different setpoint as well. This is illustrated in figure 4.7. As in this case the controller is implemented with programmable hardware, these programs can be adjusted to allow to add a constant to the input (error signals) so the loop will lock to its assumed zero which is then lower by this constant. This constant can be varied slightly over time and the loop will compensate for it just as it did for drifts of the reference. The loop does not make a difference between the drift of the oscillator or the reference, or the setpoint as it is only reacting on differences between them. Hence it is possible to set the setpoint of one of the 83 MHz loops to the value that its error signal does have in the state locked to 500 MHz and then switch from 500 MHz loop to 83 MHz loop without loosing the lock. Then the setpoint is slightly varied until one reaches the next zero of the 500 MHz loop and it is possible to switch back to it for less jitter. This, however, is only possible in regions where the error signal is rather linear. As there are two 83 MHz loops available which are well tuned to fulfill the requirement that their phaseshift needs to be in a way, that between all zero crossings of the 500 MHz loops there is at least in one of them no peak but a slope to be approximated as rather linear. Because of the same effect that leads to "negative zeros" (see above) in some cases the input needs to be inverted so the inverted slopes can be used for this jumps as well. Between every neighboring zero crossing of the 500 MHz loop the controller is programmed to decide which 83 MHz loop connects them, how to put the setpoint and if inverting the signal is necessary. The overall process can be depicted in figure 4.8. An actual tuning curve for the 2 ns delay is depicted in figure 4.9.

In principle by inverting the 500 MHz reference as well a 1 ns grid could be provided the same way.

2 ns steps can also be done via the vector modulator, see chapter 4.2.3. However, monitoring the zero crossing is a worthwhile tool to ensure that locking is stable (it is not for sure if the zero crossings change) and performing a manual jump from each zero crossing to the next is a good cross check if all the levels of the input signals are adapted in the right way. As this demands stable short term locking also in regions where the linear approximations are less valid a successful circle through all six zeros suggests a stable setup with proper levels thus providing long term synchronization.

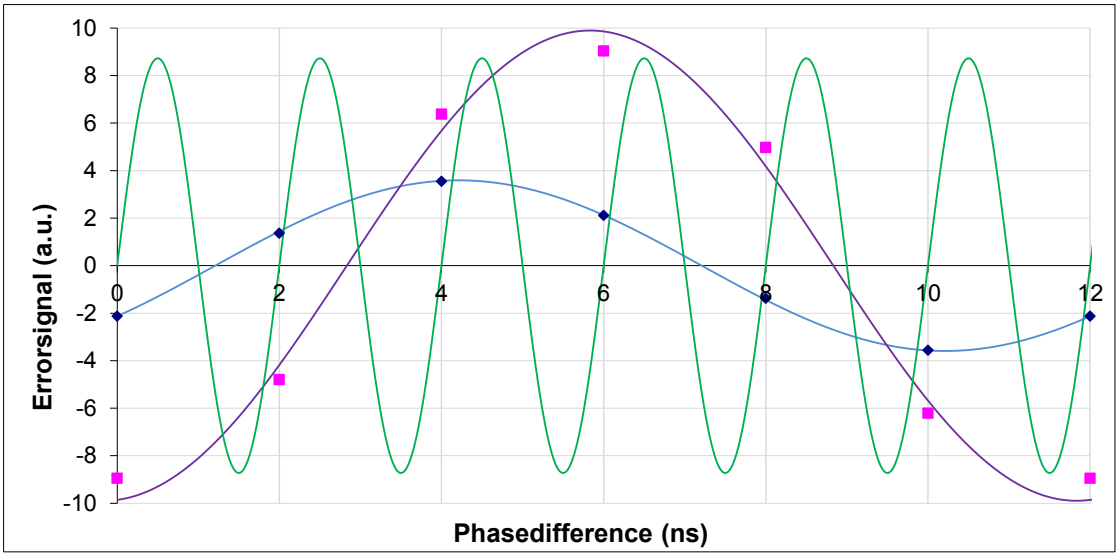

Figure 4.9.: Tuning scheme of the 2 ns delay grid. These are measured pairs of values for the 83 MHz loops when the 500 MHz loop is locked. They were sorted to fit sines and, therefore, identify their temporal position. These values have to be measured and slightly adjusted when the output signal of the PHAROS photodiode or the reference amplitude changes.

4.2.3. Smooth Delay

Finally a smooth delay opportunity is provided by a vector modulator. This is carried out inspired by [46] as well as by Dr. Christopher Milne who introduced the author of this work to a similar system at SLS. Both examples apply a similar vector modulator (in the case of this work QPMX-500-S by I.F. Engineering). The vector modulator is used to phase shift the reference signal.

A vector modulator's functional principle is illustrated in 4.10. The sinusoidal input signal is split into two branches. One branch is phase shifted by 90 degrees (i.e. derived). Both branches then contain an adjustable attenuator with an amplification factor in the range ±1 (i.e. also inverting is possible). The factor is set by applying voltages called I and Q proportional to the desired amplification. Those two branches are then combined again. The sum of two sines with identical frequency and different phase is again a sine of the same frequency (and a different phase). This can be shown mathematically, assuming an input signal given by equation 4.1:

$$\Re\left[Ae^{i\omega t}\right] \tag{4.1}$$

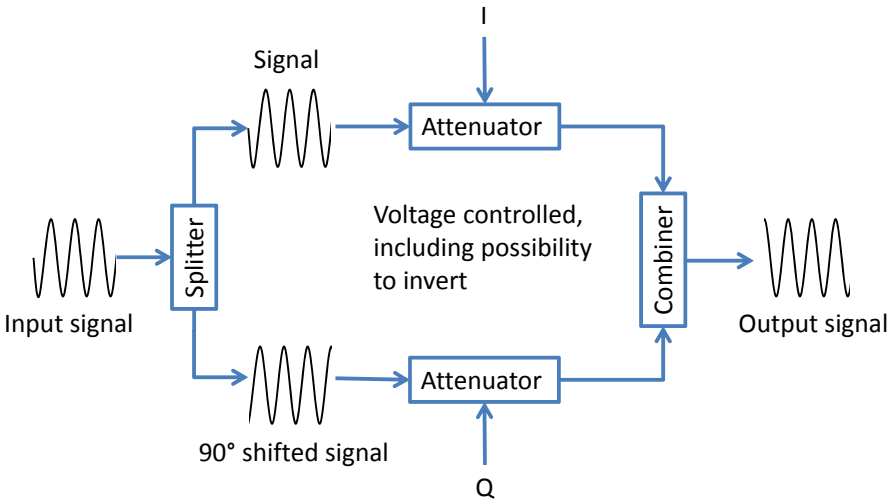

Figure 4.10.: Functional principle of a vector modulator.

Which gets modified by the attenuation factors I and Q

$$\Re\left[A\left(Ie^{i\omega t}+Qe^{i\left(\omega t+\frac{\pi}{2}\right)}\right)\right]=\Re\left[A\left(Ie^{i\omega t}+iQe^{i\omega t}\right)\right] \tag{4.2}$$

$$=\Re\left[A\left(I+iQ\right)e^{i\omega t}\right] \tag{4.3}$$

$$=\Re\left[A\sqrt{I^2+Q^2}e^{i\cdot atan2(Q,I)}e^{i\omega t}\right] \tag{4.4}$$

(Calculations adapted from [46])

From this equation it can be seen that the complex number $I+iQ$ defines amplitude and phase of the output signal. To ensure proper operation of the following PLL the amplitude $|I+iQ|=\sqrt{I^2+Q^2}$ needs to be kept constant while the ratio between Q and I defines the phase[6].

This is quite obvious when considering the complex plane where the complex part is here represented by Q and the real part by I.

The calibration curves for the vector modulator as well as the interpolation code are attached in appendix A.3. Data on the precision of the temporal position set by the delay are presented in chapter 5.3.

[6] please note that equation 4.4 contains atan2 which is the atan with extended range definition to cover 2π as used in many programming languages

4.3. User Interface

The user interface on PHAROS control PC is shown in figure 4.11.

Here all necessary settings can be done. The interface is roughly divided into 4 major parts:

Basic synchronization parameters at the upper left region

Visualization of the actual synchronization state in the diagram in the middle

Various delay parameters below the diagram

Control Values for communication and delay at the right

4.3.1. Basic Synchronization Parameters

Some general settings for the synchronization can be tuned here.

`PID_1_net, PID_2_net, PID_3_net` are basically the values for the three PID constants (see equation 2.6). They have been optimized for performance (jitter and stabilization). Usually, they need not be changed unless performance drops (optimizing input signals should be done first).

`FPGAperiod_net` sets the period for the clock in μs. It needs to stay below the first resonances of the piezo (see figure 4.4) and basically can be changed if the real time timing causes a pseudo locking of the error signal to an even multiple of this clock (then the error signals zero crossings in phase with the clock appear like if the error signal was zero all the time).

`Modus` allows to switch between different operation modes of the loop: It is possible to lock to 500 MHz (setting: "0", standard, highly suggested!), 83 MHz and also some variations or combinations of those loops (inverted, sum, multiplication). These settings are merely to study the PLL and are not suggested to be used in scientific use of the system.

`Reset PID` resets the PIDs "memory" by setting all PID constants temporarily to zero (while keeping the original constants).

`POS_set` is the initial value for the piezo. Together with `RESET PID` it is necessary to lock the loop (See chapter A.4).

`RT Communication` is an indicator that basic communication is established. If it is not flashing something went dramatically wrong.

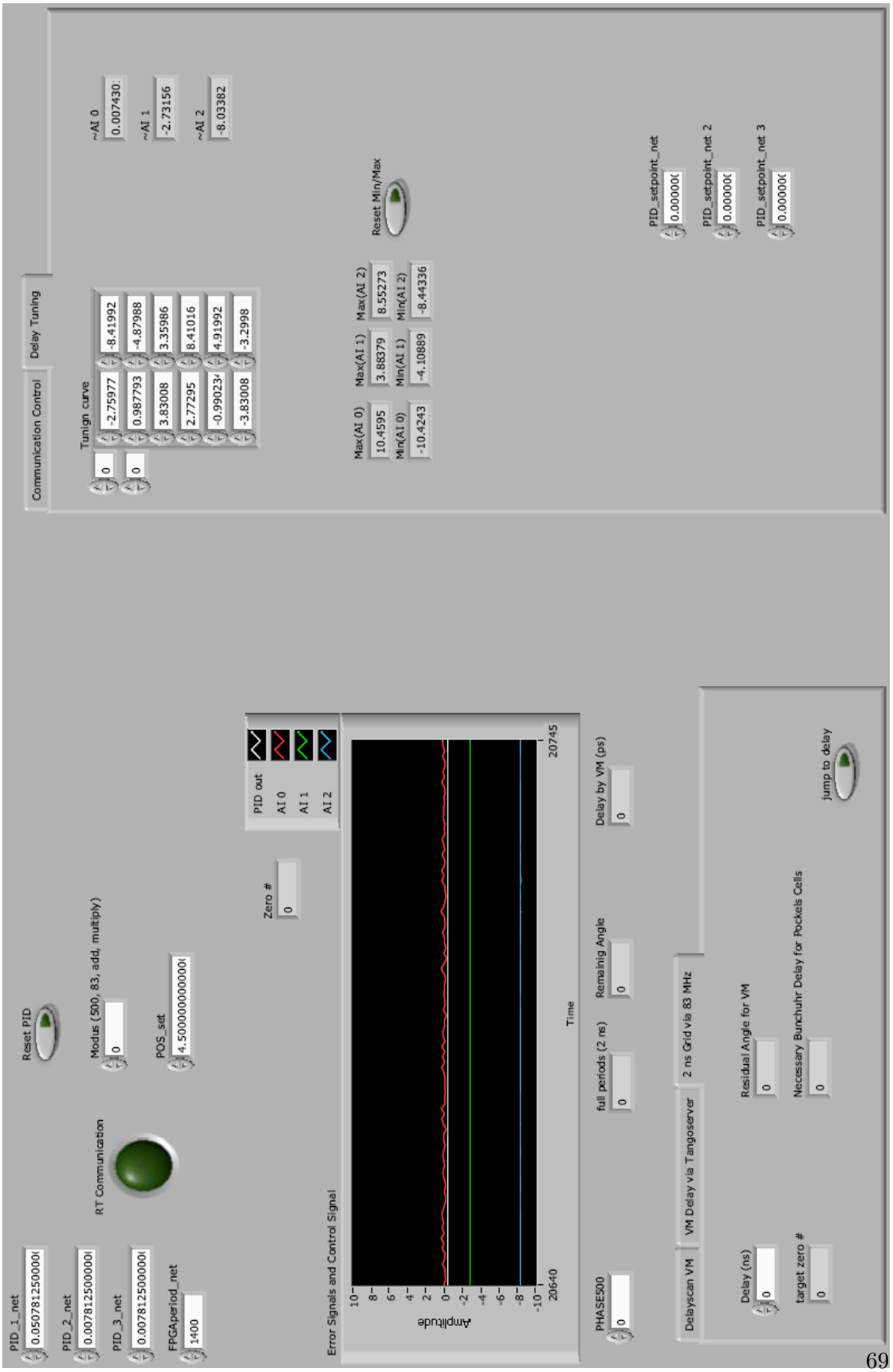

Figure 4.11.: User interface of the synchronization unit.

4.3.2. Visualization of the Actual Synchronization State

The graph shows the error signals for the 500 MHz loop (`AI 0`), the two 83 MHz loops (`AI 1` and `AI 2`), and the output of the PID (the control signal, `PID out`). Furthermore,

`Zero #` states which of the 6 possible zero crossings the 500 MHz loop is locked to. To have this working properly, the delay tuning has to be accurately set (see section 4.3.4)

4.3.3. Various Delay Parameters

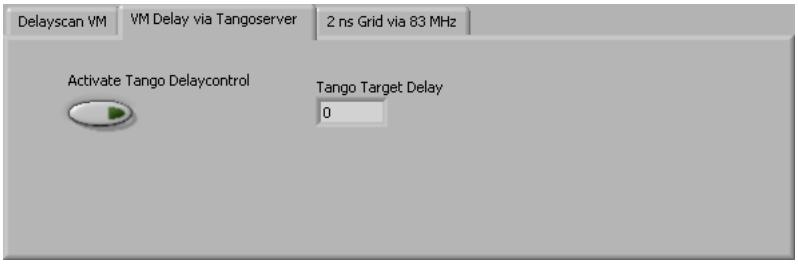

Figure 4.12.: `VM Delay via Tangoserver`

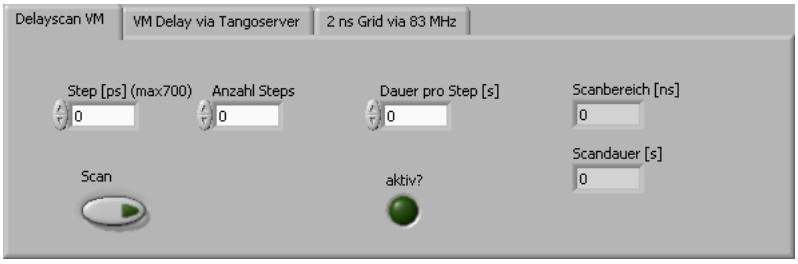

Figure 4.13.: `Delayscan VM`

`PHASE500` is the phase (in degree) the vector modulator applies onto the reference. It is possible to shift more than 360° = 2π, however, the steps need to be small (100 degree or less). Bigger steps need to be divided into smaller ones to keep the vector modulator rotating the phase (for example, a step of 360 would cause it just to stay at its position).

`full periods (2 ns), Remainig Angle, Delay by VM (ps)` translates the `PHASE500` setting into full 500 MHz periods (Euclidean division of `PHASE500` by 360), the remainder (`PHASE500` modulo 360) and its equivalent in ps (`PHASE500` / 0.18).

`2 ns Grid via 83 MHz` allows to select one of the six zero crossings and jump between them (see 4.2.2). To this end `Delay (ns)` has to be set. Then `jump to delay`

needs to be activated. The graph will show the jumps until the desired zero crossing is reached. **It is important to deactivate jump to delay again!** Otherwise the PLL will stick at a 83 MHz loop with higher jitter. If the PLL looses its lock during those jumps, the delay tuning curve (as described in chapter 4.2.2 and explained how to adjust in chapter 4.3.4) might not be valid any more. As the amplitude depends on both, the amplitude of the reference as well as the amplitude of 'PD OUT', new alignments or different attenuation, for example, by different cable length depending on the experimental position can cause variations.

It is suggested to check if the synchronization parameters are suitable by selecting each zero once.

It has to be remembered that after 6 steps the original position is reached again if the bunch-clock has not been adjusted. Typically one zero is selected then and delay is set by the smooth delay via `PHASE500`. However, the `Zero #` schould be checked regularly to ensure that the lock has not been lost.

`VM Delay via Tangoserver` (see figure 4.12) offers the possibility to activate remote controlling the delay via TANGO. More details and instructions to operate the delay via TANGO are given in chapter 6.1.1 and appendix A.5.3. `Activate Tango Delaycontrol` should not be active if remote control is not desired.

`Delayscan VM` (see figure 4.13) offers the possibility to perform a delay scan by setting step length, number of steps and time to stay at each step. The scan is then activated via `Scan`. This tool might be useful to set up an experiment, however, the synchronized delayscan controlled via TANGO by the control software for the rest of the experiment is much more powerful.

4.3.4. Control Values

Two set of control values exist:

`Communication control` is merely for debugging purpose. PID parameters are sent back from the realtime system so an easy check for proper communication is slightly changing `FPGAperiod_net` on the left and check if `FPGAperiod_net_out` receives that change. Also the error signals and control signal can be monitored numerically. Additionally `OUT_NET (AO 0)` indicates the actual output for the piezo. This value can be compared to `POS_set` directly after locking to get an idea of the locking range and once a while to monitor the drifts of the cavity. The last indicated number allows to cross check the interpolation of the values for the vector modulator (see appendix A.3.2).

`Delay tuning` Here the tuning curve to identify the zero crossings of the 500 MHz loop are set. The table `Tuning curve` lists the pairs of values that the two 83 MHz loops state as errorsignal[7] when locked to the `Zero #` numbered 0-5. These values

[7] `AI1` and `AI 2`

correspond to those marked in figure 4.9. To adjust this table if necessary it is possible to lock to each `Zero #` and when locked activate and deactivate the `Reset Min/Max` button. Then `Max(AI 1)` and `Min(AI 1)` indicate the value for the first 83 MHz loop (first column in `Tuning curve`) for the locked `Zero #` (corresponds to the row in `Tuning curve`). If the real values differ too much from the `Tuning curve` then the 83 MHz grid can not be used and especially the indicator `Zero #` might be less reliable[8]. Especially if the values in `Tuning curve` are bigger than the actual error signal can reach the lock gets lost when switching to this setpoint. Dramatic changes might even cause the indication of `Zero #` become wrong. Then all six pairs of values need to be measured and re-fit to two shifted sines. In this case targeting `Zero #` will not work and several tries of re-locking might be necessary to reach all zeros.

[8] This might be the most important part to have a good indication for proper locking

5. Benchmarking Measurements

In this chapter the synchronization described in chapter 4 is characterized. The relevant parameter for synchronization is the jitter between the reference and the laser. Two different ways to measure jitter are presented and explained. Jitter is measured for different kinds of references and output signal combinations to demonstrate the actual temporal limitations when using references and internal signals of the laser system but also to prove the applicability in scientific context when measuring with the actual pulses. Furthermore, the precision of the delay setting is measured. The last section describes the established setup for time-resolved electron-ion-coincidence spectroscopy.

5.1. Synchronization to a Signal Generator

5.1.1. Method of Measurement

The used Oscilloscope 'LeCroy WaveRunner 204Xi' (2 GHz, 10 GS/s) allows a comfortable way of measuring jitter. In this work jitter is usually considered the standard deviation of the zero crossing of one signal when triggered on the zero crossing of another if not stated otherwise. Zero in this case could be any chosen set point. In case of pulses on a photo diode a smart offset is used of course. The LeCroy measurement "time at level" can be used to measure this property as illustrated in figure 5.1. The red reference signals (A) zero crossing is used as trigger in this example, while the temporal offset Δt of the synchronized blue signal (B) is measured. This measurement is repeated and the values for Δt stored in a histogram (green). The standard deviation of Δt is the jitter σ.

The described measurement is accurate down to the order of single picoseconds, depending on the quality of the reference. This can be shown by splitting the reference and performing the described measurement with the reference and its own copy as A and B (corresponding to red and blue signals in figure 5.1). The result can be seen in figure 5.2. The signal triggered to itself states a jitter of $\sigma \approx 3$ ps thus this is the limit of this method to measure. This limit, however, is not only depending on the oscilloscope but also on the actual shape of the signals. As for any timing and trigger related measurements on oscilloscopes especially a steep rise of the signal at the position of the trigger or measuring (for sine signals usually the zero crossing) is mandatory for best results. If the amplitude or the shape of photodiode signals is small (leading to a less steep rise) or fluctuating or suffers an unstable background (both leading to amplitude to phase noise conversion as the trigger level is not reached at the same relative level) this limit can not be reached.

The stated trigger and interpolator jitter for the used model is according to the manufacturer homepage RMS < 3 ps (typical) [8]. This is in good agreement with the presented

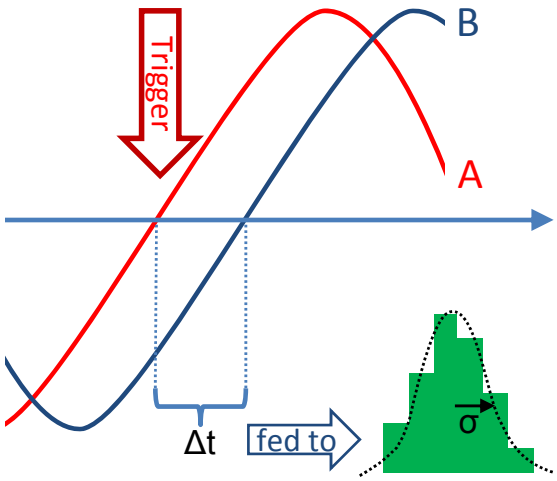

Figure 5.1.: Method of jitter measurement with fast LeCroy oscilloscopes.

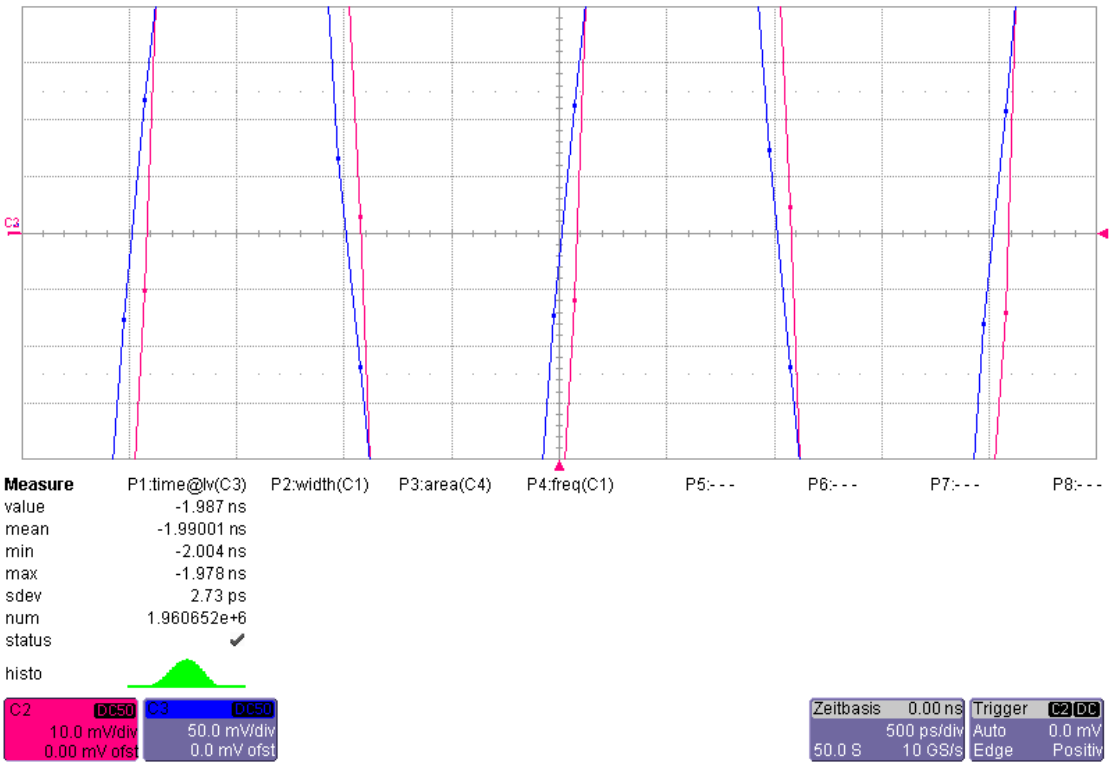

Figure 5.2.: The method of measurement is limited to a jitter of $\sigma \approx 3$ ps (see chapter 5.1.1).

measurement.

5.1.2. PHAROS vs HP 8657B Signal Generator

The synchronization was set up in the lab using a signal generator to emulate the PETRA III masterclock. The used signal generator is a 'Hewelt Packard 8657B 0.1-2000 MHz Signal Generator' and was set to 499.662 MHz after PHAROS had been synchronized to PETRA III the first time. Hence either the signal generator has a small off-set or the PETRA III design value of 499.564 MHz is not reached exactly (or both). As the piezo in PHAROS allows tuning in the range of a few kHz only, the cavity needed to be adjusted to the actual PETRA III values. The effect of the synchronizations jitter on the total temporal resolution can be limited by considering other sources that contribute to the overall temporal resolution: In a pump probe setup the temporal resolution is governed by the pulse length of pump and probe pulse as well as the jitter between them (so to say the jitter of the synchronization). As the pulse shape in time as well as the jitter are considered to be gaussian the convolution of those three parameters to the total temporal resolution is the square root of the squared sum of the three contributing sources:

$$\sigma_{total} = \sqrt{\sigma^2_{PETRAIII} + \sigma^2_{PHAROS} + \sigma^2_{sync}}$$

This means that the largest number contributes dominantly to the temporal resolution. As PETRA III is designed to have bunch length of 44 ps RMS [4] - which then also is approximately the pulse length - the length of PHAROS pulses can be neglected, as they are in the sub picosecond range they will contribute only in the sub per-mill order. Therefore the temporal resolution can be considered as:

$$\sigma_{total} = \sqrt{\sigma^2_{PETRAIII} + \sigma^2_{sync}} \tag{5.1}$$

The synchronization, therefore, is designed to reach the sub-10-ps region as it then will only contribute roughly 1 ps or 2.5 % to the overall temporal resolution. Some key values for the influence of the synchronization jitter on the overall temporal resolution can be seen in table 5.1. It contains the overall temporal resolution σ_{total} for an assumed PETRA III pulse length of $\sigma_{PETRAIII}$ = 44 ps depending on the jitter of the synchronization σ_{sync} as well as the difference to the ideal case with no jitter relative (in %) as well as absolute (in ps). The values are calculated based on formula 5.1.

The measurement has been performed as described in chapter 5.1.1 above using the 'PD OUT' of PHAROS as A and a 500 MHz signal generator as B. 'PD OUT' is the output of an internal photo diode within PHAROS to monitor the outgoing pulse train. The result can be seen in fig. 5.3 showing a jitter of $\sigma < 8$ ps. This already fulfills the requirement of a sub-picosecond contribution to the overall temporal resolution. The synchronization is, however, not optimized for the signal generator but the real PETRA III references.

σ_{total}	σ_{sync}	Contribution of σ_{sync}	
		in ps	in %
44,00	**0,00**	**0,00**	**0,00**
44.08	**2.73**	0.08	0.19
44.22	**4.40**	0.22	0.50
44.67	**7.70**	0.67	1.52
46.41	**14.76**	2.41	5.48
47.11	**16.83**	3.11	7.07
44.44	6.24	0.44	**1.00**
48.40	20.16	4.40	**10.00**

Table 5.1.: The influence of the synchronization jitter on the overall temporal resolution σ_{total} for an expected PETRA III pulse length of $\sigma_{PETRAIII}$ = 44 ps. Stated are mentioned or measured values (upper part) within this work as well as a selection of milestone values for an better overview.

5.2. Synchronization to PETRA III

5.2.1. PHAROS vs PETRA III Masterclock

The measurement has been performed as stated in chapter 5.1.1 using the 'PD OUT' of PHAROS as A and the 500 MHz reference from the PETRA III masterclock as B. The result can be seen in fig. 5.4. Towards the reference that PHAROS is phase-locked to the jitter is below 5 ps which is close to the limitations of the method to measure.

It also is sufficient as PETRA III is designed to have a bunch length of 44 ps rms [4] and, therefore, the temporal resolution will be governed by the pulse length being in that order as well.

The value of $\sigma < 5$ ps is also the number for the expected jitter between the laser and X-ray pulses. This is because the PETRA III reference should be synchronized much better than this towards the real PETRA III X-ray pulses. The quality of the reference signal is according to discussions and data by Jens Klute from DESY depending on the position along the PETRA III ring as distribution over long distances causes further noise. Measurements by his group indicate a RMS jitter via integrated spectral power density over a broad bandwidth being between 300 fs and 1.47 ps depending on different locations along the ring to measure. For further understanding of RMS jitter see chapter 5.2.4. This indicates that possible contributions of jitter between the reference and the real synchrotron pulse-train will not have a major impact on the overall temporal resolution and can be neglected in the following. The origin and distribution of the reference signals at PETRA III is described in [48] as 'The Carrier Frequency Generator PLL'.

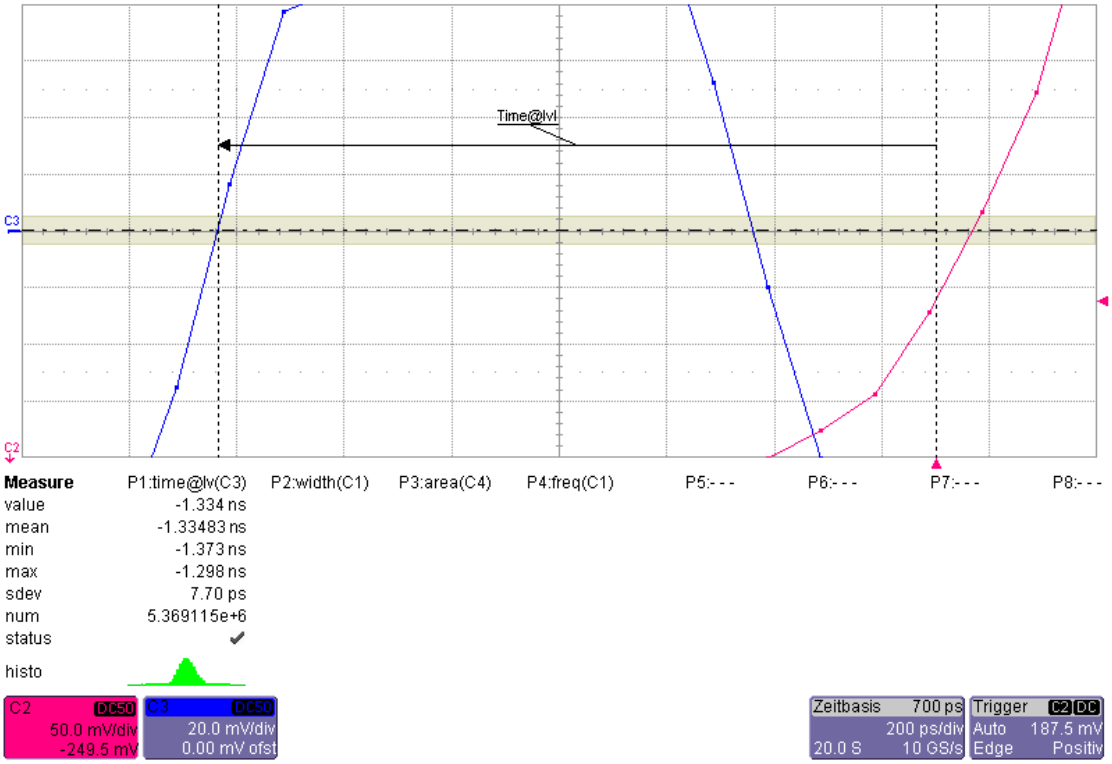

Figure 5.3.: PHAROS synchronized towards a lab reference reached a jitter with $\sigma < 8$ ps

5.2.2. PHAROS vs PETRA III on Photodiodes

To ensure the proper working of the synchronization not only the synchronization towards the masterclock but also the synchronization between the physical pulses needs to be checked. Even though it can not be expected to measure as small values here as various further noise sources contribute. This measurement has been performed as stated in chapter 5.1.1 now using the 'PD OUT' of PHAROS as A and the signal of a photodiode hit by the X-ray pulses as B.

In late 2010 first tests of the synchronization of PHAROS pulses and actual synchrotron radiation could be performed at P11. A photodiode had been set up in the optics hutch to provide a signal of the synchrotron pulses. The result can be seen in fig. 5.5

This first measurement of the actual light pulses being synchronized stated a jitter of $\sigma < 17$ ps. This was obviously limited by noise on the cables, as the X-ray beam did not reach further than into the optics hutch, yet, while for safety reasons the laser had to be situated within the experimental hutch of P11. Therefore, each signal had to be provided with BNC cables with a length of more than 20 m each. They worked as antennas and received various noise signals which added to the signals. The changed trigger level causes that amplitude noise leads to more phase noise as well. This is the well known amplitude-to-phase-noise conversion.

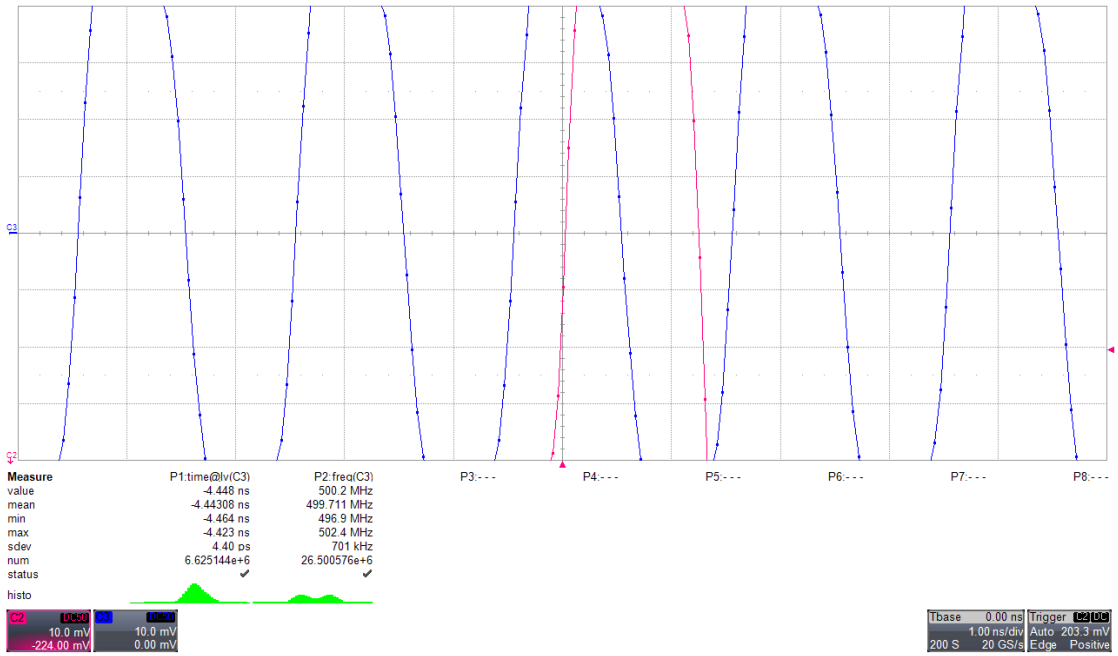

Figure 5.4.: PHAROS vs the PETRA III 500 MHz reference reached a jitter with $\sigma < 5\ ps$

5.2.3. PHAROS vs PETRA III on one Photodiode

In late 2011 for the first time X-ray and laser pulses have been synchronized in space and time at P11. This is proven by the measurement of both pulses on one photodiode and can be seen in fig. 5.6. The laser pulses have been the 3rd harmonic of PHAROS (343 nm).

Jitter has again been measured as described in chapter 5.1.1 with the slight adjustment that A and B are now on the same signal but in different ROIs. The pulse of the 3rd harmonic of PHAROS leads to a peak with a much higher amplitude than the pulse of the X-rays. This is due to the very different efficiency of the photodiode for X-rays in the keV range than for UV light. Hence the trigger level was set above the amplitude of the X-ray pulses to ensure always to trigger on the UV pulses. Then "time@level" has been applied within the region in front of the trigger event. The limitations of this method are obvious from this description: Various factors contribute mainly to effects that cause unstable amplitudes or a higher dependency on stable amplitudes, therefore, leading to more jitter due to amplitude-to-phase-noise conversion. First, the high trigger level which is necessary to distinguish between the two pulses introduces a higher dependency on stable amplitudes. Second, the monochromator has not been stable in pointing at that time as we figured out in later experiments. This means the photodiode is not always hit optimal on its small sensitive area which leads to further amplitude fluctuations directly leading to another contribution to phase noise. Finally, the photodiode is not made to be equally sensitive for uv and X-ray photons, therefore, the 3rd harmonic needed to be attenuated a lot and even the harmonics generator needed

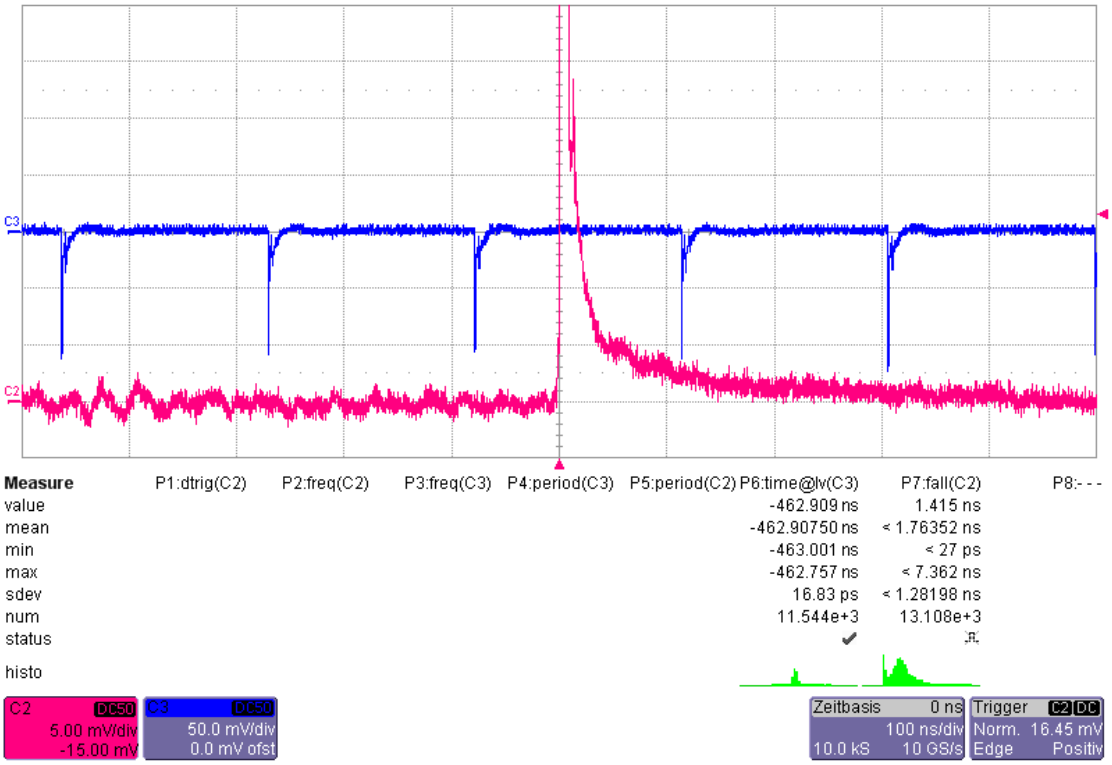

Figure 5.5.: PHAROS vs PETRA III on two Photodiodes on LeCroy Oscilloscope reached a jitter with $\sigma < 17$ ps

to be misaligned as one would not have gotten a comparable X-ray signal otherwise. This is obviously not the most stable way to use the harmonics generator. As it is based on non-linear effects, driving it at the starting-point of third harmonic generation makes it more sensitive for minor fluctuations of the input pulse power. Therefore the third harmonic amplitude is also expected to be less stable than usual possibly in amplitude but as well in space. For those reasons the measured jitter with a $\sigma < 15$ ps is again just an upper border approximation. However, having synchronized PHAROS and PETRA III in time and space the first time represents the first major milestone towards time resolved experiments at PETRA III using the pump-probe method. Even this upper border would - as can be seen in table 5.1 - only contribute below 2.5 ps to the overall temporal resolution or in other words would increase it by less than 6 % compared to a theoretical ideal synchronized case.

5.2.4. PHAROS vs PETRA III via Agilent E5052B SSA

During the setup of the synchronization at P11 an Agilent E5052B signal source analyzer (SSA) from DESY could be used for a short period of time as well. This measurements and also parts of the explanation follow the description and considerations in [76].

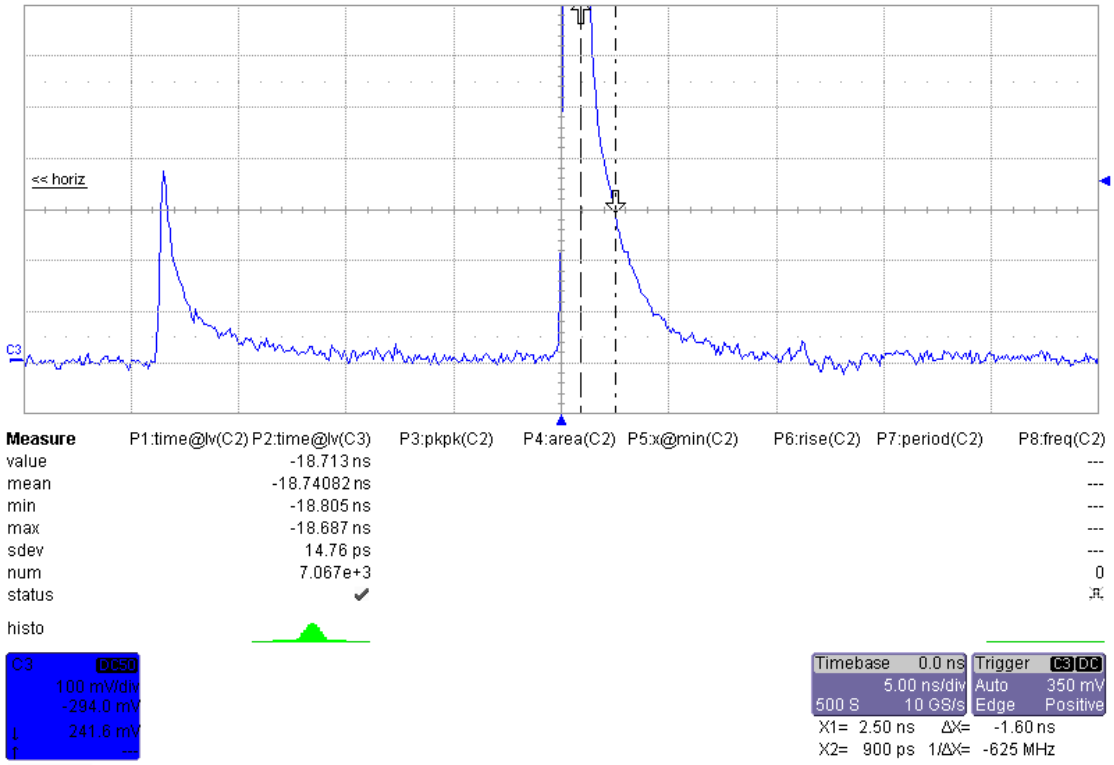

Figure 5.6.: PHAROS vs PETRA III on the same Photodiode on LeCroy Oscilloscope reached a jitter with σ below 15 ps

Single Side-Band Phase Noise

This device offers a spectral examination of the synchronization and its properties. It measures the so called *single side-band phase noise*. Single side-band phase noise $\mathcal{L}_\phi(f_i)$ gives the power ratio between a frequency f_i and the carrier frequency f_0 per bandwidth. To illustrate that one could imagine measuring it with an ideal frequency-tunable band-pass filter of 1 Hz width and then measuring the output power of the bandpass depending on its set frequency and normalized to the power of the carrier frequency (i.e. the desired repetition rate). From this single side-band phase noise the signal source analyzer computes the 'RMS Jitter' which is a similar property as the jitter σ defined in chapter 5.1.1. It, however, contains only the part contributed by the considered spectral band. A detailed discussion on single side-band phase noise and its relation to jitter the way it is used in this work can be found in appendix A.1. The derivation of the following statements can be found there as well.

The RMS Jitter on the interval $[f_1, f_2]$ referred to as $\Delta t_{RMS}(f_1, f_2)$ is calculated according to formula 5.2 (derived as A.32).

$$\Delta t_{RMS}(f_1, f_2) = \sqrt{\int_{f_1}^{f_2} \frac{2}{(2\pi f_0)^2} \mathcal{L}_\phi(f_i) df_i} \tag{5.2}$$

For $f_1 \to 0$ and $f_2 \to \infty$ in ideal case follows $\Delta t_{RMS}(f_1, f_2) \to \sigma$. Therefore the stated RMS Jitter of the SSA is highly related to the jitter σ especially if chosen for a suitable frequency interval.

Setup of the Measurement with the SSA

The measurement scheme with the signal source analyzer is illustrated in figure 5.7. The

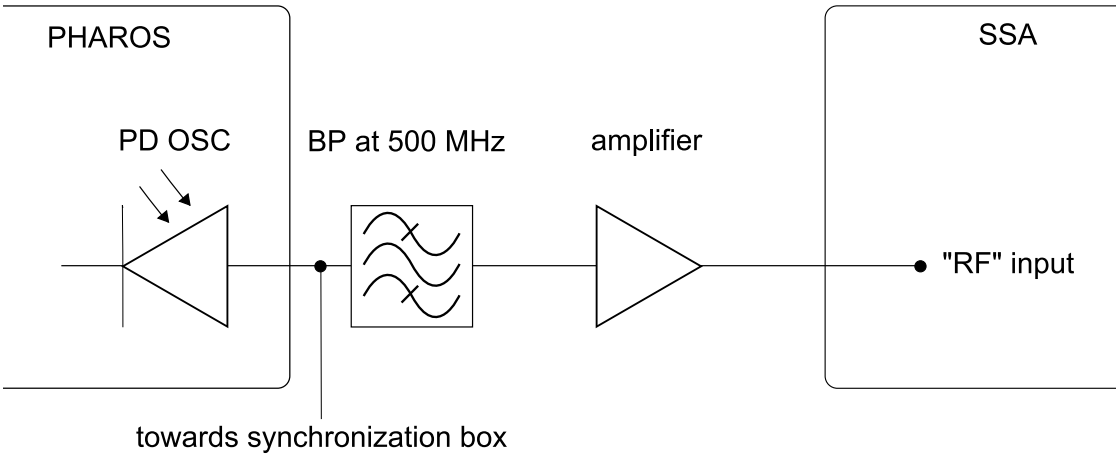

Figure 5.7.: Scheme for the measurement of the phase noise with the signal source analyzer.

internal photodiode of the PHAROS oscillator is used via the 'PD OSC' port offered by PHAROS. As this is as well the signal used to synchronize PHAROS the performance of the synchronization might be slightly different as usual as the signals amplitude might be slightly different. More important - especially if comparing with the measurements performed and described by Sebastian Schulz [76] and Dennis Göries [40] - the internal photodiode of this PHAROS oscillator is not saturated and, therefore, fluctuations of the amplitude might lead to bigger phase noise due to amplitude-to-phase noise conversion.

The SSA measures the spectral power density by comparing the signal with an internal reference. This is a similar concept as the PLL for synchronization. To reduce the influence of the noise of the internal reference correlation techniques can be applied reducing the noise of the measurements, furthermore.

SSA Measurements and PLL Tuning

The measurement of PHAROS synchronized to PETRA III at beamline P11 can be seen in figure 5.8 (dark curve). The spectrum shows some dominant features such as 50 Hz AC noise and its harmonics or the 130 kHz peak and its harmonics directly connected to the amplifiers repetition rate thus leading to the conclusion that it is slightly backfiring into the oscillator diode. The peak on the far right is the 83 MHz reference signal also still occurring within the error signal. A further mentionable feature is the broader bump

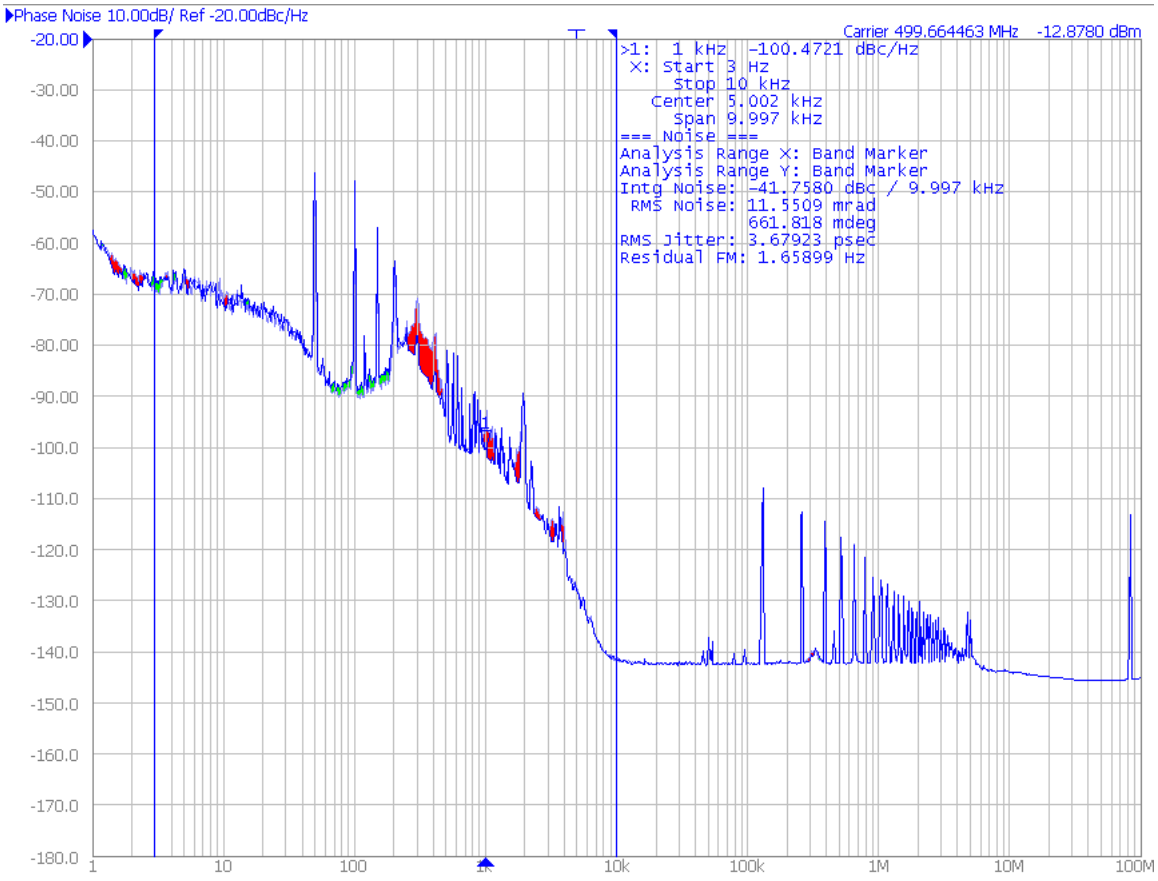

Figure 5.8.: Single side-band phase noise measurement with signal source analyzer before optimization of the PID parameter (dark). After optimization for comparison (bright) - for better perceptibility the difference is marked in red /green. Dominant features that could not be avoided are 50 Hz AC noise as well as 130 kHz from the amplifier and the respective harmonics.

around 200 Hz up to approximately 400 Hz which is determined by the PID parameters directly. This can be shown by tuning them slightly. The brighter curve is based on optimized PID parameter settings for reference as described below. As both curves are rather similar deviations have been marked in red and green. The stated value RMS Jitter can be used to optimize PID parameters further, as the temporal resolution of the oscilloscope is already reached here so small effects cannot be distinguished any more. For comparison for the same settings as in figure 5.8 a measurement as described in 5.1.1 has been performed. The value for the RMS Jitter $\Delta t_{RMS}(f_1, f_2)$ in the interval $[f_1, f_2]$ on the SSA as discussed above is $\Delta t_{RMS}(3\text{ Hz}, 10\text{ kHz}) = 3.7$ ps while for the Jitter on the oscilloscope the stated value is $\sigma = 4.8$ ps. The interval of [3 Hz, 10 kHz] has been chosen to optimize the PLL and especially the PID parameters as the PLL can only operate with a cycle frequency below 1 kHz to avoid resonances of the piezo as can

be seen in figure 4.4. Therefore, major effects of the synchronization will be in the lower frequency range. Furthermore, the values for RMS Jitter will be highly influenced by the 130 kHz signals from the amplifier which are undesired but not actual noise to be eliminated with the PLL circuit. In figure 5.9 can be seen that for long times (i.e. small frequencies) the RF source is less noisy while for short times (large frequencies) the laser oscillators noise falls below that ov the reference. Hence it is reasonable to lock the laser oscillator especially for the small frequencies.

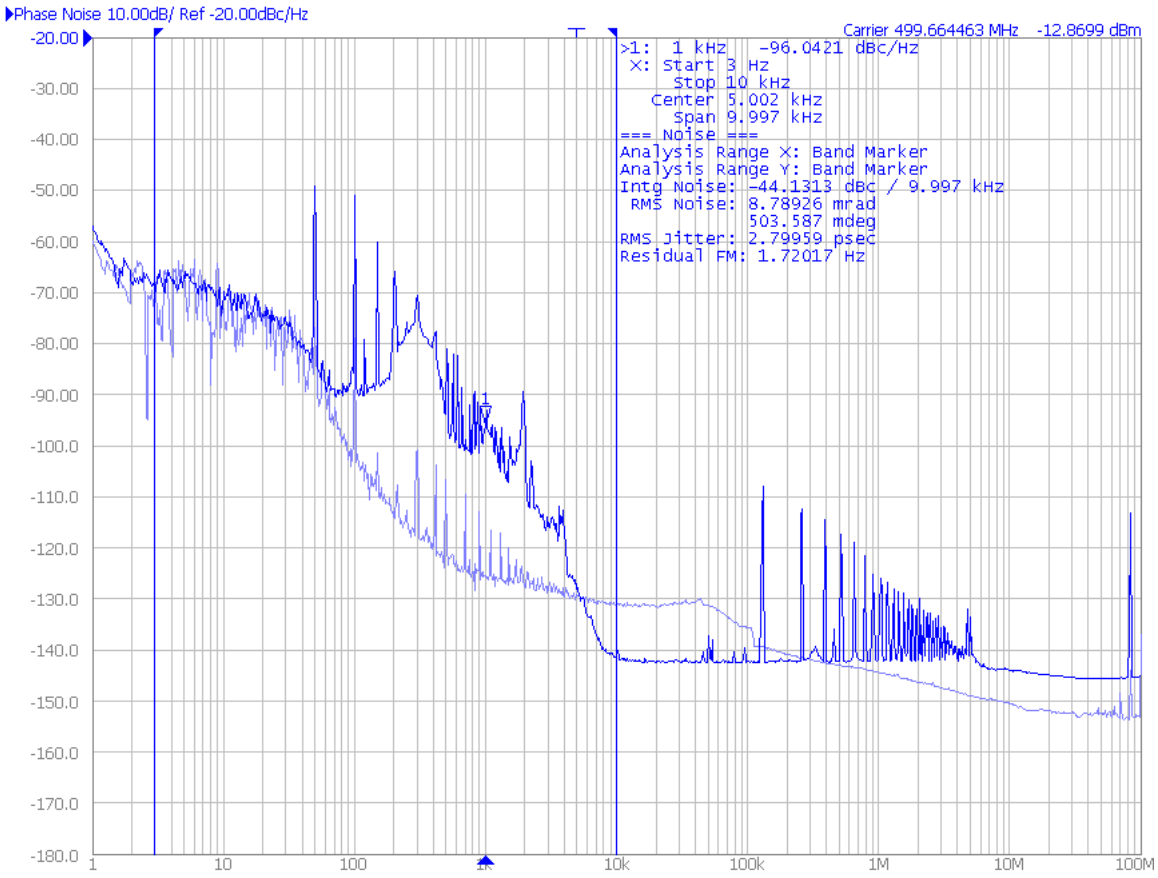

Figure 5.9.: Single side-band phase noise measurement with signal source analyzer after optimization of the PID parameter (dark). Noise spectrum of the reference signal (bright).

Here the dark curve is the noise of the synchronized PHAROS after optimization of the PID parameters in matters of the RMS Jitter. The brighter curve, however, is the noise of the 500 MHz reference. It can be seen that in locked case the noise of the oscillator is locked to the reference up to somewhere around 100 Hz. Above that level more noise than in the reference occurs but starting from 5 kHz the oscillators noise even falls below that of the RF reference. A higher possible control frequency (i.e. higher piezo resonances) would allow to further reduce the noise in this transition region as

can be seen by the newer PHAROS system available at beamline P11 which was also designed and synchronized considering the experience with this system. Comparable measurements for the P11 PHAROS system are presented in [40].

The result of the optimization of the PLL and its PID parameters with the help of the SSA can be seen by comparing figure 5.8 stating the performance of the synchronization using the parameters at the beginning of the process, with figure 5.9.

The value for 'RMS Jitter' was reduced from Δt_{RMS}(3 Hz, 10 kHz) = 3.7 ps to Δt_{RMS}(3 Hz, 10 kHz) = 2.8 ps, the value for jitter as used in the further chapters reduced from σ = 4.8 ps to σ = 4.1 ps.

Deconvoluting the temporal resolution of 2.7 ps for the 'RMS Jitter' (see chapter 5.1.1) from σ = 4.8 ps or σ = 4.1 ps shows good agreement of both measurements and the close relation between single side band phase noise and jitter as defined here:

$$\sqrt{(4.8\ ps)^2 - (2.7\ ps)^2} = 4.0\ ps \approx \Delta t_{RMS}(3\ Hz, 10\ kHz) = 3.7\ ps \tag{5.3}$$

$$\sqrt{(4.1\ ps)^2 - (2.7\ ps)^2} = 3.1\ ps \approx \Delta t_{RMS}(3\ Hz, 10\ kHz) = 2.8\ ps \tag{5.4}$$

5.3. Temporal Position

The accuracy of hitting the desired delay can be seen in figure 5.10. It was measured the same way as described in 5.1.1, however, this time the actual position is considered. Of course the minimum standard deviation possible is again the limitation for this method. The standard deviation of the delay positions is σ = 0.85 ps $\widehat{=}$ 0.15°. The maximum offset against the reference is around 4 ps which is around or below the possibilities the measurement offers (see chapter 5.1.1).

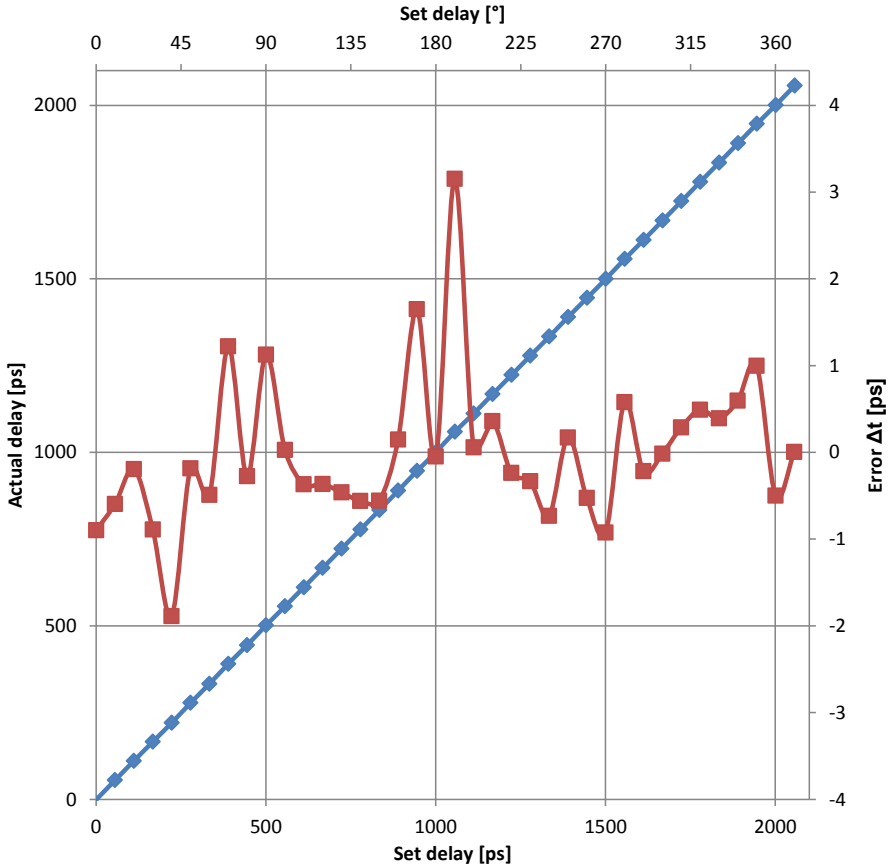

Figure 5.10.: The accuracy of the delay setting of the delay with the vector modulator. The blue curve gives the actual delay (left y-axis) depending on the delay setting. The red curve is the corresponding discrepancy in ps (right y-axis).

5.4. Electron-Ion Coincidence Spectroscopy in the Gas-Phase at P04

Time resolved pump-probe experiments on samples in the gas phase have been conducted at other synchrotron radiation facilities in the past [87]. Also at the Freie-Elektronen-Laser in Hamburg (FLASH) such studies on atoms (see for example [50], [70] for studies on Xe) and molecules (for example Iodine [51]) have been conducted. The presented synchronized laser system allows to conduct similar experiments at PETRA III as well.

A setup for such experiments is presented and had been aligned at P04. All experiments at P04 have been performed together with the group operating the beamline. For further information especially on the coincidence spectrometer and other aspects of these experiments see PhD thesis of Sascha Deinert [27].

5.4.1. Experimental Setup

The experiment is based on combining the presented laser system with the aforementioned electron-ion coincidence spectrometer. Its setup is an adaption of the coincidence spectrometer described in [33] based on the combination of a time-of-flight spectrometer (ToF) for ions combined with an electron ToF utilizing a magnetic bottle . This setup allows to detect ions and electrons from the interaction region. For electrons the ToF obtains the energy, for ions the mass to charge ratio. The magnetic bottle increases the detection efficiency for electrons. A trade-off between detection efficiency and resolution is a major challenge in developing and using such a device. The experimental setup is illustrated in figure 5.11. As the experiment took place at the XUV beamline P04 a vacuum setup needed to be used. All parts in the gray shaded area are part of the vacuum system and either within or attached to it. The double dashed line marks parts located within the laser hutch. The necessary laser safety concept including the design and installation of the mobile laser hutch including an interlock system (see appendix A.6) in accordance with the DESY safety regulations has also been part of this work. Besides the entrance of the hutch as well the pressure of the vacuum system and a valve needed to be integrated within the interlock system to avoid operating the laser when the experimental chamber is not sealed and thus prevent any laser radiation ever to cause potential danger. All windows in the vacuum system (dotted circles) outside the hutch were equipped with an additional laser safety window. The full laser safety concept and all forms necessary to get the permission by the responsible laser safety contact at DESY is attached in appendix A.6.

The XUV beam is led through aperture A1 consisting of two perpendicular slits of $100\,\mu m$ each thus remaining a square-shaped spot. As focusing has not yet been possible at P04 this caused a huge loss in flux. The XUV could be monitored on the screen S1 behind the interaction region and as well on a screen S2 movable directly into the interaction zone for alignment.

The laser beam needed to be pre-aligned with a laserpointer as otherwise an opening of the vacuum chambers is not possible for safety reasons. Its beampath is then fixed by two apertures A3 and A4 thus making it possible to follow the same path by the

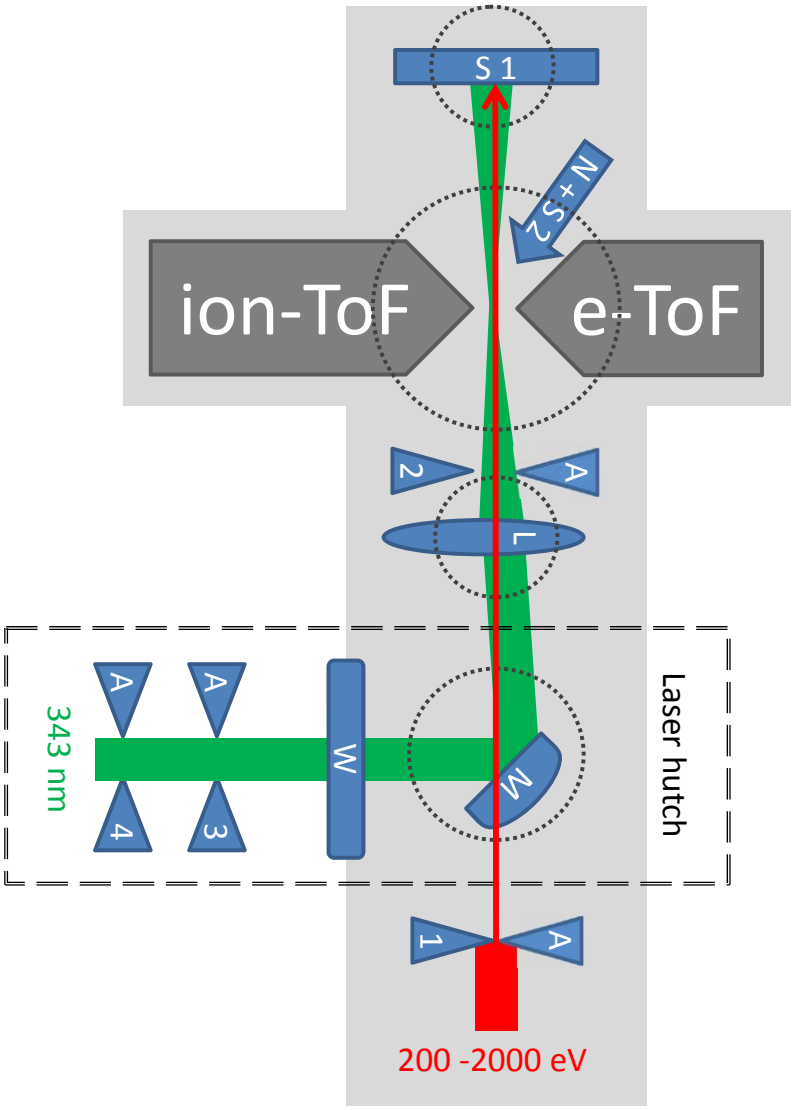

Figure 5.11.: Scheme of the time resolved e-I-coincidence spectroscopy experiment at beamline P04. The gray shaded area stands for vacuum surrounding, S marks screens, A stands for apertures, L for a lens, M for a motorized mirror, W for laser incoupling window and N for a gas nozzle. The dotted circles illustrate windows within the vacuum chambers, the double-dashed line marks the part of the experiment that was inside the laserhutch for safety reasons. The green line shows the beampath of the laser pulses, the red line that of the synchrotron radiation.

UV laser beam later on by leading it through those to apertures as well. Otherwise a systematic alignment within a reasonable time hardly was possible. The beam propagates through the incoupling window W which was chosen with a suitable coating for the used wavelength to minimize losses. A motorized D-shaped mirror M necessary for fine adjustment within vacuum has been positioned as close to the XUV beam as possible without clipping. It was aligned to lead the UV beam as parallel as possible with the XUV beam. The following lens L has either been D-shaped as well or contained a hole so the XUV can pass without disturbance while the UV beam now gets focused in the interaction region. Further apertures A2 had been necessary to reduce stray light and reflections from the various surfaces inside the beam path as much as possible as any photons hitting parts of the spectrometers or vacuum chamber close to the interaction region cause a lot of electrons also detected by the spectrometer and thus producing undesirable background. Finally, the now focused beam reaches the interaction zone where the target gas can be released by the nozzle N. The now divergent beam after the interaction zone can also be monitored on screen S1.

The coincidence spectrometer is triggered by the bunch-clock and enables to map not only the time-of-flight spectra of electrons and ions respectively but as well correlations thereof. This allows to obtain rather background free spectra if the countrates are kept reasonable. Furthermore, the detection of the energy of the electrons and the corresponding ion gives additional information.

5.4.2. Results: Temporal and Spatial Overlap in Vacuum, Setup Ready for Experiments

Temporal Overlap

The temporal overlap has been achieved by the signal of photons on the micro-channel plate (MCP) inside the ToF. To see those signals all voltages within the coincidence spectrometer had been set to not guiding any electrons or ions on the detector[1]. Then the gas nozzle was put into the interaction zone to reflect laser photons as well as those of the white light beam of beamline P04. These reflected photons are detected by the spectrometer's MCP detector appearing as a very narrow peak. The adjustable delay of the bunch-clock used to trigger the pockels cells is used to shift the laser peak close to one desired XUV peak within a grid of 12 ns steps. Final overlapping is reached with the smooth delay setting of the vector modulator within the synchronization unit. The spectrometer and its data acquisition allow a temporal overlap to be at best within one bin width of the generated temporal histogram, namely 120 ps at PETRA III. However, the intrinsic temporal resolution of the MCP depending on the position it is hit might be worse. Thus in any case where faster dynamics have to be studied or expected a delayscan is necessary and also suggested for higher contrast in any other case.

Figure 5.12 illustrates white light as temporal marker, the purple markers have been set to the borders of the pockels cell gate (the 12 ns delay setting window which is covered by the vectormodulator). Those borders have been measured the same way with UV

[1] so the voltages got heavily misaligned compared to typical use

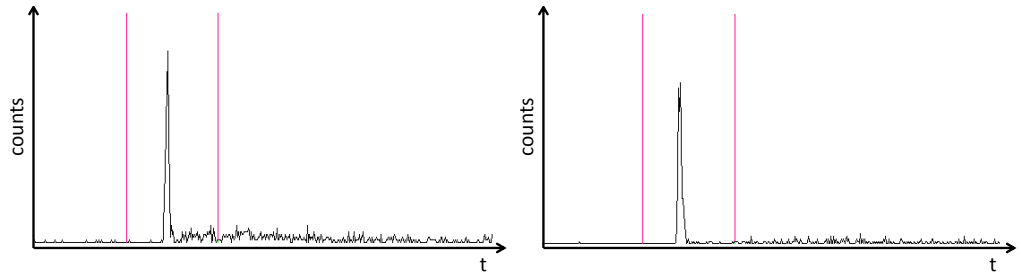

Figure 5.12.: Synchrotron white light used as temporal marker located within the window for the possible temporal position with that pockels cell trigger setting. This setting allows a delay scan where the step needs to be within the examined region. The left figure shows the marker measured by the electron spectrometer, the right figure by the ion spectrometer.

instead of white light being used as marker. This can be seen in figure 5.13 where the UV pulses are shown to be shifted through the pockels cell window and thus marking its borders. The XUV marker needs to be inside this window to be possibly overlapped during a delay scan or by adjusting the vector modulator.

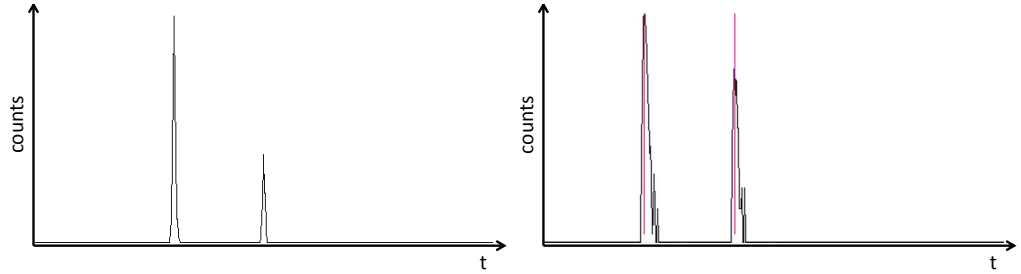

Figure 5.13.: Obtaining the temporal gate allowed by the pockels cells for a particular setting of the bunch-clock: The UV marker can be moved within a 12 ns window, shiftable with the pockels cell trigger. The figure shows UV markers at the borders of the 12 s window in the electron ToF (left figure) and in the ion ToF (right figure).

Spatial Overlap

The spatial overlap is ensured by monitoring both beams on a fluorescent screen offering the opportunity to be positioned with micrometer screws directly in the interaction zone (S2). Cameras allow to reproduce positions to the limit of their resolution. Such a camera image is shown in figure 5.14.

Further cross checks can be performed as the focus of the visible light can be probed with the gas nozzle (N) on the screen behind the interaction zone (S1): If the nozzle is inserted early in the beam path (i.e. in front of the focus), the later screen darkens from

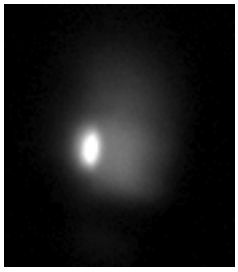

Figure 5.14.: Spatial overlap on the screen in the interaction zone: The bright spot is the XUV radiation from PETRA III, the darker slightly bigger spot is the UV laserspot (PHAROS being dramatically reduced in output power). Both spots can be monitored and are reproduceable by comparison of actual camera images with saved images.

the other side than the gas nozzle enters. If the gas nozzle is inserted behind the focus its shadow will be appearing from the same side on the later screen. If the focus is hit the spot disappears without a direction can directly be assigned. The gas nozzle itself can be used not only to block the beam and cast a shadow on the screen S1. It also offers the possibility to be used as a source of photo electrons when hit by light, thus the vertical position and size of the spots can be scanned with the nozzle. The horizontal position can be scanned the same way.

Experiments

By achieving temporal and spatial overlap the basics to perform time resolved electron ion coincidence spectroscopy in a pump probe approach have been established. The goal was to conduct an experiment similar to that described in [50]. There Xe has been pumped to highly excited Rydberg states[2] by the XUV pump pulse delivered by the XUV Free-Electron-Laser FLASH at DESYand probed by visible or UV pulses. While the experiments at FLASH have been conducted with 92 eV, the XUV beamline P04 at PETRA III offered energies starting from around 200 eV up to around 800 eV at the time of this work. Therefore, different excitations have to be considered. An advantage of the FLASH facility is with no doubt the achievable temporal resolution which is more than three orders of magnitudes better. However, the synchrotron facility offers a broader range of available energies and the presented lasersystem is tunable in wavelength as well. The coincidence approach also enables to measure almost noise-free thus allowing statistically significant measurements with little countrates already. Krikunova et al [50] excited 4d shell electrons while the available energy range at P04 demands a different excitation. As shown in [68] a resonant excitation of $3d_{5/2}$ electrons to the 6p shell is possible at 674 eV. Furthermore, table 1 in [68] illustrates the difference in ion yield to be expected for resonant excitation and direct ionization respectively. From these values

[2]Highly excited valence electrons that are hardly bound any more thus laser photons can further ionize the sample.

it is reasonable to expect a possible change of ion yield by UV pumping the resonant excitation would be in a similar typical order of a few percent (what is still below the discrepancy towards the theoretical models mentioned in that source).

At the time of this experiment P04 was still in the commissioning phase and not reaching specifications yet. Thus the energy resolution was worse than expected making it hard to hit a resonance to create Rydberg electrons only. Also focusing has not yet been possible and some of the final XUV optics had not been installed yet thus the flux was less than expected.

Under these conditions not enough relevant Ions were generated to obtain proper statistics within reasonable time. For example, the countrate for Xe^{6+} was around 8 to 13 counts per minute, so to be able to observe a comparable 10% effect as mentioned in [68] with 2 σ significance taking a set of data would last around 40 minutes, if only poisson statistics are considered. Of course further sources of noise have to be taken into account as well as the fact that most likely due to the energy resolution not all ions originate from Rydberg states and the laser and synchrotron overlap might not be preserved over long times due to drifts. As such a big effect would only take place for ideal delay and energy settings, these needed to be scanned and thus the experiment needed to be repeated for every point of data. Additional errors caused by declining sample pressure unfavour long termed measurements. Due to the additional aperture and the low energy resolution, possible pointing instabilities could even cause energy drifts. The laser system was located within the sealed laser hutch causing uncommon thermal conditions as well as hindered tuning access, therefore, also demanding regular checks thus making even longer periods to measure impossible. We observed a long term damage on the UV coated optics inside the vacuum caused by the laser also worsening the long term stability of the setup.

Taking all these aspects into account, the results obtained within the scope of this work are limited to the demonstration of a working setup for pump-probe experiments at P04.

Further experimental experience with various other samples with an inner shell electron binding energy within the available energies such as N_2 or CO_2, for example, could be gained, however, the basic situation was persistent.

6. Time-resolved studies at PETRA III

Two different kind of experiments have been carried out in combination with the developed synchronized laser system:

X-ray Absorption Spectroscopy (XAS) of laser-pumped fluorescent samples soluted in a liquid jet were probed with X-rays with energies between 7 keV and 12 keV (the beginning of the hard X-ray regime according to the classification from [12]). Samples were molecules that can be used for organic light-emitting diode (OLED) applications such as Gaq3 and Znq2.

Furthermore, at beamline P04 XUV-pump laser-probe experiments were set up. This benchmarking measurements are described in chapter 5.4. The target were inner shell electrons of gas molecules having been pumped into rydberg states just below the ionization threshold with photon energies at some hundreds of eV usually being considered extreme ultraviolet (XUV) or soft X-ray (still according to the classification used in [12]).

6.1. XAS at P11

All experiments at P11 have been performed together with Benjamin Dicke and Dennis Göries. For further information especially on the samples and other aspects of these experiments see PhD thesis of Benjamin Dicke [30]. At beamline P11 X-ray Absorption Spectroscopy (XAS) experiments have been performed. Actually X-ray fluorescence yield has been measured as a measure of absorption. Therefore, X-ray pulses and UV laser pulses were overlapped in time and space on the target. It was dissolved and provided in a liquid jet to avoid probing radiation damaged targets. The jet was set up on the basis of [84] and [34] and is described in detail in [30].

The sample was pumped with UV pulses of a wavelength of 343 nm and visible fluorescence could be observed. Emission and absorption spectra of Gaq3 can be found in figure 6.1. Additionally X-ray fluorescence was caused by the X-ray probe and detected with the *avalanche photodiode* (APD). The change of X-ray fluorescence yield depending on the excitation of the sample by the pump pulses is the observed quantity. By changing the relative timing t between pump and probe the temporal evolution of the excitation caused by the pump pulse was observed. As de-excitation processes occur this leads to a (possibly combined) exponential decay which allows to define a lifetime τ as the characteristic constant:

$$A(t) = A_0 \cdot e^{-\frac{t}{\tau}} \tag{6.1}$$

In the following sections the term lifetime will be used in that way.

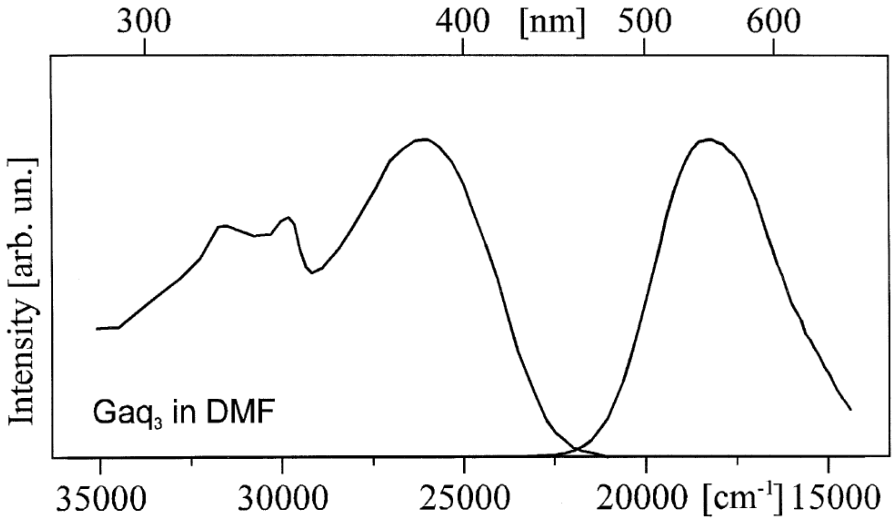

Figure 6.1.: Absorption and emission spectra of Gaq3 (dissolved in DMF) in the visible light regime - adapted from [43].

6.1.1. Experimental Setup

The experimental setup consists of five major parts:

- The lens packet used to focus the X-ray beam. A spot size slightly above 20 μm FWHM was reached.
- The hexapod[1] enabling remote control of the experiments positioning including the nozzle of the jet with the solved sample and its collecting vessel, the avalanche photo diode (APD) to measure the X-ray fluorescence and the optics for the laser to be focused on the interaction region.
- Flux diodes used to align the hexapod and normalize the data to.
- The electronics used to process the signals from the APD
- The software allowing to control everything and save data via the TANGO system of PETRA III

More details on the first three parts and their performance are presented in [30]. The software is part of the upcoming thesis of Dennis Göries [40]

The hexapod including jet tower, flux diodes, Schwarzschild objective[2] and camera can be seen in the picture 6.3.

[1] see figure 6.3

[2] a commercial reflective microscope objective by Newport, see http://www.newportfranklin.com/products/ReflMicroscopeObj/refMicObj.htm (May 13, 2013)

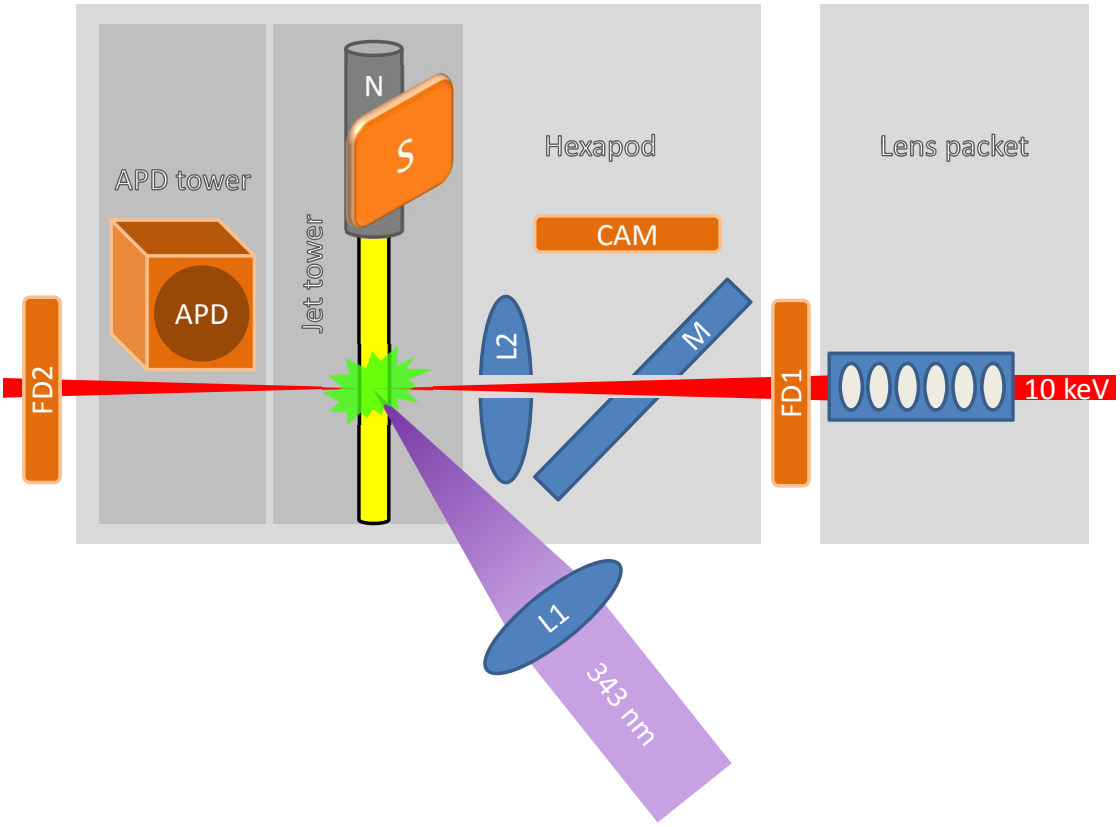

Figure 6.2.: The setup at P11: Detectors are displayed orange, optics blue and gray shaded boxes group elements that belong to the same remotely adjustable unit. L marks a lens, M a mirror, S a screen, N the nozzle, FD flux diodes, and CAM a camera.

For a schematic description of the general setup see figure 6.2: The synchrotron beam (red) propagates from the right side through the lens packet[3]. The lens packet contains several X-ray lenses, the number needs to be adjusted for the desired wavelength and focal length. In further setups focusing will be done by the beamline instead. The six degrees of freedom of the lens packet (all three directions plus the rotations around the axes perpendicular to the beam) are used iteratively to obtain a maximum flux measured by flux diode FD1. The now collimated X-rays pass a hole in a mirror and in an objective, here symbolized by lens L2, in the described setup it is a Schwarzschild objective[2]. The six degrees of freedom of the hexapod are used to ensure the X-rays propagate through these holes by maximizing the flux on FD2. Then the jet is moved into the beam and its three degrees of freedom are scanned for optimal flux of X-ray fluorescence on the APD. As screen S is mounted on the jet tower as well, it is possible to control beam size

[3]X-ray optics based on refraction as presented in [77] and extended to axially symmetric design [78]. Due to the little contrast of the refractive index in the X-ray regime lens arrays need to be applied.

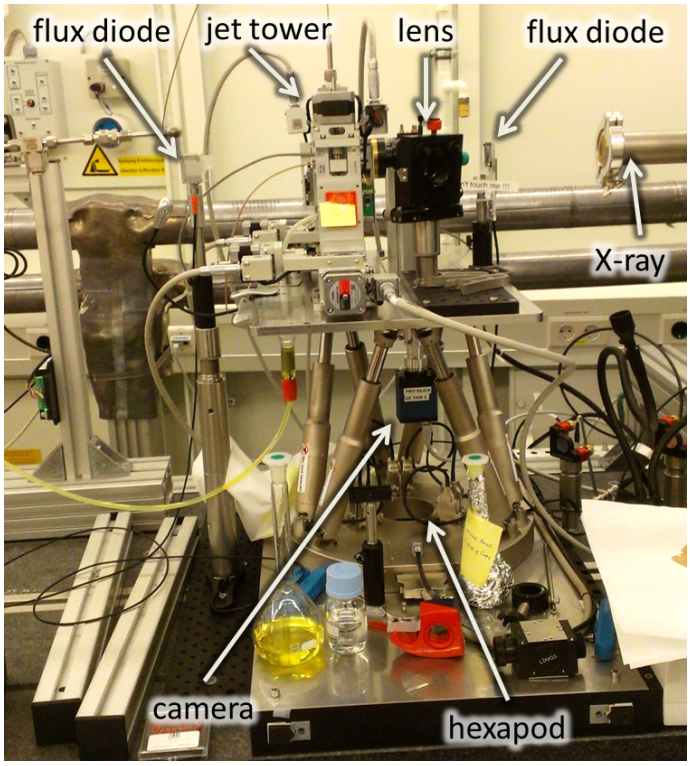

Figure 6.3.: The setup at P11: All major parts of the experiment are situated on the hexapod. The nozzle to produce a jet (various nozzles are available to get jet diameters between 30 and 200 μm) as well as the APD to measure the X-ray fluorescence are further motorized on the platform to be able to remotely control the whole setup. Further tools are fluorescent screen, knife edge and an on-axis camera available for calibration purposes.

and profile by doing knife-edge scans and also to monitor the X-rays on the fluorescence screen with the camera CAM via M and the objective L2. They need to be adjusted to give a sharp image in the focal plane of the X-rays as well. This can be achieved by focusing on the jet in optimized position. Then it is possible to move S at the same position along the beam by moving it into the focal plane of the objective. This allows to get an image of the fluorescence of the X-ray spot and later tuning the spatial overlap at the desired target position is possible as both beams are visible on this fluorescent screen. Finally, the APD has to be moved into an optimized position to achieve a useful countrate. To avoid multi photon counting but still obtain good statistics, a trade-off has to be done based on poisson statistics.

Some of the steps - especially those with hexapod and the two x-y-z stages called APD tower and Jet tower that are situated on the hexapod - may need to be optimized iteratively.

Finally, the laser (purple) has to be focused by a lens L1 onto the jet. The desired position is known and can be reproduced by the on axis-monitoring by CAM.

As it is impossible to calibrate and fine-tune such an X-ray experiment manually for obvious safety reasons alone, all described degrees of freedom are implemented within the TANGO[4] system, the software used at PETRA III to offer interfaces to all necessary parameters. Software connecting to those TANGO servers that provide access to the hosted devices[5] was written in python[6]. All devices that needed to be controlled or read out had to be implemented in TANGO so the whole experiment including all parameters that need to be changed or read out while taking a set of data can be controlled from one program. This includes not only parameters directly in the experimental setup but also within the laser system and the beamline.

Further information on the design of the described setup can be found in [30].

Temporal Overlap

The temporal overlap between PHAROS and PETRA III pulses is necessary as well. PHAROS pulses are around 300 fs long while PETRA III has a pulse width of below 100 ps. Depending on the bunch mode the bunches are separated by 32, 128 or 192 ns. Thus a broad tuning of the delay with the bunch-clock needs to be done. To monitor the relative temporal positions (in the point of interaction) while avoiding the temporal influence of different cable length or amplification devices, the APD and one of the fast photodiodes (from the AXUV High Speed series by IRD-INC, now Opto Diode Corp., as used i.e. in chapter 5.2.3) have been connected in parallel via a splitter to the APDs amplifier. As both photodiodes produce inverse peaks, they can be easily identified on the oscilloscope and the desired delay can be set.

It would also have been possible to reach temporal overlap using one photodiode as described in chapter 5.2.3, however, adjusting the photodiode to catch suitable amounts of X-ray and UV photons (taking into account its dramatically different efficiency for those energies) would have needed more space on the hexapod while the APD was installed there already and the efficient photodiode within the UV range could be stationed

[4] TANGO (TAco Next Generation Objects) is an object oriented distributed control system developed by various facilities (ALBA, DESY, Elettra, ESRF, FRM II, MAX-IV, Solaris and SOLEIL) - see official homepage: http://www.tango-controls.org

[5] anything with remotely controllable parameters can be implemented as a device, for example, the monochromator allowing to select the desired energy (or the corresponding grating positions), the undulator allowing to tune the gap (and, therefore, energy), but also the hexapod and all its degrees of freedom as well as ADC/DAC hardware allowing to read out devices such as flux diodes or providing control voltages for rudimentary devices not directly implemented in TANGO (see, for example, the shutter in 6.1.1). An overview of devices available and already implemented in TANGO at DESY can be found at http://hasyweb.desy.de/services/computing/Tango/Tango.html including manuals and sample code.

[6] python is a high-level and general-purpose programming language, for more information see http://www.python.org/

rather insensible.

Optimal temporal position for a certain measurement can then be detected by a delay scan around the optimal position according to the oscilloscope.

Electronic Measuring Equipment

As statistical analysis as shown later in this chapter and its errors need to consider how the analyzed counts were obtained a closer look on the measurement chain is offered. An overview is illustrated in figure 6.4, a description of the involved devices is listed below.

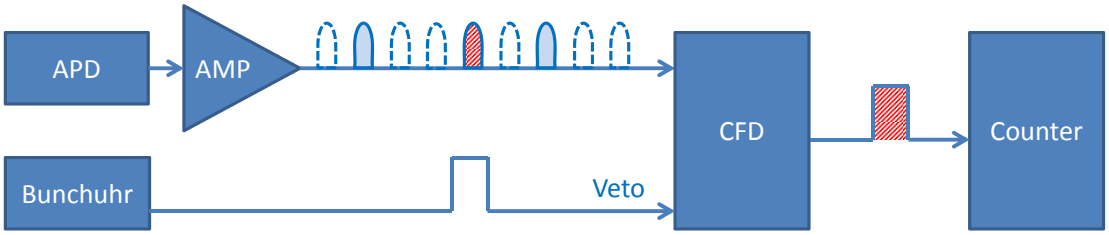

Figure 6.4.: Measurement chain: All devices in use to transform an X-ray photon into a count. Dashed pulses represent the synchrotron pulse train while indicating that not every pulse causes a counting event on the APD.

Used devices are:

APD Avalanche Photodiode (APD) detector head by FMB Oxford (APD0001)

AMP The belonging amplifier APD ACE by FMB Oxford (developed at ESRF) delivers the bias voltage and further electronic possibilities not used here.

CFD Constant Fraction Discriminator by ORTEC (Quad CFD 935) with veto input.

Bunchuhr PETRA III bunch-clock provides references in phase with the bunches to trigger experiments with. Various different frequencies are available to trigger on all, some or only one bunch (130 kHz). Even a trigger only every second bunch (65 kHz) and so on can be delivered by customized bunch-clocks.

Counter A SIS3820 Multi Channel Scaler that can be read out via TANGO.

A photon reaching the photodiode (APD) generates a signal which gets amplified in the electronics (AMP).

These signals are transferred by the CFD into standardized signals to feed the counter. Furthermore, as also for the unpumped bunches signals are generated by the APD the CFD is used to discriminate. It offers a veto input to suppress generating an output. With the help of an oscilloscope the single bunch trigger (130 kHz) from the bunch-clock is temporally shifted over the desired pumped signal[7] (ideally during the tuning of the

[7] marked with red stripes if figure 6.4

temporal overlap as described in chapter 6.1.1 where this can easily be identified) and used to suppress the signals from all other bunches. To this end it can be necessary to invert the bunch-clock signal by further electronics depending on the actual specifications of the bunch-clock output and the CFD veto input. The CFD output is fed into the counter that can be started, stopped and read out via TANGO thus allowing a comfortable digital processing of the data further on.

As the amplitude of the APD signal is energy dependent but with a rather large spread, it is not always possible to discriminate multi photon signals in the APD. The CFD does not discriminate them at all as it generates a binary output (signal? yes / no). Therefore, it is necessary to keep the count rate low enough to avoid multi photons being counted as one photon. This would lead to underrate high yields of X-ray fluorescence. On the other hand, a high count rate is desired for better statistics and shorter acquisition times. This trade-off needs to be done with the help of Poisson statistics. It shows that for around 20 000 counts per second still ca. 95% of the counts originate from single photon events. Therefore the experiment is adjusted to not exceed this count rate. Available parameters for count rate adjustment are mainly the APD position however jet diameter, sample concentration, and basically all further positioning parameters the setup offers contribute as well. Roughly only every sixth synchrotron pulse causes a signal on the APD when measuring the peak value. This is denoted in figure 6.4 by marking most of the pulses dashed, i.e. illustrating the pulse train while indicating that only some X-ray pulses cause an APD signal.

The opposite effect can be caused by too high thresholds of the CFD. Then multi photon signals are overrated. This has a major effect on the absolute count rate, however, not so much on the transient.

Second Shutter for Pumped-Unpumped Measurements Remotely Controlled

It turned out that long-term stability of the signal is very hard to realize as the sample and / or the solvent show radiation damage. Also slow temporal drifts of the setup cannot be excluded, even though an own feedback for the monochromator position needed to be programmed during this experiment (see [40] for details on the implemented feedback system). As the transient signal is much smaller than the absolute counts even very small drifts would cause dramatic errors in the transient if the pumped and unpumped signals were measured with a notable temporal retardation. Thus for any value of X-ray energy several pairs of pumped/unpumped signals have been measured alternating (instead of measuring first an entire pumped and later an unpumped spectrum. To this end it was necessary to switch the pump beam on and off remotely via TANGO so the software controlling the whole experiment could also cause the sample to be pumped or not. Therefore, an additional shutter has been installed after HIRO and a relay based circuit[8] was build to allow opening and closing via available analog voltages controllable via TANGO.

[8] A MES1A05 type relay was used to switch the fixed voltage from a lab power supply to open or close the shutter. The Relay was controlled via the TANGO implemented TIP551-10 DAC.

Integration of the Synchronization Unit into the Tango System to allow Automatized Delayscans

To be able to run delay scans the delay setting of the PHAROS synchronization software needed to allow to set the delay not only manually or by a local scan routine but to offer an interface to communicate with the TANGO based control software. Thus an own TANGO server has been installed on the PHAROS control computer. For this server a "device" was programmed offering two values: One delay value to set and one control value to read back if the delay setting has reached the PHAROS synchronization. These values can be read and in case of the first also written from all machines running TANGO within the same network. Also the synchronization software can connect to this device, reading the delay value and writing back the actual set delay to the control value. This is implemented by LabVIEWs ability to execute external programs by running similar pyTANGO based python scripts as used for the other communication to this TANGO server. As a windows system is not the original environment for TANGO servers a lot effort had to be put into making it running at all. The only stable combination of required programs and libraries turned out to be:

- Python 2.6.6
- Python2.6 numpy-1.6.0
- mysql-essential-5.1.63-win32.msi
- PyTango-7.1.1.win32-py2.6.msi
- TangoSetup-7.2.1.b.exe

Example code to set or read out the delay remotely is attached in appendix A.5.3. Also the necessary settings that need to be enforced before proper operation can be found there.

6.1.2. Temporal Resolution and PETRA III Pulse Length Measurement

The temporal resolution obtained in the pump-probe experiments can be stated by analyzing the delayscans (see chapter 6.1.3 for detailed description of the delayscans). Only one Gaq3 delayscan (set 1, see section 6.1.3) offers enough statistics to perform meaningful fits as the delay steps had been set short for this purpose. It shows the change in the transient signal depending on the delay between pump and probe pulse. As long as the probe arrives at the target before the pump the difference will of course be zero, jumping to maximum level at delay equals zero and then starts to decay exponentially, depending on the lifetime of the excitation. For an ideal system there would be a perfect step when the relative delay is set to zero, i.e. laser and synchrotron pulses overlap in time.

In the real setup there is a slope depending on three parameters:
The pulse length of the laser, the pulse length of the synchrotron and the jitter between them which is the jitter of the synchronization.

Therefore, the temporal resolution is a convolution of these three numbers. Assuming gaussian shaped pulses and jitter the convolution leads to a new gaussian which then according to the rules for convoluting independent gaussians equals:

$$f_{total}(t) = f_{X-ray}(t) \otimes f_{UV}(t) \otimes f_{sync}(t) \tag{6.2}$$

leading to

$$\sigma_{total} = \sqrt{\sigma^2_{X-ray} + \sigma^2_{UV} + \sigma^2_{sync}} \tag{6.3}$$

where $f_{X-ray}(t)$ is the temporal shape of the synchrotron pulse, $f_{UV}(t)$ the temporal shape of the 3rd harmonic of PHAROS and $f_{sync}(t)$ the distribution of the relative temporal position of laser and synchrotron pulses, i.e. its deviation is the jitter of the synchronization. $f_{total}(t)$ is the temporal distribution of overlapping of the two pulses and, therefore, the distribution where our pumped excitation occurs with zero delay between the pulses. This is the temporal broadening of the step at relative delay corresponding to zero. Therefore, $f_{total}(t)$ needs to be folded with a step function (Heaviside) to gain the function to be fitted to the curve. A function convoluted with the step function gives the integral of that function, therefore, the gaussian $f_{total}(t)$ folded with the step gives an error function (with some offset, scaling or temporal shift that, however, do not affect the standard deviation) to fit with.

The data was taken in pairs of values with an additional lasershutter to perform pumped-unpumped pairs several times at each delay to compensate for possible drifts over time due to radiation damage, pointing drifts, drifts in intensity and so on that were observed as the beamline was still in the commissioning phase. The sample Gaq3 was dissolved in benzyl alcohol Each pair consists of a number of counts taken during 8 s with laser pump and a second value of 8 s unpumped counts, normalized to the corresponding flux diode values. As several such pairs were measured for each delay step and, furthermore, delaysteps had been measured several times to improve statistics, a scatter plot was obtained - see fig 6.5. This needed to be fitted to get the temporal resolution. The fitting has been performed using the following equation[9]:

$$f_{edge}(x) = \frac{A_{edge}}{2} \cdot \left(1 + erf\left(\frac{x - offset_{edge}}{\sqrt{2 * \sigma^2_{edge}}}\right)\right) \tag{6.4}$$

The rawdata and the fit can be seen in figure 6.5.

As for the temporal resolution only the step matters, only this part of the data is considered for this purpose.

[9] The EMG could have been used to describe the overal measured curve, however, as here the focus is on the broadening of the step this would not be as accurate for this purpose as there are much more data points on the decaying branch.

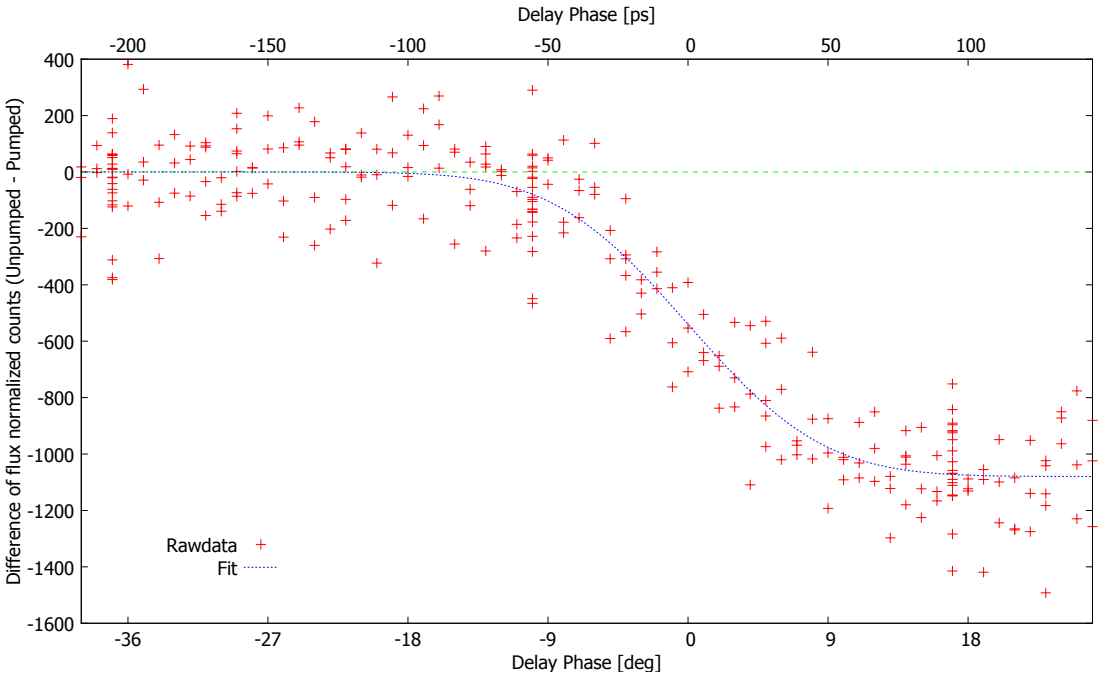

Figure 6.5.: The edge of the delayscan with Gaq3 fitted with an error function to gain the temporal resolution.

The result for this fit is :

$$\sigma_{edge} = 6.88^{\circ} \pm 0.53^{\circ} \tag{6.5}$$

$$\sigma_{edge} = 38.22\,ps \pm 2.98\,ps \tag{6.6}$$

$$FWHM_{edge} = 90.01\,ps \pm 7.03\,ps \tag{6.7}$$

where the given error is the 'Asymptotic Standard Error' as stated by the gnuplot fitting routine. The value of $\sigma_{edge} = 38.22 \pm 2.98$ ps is basically the pulse length of PETRA III as this value is considerably larger than the jitter of the synchronization (see chapter 5.1.2 and especially table 5.1 and equation 5.1) and the laser pulse duration.

Influence of the Reference Signals Amplitude

It turned out that the levels of the 500 MHz reference were not identical on all distribution device outputs and/or after some month. The influence of poor reference levels on the synchronization is rather big. A typical value for the output level should be above 12 dBm (i.e. 2.5 V peak-to-peak). The input attenuators of the synchronization unit are usually adapted to this value so the maximum level of 0 dBm - or approx. 632 mV peak-to-peak - for the vector modulator is not exceeded (see data sheet [44] and also appendix A.3 for more details on the complex phase modulator and its properties). Figure 6.6 illustrates the effect of a dramatic drop of the reference level.

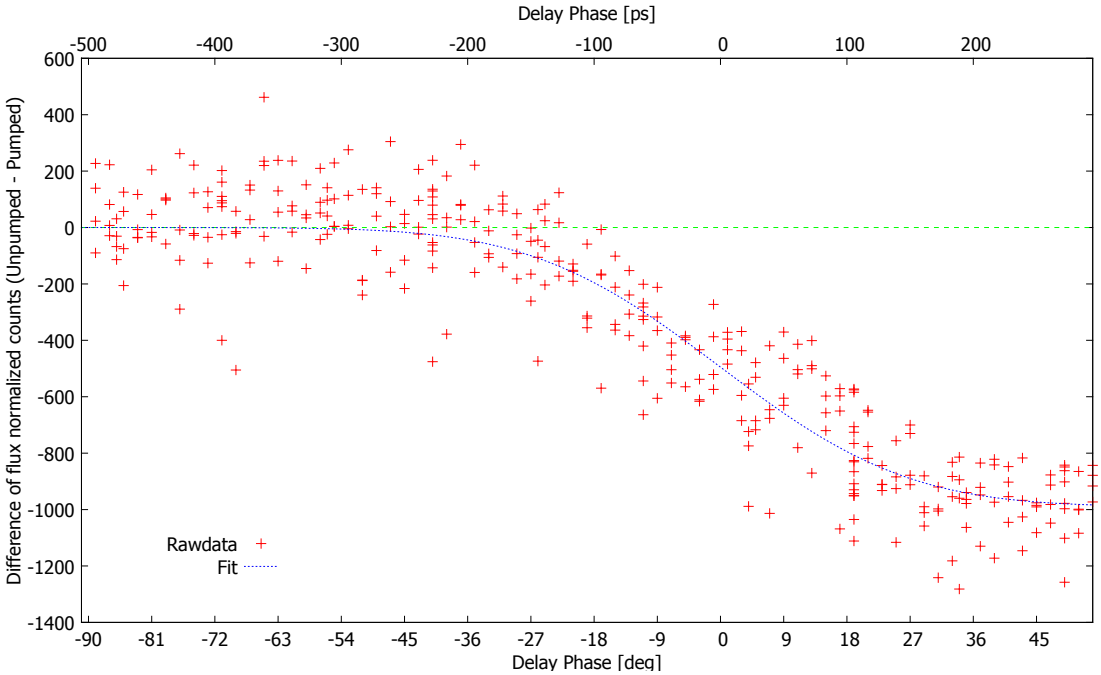

Figure 6.6.: Example for the effect of bad reference levels on the temporal resolution

The result for this mistuned synchronization measured and fitted just as in chapter 6.1.2 above is:

$$\sigma_{edge} = 21.12^{\circ} \pm 1.58^{\circ} \tag{6.8}$$

$$\sigma_{edge} = 117.33\,ps \pm 8.80\ ps \tag{6.9}$$

$$FWHM_{edge} = 276.30\,ps \pm 20.73\ ps \tag{6.10}$$

The drop in the reference level of more than 12 dB worsens the overall temporal resolution dramatically by a factor of more than 3. Therefore, the level of the reference needs to be checked and attenuated to a level close to 0 dBm directly in front of the synchronization unit for optimal performance.

6.1.3. Results: Lifetime Measurements for Gaq3 and Znq2

The setup allows to perform measurements where two parameters can be varied. One being the X-ray energy, the other the relative temporal position of the laser pulses with respect to the X-ray pulses (also called delay). Taking an energy scan is necessary to chose an energy with an notable effect of the pump laser. Such an energy scan can be seen in figure 6.7. The transient of the pumped and unpumped energy scan contains

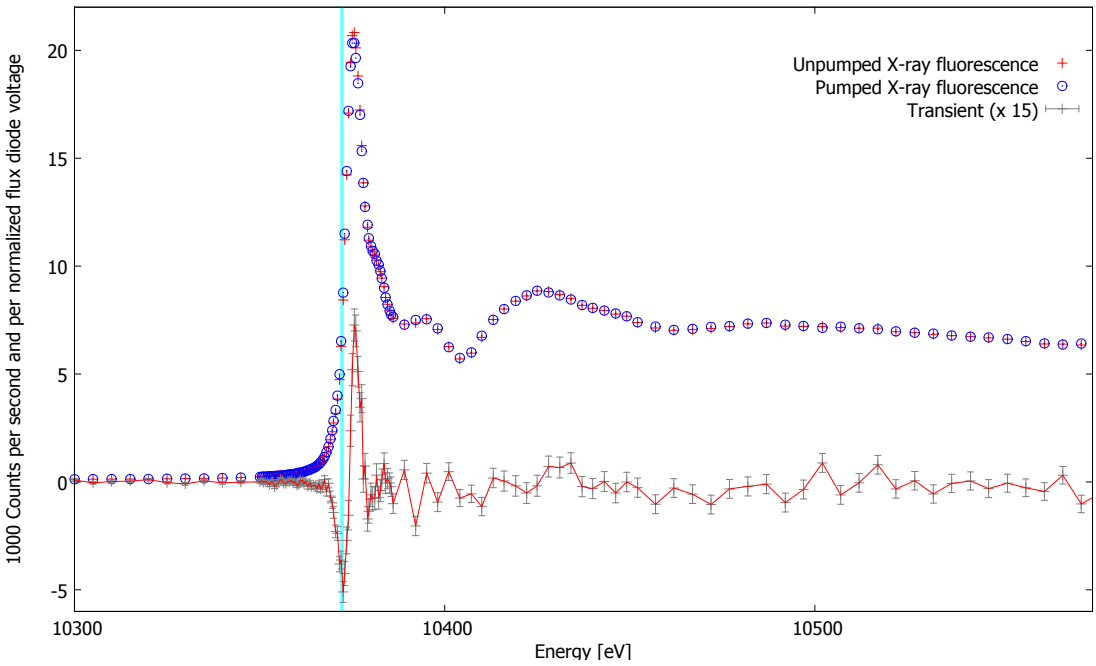

Figure 6.7.: Energy scan of Gaq3 around the Ga K edge. The transient signal between the unpumped and the pumped spectrum is used to chose an energy for the delay scan. Here the transient is inverted compared to the typical definition of pumped-unpumped for better perceptibility. The units are 10^3 counts per second and normalized flux diode signal. The flux diode is used to compensate for X-ray drifts. The flux diode is normalized to its lowest value in the data set, thus the absolute number is in the order of the real number of counts. The flux diodes signal varies less than 10% in this data set. The error bars based on poisson statistics are smaller than the size of the markers for the energy scan, for the transient they are plotted according to equation 6.13. Vertical markers flag the energy of delay scans (see figure 6.8). This energy scan was taken with the same general settings as the delay scan data set 2 (see section 6.1.3 for more details).

information on the structural change of the molecules. This is analyzed and described in detail in [30].

The transient between unpumped and pumped energy spectrum also contains the

information for which energy the effect of pumping is most notable. Hence for delay scans an extremum of the transient is chosen as X-ray energy.

The goal of delay scans is to gain information on the temporal evolution of the excitation and, therefore, of the structural changes as well.

Two delay scans are presented in figure 6.8 (data set 1: red, data set 2: blue). Every marker in this graph represents a pair of values consisting of an unpumped number of counts $N_{unpumped}$ normalized to the corresponding flux diode value $V_{unpumped}$ subtracted from a pumped number of counts N_{pumped} normalized to the corresponding flux diode value V_{pumped} (see equation 6.11).

$$y = \frac{N_{pumped}}{V_{pumped}} - \frac{N_{unpumped}}{V_{unpumped}} \tag{6.11}$$

Such pairs of values are measured repeatedly for various delay settings between pump and probe pulse (x axis). As long term stability of the setup is hard to achieve, those pairs have been measured consecutively by using the additional shutter (see chapter 6.1.1). To improve statistical foundation, pairs of values have been measured repeatedly. In early commissioning phase of the beamline only short periods of a few seconds for each value of such a pair could be taken. The first data set applied 8 s for each counting value. The latest measurements - such as figure 6.7 and data set 2 - applied 16 s measurement time for pumped and probed values each.

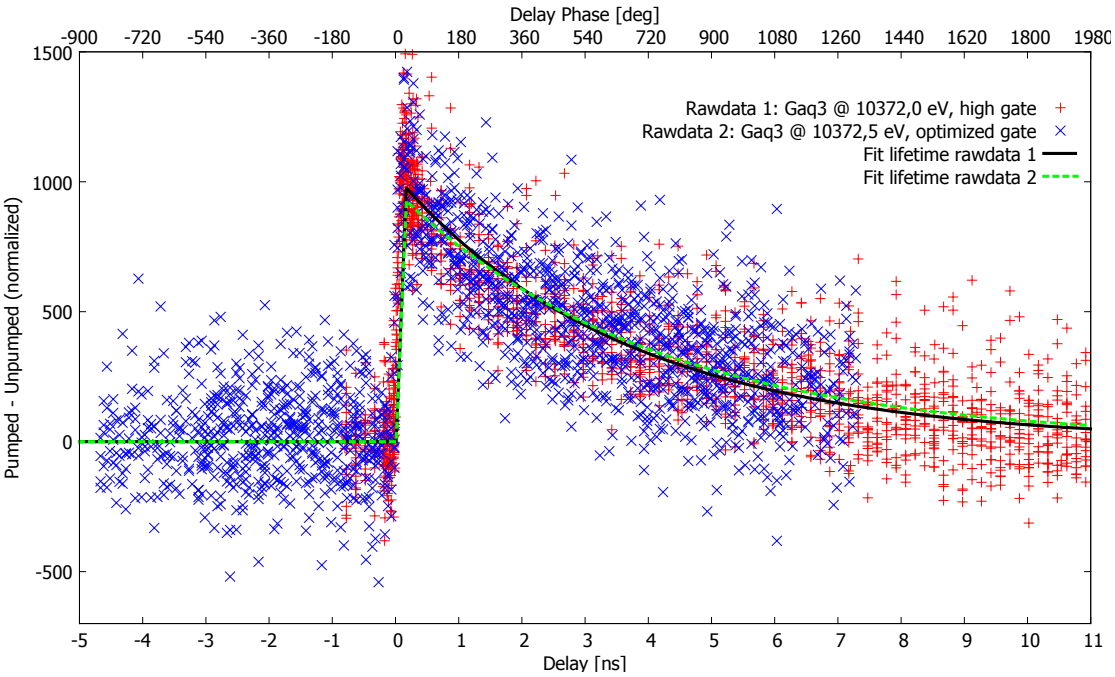

Figure 6.8.: Lifetime of the laser-pumped state in Gaq3 probed with X-rays at 10372.5 eV and 10372.0 eV and different thresholds within the counting logic.

Gaq3

The first and major sample examined has been tris(8-hydroxyquinolinato)gallium, usually abbreviated Gaq3. Its structural formula is shown in figure 6.9. The used solvent

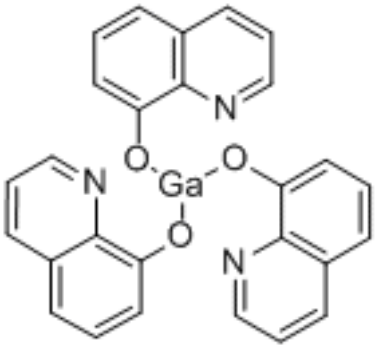

Figure 6.9.: structural formula for Gaq3, taken from [5]

was benzyl alcohol. In this work two set of data taken during two different beamtimes are considered.

Set 1 was taken with a rather high threshold for the counting electronics (see chapter 6.1.1) so potentially multi photon detection on the APD might be overrepresented. This would of course lead to dramatic nonlinear distortions in an energy spectrum. In a delay scan, however, the effect is negligible as the countrate stays rather stable over the whole scan. The considered difference between pumped and unpumped counts is much smaller than the total number of counts. The X-ray energy had been set to 10372.0 eV. The sampling time was 8 s for every pumped and every unpumped counting value leading to 18 s for one measured pair (including 1 s for shutter operation between pumped and unpumped data acquisition). The concentration was 2.38 g / 121 ml.

Set 2 was taken in a later beamtime with optimized settings within the electronic measuring chain. The X-ray energy had been set to 10372.5 eV. The sampling time was 16 s for every pumped and every unpumped counting value. The concentration was 2.5 g / 100 ml.

Statistical and Error Considerations

As the beamline was in commissioning mode and had not yet been fully characterized and still suffered various instabilities, it was necessary to measure pumped and unpumped signal for each energy alternately. Many of those pairs have been measured repeatedly. As countrates directly imply poisson distributed errors it is possible to assign the statistical error to each value. To get these statistical errors for the transient it is necessary to apply error propagation as the transient is not directly measured but calculated from measured values. Each data point within the transient spectrum consists of the combination of four measured values: A number of counts during the unpumped measurement, a voltage of a flux diode measured during the same time, and this number and voltage measured during the pumped measurement directly afterwards. The flux diode's value has been used to normalize the number of counts to compensate for possible drifts of the X-ray beam pointing, intensity or other effects limiting the number of X-ray flux at the sample. It also allows to identify data where the synchrotron failed or the beam was lost entirely or partly during the measurement. Therefore, the y value of the transient spectra is calculated as described in formula 6.12 (as already introduced in equation 6.11 above):

$$y = \frac{N_{pumped}}{V_{pumped}} - \frac{N_{unpumped}}{V_{unpumped}} \tag{6.12}$$

With N being the counted number and V the corresponding measured voltage. The statistical error of y by the propagation of the poisson errors of the count numbers N according to gaussian error propagation law and using poisson errors for number of counts N being $\sigma_N = \sqrt{N}$ is:

$$\sigma_y = \sqrt{\left(\frac{\partial y}{\partial N_{pumped}} \cdot \sigma_{N_{pumped}}\right)^2 + \left(\frac{\partial y}{\partial N_{unpumped}} \cdot \sigma_{N_{unpumped}}\right)^2} \tag{6.13}$$

$$= \sqrt{\left(\frac{\sigma_{N_{pumped}}}{V_{pumped}}\right)^2 + \left(\frac{\sigma_{N_{unpumped}}}{V_{unpumped}}\right)^2} \tag{6.14}$$

$$= \sqrt{\frac{N_{pumped}}{V_{pumped}^2} + \frac{N_{unpumped}}{V_{unpumped}^2}} \tag{6.15}$$

However, this is merely the best case error, as it does not take into account any errors caused by setup and instrumentation. Also the error of the flux diode was neglected. It could not directly be measured as the flux diodes value is highly correlated with the synchrotron flux and thus the number of counts. As the flux diodes reduced the spread of the data it seemed appropriate to neglect its error which seemed considerably lower than that of the flux itself.

Approximating these poisson distribution based values as gaussians is valid according to the central limit theorem. It can also be shown that the gaussian distribution is the limit of the poisson distribution (see, for example, [15] chapter 3.4.5).

It has been possible to check the validity of the assumed poisson errors due to the

way of measuring pumped-unpumped-pairs as described above. On the one hand it is possible to combine all pairs for each delay value to one single pair by simply adding all single N_{pumped} values together to a combined N_{pumped} and continue doing so as well for all $N_{unpumped}$, V_{pumped} and $V_{unpumped}$ values. Poisson errors can be assigned to these single pairs just as described above. On the other hand it is also possible to calculate an error from the distribution of the measured pairs for each delay value. To get an unbiased estimator for the standard deviation of the parent distribution (i.e. what has been estimated with the Poisson approach before) one has to calculate the σ_{N-1} standard deviation[10]. These obtained errors also show a Gaussian like distribution that can be described by mean and standard deviation (see figure 6.10 for this analyzed for the two sets of Gaq3 data). The distribution of these errors is independent of the delay (see figure 6.11 for the same Gaq3 data sets) and its mean value is independent of the number of pairs contributing to it.

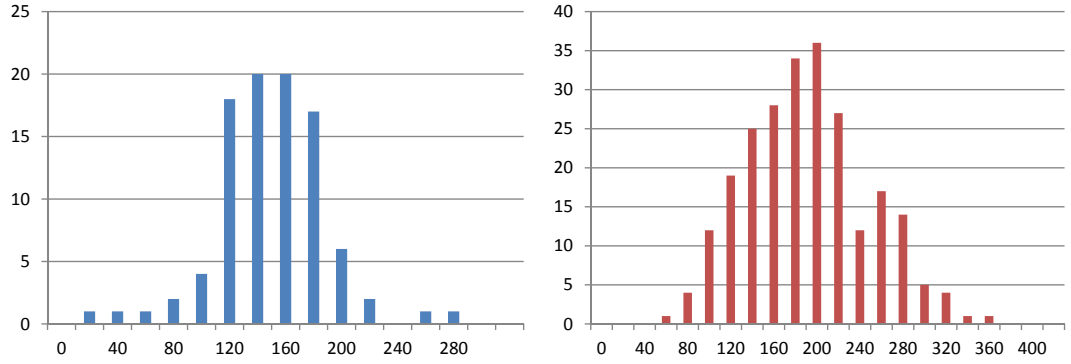

(a) $\sigma_1 = 141 \pm 40$ (b) $\sigma_2 = 181 \pm 57$

Figure 6.10.: Distribution of the standard deviations of the distribution of various values for one delay setting in delay scans for data set 1 (6.10a) and data set 2 (6.10b). For every delay value the standard deviation of all the corresponding pairs is calculated and put into those histograms. There are 94 delay positions (entries) in figure 6.10a and 240 in figure 6.10b

Therefore, the obtained values are better estimators for the statistical error of the data than those based only on the poisson distribution. These are namely (σ_1 being the error for data set 1 and σ_2 for data set 2):

$$\sigma_1 = 141 \pm 40 \tag{6.16}$$

$$\sigma_2 = 181 \pm 57 \tag{6.17}$$

Units are flux-normalized count differences. This is of major importance for later evaluation of various fits or models. However, there are still no systematic errors considered. Those could arise from a change of the sample concentration due to radiation damage

[10] see [15] chapters 2.4.3 and 5 for further information

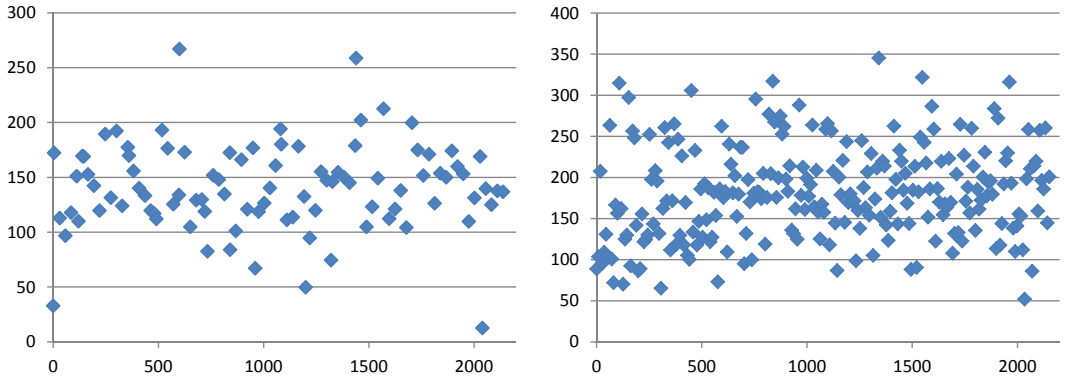

(a) [ps] (b) [ps]

Figure 6.11.: Standard deviations of the distribution of various values for each delay setting in delay scans for data set 1 (6.11a) and set 2 (6.11b). The distribution shows no delay dependency thus supporting the assumption of the same statistical error for every delay setting.

and vaporization of the solvent as well as temporal drifts of different variables of the beamline among others.

Fits and Models and the Recorded Data

After the discussion of expectable characteristics of the delay scans in chapter 2.5.3 the reasonable models to fit are limited to:

A: One exponential decay with one lifetime - possibly a combined lifetime (as model for the possible decay scenarios illustrated in figure 2.18a and 2.18b as well).

B: The sum of two exponential decays. Here as well the lifetimes could also be a combined one (as model for the scenario from figure 2.18c, possibly also combined with those above)).

It is not necessary to try and fit a difference of exponentials (see figure 2.18d) as this would have a different shape and could be motivated by looking at the raw data directly. Furthermore, it would be included within the sum-model if the fit produces a negative amplitude.

Further additive terms could be motivated, however, the data is too noisy to be able to distinguish between more than two summed exponentials significantly.

Models A and B are put to the test which describes the available data best.

$$f_A(t) = A_A \cdot e^{-\frac{t}{\tau_A}} \tag{6.18}$$

$$f_B(t) = A_{B1} \cdot e^{-\frac{t}{\tau_{B1}}} + A_{B2} \cdot e^{-\frac{t}{\tau_{B2}}} \tag{6.19}$$

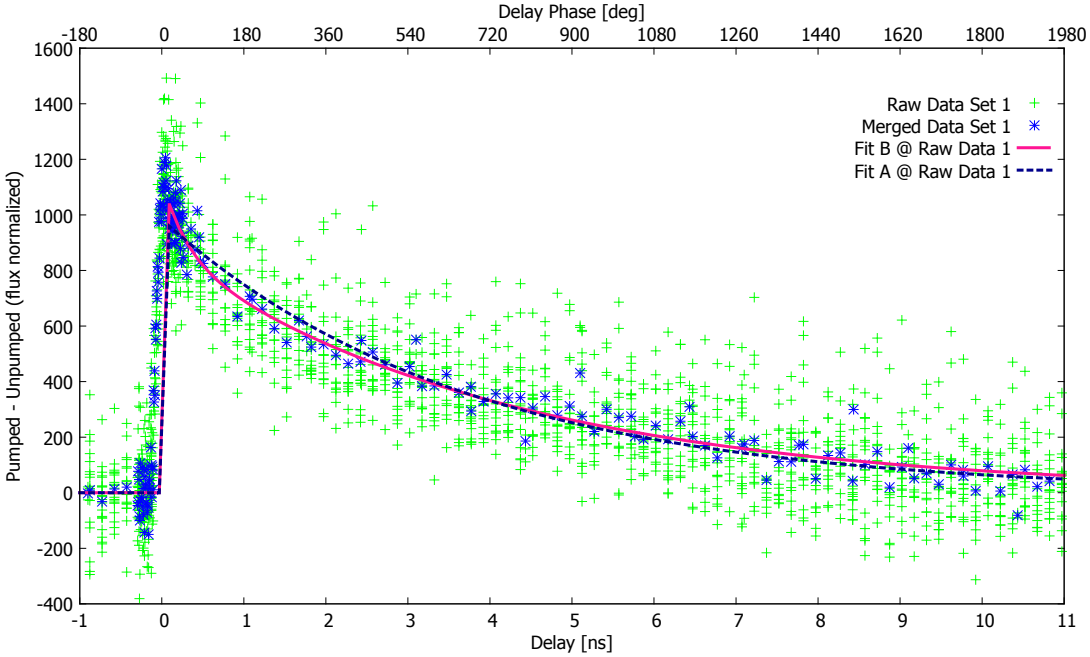

(a) Data set 1: Fitted models

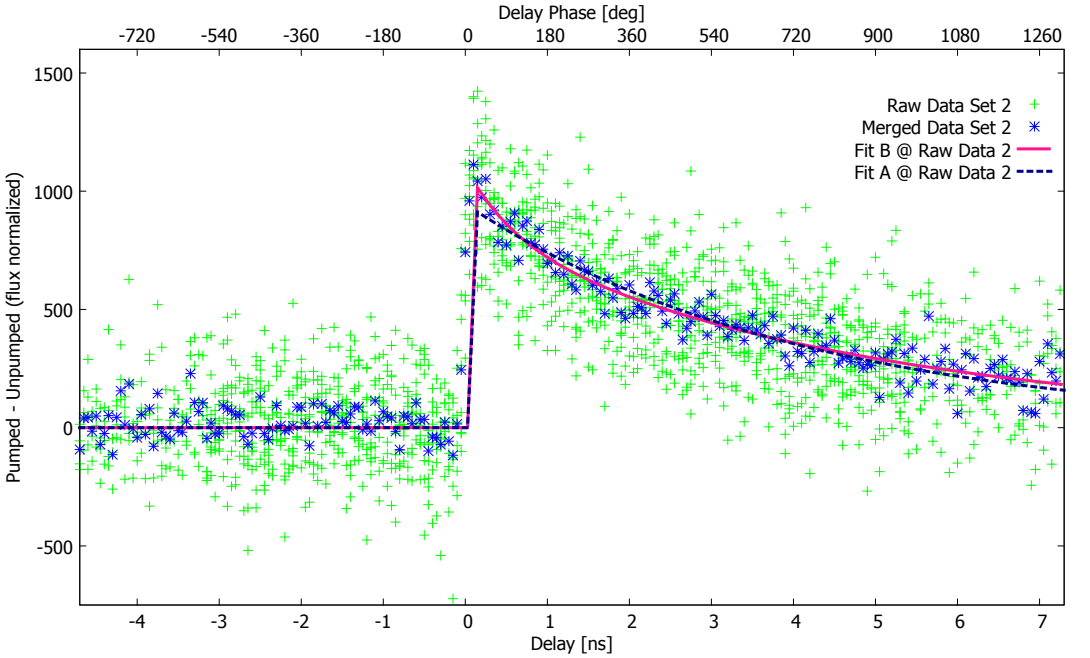

(b) Data set 2: Fitted models

Figure 6.12.: Model A and B fitted to data set 1 and 2

These models are fitted to the data sets 1 and 2 each.

This can be seen in figure 6.12. The two sets of raw data are shown together with plots of the fitted models A and B. The obtained parameters are given in table 6.1. Furthermore, there are merged data in the figure. While the raw data represent one green marker for each measured pair of pumped and unpumped data, the merged data (blue marker) shows a combined value for each delay value. This merged data do not only give a further perspective for judging the models visually but, furthermore, are used for the *Run test* as well. The models could have been fitted to the merged data as well, however, as not for each delay value the same amount of pumped unpumped pairs have been measured it would have been necessary to weight each data point correspondingly.

To judge the quality of a fit there are various statistical methods. Two have been applied: The χ^2 test and the *Run test*. Both are performed as described in [15] and the explanation is following this source in a broader sense.

Performing the χ^2 test is usually done to test if the data is consistent with the fit. By comparing the obtained χ^2 with tabulated χ^2 probabilities (or for many data points using a Gaussian approximation) it is possible to state how likely it is to obtain such a χ^2 from data following the fit function. In this case it is used to motivate if one of the two models is superior to the other one.

χ^2 in our case is defined as:

$$\chi^2 = \sum_{i=1}^{N} \frac{(y_i - f_X(t_i))^2}{\sigma_i^2} \tag{6.20}$$

With N being the number of data points (t_i, y_i), $f_X(t_i)$ being the value of the fit function $f_X(t)$ (with X being either A or B) at the temporal position t_i and σ_i the corresponding error of the data.

This term gets for every i a contribution of roughly one as the difference between data value and fit value should typically be in the order of the belonging error. Therefore χ^2 is expected to be roughly N. That is only valid if the fit function really describes the data and if the errors are correct. The corrected error estimation above is, therefore, necessary for this calculation. A large χ^2 can be an indicator for underestimated errors or for an unsuitable fit that does not describe the data. For large N the χ^2 probability can be calculated by using that $\sqrt{2\chi^2}$ becomes gaussian distributed. The mean is $\sqrt{2 \cdot (N-m) - 1}$ where m is the number of degrees of freedom within the fit function, if the fit originates from the same set of data (as it is the case here). The standard deviation is 1. Thus this calculations allow to judge the probability of the data occurring for the fit.

The result of the fits as well as the χ^2 tests are presented in table 6.1. Here χ^2 has been calculated according to formula 6.20 for fitted models A and B defined as in equations 6.18 and 6.19 from the peak of the curve (and 0 before).

χ^2 has been calculated with the empirical error as discussed in figures 6.10 and 6.11 and given in formula 6.16 and 6.17 as well as with the theoretical poisson errors. It can be seen that χ^2 is dramatically high for the poisson error in data set 1 for both models which implies either that both models are not suitable (what is not likely as those are the only

		Data Set 1	Data Set 2
Number of data points N		1513	1004
empirical σ (see fig. 6.10)		141 ± 40	181 ± 57
raw poisson σ (see eq. 6.15) avg. [range]		103 [99; 106]	180 [170; 184]
merged poisson σ (see eq. 6.15) avg. [range]		40 [23; 72]	71 [62; 90]
Fit A	A_A	975.7 ± 16.6	923.1 ± 19.7
	τ_A [ns]	3.673 ± 0.113	4.082 ± 0.156
	χ^2 with empirical error	1754	1139
	Discrepancy to expected value [std. dev.]	4.2	2.9
	χ^2 with poisson error	3265	1150
	Discrepancy to expected value [std. dev.]	25.8	3.2
Fit B	A_{B1}	234.6 ± 50.1	238.2 ± 72.1
	τ_{B1} [ns]	0.306 ± 0.153	0.596 ± 0.363
	A_{B2}	859.1 ± 39.7	803.7 ± 75.0
	τ_{B2} [ns]	4.180 ± 0.222	4.850 ± 0.543
	χ^2 with empirical error	1687	1114
	Discrepancy to expected value [std. dev.]	3.1	2.4
	χ^2 with poisson error	3140	1125
	Discrepancy to expected value [std. dev.]	24.3	2.7

Table 6.1.: Results of the χ^2 test

two reasonable possibilities from a theoretical point of view as discussed above) or the errors are dramatically underestimated. This is supported by the error considerations in the previous section. The same effect cannot be seen in data set 2 as here the statistics are worse so the poisson error is in the same order as the empirical one. Most likely the poisson error is still governing the overall error and is, therefore, also the obtained empirical error. In this case measuring more data could have improved the result.

The obtained fit parameters are stated with the given "Asymptotic Standard Error" as stated by the gnuplot fit routine. They are known to be underestimating the real error if the parameters are highly correlated [85] what is slightly the case as an error in the amplitude of the fit can roughly be compensated by a change of the decay constant - i.e. if the amplitude is too high there can still be many data points reached by the model if the lifetime gets shorter bringing the curve to a lower level quickly and vice versa.

To judge which model is most suitable it is necessary to consider the χ^2 values and their probability. As described above the χ^2 probability distribution converges towards a gaussian with known properties. This leads to the number "Discrepancy to expected value [std. dev.]" which states how many standard deviations the obtained χ^2 is away from the expected value. Hence the probability can be calculated by integrating a normalized standard gaussian up to this number of sigmas. Usually, this is done to state if the fit is consistent with the data at all i.e. if it was likely to obtain the measured data if the fitted model was the truth behind it. In this case it is used only to decide

which model is more suitable. Therefore, the rather huge numbers for those std. dev. do not exclude both models immediately as it would most likely be the case for values above three sigma and more. It can be calculated that small changes of the error used to calculate χ^2 have already a dramatic effect on this std. dev. ranging from dramatic increase down to entirely disappearing. Therefore varying the empirical σ slightly and way below its own one standard deviation range can dramatically change this stated probability. As the error on the empirical σ is large and possible systematic errors are not included, this reduces the power of the std. dev. to reject the model. However, what does hardly change is the difference between the std. dev. probability for fit A and fit B. For data set 1 the discrepancy to expected value [std. dev.] is always at least one σ[11] further off for model A than for model B when varying the used empirical σ between 100 and 149. This, however, changes if one further increases it. For 149 the discrepancy to expected value [std. dev.] for model B is around zero meaning that half the expected χ^2 values are larger, half of them smaller i.e. here the question starts turning: Until here the integral over a gaussian stated the probability to measure up to such a big χ^2. Now the interesting question is how likely it is to obtain down to such a small χ^2. Here model B starts to become less likely than model A. This, however, does not argue against model B, as this is exactly what to expect if errors get overestimated.[12] A too good fit also is statistically unlikely, and a less good model will, therefore, still be considered more likely if the error bars get too big.

The same is valid for data set 2 where model B is half a std. dev. closer to the expectation value in the close surrounding of the estimated empirical error.

Thus both data sets show a tendency to prefer model B when performing χ^2 considerations.

Fit A in figure 6.12 shows a further property that needs to be investigated: The curve seems to be below the majority of the data in the peak but above most of those one or two *ns* later finally matching rather good in the tail. Of course this needs to be quantified. A suitable method to check if this is a reasonable case against model A is the so called *Run test*. The Run test is - again - described following [15] and also carried out as suggested ibidem. Usually, if a measured point of data is above (or below) the prediction of the model this should (if the model is correct) not have any influence on the next measured point being above (or below) at all. As a first guess one expects data being randomly distributed above and below the model. To check if an accumulation of a certain sign of the deviation is still statistically probable the Run test can be applied. It basically states the probability for a given number of data points above (N_a) and below (N_b) the model to obtain an observed number of "runs" (r) i.e. changes of the sign of the

[11] for an empirical σ of 100 it is 1.6, for 149 it is still 1.1

[12] An easy example can explain that:
Having a set of data and a fit that is hit by roughly two thirds of the one σ error bars of the data is usually considered a reasonable fit. A second fit simply being the first with an additional offset might not be hit by as many error bars. If one now increases the error bars until two thirds hit the second fit, even more will hit the first one. This then has to be considered a bad fit, as it is too good - given that the errors are reasonable. It would typically be interpreted as fitting the noise if the data is closer to the fit than its errors would suggest.

deviation compared to the last one. The math behind it is based on Binomial coefficients to calculate the probability for a certain number of runs from the number of ways to arrange the data points above, the number of ways to arrange the data points below, and the overall possibility to arrange N_a and N_b. From this probability the expectation value for the number of runs $< r >$ and variance V can be calculated. The difference between the measured number of runs and the expectation value is divided through the root of the variance to obtain the deviation in standard deviations. The one tailed Gaussian integral then states the probability to see such a number of runs.

As the spread of the raw data is much bigger than the effect to judge the Run test is performed with the merged data. Using the merged data is possible without limitations as the Run test does not consider the deviation but only its sign. This leads to an important conclusion on the relation between Run test and χ^2 test (cited from [15]):

> The Run test is much less powerful than the χ^2 test, but it provides *additional* useful independent information. A fit may have an acceptable χ^2, perhaps because of overestimated errors, and still be wrong and rejectable by the Run test. The χ^2 test ignores the sign of deviations; the Run test looks only at the signs.

For the models A and B and the data set 1 and 2 the Run test leads to the results to be seen in table 6.2.

		Model A	Model B
Data Set 1	N_A	56	65
	N_B	78	69
	r	56	64
	$< r >$	66.2	67.9
	V	31.5	33.2
	# of std. dev. = $\frac{<r>-r}{\sqrt{V}}$	1.82	0.68
	Probability[13]	3.46 %	24.70 %
Data Set 2	N_A	105	110
	N_B	82	77
	r	76	80
	$< r >$	93.1	91.6
	V	45.1	43.6
	# of std. dev. = $\frac{<r>-r}{\sqrt{V}}$	2.54	1.75
	Probability	0.55 %	3.97 %

Table 6.2.: Results of the Run test

Model B is more likely for both set of data. Data set 1 has a quite high but not totally impossible probability for model A with only around 3% probability of obtaining

[13] to measure so few runs or less

a number of runs as little as this while the distribution of data could occur for model B in 1 out of four cases. Data set 2 shows a considerably small number of runs for both models what could be interpreted as noise in the setup on a larger timescale as a one delay step leading to deviations being correlated for neighboring points of data. Also the difference between the two models is not so big in absolute numbers which is caused by having not so many data points at the positions where the models differ the most. However, still model B is more likely and the measured data has a less little probability to occur as is if model B is the truth.

Altogether none of the shown test results alone would be strong enough to support the more complex model B, however, as two independent tests on two set of data taken at different times, settings and most likely beamline performance all have the tendency to support model B it can be considered justified to claim that the presented data can be described best with model B.

The result for the lifetimes of the probed Gaq3 exited states can be stated as:

$$\tau_{B1} = 0.4\ ns \tag{6.21}$$

$$\tau_{B2} = 4.4\ ns \tag{6.22}$$

It is the error-weighted average of both data set. However, it is hard to state serious errors for several reasons:

- There are not enough different set of data to obtain enough fitted values to perform an independent statistical analysis on them.
- The short lifetime τ_{B1} is close to the limit of the temporal resolution[14].
- The errors from the fit are over optimistic (see above).
- There might be further parameters that influence the lifetime and might not have been absolutely identical for both sets of data (p.a. temperature etc. - more in the next sections).

Therefore these results should be considered basically as starting point for further examinations.
They raise the question which excited states have been probed and where do those two lifetimes belong to.
As the excited Gaq3 also shows visible fluorescence further experiments have been conducted to obtain further hints. The lifetime of the visible fluorescence and its dependence on temperature and laser intensity have been measured as described within the following section.

[14] of 90 ps FWHM (see chapter 6.1.2)

Comparison with Visible Fluorescence Lifetime Measurements

To obtain additional information and to be able to further specify the findings from the last chapter, further complementary experiments have been conducted. If the laser excited state only decayed via visible fluorescence and this state was the only state probed by the X-ray pulses in the XAS experiment, the measured lifetimes of visible fluorescence in this section and X-ray fluorescence (see above) needed to be identical. As this is not the case, the complementary research indicates further decay channels and / or states. The lifetime of visible fluorescence of Gaq3 has been considered - again dissolved in benzyl alcohol (2.5 g Gaq3 per 100 ml benzyl alcohol) - after excitation with 343 nm UV laser pulses. The visible fluorescence has been measured with an oscilloscope and a photodiode. However, it is not trivial to ensure to only get fluorescence and no scattered light from the excitation process on the photodiode. Therefore, a setup with a microscope objective, a fiber and a mount with all degrees of freedom needed to be used. The possibility to apply a spectrometer was necessary as well to ensure measuring the fluorescence only. In figure 6.1, the absorption and emission spectra of Gaq3 according to [43] are shown. More information can also be found in [30].

Temperature Dependent Visible Flurescence Lifetime Measurements

The temporal evolution of the visible fluorescence can be seen for different temperatures of the reservoir with the sample in figure 6.13.

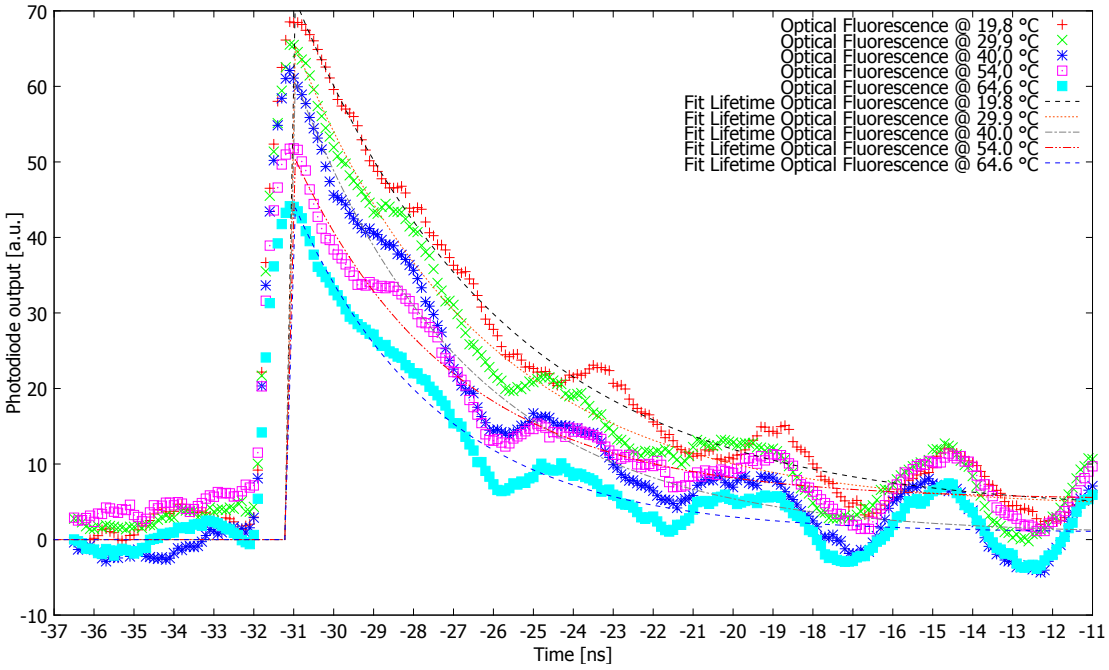

Figure 6.13.: Lifetime of the visible fluorescence for different temperatures

The shape of the curve looks slightly different than for the X-ray fluorescence. The first notable thing is the temporal resolution which is worse due to the used photo diode. Therefore, a possible second short-lived lifetime would be much harder to observe, if possible at all. Secondly there has been an undesirable ringing (which could not be removed) modulating the signal and worsening the fit results. The fitting routine refused to fit model B to this data as there is no statistical base for the additional exponential.

Two different observations can be made: First, with increased temperature the amplitude decreases. Second, with increased temperature the fitted lifetime decreases (to be seen in figure 6.14).

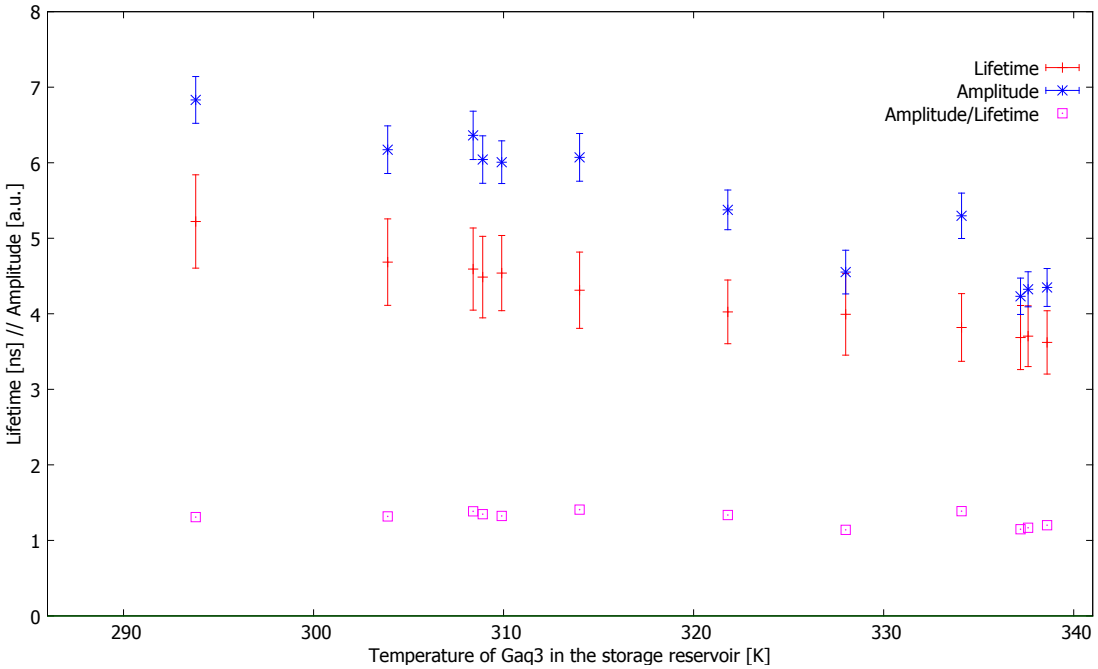

Figure 6.14.: Lifetime of the visible fluorescence depending on Temperature.

The decreasing amplitude could be explained in different ways. One possibility could be that samples get destroyed by heat and so there are less fluorescent molecules left. This is not the case, as the effect is reversible i.e. if the temperature is decreased the amplitude increases again. Furthermore, a change in the number of available samples would not cause a change in the lifetime. Thus the effect needs to be explained in terms of excitation. As in the case of Gaq3 fluorescence lifetime as well as the signals amplitude (i.e. the amount of excitations decaying via visible fluorescence) decrease with increased temperature this suggests a second temperature depending and non-radiative decay channel. The easiest possible model is illustrated in figure 6.15.

This easy model shows an exponential decay with a combined decay constant τ_0:

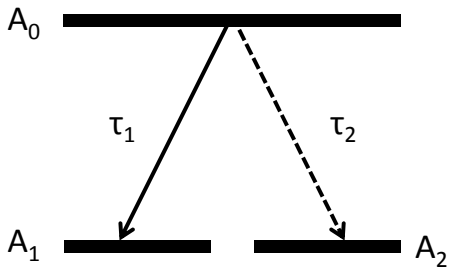

Figure 6.15.: Easiest model for a temperature dependent lifetime with second temperature dependent decay channel.

$$A_0(t) = A_0(0) \cdot e^{-\frac{1}{\tau_0}t} \tag{6.23}$$

$$= A_0(0) \cdot e^{-\left(\frac{1}{\tau_1}+\frac{1}{\tau_2}\right)t} \tag{6.24}$$

$$A_1(t) = \frac{\frac{1}{\tau_1}}{\frac{1}{\tau_0}} A_0(0) \left(1 - e^{-\frac{1}{\tau_0}t}\right) \tag{6.25}$$

$$A_2(t) = \frac{\frac{1}{\tau_2}}{\frac{1}{\tau_0}} A_0(0) \left(1 - e^{-\frac{1}{\tau_0}t}\right) \tag{6.26}$$

Where $A_x(t)$ is the number of samples in state A_x and $\frac{1}{\tau_0} = \frac{1}{\tau_1} + \frac{1}{\tau_2}$ being the combined reciprocal lifetimes (or decay rates).

Obviously

$$A_0(t) + A_1(t) + A_2(t) = const. \tag{6.27}$$

$$A_0(0) = A_1(\infty) + A_2(\infty) \tag{6.28}$$

as in this model no other states are allowed.

In the data from figure 6.13 the measured curve would be the derivative of A_1 in this model:

$$A_1'(t) = \frac{1}{\tau_1} A_0(0) \cdot e^{-\frac{t}{\tau_0}} \tag{6.29}$$

And again the amplitudes are connected:

$$A_0'(0) = -A_1'(0) - A_2'(0) \tag{6.30}$$

It might not be possible without a model for the temperature dependence of τ_2 (and, therefore, of $A_1(0)$ and $A_2(0)$ as well) to obtain values for the non measured variables, however, taking a closer look this model offers an interesting possibility to be possibly refused by data. For easier understanding the variables measured are marked with an "M", those that are assumed to be constants (i.e. independent of temperature) with a

"C".

From equation 6.29

$$A_1'^M(0) = \frac{1}{\tau_1^C} A_0^C(0) \cdot e^{-\frac{0}{\tau_0}} \tag{6.31}$$

$$A_1'^M(0) = \frac{A_0^C(0)}{\tau_1^C} \tag{6.32}$$

and thus the amplitude should be independent of the temperature. Therefore, this model is not sufficient.

At this point the influence of the temporal resolution needs to be considered. As within the measured data the exponential decay is folded with the temporal resolution gaussian - strictly speaking one needed to fit the so called *Exponentially modified Gaussian distribution* (EMG)(see equation 6.33).

$$f(t,\mu,\sigma,\lambda) = \frac{\lambda}{2} \mathrm{e}^{\frac{\lambda}{2}\left(2\mu+\lambda\sigma^2-2t\right)} erfc\left(\frac{\left(-t+\mu+\lambda\sigma^2\right)}{\sqrt{2}\sigma}\right) \tag{6.33}$$

With $erfc$ being the complementary error function, σ the temporal resolution, μ a parameter to shift the temporal position of the EMG, and λ the reciprocal lifetime ($\tau = \frac{1}{\lambda}$). This is the form listed in [61][15], while some different versions and approximations exist in different scientific fields still often reffered to as EMG. There is even a paper about various errors with this function in literature [42] and discussing its derivation. That source defines it as a convolution of the unit area Gaussian with a normalized exponential decay, however, both defined to be zero for times $t < 0$. This would lead to problems as the result would depend on the gaussians mean μ which is not a meaningful physical property if the gaussian is representing the temporal resolution. Thus the folding needs to be independent of this parameter. This is the case if the gaussian (and thus the convolution integral) is defined not starting at zero but at $-\infty$. This is described in [42] as an acceptable approximation for their definition of the EMG in some cases, thus also giving this equation.

Equation 6.33 is also in agreement with the version presented in [23] where the derivation of highest educational value known to the author of this work is presented.

The EMG is non-trivial to handle as the contained error function combined with the exponential is not easily approachable analytically. However, it can be considered numerically. In the considered data the resolution is constant and thus σ does not change. Furthermore, μ is of no physical relevance simply shifting the peak in time and thus can be set 0 without limiting the explanatory power. Such calculated EMG graphs can be seen in figure 6.16.

Even though the maximum slightly shifts with τ in this region one can fix one certain time t around the maximum (and thus amplitude) of those peaks and plot the amplitude depending on τ. This illustrated in figure 6.17.

[15] It is also the version to be found in wikipedia http://en.wikipedia.org/wiki/Exponentially_modified_Gaussian_distribution (2013-02-25)

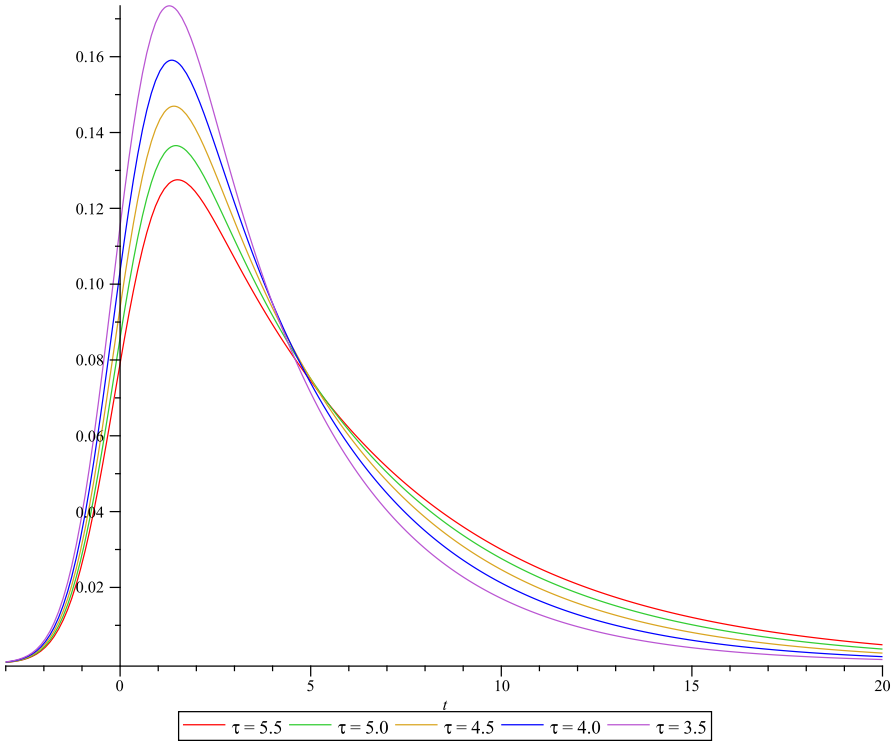

Figure 6.16.: EMG for different values of τ ($\mu = 0, \sigma = 1$)

The amplitude decreases with increased lifetime. This is even contradicting the measured data! The measured data (figure 6.13) show the interesting property that the amplitude is proportional to the lifetime, i.e. $\frac{A_0'^M}{\tau_0^M}$ is constant. Thus for comparison in figure 6.17 also the property $\frac{f(t=1.25,\mu=0,\sigma=1,\tau)}{\tau_0^M}$ (this corresponds to $\frac{A_0'^M(\tau)}{\tau_0^M}$) is shown. It is not constant and thus the easy model with the extension of the influence of the temporal resolution is also no suitable model.

After the trivial ansatz to develop a suitable model has failed a comparison with a known example is a possible way to suggest further steps.

It has been described for $[Ru^{II}(bpy)_3]^{2+}$ in [37] that there does exist an excited Metal-to-Ligand Charge Transfer state that can decay radiatively but as well non-radiatively via high vibrational levels of the ground state. The temperature dependence of lifetimes in the $[Ru^{II}(bpy)_3]^{2+}$ case is discussed and modeled in [47]. The described mechanism contains a temperature dependent decay channel (or a cascade thereof) between two states (namely in the example the excited Metal-to-Ligand Charge Transfer state and the high vibrational levels of the ground state) so a similar concept could be suggested to explain the data for Gaq3 as well. An abstract model of the decay process is illustrated in figure 6.18.

It can also be considered as a possible example for linearly combined exponential decays as observed for the X-ray fluorescence in chapter 6.1.3 The belonging coupled

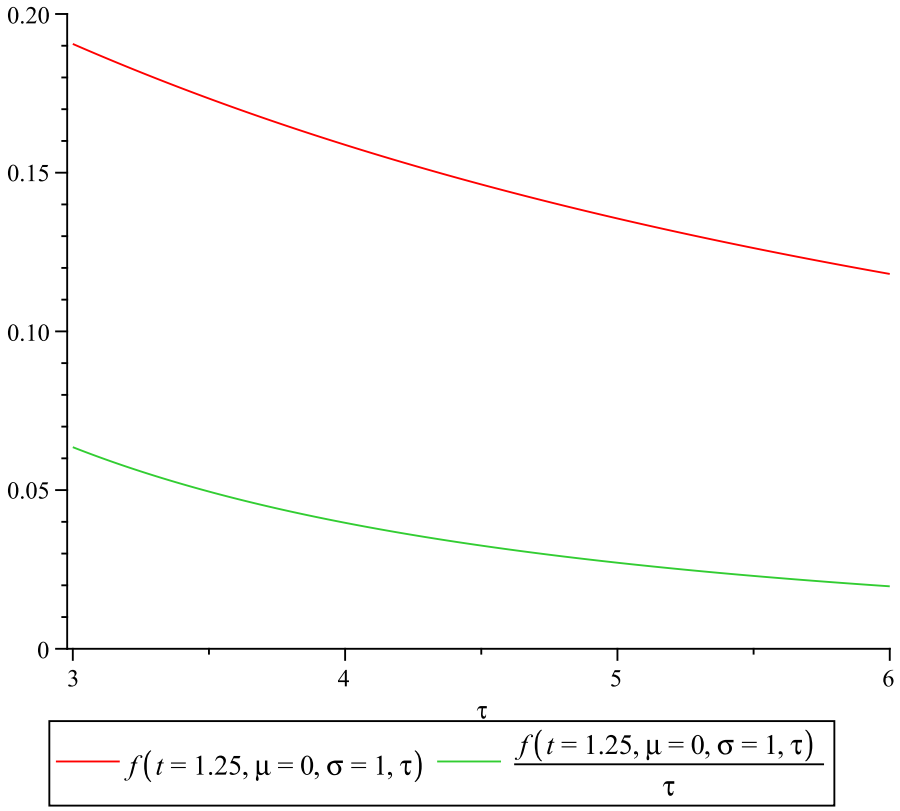

Figure 6.17.: Illustration of the dependence of the amplitude of the EMG (equation 6.33) from the lifetime.

differential equations for this model would be

$$\frac{dN_A}{dt} = -\frac{1}{\tau_1} \cdot N_A - \frac{1}{\tau_2} \cdot N_A + \frac{1}{\tau_3} \cdot N_B \tag{6.34}$$

$$\frac{dN_B}{dt} = -\frac{1}{\tau_4} \cdot N_B - \frac{1}{\tau_3} \cdot N_B + \frac{1}{\tau_2} \cdot N_A \tag{6.35}$$

With N_A being the number of samples in state A and N_B those in state B.

The solution[16] is dependent on initial conditions and not rather easy to interpret. However, it can be shown that for long lifetimes of τ_2 and τ_3 (compared to τ_1 and τ_4) the system gets uncoupled again, showing two states A and B decaying dominantly via τ_1 or τ_4 respectively. Another limit consideration is, that if τ_4 is much shorter than τ_2 and τ_3 basically every sample in state B will decay via τ_4 thus τ_3 will have no effect and the system will be again the case of the easy model from the beginning (with B being

[16] basically leading to combinations of exponentials with two possible combined lifetimes
$\frac{1}{\tau 0_{1;2}} = \frac{1}{2}\left(\frac{1}{\tau_1} + \frac{1}{\tau_2} + \frac{1}{\tau_3} + \frac{1}{\tau_4} \pm \sqrt{(\frac{1}{\tau_1} + \frac{1}{\tau_2} - \frac{1}{\tau_3} - \frac{1}{\tau_4})^2 + (4\frac{1}{\tau_2}\frac{1}{\tau_3})}\right)$
and with amplitudes depending on the inital conditions but looking at least as complicated.

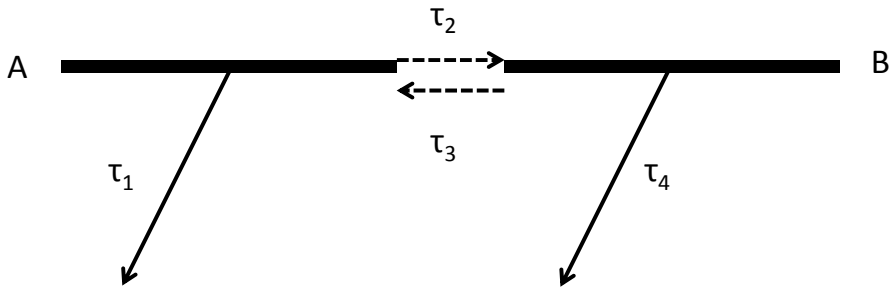

Figure 6.18.: Model for a temperature dependent lifetime based on the descriptions in [36] and [47]. Dashed decay channels are assumed temperature dependent.

A_2). Hence this scenario can be excluded as well.

To continue modeling this case it would be reasonable to fit a model including a temperature dependent decay constant, however, the data and the examined temperature range would hardly allow reasonable conclusions. This is even more the case as in the example mentioned above from [47] the suggested temperature dependent lifetimes contain further fit constants and exponential dependencies as well as combinations thereof. Nevertheless, please note that this example is not totally comparable as Ga is not a transition metal and thus does not offer the same d-shell electron properties that play an important role in the discussion for Ru and Fe based molecules in [36].

The temperature dependent visible fluorescence measurements support the idea of a more complex model with summed up exponential decays. To make further progress in modeling further experiments will be necessary, studying X-ray fluorescence and visible fluorescence at the same time and over a broader temperature range.

Visible Fluorescence Lifetime Measurements for Gaq3 in Powder, Film or Crystal

In order to examine the importance of the actual modification of the sample, Gaq3 has also been examined as powder, as film and as crystals. The sample preparation is described in [30]. The lifetime plots including fits are presented in figure 6.19. It is notable that the lifetime of Gaq3 excitation is varying from ≈ 5.3 ns in powder via ≈ 6.2 ns in a film to up to ≈ 14.1 ns as a crystal. These measurements illustrate the importance of the environment surrounding the molecule when considering effects of electronic excitation. It suggests that in future experiments even more effort could be made ensuring the sample has a constant environment (i.e. avoiding or compensating the vaporization of the solvent).

The plots also suggest that fitting a combined sum of two exponentials might be the better model if noise and ringing could be avoided or a stronger signal created. This is already the case for powder (figure 6.19a), however with huge error bars and cannot be

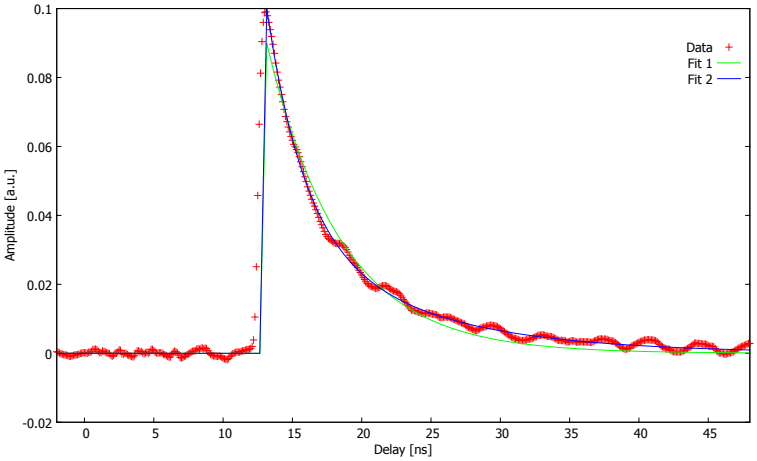

(a) Lifetime of visible fluorescence of Gaq3 as powder $\tau \approx (5.3 \pm 0.2)$ ns (fit 1) or a combined fit of two exponentials $\tau_1 \approx (9.4 \pm 2.5)$ ns and $\tau_2 \approx (2.6 \pm 0.8)$ ns (fit 2)

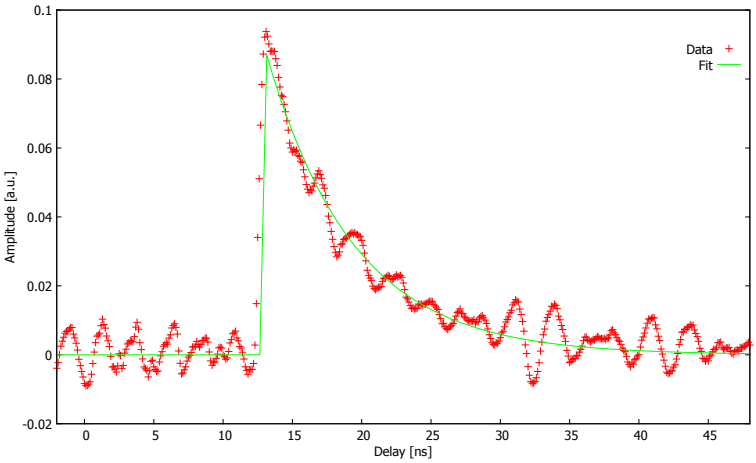

(b) Lifetime of visible fluorescence of Gaq3 as film $\tau \approx (6.3 \pm 0.3)$ ns

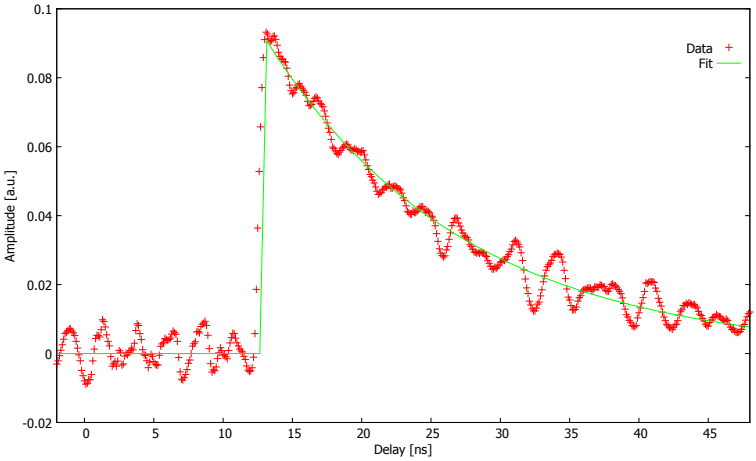

(c) Lifetime of visible fluorescence of Gaq3 as crystal $\tau \approx (14.1 \pm 0.4)$ ns

Figure 6.19.: Lifetime measurements of the fluorescence in different modifications of Gaq3

statistically justified with the data for film and crystal. However this might change if a better signal, a better temporal resolution or a noise- or ringing-reduced measurement could be achieved.

Thus these measurements also support the idea of a combined electronic state with (at least) two decay constants and illustrate the strong dependence of the lifetime on the modification of the sample.

Visible Fluorescence Lifetime Measurements for Different Laserpowers

Having observed the temperature dependent visible fluorescence the question occurred if the laser might heat up the jet noticeably. As a consequence the fluorescence from different areas within the laser spot might have different (temperature dependent) lifetimes. In this case, the apparent lifetime would depend on the laserpower as well. Figure 6.20 shows lifetime plots for various laser powers.

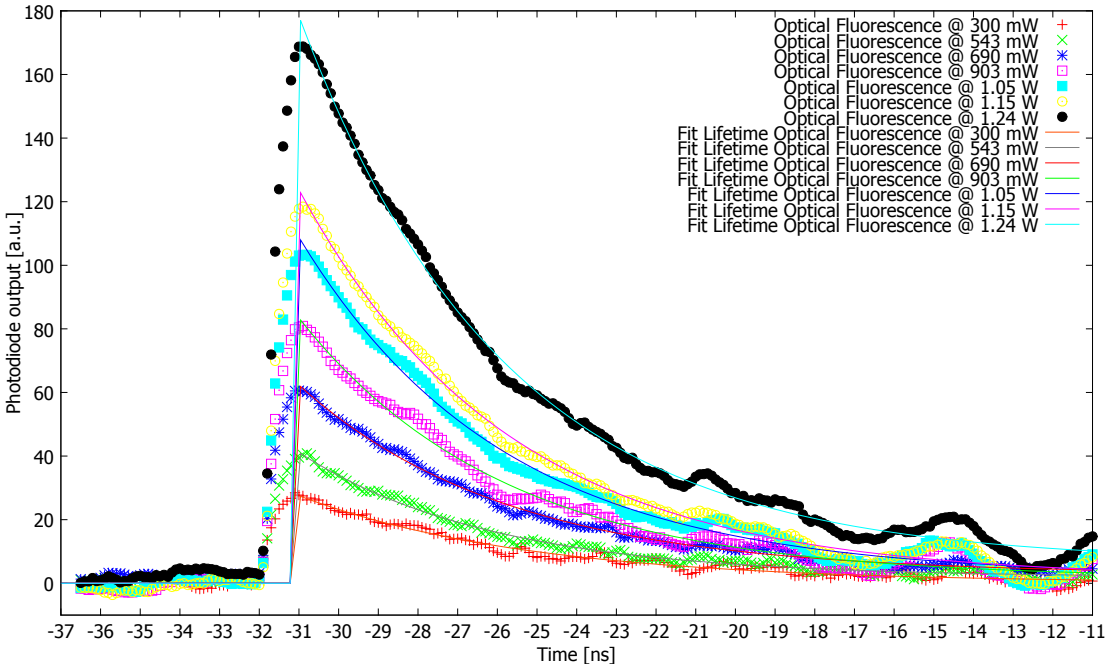

Figure 6.20.: Lifetime of the visible fluorescence for different laserpowers

The fitted lifetimes and amplitudes are plotted against laserpower in figure 6.21. There seems to be no effect from the laser heating up the jet on the lifetime, within the error bars the measured lifetime stays constant. This is experimentally desirable as it suggests that the results will not vary depending on the actual parts of the fluorescent sample where the detected fluorescence originated from.

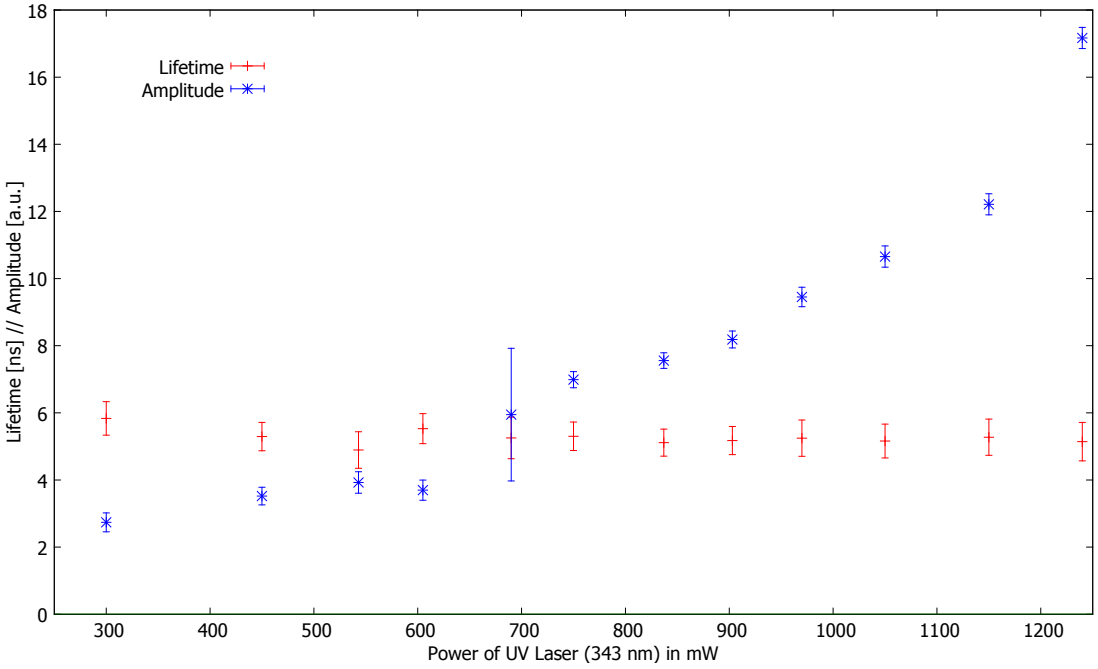

Figure 6.21.: Lifetime of the visible fluorescence of Gaq3 depending on laserpower

Znq2

The same XAS experiment has been been conducted for bis(8-hydroxyquinolinato)zinc, usually referred to at Znq2. Its structural formula can be seen in figure 6.22.

Dimethyl sulfoxid (DMSO) has been used as solvent. A smaller fluorescence yield has been observed with this setup leading to much noisier spectra. Therefore, an as extensive analysis as for Gaq3 cannot be performed. The delay scan is shown in figure 6.23 including a fit. For statistical reasons everything except a single exponential decay cannot be legitimated. The scan was conducted at 9666.5 eV which is at the K edge of Zn. The concentration of Znq2 in DMSO has been 2.8 mg/ml.

The observed (possibly combined) lifetime is (2.02 ± 0.23) ns- again with the errors stated by the GNUplot fitting routine (and known to be rather optimistic for correlated errors, as mentioned earlier).

Repeating the experiment with Znq2 mainly shows the flexibility of the setup and the possibility to extend these experiments in terms of sample, solvent and X-ray energy. The observed lifetime can be seen as a starting point for further examinations of the sample. Two additionally taken spectra of the visible fluorescence at two different temperatures support the working hypothesis that the sample might have similar properties as Gaq3.

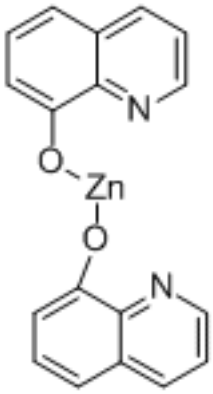

Figure 6.22.: Structural formula for Znq2, taken from [5].

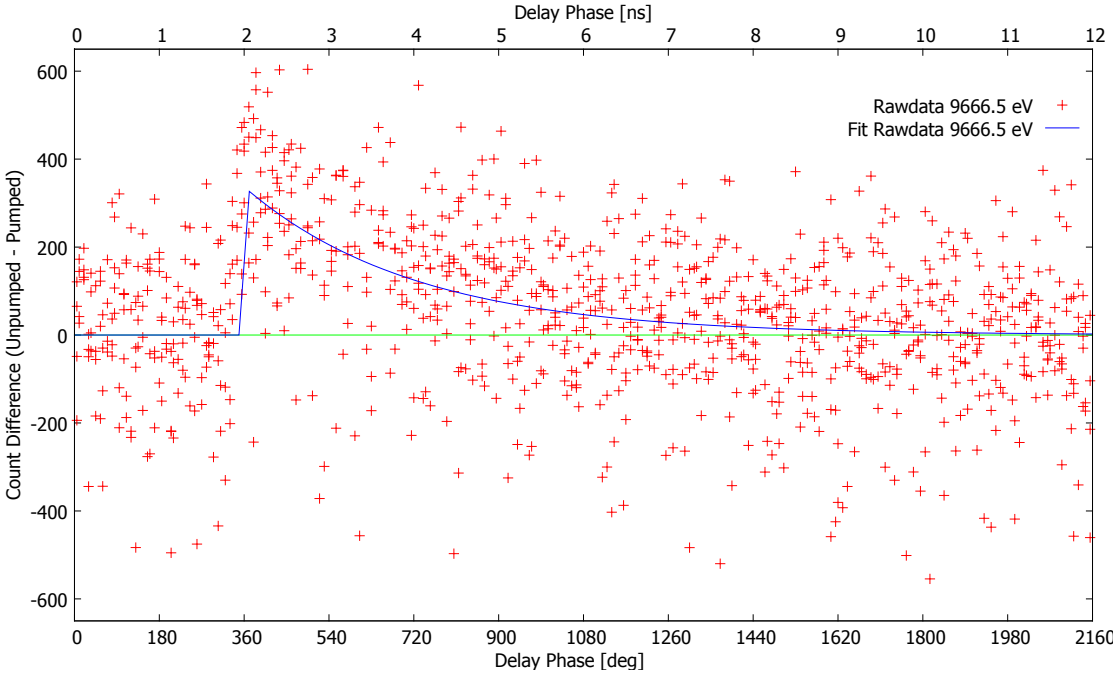

Figure 6.23.: Lifetime of the laser-pumped state in Znq2 probed with X-rays at 9666.5 eV (at the K edge of Zn).

6.1.4. Conclusion on the Experimental Findings in X-ray and Visible Fluorescence Lifetime Measurements

The time resolved XAS studies suggest the existence of at least two probed excited states with independent (possibly combined) decay constants in Gaq3. Further examinations of the visible fluorescence of the jet also support the idea of (at least) two excited states that exist in a temperature dependent ratio thus leading to a temperature dependent combined lifetime. This combined lifetime is most likely resolvable as sum of exponentials if the temporal resolution of the measurement can be improved and the noise reduced. For Gaq3 in powder modification this is already the case and the two excited states model for fluorescence is supported by the data as well. Together with the data for Gaq3 as film or crystals (which do not show two time constants, possibly due to poor resolution and noise) the different lifetimes of these modifications also support the idea of a strong dependence of the lifetimes from the surrounding. This, as well as the temperature dependent lifetimes, can be explained by the importance of vibrational relaxation as possible radiationless de-excitation path.

In detail the findings are:

- The XAS delay scans of Gaq3 are best fitted with the linear combination of two exponential decays. This suggests a model with two excited states and two (or more) decay constants. For two exponentials the data suggest lifetimes of $\tau_1 = 0.4$ ns and $\tau_2 = 4.4$ ns.

- The examination of visible fluorescence depending on the samples temperature also refuses an easy model with only one excited state. It suggests at least one vibrational and thus temperature dependent de-excitation channel.

- The examination of visible fluorescence of Gaq3 in other modifications such as powder, crystal or film confirms the dependence of the properties from the chemical environment. Furthermore they do not contradict the suggestion of two combined decays.

- No influence of the laser power on the considered parameters could be observed.

Full Jablonski diagrams or similar representations of possible excited states within Gaq3 are not known to the author of this work. In [30] a general model for the energy scheme of metal-quinolines (Mq3) is suggested. It can be seen in figure 6.24. Besides the S0 and S1 singlet states the existence of a Triplet state T1 is assumed. The model is based on the combination and generalization of various sources, often taking into account other metal-quinolines (such as Alq3 as discussed in [26]). The singlet to triplet state transition is quantum mechanically forbidden therefore occurring less likely, i.e. showing longer lifetimes.

The photo excitation (vertical arrow from S0 to S1) has an impact on the other electron energies within the molecule, thus the described transient between pumped and unpumped XAS spectra can be measured. The easiest illustration is that the excited

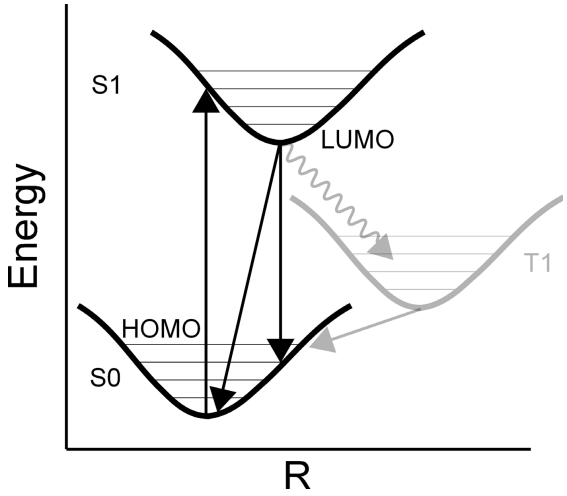

Figure 6.24.: Energy scheme for Mq3, adapted from [30]. This scheme shows three possibly involved states after photo excitation. The inner shell electrons probed with XAS hence see a slightly different potential and can be probed to gain information on the photo excited states as well. Hence also XAS can contribute complementary information on the photo excited orbitals. HOMO is short for highest occupied molecular orbital, LUMO for lowest unoccupied molecular orbital.

electrons are less tightly bound, therefore the inner shell electrons are subject to a slightly different potential.

In general, the Mq3 model from figure 6.24 could explain the observed two excited states and decay constants. Within the Mq3 energy scheme possible candidates would be the S1 and T1 states. However, it needs to be pointed out, that the known lifetimes for the triplet state in Alq3 for example are in the order of $10^3 - 10^6$ longer (i.e. in the μs and ms range) [22], [26] than the XAS transient and visible fluorescence lifetimes presented in chapter 6.1.3 for Gaq3. Such long lifetimes would have led mainly to an offset as the visible fluorescence has been excited with 130 kHz. Therefore without further research no concluding statement on the two involved states can be made.

In summary all experimental results support the proposed model of at least two probed excited states with different decay constants. Those show a dependence on possible vibrational de-excitation as represented by the surrounding and temperature. To the best of the author's knowledge, to date no data for comparison can be found in the literature. The lifetime of visible fluorescence for Gaq3 (in DMF) has been reported in [43] as a double exponential decay with one lifetime in the single pico second range (depending on excitation wave length) and the second one being $\tau = 4.2$ ns. The first lifetime is way below the temporal resolution of PETRA III as well as of the photodiode applied in this work, the second lifetime is in agreement with both, the longer XAS lifetime and the combined visible fluorescence lifetime.

The structural information obtainable from the presented data is included in [30].

The data for Znq2 is to noisy to state or claim anything, however they do not contradict the hypothesis, that the findings of Gaq3 might be transferable.

7. Summary and Outlook

To enable time resolved pump-probe studies at PETRA III a highly repetitive laser system has been synchronized to the PETRA III X-ray pulses. A high level of flexibility has been reached with a mobile system including various frequency conversion options and flexible laser safety precautions. Furthermore, first experimental setups for time resolved experiments have been established in cooperation with DESY scientists, namely a setup for electron-ion coincidence spectroscopy in the gas-phase and a setup for XAS experiments with solute samples prepared in a liquid jet.

The presented laser system has been successfully synchronized to PETRA III. The temporal Jitter of the synchronization is $\sigma < 5$ ps and thus way below the PETRA III pulse length and, therefore, the temporal resolution is practically limited by PETRA III pulse duration. This pulse length can, hence, be directly seen in the temporal resolution of time resolved experiments with this system and has been measured that way to be FWHM = 90.01 ps ± 7.03 ps; thus within the expected range.

The flexible system allows pump-probe experiments with a broad range of laser wavelengths from the UV to the infrared with the relatively high repetition rate of 130 kHz corresponding to PETRA III single bunch mode and, therefore, being in principle usable at all bunchmodes - limited only by the temporal bunch distance as upper temporal limit for the dynamics[1].

The synchronization has been demonstrated at different beamlines, therefore allowing to cover a broad range of X-ray energies as offered by PETRA III as well.

An extended PLL concept of three interconnected control loops with targeted switching ability has shown to provide extended lock control as well as further delay and tuning opportunities. Especially the option to select and monitor the bucket enables to ensure long term stability.

A setup for time-resolved electron-ion coincidence spectroscopy in the gas-phase has been established at P04 in close cooperation with the beamline scientists [27]. Temporal and spatial overlap have been demonstrated and the system is scheduled for future beamtimes.

The successful demonstration of the presented system at P11 and first pump-probe experiments on OLED molecules led to an almost identical system being installed there permanently, substantiating the value of such a tool. Experiences with the synchronization during this work have contributed to the design and specifications of this newer system in cooperation with the scientists at P11 and the engineers at the manufacturer Light Conversion.

First experimental results applying X-ray absorption spectroscopy show dynamics of

[1] what can be bypassed in coincidence measuring setups

the electronic excitation on the timescale of a few hundred pico seconds up to a few nano seconds in Gaq3 and Znq2 and can provide basic understanding for further research on those molecules. In case of Gaq3 these findings have been analyzed in detail and compared with visible fluorescence measurements suggesting at least two excited and probed states with different decay constants. The observed lifetimes are $\tau_1 = 0.4$ ns and $\tau_2 = 4.4$ ns. The demonstrated dependency of the lifetimes of visible fluorescence on chemical environment and temperature back up future monitoring and stabilization approaches for further parameters such as concentration changes due to vaporization or the temperature. To extend the suggested model also a simultaneous acquisition of visible and X-ray fluorescence could offer even more complementary information. Also cross-checking the effect of the wavelength of the pump pulse might allow to further limit the possible models.

Further experiments with the demonstrated system as well as with other laser systems are meanwhile scheduled or have even been taking place. Experiments will cover further time-resolved XAS experiments, time-resolved electron-ion coincidence spectroscopy and time-resolved XMCD microscopy.

A. Appendix

A.1. Understanding Single Side-Band Phase Noise and its Relation to Timing Jitter

An ideal oscillator would have no other spectral components than the desired repetition rate. A real oscillator in contrast will show noise as sidebands. This undesired contributions originate from random noise within the examined signal and are interpreted as the occurrence of other frequencies in frequency space. This is obvious considering the fourier transformation of a perfect sine being a delta-peak in frequency space thus all discrepancies from the ideal case will be the occurrence of further frequencies. One can model this as a sine of the carrier frequency ω_0 with a slightly modified phase over time (illustrated in figure A.1):

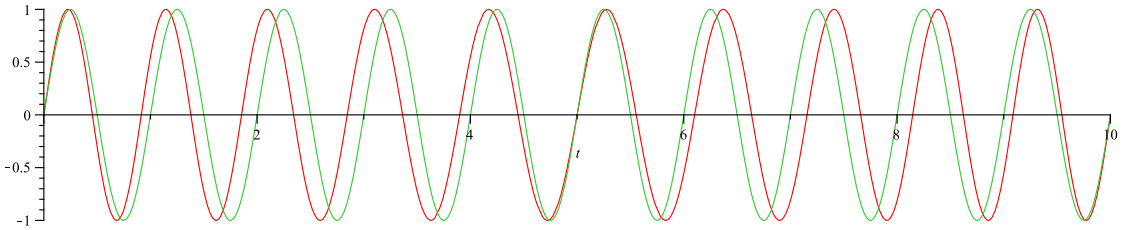

Figure A.1.: Example for the easiest model of phase noise of one frequency. The fourier transformation of real phase noise will contain many different frequency components of course. The shown curves show $sin(2\cdot\pi\cdot t+sin((2\cdot\pi\cdot 0.1)\cdot t))$ and the noise free $sin(2\cdot\pi\cdot t)$

$$f(t) = A\cdot sin(\omega_0 t + B\cdot sin(\omega_1 t)) \tag{A.1}$$

By applying the addition theorem this can be written as:

$$f(t) = A\cdot(sin(\omega_0 t)\cdot cos(B\cdot sin(\omega_1 t)) + cos(\omega_0 t)\cdot sin(B\cdot sin(\omega_1 t))) \tag{A.2}$$

Considering only small amplitudes B of noise being much smaller than the carrier sines period the small angle approximations $sin(x)\approx x$ and $cos(x)\approx 1$ for $x << 1$ get valid and it can be rewritten as:

$$f(t) \approx A\cdot(sin(\omega_0 t) + cos(\omega_0 t)\cdot B\cdot sin(\omega_1 t)) \tag{A.3}$$

Finally applying the product-to-sum identities leads to:

$$f(t) = A\cdot\left(sin(\omega_0 t) + \frac{B}{2}\cdot sin((\omega_0+\omega_1)t) - \frac{B}{2}\cdot sin((\omega_0-\omega_1)t)\right) \tag{A.4}$$

Here one can easily see the occurrence of sidebands $\pm\omega_1$ away from the carrier frequency ω_0. Thus the phase modulation can be found and identified within the noise spectra as long as the noise fulfills the assumptions to be small. This can be generalized for the

combination of noise of a lot of different frequencies:

$$f(t) = A \cdot sin\left(\omega_0 t + \sum_N B_N \cdot sin(\omega_N t)\right) \tag{A.5}$$

$$= A \cdot \left(sin(\omega_0 t) \cdot cos\left(\sum_N B_N \cdot sin(\omega_N t)\right) + cos(\omega_0 t) \cdot sin\left(\sum_N B_N \cdot sin(\omega_N t)\right)\right) \tag{A.6}$$

$$\approx A \cdot \left(sin(\omega_0 t) + cos(\omega_0 t) \cdot \left(\sum_N B_N \cdot sin(\omega_N t)\right)\right) \tag{A.7}$$

$$= A \cdot \left(sin(\omega_0 t) + \sum_N cos(\omega_0 t) \cdot B_N \cdot sin(\omega_N t)\right) \tag{A.8}$$

$$= A \cdot \left(sin(\omega_0 t) + \sum_N \left(\frac{B_N}{2} \cdot sin\left(\left(\omega_0 + \omega_N\right) t\right) - \frac{B_N}{2} \cdot sin\left(\left(\omega_0 - \omega_N\right) t\right)\right)\right) \tag{A.9}$$

Obviously those sidebands are always symmetric to the carrier frequency. Therefore, the signal source analyzer only provides one half of the spectrum as can be seen in later figures without losing any information.

Having now motivated why to interpret spectral sidebands as phase noise of a corresponding frequency it is important to relate that to spectral power.

To explain spectral power the earlier image of measuring the single-side band phase noise with the tunable ideal bandpass is helpful again. The first step is assuming this bandpass will filter out exactly (and only) one frequency $\omega_0 + \omega_1$ from our signal $f(t)$ from equation A.9. The filtered signal looks like:

$$f_{BPF_1}(t) = \left(\frac{A \cdot B_1}{2} \cdot sin\left(\left(\omega_0 + \omega_1\right) t\right)\right) \tag{A.10}$$

If the power of its output is measured one gets the squared RMS value of the filtered frequency. The RMS value for sinusoidal signals with an amplitude A is $\frac{A}{\sqrt{2}}$ as electric power P is defined as:

$$P = \frac{1}{T} \int_0^T u(t) \cdot i(t) dt \tag{A.11}$$

For periodic signals T is the period, in other cases one needs to consider $T \to \infty$. In ohmic case it can be rewritten (using Ohm's law):

$$P = \frac{1}{T} \int_0^T \frac{u(t)^2}{R} dt \tag{A.12}$$

For a sinusoidal signal $u(t) = A \cdot sin(\omega t)$ thus the power becomes

$$P = \frac{1}{T}\int_0^T \frac{A^2 \cdot sin^2(\omega t)}{R} dt \tag{A.13}$$

$$= \frac{A^2}{RT}\left[\frac{1}{2}\left(t - \frac{sin\,(2\omega t)}{2\omega}\right)\right]_0^T \tag{A.14}$$

$$= \frac{A^2}{2R} \tag{A.15}$$

This is independent of the frequency. The result for the filtered single frequency $f_{BPF_1}(t)$ thus is:

$$P = \frac{\left(\frac{A \cdot B_1}{2}\right)^2}{2R} \tag{A.16}$$

$$= \frac{A^2}{4R} \cdot B_1^2 \tag{A.17}$$

As relative power is considered this needs to be normalized to the power P_0 of the carrier frequency that could be derived the same way with a filter at ω_0 or just by considering the signal at the carrier frequency i.e. setting $B = 0$ in equation A.1 and then identifying the remaining function as the $u(t)$ put into equation A.13. The power ratio then is with $P_=$ from equation A.15:

$$\frac{P}{P_0} = \frac{\frac{A^2}{4R} \cdot B_1^2}{\frac{A^2}{2R}} \tag{A.18}$$

$$= \frac{B_1^2}{2} \qquad =: \Delta\phi_{RMS}(\omega_1) \tag{A.19}$$

This is the squared RMS phase variation of the carrier frequency at the chosen frequency $\omega_0 + \omega_1$. It can, therefore, be considered as $\Delta\phi_{RMS}(\omega_1)$ In reality a single frequency can never be filtered out but a whole bandwidth will be measured. In this case the values for P will sum up for different frequencies (while the values for B sum up for same frequencies [1]). This RMS phase variation summed up squared is the sum of all the RMS phases at different frequencies within the bandwidth and, therefore, following the

[1] To understand this again equation A.13 has to be considered this time inserting $u(t) = A_1 \cdot sin(\omega_1 t) + A_2 \cdot sin(\omega_2 t)$

$$P = \frac{1}{T}\int_0^T \frac{(A_1 \cdot sin(\omega_1 t) + A_2 \cdot sin(\omega_2 t))^2}{R} dt \tag{A.20}$$

$$= \frac{1}{T}\int_0^T \frac{A_1^2 \cdot sin^2(\omega_1 t)}{R} + \frac{A_2^2 \cdot sin^2(\omega_2 t)}{R} + \frac{2 \cdot A_1 A_2 \cdot sin(\omega_1 t) \cdot sin(\omega_2 t)}{R} dt \tag{A.21}$$

$$= \frac{1}{T}\int_0^T \frac{A_1^2 \cdot sin^2(\omega_1 t)}{R} dt + \frac{1}{T}\int_0^T \frac{A_2^2 \cdot sin^2(\omega_2 t)}{R} dt + \frac{1}{T}\int_0^T \frac{2 \cdot A_1 A_2 \cdot sin(\omega_1 t) \cdot sin(\omega_2 t)}{R} dt \tag{A.22}$$

The first two integrals can directly be solved by comparing them with equation A.13. The third

central limit theorem (see, for example, [15]) is gaussian distributed even if the original contributers are based on other distributions.

To get the single side-band phase noise the relative spectral power has to be normalized to the bandwidth Δf. Here the description now follows the description in 'Phase Noise and Timing Jitter' in [76]. The single side-band phase noise is in agreement with the literature called $\mathcal{L}_\phi(f_i)$ where $f_i = \frac{\omega_i}{2\pi}$.

$$\mathcal{L}_\phi(f_i) = \frac{\Delta\phi^2_{RMS}(\omega_i)}{\Delta f} \tag{A.29}$$

With the general consideration of a phase difference being directly connected with a difference in the temporal position $\Delta\phi = 2\pi f \Delta t$ the timing jitter can be related to the phase noise:

$$\mathcal{L}_\phi(f_i) = \frac{\Delta t^2_{RMS}(\omega_i)(2\pi f_0)^2}{2\Delta f} \tag{A.30}$$

where $f_0 = \frac{\omega_0}{2\pi}$ is the carrier frequency (that suffers the phase difference) and the additional factor of 2 in the denominator compensates that $\mathcal{L}_\phi(f_i)$ only describes a single side-band of the symmetric spectra. To get the timing jitter as described in the chapters above, it is necessary to rewrite the formula:

$$\frac{\Delta t^2_{RMS}(\omega_i)}{\Delta f} = \mathcal{L}_\phi(f_i)\frac{2}{(2\pi f_0)^2} \tag{A.31}$$

Which needs to be integrated to get the timing jitter from the squared timing jitter spectral density of the desired frequency range.

$$\Delta t_{RMS}(f_1, f_2) = \sqrt{\int_{f_1}^{f_2} \frac{2}{(2\pi f_0)^2}\mathcal{L}_\phi(f_i)df_i} \tag{A.32}$$

integral can be rewritten using the product-to-sum identities.

$$P = \frac{A_1^2}{2R} + \frac{A_2^2}{2R} + \frac{1}{T}\int_0^T \frac{2\cdot A_1A_2\cdot sin(\omega_1 t)\cdot sin(\omega_2 t)}{R}dt \tag{A.23}$$

$$= \frac{A_1^2}{2R} + \frac{A_2^2}{2R} + \frac{2\cdot A_1A_2}{2\cdot R}\int_0^T \frac{cos((\omega_1+\omega_2)t) - cos((\omega_1-\omega_2)t)}{T}dt \tag{A.24}$$

As integration over cosines leads to zero this two terms can be ignored except for the case $\omega_1 = \omega_2$ where in the first part is $cos(0) = 1$ and, therefore, two solutions are possible:

$$P \overset{\omega_1\neq\omega_2}{=} \frac{A_1^2}{2R} + \frac{A_2^2}{2R} \tag{A.25}$$

$$P \overset{\omega_1=\omega_2}{=} \frac{A_1^2}{2R} + \frac{A_2^2}{2R} + \frac{2\cdot A_1A_2}{2\cdot R} \tag{A.26}$$

$$= \frac{A_1^2 + 2\cdot A_1A_2 + A_2}{2R} \tag{A.27}$$

$$= \frac{(A_1+A_2)^2}{2R} \tag{A.28}$$

This is the expected result: Identical frequencies add up linearly, different frequencies quadratically.

According to formula A.32 the signal source analyzer computes the temporal jitter as well. It is called *RMS Jitter* there. This $\Delta t_{RMS}(f_1, f_2)$ correspond to what was called σ in chapter 5.1.1, however, only the contributions from frequencies between f_1 and f_2 are considered. For $f_1 \to 0$ and $f_2 \to \infty$ in ideal case $\Delta t_{RMS}(f_1, f_2) \to \sigma$.

A.2. Timing Box Details

The timing box is constructed from many electronic parts. While a principal scheme has already been shown in figure 4.2 the technical realization is illustrated in the extended version to be found in figure A.2. All involved parts are listed in table A.1. Many additional devices mentioned in figure A.2 are devices like amplifiers, voltage followers or splitters that are necessary to ensure the correct signal levels or avoid impedance problems. They have not been included when explaining the basic principle to avoid confusion.

Table A.1.: Detailled description of the involved parts of the timing box.

#	**Description**	**Name**	**Manufacturer**
1	Various Attenuators (to limit the input to 0 dBm)	adapted according to actual reference level	Mini-Circuits
2	Vector Modulator (see appendix A.3)	QPMX-500-S	I.F. Engineering Corp
3	Voltage follower (unity gain buffer)	Based on OP37G op-amp	
4	Coaxial Low Noise Amplifier (50 - 3000 MHz)	ZX60-33LN-S+	Mini-Circuits
5	Coaxial Power Splitter / Combiner (DC - 10 GHz)	ZX10R-14-S+	Mini-Circuits
6	Frequency Divider / Prescaler	FPS-6-15	RF Bay Inc
7	Coaxial Low Pass Filter (DC - 98 MHz)	SLP-100+	Mini-Circuits
8	Coaxial Frequency Mixer (100 - 2000 MHz)	ZFM-2000+	Mini-Circuits

Continued on next page

Table A.1 – *Continued from previous page*

#	Description	Name	Manufacturer
9	Coaxial Low Pass Filter (DC - 1.9 MHz)	SLP-1.9+	Mini-Circuits
10	Coaxial Power Splitter / Combiner (DC - 4.2 GHz)	ZFRSC-42-S+	Mini-Circuits
11	2 Channel Amplifier		Electronic Workshop UHH
12	Adjustable Amplifier	Based on LF356 op-amp	Electronic Workshop UHH
13	Audio Monitoring System	Adapter 2 x BNC -> stereo jack (3.5 mm, female) for acoustic monitoring of the error signals. Any active speaker system can be connected.	
14	Coaxial Frequency Mixer (1 - 1000 MHz)	ZFM-2S+	Mini-Circuits
15	SMA Fixed Attenuator (3 dB, DC - 6 GHz)	VAT-3+	Mini-Circuits
16	Amplifier	Based on LM7171 op-amp	
17	SMA Fixed Attenuator (1 dB, DC - 6 GHz)	VAT-1+	Mini-Circuits
18	Coaxial Low Noise Amplifier (0.1 - 500 MHz)	ZFL-500LN+	Mini-Circuits
19	SMA Fixed Attenuator (4 dB, DC - 6 GHz)	VAT-4+	Mini-Circuits
20	Realtime Controller consisting of		

Continued on next page

Table A.1 – *Continued from previous page*

#	**Description**	**Name**	**Manufacturer**
	Integrated 400 MHz Real-Time Controller and 2M Gate FPGA	NI cRIO-9074	National Instruments
	4-Channel, 100 kS/s, 16-bit, ±10 V, Analog Output Module	NI 9263	National Instruments
	4-Channel, 100 kS/s/ch, 16-bit, ±10 V Analog Input Module	NI 9215	National Instruments
	Power Supply 5 A, 24 VDC	NI PS-15	National Instruments
21	500 MHz Bandpass Filter (SMA)	KR 2659-SMA	KR Electronics
22	Piezo Positioning System consisting of		
	Piezo Translation Stage	P-753.11C	Physik Instrumente (PI)
	Calibrated Adapter	E-750.CP	Physik Instrumente (PI)
	Digital Piezo Controller	E-753	Physik Instrumente (PI)
-	Power Supply for all active parts not powered by NIPS15 (20)	MTMKE-02 (DESY27179)	Kniel

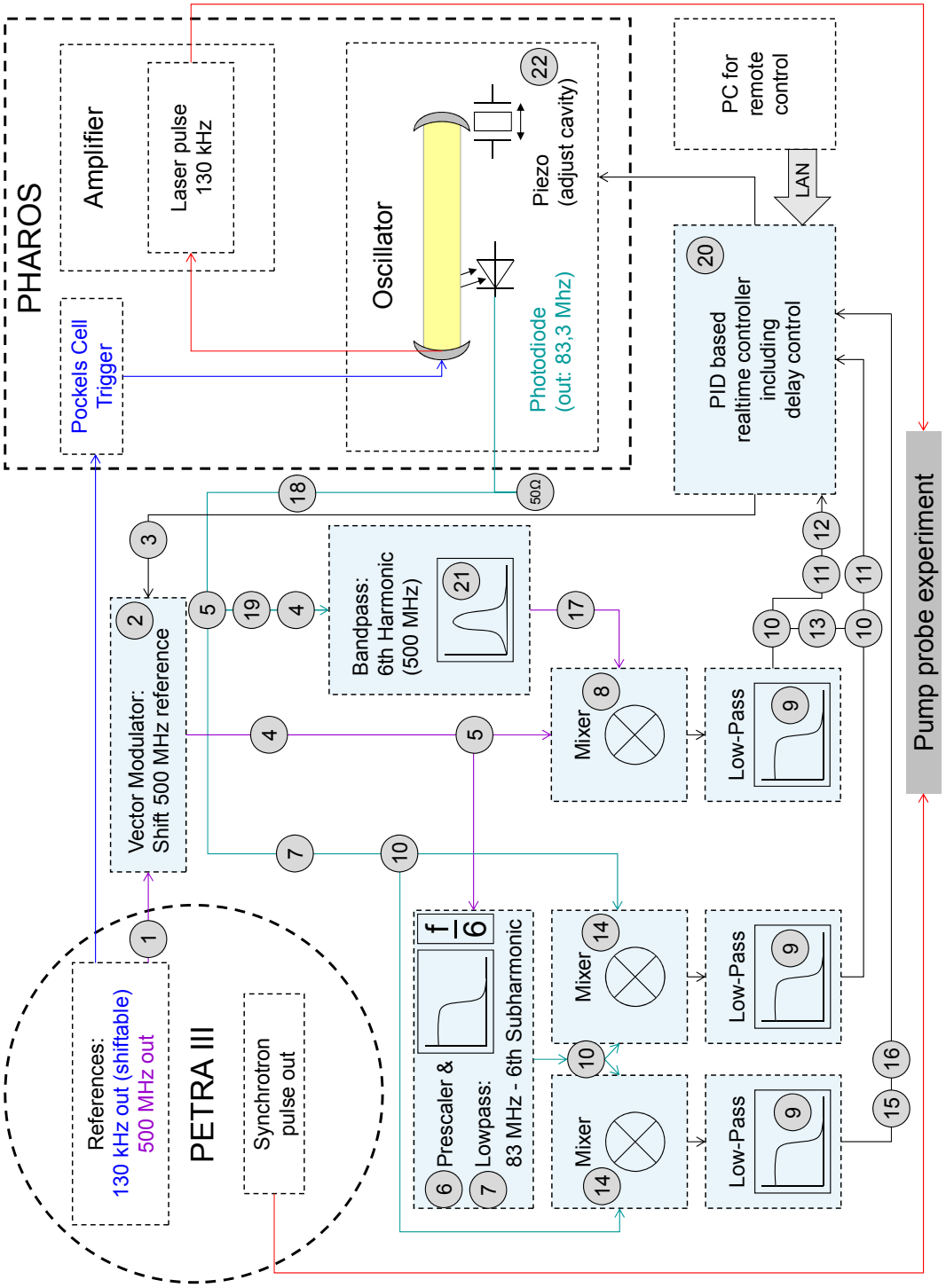

Figure A.2.: Extended scheme of the timing box

A.3. Electronic phase shifter

A vector modulator has been used to be able to set the delay smoothly. It is the commercially available Complex Phase Modulator QPMX-500-S by I.F.Engineering. The vector modulator as a phase shifter is described in detail in chapter 4.2.3. However, it needs to be calibrated first. The calibration is performed similar as in [46].

A.3.1. Calibration of I and Q voltages

The output of the vector modulator is linear in ideal case. As the two branches are added quadratically however small discrepancies can cause bigger errors. The first step performed is now to measure the linearity for the output amplitudes depending on the input voltages at I or Q independently. To do so an offset I_0 and Q_0 is implemented as well via minimizing the total output amplitude. The result of this measurement is shown in figure A.3.

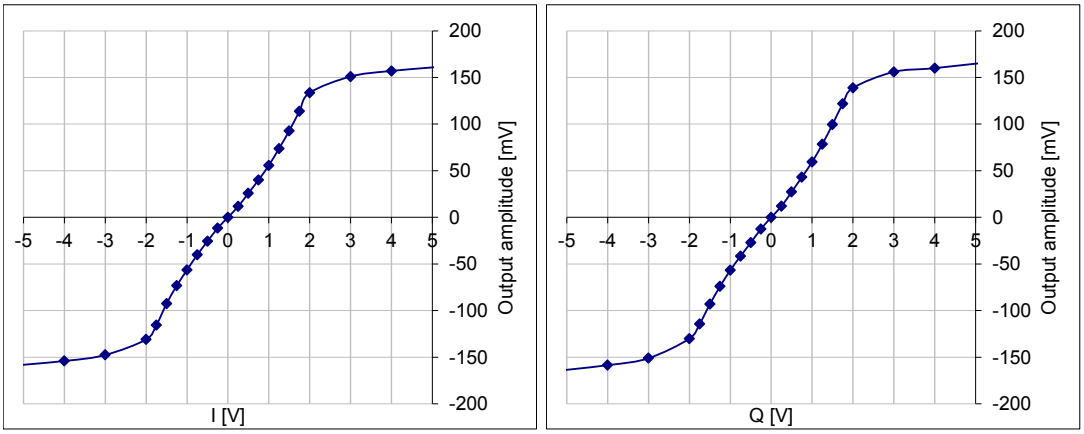

(a) (b)

Figure A.3.: The output amplitude of the vector modulator for I and Q respectively

These values are fed into an interpolation algorythm within the communication code to be seen in figure A.4. The desired output is calculated by splitting the desired phase into its I and Q part. Those are scaled to fit the max linear range of the vector modulator. Now the interpolation algorythm searches the necessary position (or more intermediate position) within the 'Output Amplitude' row of table A.2 and interpolates the respective I or Q value from the corresponding row. The result is fed to the FPGA that sets the DAC to the desired values.

A.3.2. Calibration of timing accurancy

After the calibration of the I and Q inputs of the vector modulator in chapter A.3.1 the accuracy of the delay setting is still not good enough. As there are other sources for discrepancies an overal interpolation is performed. Possible sources for these errors may

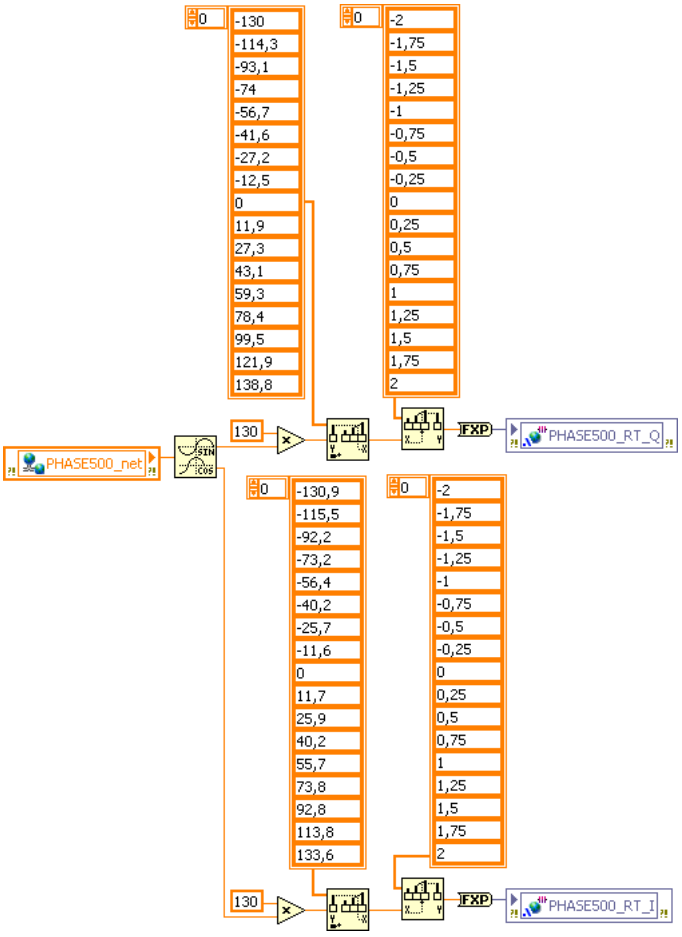

Figure A.4.: LabVIEW code to interpolate the desired voltage the DAC has to output to the I and Q input of the vector modulator.

be discretisation artefacts from the DAC, calibration offsets of the DAC or remaining inaccuracies in the I and Q calibration and especially a combination of all of these. As these are systematic errors it is possible to compensate them. To do so the delay is measured towards its reference. The actual phase depending on the desired (set) phase is fed into the LabVIEW interpolation algorythm similar as in chapter A.3.1. This can be seen in figure A.5 The result of the calibration can be seen in figure A.6. Further information on the obtained accuracy with the delay settings can be found in chapter 5.3.

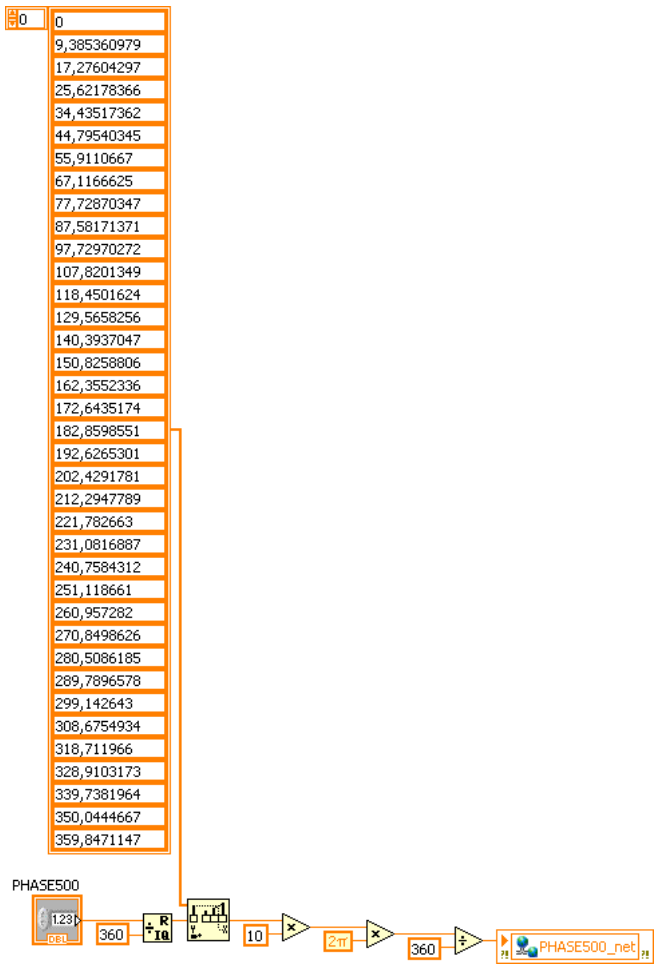

Figure A.5.: The LabVIEW code to interpolate the delay to improve the accuracy of delay settings.

I [V]	Output Amplitude [mV]	Q [V]	Output Amplitude [mV]
-10	-168	-10	-176,2
-8	-166	-8	-173
-6	-161,5	-6	-167,7
-4	-154	-4	-158,5
-3	-147,5	-3	-151
-2	-130,9	-2	-130
-1,75	-115,5	-1,75	-114,3
-1,5	-92,5	-1,5	-93,1
-1,25	-73,2	-1,25	-74
-1	-56,4	-1	-56,7
-0,75	-40,2	-0,75	-41,6
-0,5	-25,7	-0,5	-27,2
-0,25	-11,6	-0,25	-12,5
0	0	0	0
0,25	11,7	0,25	11,9
0,5	25,9	0,5	27,3
0,75	40,2	0,75	43,1
1	55,7	1	59,3
1,25	73,8	1,25	78,4
1,5	92,8	1,5	99,5
1,75	113,8	1,75	121,9
2	133,6	2	138,8
3	151	3	156
4	157	4	160
6	164	6	169,5
8	168	7	172,9
10	172	8	174,9
		10	180,5

Table A.2.: The output amplitude of the vector modulator for I and Q respectively

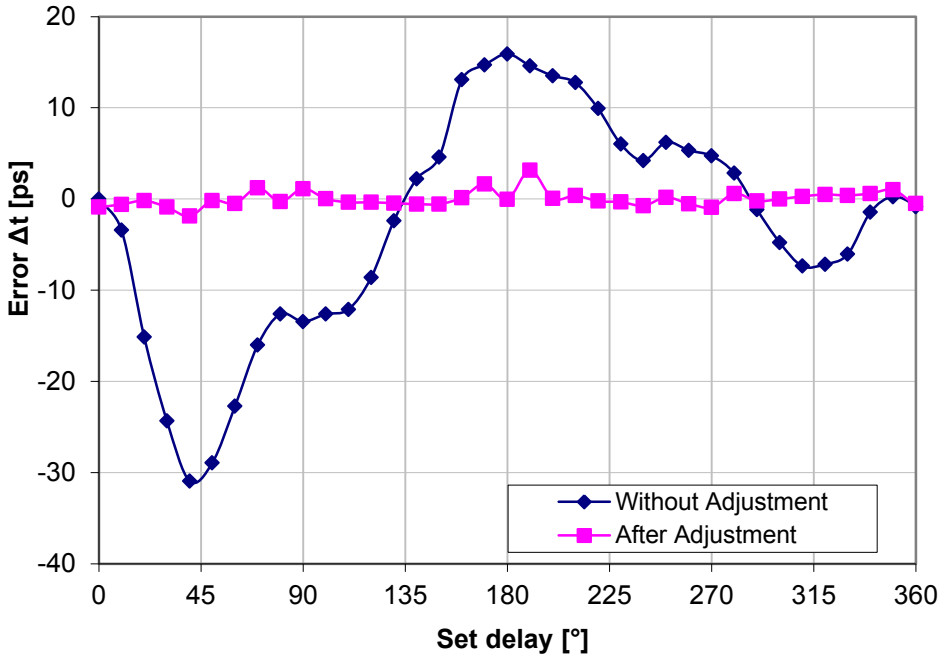

Figure A.6.: The systematic error of the delay accuracy before and after the adjustment.

A.4. Locking the PLL

To start the locking of the loop and thus synchronizing PHAROS with the attached reference (typically PETRA III masterclock) some preconditions need to be fulfilled:

PHAROS must be running and modelocked (so the internal photodiode "PD OSC" delivers a 83 MHz signal). The reference must also be connected (and ensured that the level is suitable for the vector modulator - attenuators need to be used to guarantee 0 dBm at its input). The synchronization unit must be put on and the software is started. Furthermore, the speakers need to be put on and channel A at the line switch has to be selected. As the error signals are in the order of Hz to kHz the easiest and cheapest way to monitor the error signals are speakers.

Then the locking is achieved as follows:

1. `Reset PID` has to be activated
2. The speakers deliver a sinusoidal sound.
3. `POS_set`[2] is used to tune the error signal sound to be as low as possible (tuning on 0.5 steps precision is typically sufficient)
4. If the sound is very deep (often then also very silent as) `Reset PID` has to be deactivated.
5. The sound should hush. The graph in the middle should show horizontal and rather constant signals (as in figure 4.11). The system is locked. Otherwise this instructions need to be repeated with more care on tuning the error signal. If a low sound can not be reached within the range of `POS_set` the oscillator (or the reference) might be misaligned. The oscillator can be adjusted with a prism (This has to be done following PHAROS manuals and communication with Light Conversion).

[2] Range: ±10

A.5. Scripts and code

A.5.1. FPGA code

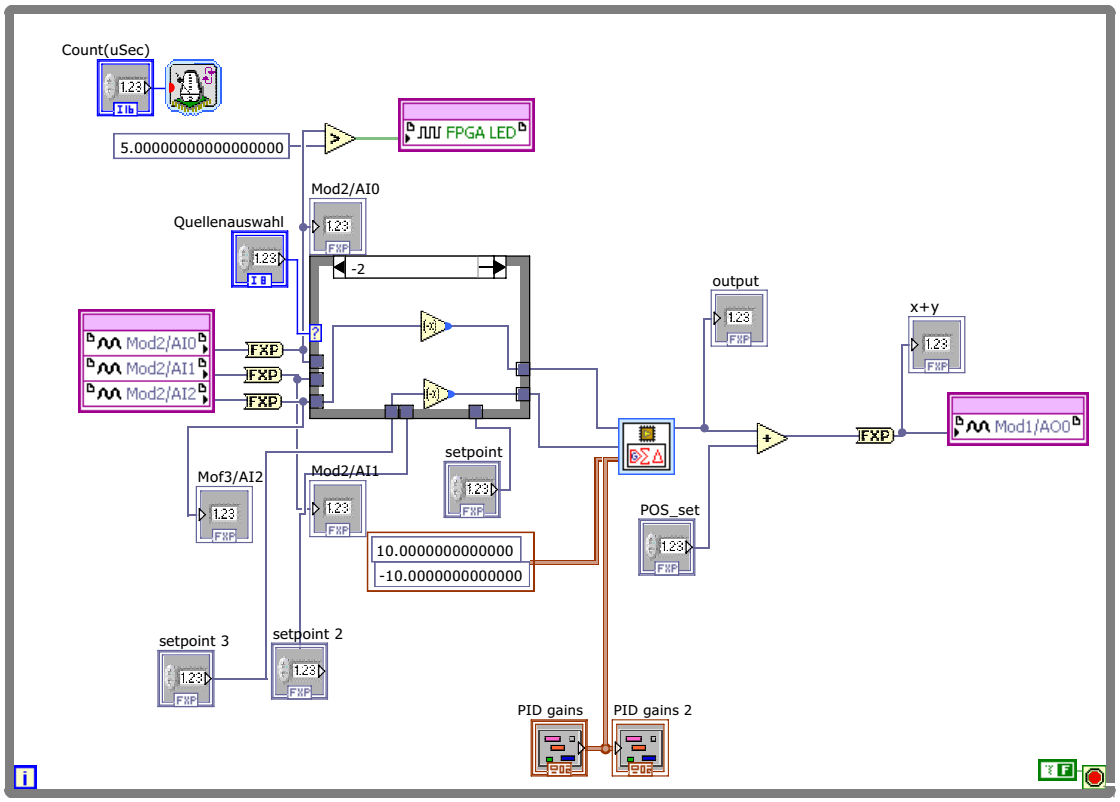

Figure A.7.: FPGA code runnig the PID, selecting the loop and processing setpoints

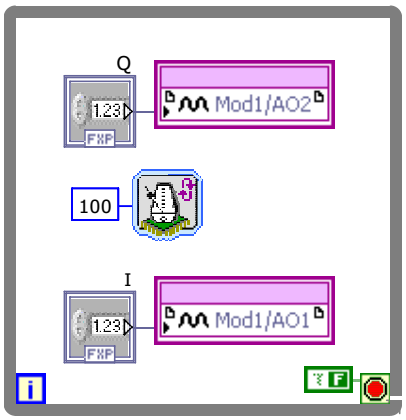

Figure A.8.: FPGA code running controlling I and Q voltages of the vector modulator. This loop is completely independent of the other implemented on the same FPGA running at a different clock.

A.5.2. Real Time Code

The RT_sync.vi handles the communication between the FPGA code and the user interface. The most important part can be found in A.9.

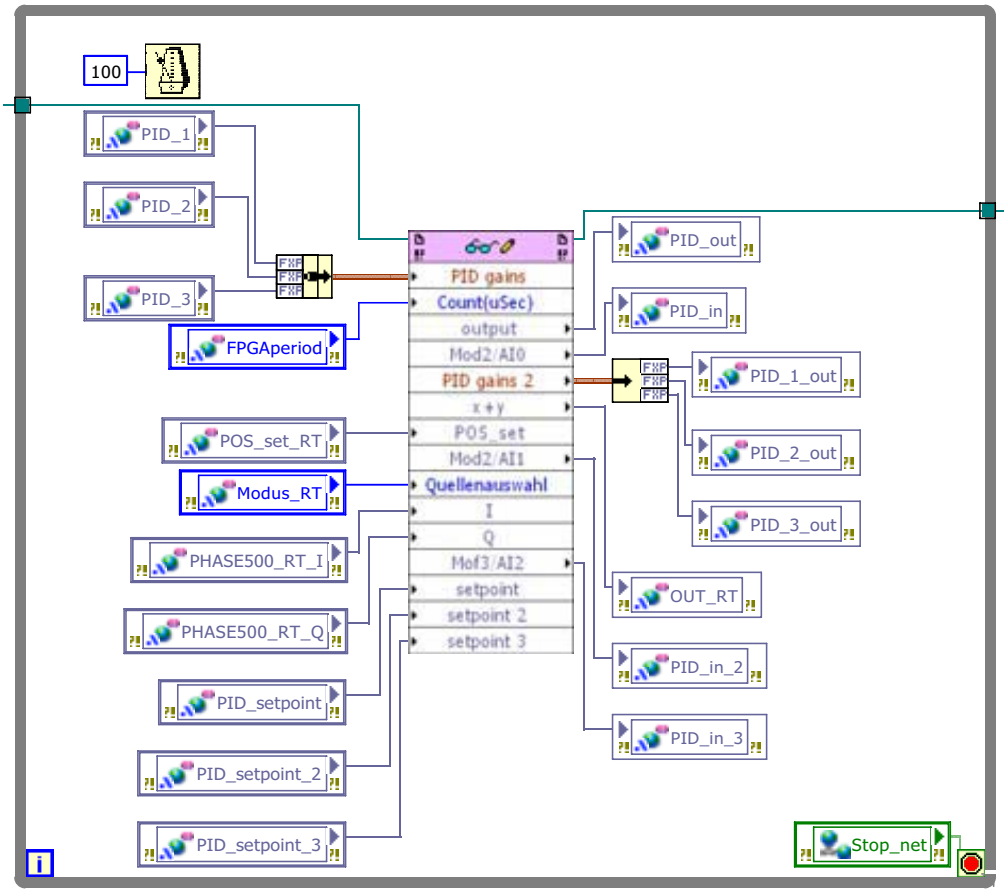

Figure A.9.: Communication with FPGA_sync.vi is the main task of RT_sync.vi. Other loops communicate these variables with the network library.

A.5.3. TANGO Communication

It is possible to control the PHAROS delay remotely via Tango. Therefore the Tango server on the PHAROS control PC needs to be started properly.

Procedure and Preconditions

1. "Tango Delaysteuerung aktivieren" is not active within the PHAROS synchronization software

2. Start the database
   `cmd C:\Program Files\tango\bin>start-db.bat 1`

3. Start the DELAYServer
   `cmd C:\Program Files\tango\bin\DELAYServer>PHAROSDelay.bat Laser -v4`

4. Cross check: Value "PHASE500" within the PHAROS synchronization software and "DelayW" on the Tango server are not too far away.
5. Activate "Tango Delaysteuerung aktivieren" within the PHAROS synchronization software
6. Delay can be controlled remotely for example with the scripts below.

Write Delay

(Assumed IP of PHAROS PC is 192.76.172.17)

```
import sys
from PyTango import DeviceProxy
x=   # enter new value here
devDelay = DeviceProxy("192.76.172.17:20000/DELAYServer/PHAROSDelay/VM")
devDelay.write_attribute("DelayW",x)
```

Read Delay control value back

(Assumed IP of PHAROS PC is 192.76.172.17)

```
import sys
from PyTango import DeviceProxy
devDelay = DeviceProxy("192.76.172.17:20000/DELAYServer/PHAROSDelay/VM")
print devDelay.read_attribute("DelayR").value
```

Implementation in WIN_sync.vi

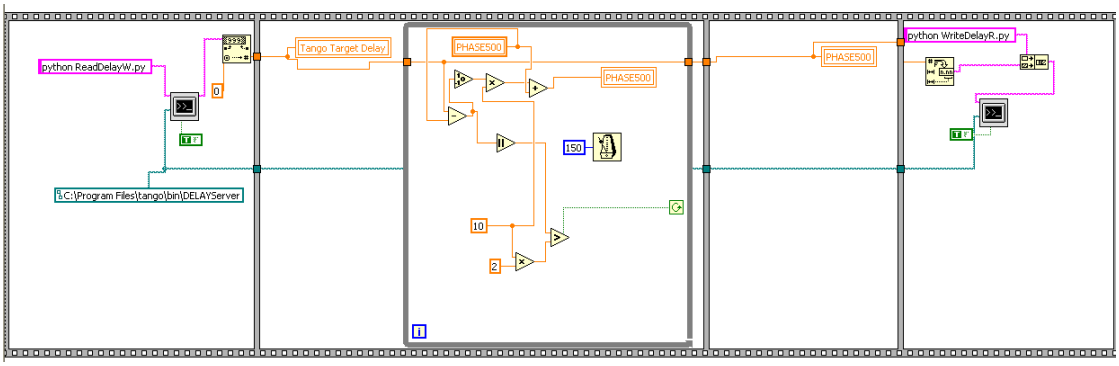

Figure A.10.: Implementation of TANGO control in WIN_sync.vi including a protection against to large delay steps.

A.6. Laser Safety

To be allowed to use a laser system at PETRA III many savety regulations have to be considered. Especially at beamline P04 an advanced safety concept needed to be developed and agreed by the responsible safety officers as there is no experimental hutch like at other beamlines. Therefore, experiments need to be sealed and the laser needs to be operated within a mobile laser hutch. Providing this mobile laser hutch and installing a state-of-the-art interlock system was also part of this work. The system is based on the Lasermet ICS-5 system and extended by DESY signal lamp and customized connectors to include vacuum sensors and valves as well.

A.6.1. Mobile Laser Hutch

Made of matt anodized aluminum, mobile and lockable in position. Equipped with certified laser curtains.

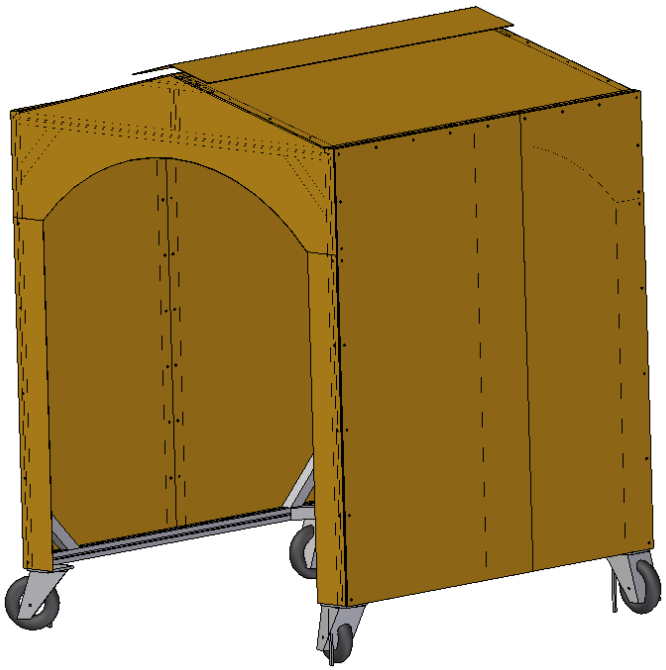

Top View:

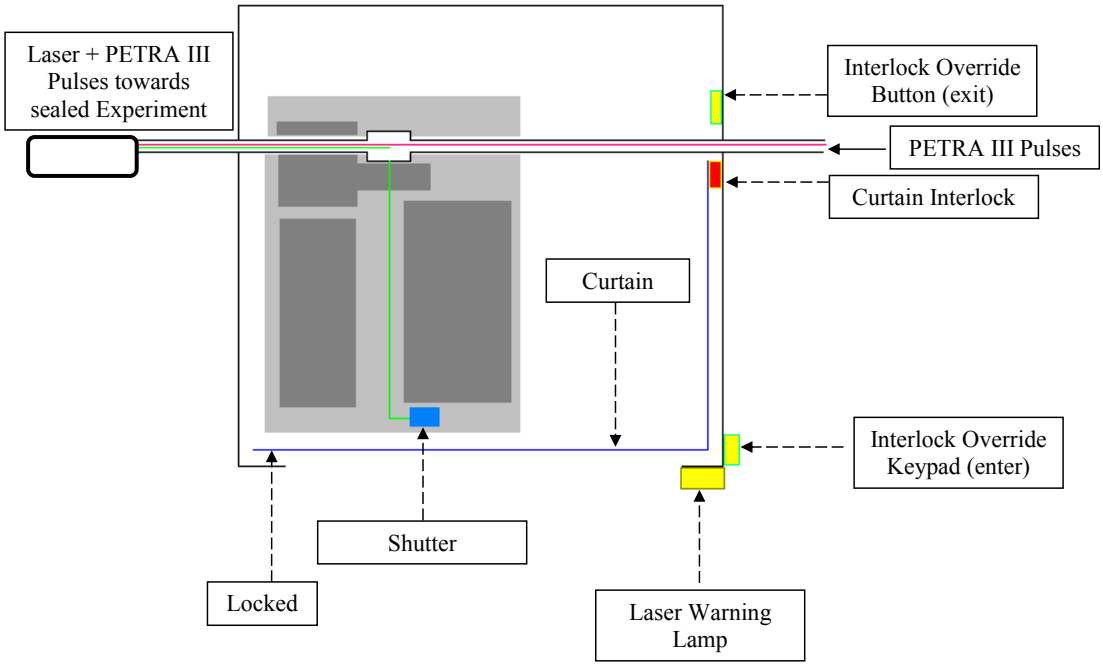
Laser + PETRA III Pulses towards sealed Experiment
Interlock Override Button (exit)
PETRA III Pulses
Curtain Interlock
Curtain
Interlock Override Keypad (enter)
Shutter
Locked
Laser Warning Lamp

Bibliography

[1] ESRF homepage:
http://www.esrf.eu/home.html (July 20, 2013)
parameters:
http://www.esrf.eu/Accelerators/Performance (July 20, 2013). (Cited on page 34.)

[2] P04 parameters:
http://photon-science.desy.de/facilities/petra_iii/beamlines/p04_xuv_beamline/unified_data_sheet_p04/index_eng.html (May 13, 2013). (Cited on page 46.)

[3] P11 parameters:
http://photon-science.desy.de/facilities/petra_iii/beamlines/p11_bio_imaging_and_diffraction/unified_data_sheet_p11/index_eng.html (May 13, 2013). (Cited on page 47.)

[4] PETRA III homepage:
http://petra3.desy.de/ (May 13, 2013)
http://photon-science.desy.de/facilities/petra_iii/index_eng.html (May 13, 2013)
machine parameters:
http://photon-science.desy.de/facilities/petra_iii/machine/parameters/index_eng.html (July 20, 2013). (Cited on pages 34, 43, 46, 75, and 76.)

[5] Source for images of structural formulas of used compounds:
http://www.chemicalbook.com/ (July 23, 2013). (Cited on pages 106, 126, and 167.)

[6] SPring-8 homepage:
http://www.spring8.or.jp/en/ (July 20, 2013)
parameters:
http://www.spring8.or.jp/en/facilities/accelerators/storage_ring/ (July 20, 2013). (Cited on page 34.)

[7] http://nobelprize.org/nobel_prizes/chemistry/laureates/1999/press.html (May 13, 2013). (Cited on page 4.)

[8] http://teledynelecroy.com/oscilloscope/oscilloscopemodel.aspx?modelid=1935 (July 30, 2013). (Cited on page 73.)

[9] http://www.rp-photonics.com/frequency_tripling.html (May 13, 2013). (Cited on page 29.)

[10] http://www.xfel.eu/overview/facts_and_figures/ (May 13, 2013). (Cited on page 2.)

[11] J. Als-Nielsen and D. McMorrow. *Elements of Modern X-ray Physics*. Wiley, 2011. (Cited on pages 38 and 39.)

[12] D. T. Attwood. *Soft X-Rays and Extreme Ultraviolet Radiation: Principles and Applications*. Cambridge University Press, 1999. (Cited on pages 33, 34, and 93.)

[13] A. Azima. *An electro-optical timing diagnostic for pump-probe experiments at the Free-Electron Laser in Hamburg FLASH*. PhD thesis, Universität Hamburg, 2009. (Cited on page 55.)

[14] K. Balewski, W. Brefeld, W. Decking, H. Franz, R. Röhlsberger, and E. Weckert. Petra III: A Low Emittance Synchrotron Radiation Source Technical Design Report. Technical report, DESY, Hamburg, Germany, Deutsches Elektronen-Synchrotron Notkestraße 85, D-22607 Hamburg Germany, February 2004. (Cited on pages 31, 33, 35, and 164.)

[15] R. J. Barlow. *Statistics: A Guide to the Use of Statistical Methods in the Physical Sciences*. Manchester Physics Series. Wiley, reprint edition, 1989. (Cited on pages 107, 108, 111, 113, 114, and 137.)

[16] D. H. Bilderback, P. Elleaume, and E. Weckert. Review of third and next generation synchrotron light sources. *Journal of Physics B: Atomic, Molecular and Optical Physics*, 38:S773 – S797, 2005. (Cited on page 1.)

[17] G. Bönsch and E. Potulski. Measurement of the refractive index of air and comparison with modified Edlén's formulae. *Metrologia*, 35:133–139, 1998. (Cited on page 22.)

[18] T. Brabec, C. Spielmann, P. F. Curley, and F. Krausz. Kerr lens mode locking. *Optics Letters*, Vol. 17:1292–1294, 1992. (Cited on page 25.)

[19] C. Bressler and M. Chergui. Molecular Structural Dynamics Probed by Ultrafast X-Ray Absorption Spectroscopy. *Annu. Rev. Phys. Chem.*, 61:263–282, 2010. (Cited on pages 1, 36, and 39.)

[20] A. Brodeur and S. L. Chin. Ultrafast white-light continuum generation and self-focusing in transparent condensed media. *J. Opt. Soc. Am. B*, Vol. 16:637–650, 1999. (Cited on page 30.)

[21] Bronstein, Semendjajew, Musiol, and Mühlig. *Taschenbuch der Mathematik*. Verlag Harri Deutsch, 5 edition, 2001. (Cited on page 7.)

[22] H. D. Burrows, M. Fernandes, J. Seixas de Melo, A. P. Monkman, and S. Navaratnam. Characterization of the Triplet State of Tris(8-hydroxyquinoline)aluminium(III) in Benzene Solution. *Journal of the American Chemical Society*, 125(50):15310–15311, 2003. (Cited on page 128.)

[23] T. Butz. *Fouriertransformation für Fußgänger*. Stuttgart: B. G. Teubner. 168 S. DM 46.00, 1 edition, 1998. (Cited on page 119.)

[24] M. Chergui and A. H. Zewail. Electron and X-Ray Methods of Ultrafast Structural Dynamics: Advances and Applications. *ChemPhysChem*, 10(1):28–43, January 2009. (Cited on pages 2 and 39.)

[25] P. E. Ciddor. Refractive index of air: new equations for the visible and near infrared. *Appl. Opt.*, 35:1566–1573, 1996. (Cited on page 22.)

[26] M. Cölle and W. Brütting. Thermal, structural and photophysical properties of the organic semiconductor Alq3. *phys. stat. sol. (a)*, 201:1095 – 1115, 2004. (Cited on pages 127 and 128.)

[27] S. Deinert. *Aufbau eines hocheffizienten Photoelektron-Photoion-Koinzidenzexperiments*. PhD thesis, Universität Hamburg, 2013. (Cited on pages 86 and 131.)

[28] W. Demtröder. *Laser Spectroscopy: Basic Concepts and Instrumentation*. Springer, 3rd edition, 1996. (Cited on page 4.)

[29] W. Demtröder. *Atoms, Molecules and Photons An Introduction to Atomic-, Molecular- and Quantum-Physics*. Springer, 2nd edition, 2010. (Cited on page 37.)

[30] B. Dicke. *Time Resolved Pump-Probe XAFS Spectroscopy of Gaq3 - to be published*. PhD thesis, Universität Hamburg, 2013. (Cited on pages 36, 37, 93, 94, 97, 104, 116, 122, 127, 128, and 168.)

[31] B. Edlén. The refractive index of air. *Metrologia*, 2(2):71–80, April 1966. (Cited on page 22.)

[32] A. Einstein. Zur Quantentheorie der Strahlung. *Physikalische Gesellschaft Mitteilungen (Zürich)*, XVI:47–62, 1916. (Cited on page 20.)

[33] J. Eland and R. Feifel. Double ionisation of ICN and BrCN studied by a new photoelectron-photoion coincidence technique. *Chemical Physics*, 327:85–90, 2006. (Cited on page 86.)

[34] J. Ewald. Liquid Jet Anodes for Electron Impact X-ray Sources. Master's thesis, RheinAhrCampus Remagen - Fachhochschule Koblenz and BIOX, KTH/AlbaNova, Stockholm, 2008. (Cited on page 93.)

[35] J. Falta and T. Möller. *Forschung mit Synchrotronstrahlung*. Vieweg+Teubner, 2010. (Cited on page 38.)

[36] W. Gawelda. *Time-Resolved X-Ray Absorption Spectroscopy of Transition Metal Complexes*. PhD thesis, École Polytechnique Fédérale de Lausanne, November 2006. (Cited on pages 1, 122, and 167.)

[37] W. Gawelda, M. Johnson, F. M. F. de Groot, R. Abela, C. Bressler, and M. Chergui. Electronic and Molecular Structure of Photoexcited [RuII(bpy)3]2+ Probed by Picosecond X-ray Absorption Spectroscopy. *Journal of the American Chemical Society*, 128(15):5001–5009, 2006. (Cited on pages 40 and 120.)

[38] T. Gebert. Messungen zur winkelintegralen Spinpolarisation nach Multiphotonenionisation von Xenon. Master's thesis, Universität Hamburg, 2010. (Cited on page 51.)

[39] E. R. Günther. Aufbau eines Analysators für spinpolarisierte Elektronen. Master's thesis, Universität Hamburg, 2010. (Cited on page 51.)

[40] D. Göries. *to be published*. PhD thesis, Universität Hamburg, 201x. (Cited on pages 81, 84, 94, and 99.)

[41] H. Haken and H. C. Wolf. *Molekülphysik und Quantenchemie*. Springer-Verlag Berlin Heidelberg, 4 edition, 2003. (Cited on pages 36, 38, and 164.)

[42] D. Hanggi and P. W. Carr. Errors in exponentially modified Gaussian equations in the literature. *Anal. Chem.*, 57:2394–2395, 1985. (Cited on page 119.)

[43] W. Humbs, E. van Veldhoven, H. Zhang, and M. Glasbeek. Sub-picosecond fluorescence dynamics of organic light-emitting diode tris(8-hydroxyquinoline) metal complexes. *Chemical Physics Letters*, 304:10 – 18, 1999. (Cited on pages 94, 116, 128, and 166.)

[44] I.F. Engineering. *Datasheet for QPMX-500-S Complex Phase Modulator by I.F. Engineering*. (Cited on page 102.)

[45] A. Jabłoński. Efficiency of Anti-Stokes Fluorescence in Dyes. *Nature*, volume 131:839–840, 1933. (Cited on page 37.)

[46] S. L. Johnson. *Ultrafast X-Ray Absorption Spectroscopy: Properties of Liquid Silicon and Carbon*. PhD thesis, University of California, Berkeley, 2002. (Cited on pages 1, 66, 67, and 143.)

[47] A. Juris, V. Balzani, F. Barigelletti, S. Campagna, P. Belser, and A. von Zelewsky. Ru(II) polypyridine complexes: photophysics, photochemistry, eletrochemistry, and chemiluminescence. *Coordination Chemistry Reviews*, Volume 84:Pages 85–277, March 1988. (Cited on pages 120, 122, and 167.)

[48] J. Klute, K. Balewski, A. Delfs, H. Duhme, M. Ebert, R. Neumann, and F. Obier. The PETRA III Multibunch Feedback System. In *10th European Workshop on Beam*

Diagnostics and Instrumentation for Particle Accelerators (DIPAC2011), Hamburg, Germany (05/16/2011-05/18/2011), pages 494–496. 10th European Workshop on Beam Diagnostics and Instrumentation for Particle Accelerators (DIPAC2011), Hamburg, Germany (05/16/2011-05/18/2011), JACoW, Geneva, 2011„ 2011. (Cited on pages 45 and 76.)

[49] F. K. Kneubühl. *Repetitorium der Physik*. B. G. Teubner Stuttgart, 5 edition, 1994. (Cited on page 28.)

[50] M. Krikunova, T. Maltezopoulos, A. Azima, M. Schlie, U. Frühling, H. Redlin, R. Kalms, S. Cunovic, N. M. Kabachnik, M. Wieland, and M. Drescher. Time-resolved ion spectrometry on xenon with the jitter-compensated soft x-ray pulses of a free-electron laser. *New J. Phys.*, 11:123019, 2009. (Cited on pages 4, 86, and 90.)

[51] M. Krikunova, T. Maltezopoulos, P. Wessels, M. Schlie, A. Azima, M. Wieland, and M. Drescher. Ultrafast photofragmentation dynamics of molecular iodine driven with timed xuv and near-infrared light pulses. *J. Chem. Phys.*, 134:024313, 2011. (Cited on page 86.)

[52] R. Kronig. Zur Theorie der Feinstruktur in den Röntgenabsorptionsspektren. *Zeitschrift für Physik*, Volume 70, Issue 5-6:317–323, 1931. (Cited on page 39.)

[53] Light Conversion Ltd. *Harmonics generator User's Manual*. Light Conversion, Sauletekio av. 10 LT-10223 Vilnius, Lithuania, April 2009. (Cited on pages 48, 51, and 164.)

[54] Light Conversion Ltd. *PHAROS User´s manual*. Light Conversion Ltd., Light Conversion Ltd. P/O Box 1485, Sauletekio al. 10 LT-10223 Vilnius, Lithuania, 2009. (Cited on page 48.)

[55] Light Conversion Ltd. *ORPHEUS Collinear optical parametric amplifier of white light continuum User's Manual*. Light Conversion Ltd., Light Conversion Ltd. Sauletekio av. 10 LT-10223 Vilnius Lithuania, 2010. (Cited on pages 48, 53, and 164.)

[56] F. A. Lima, C. J. Milne, D. C. V. Amarasinghe, M. H. Rittmann-Frank, R. M. van der Veen, M. Reinhard, V.-T. Pham, S. Karlsson, S. L. Johnson, D. Grolimund, C. Borca, T. Huthwelker, M. Janousch, F. van Mourik, R. Abela, and M. Chergui. A high-repetition rate scheme for synchrotron-based picosecond laser pump/x-ray probe experiments on chemical and biological systems in solution. *Review of Scientific Instruments*, 82:06311, 2011. (Cited on page 1.)

[57] I. Lindgren. Chemical shifts in X-ray and photo-electron spectroscopy: a historical review. *Journal of Electron Spectroscopy and Related Phenomena*, 137 - 140:59 – 71, 2004. (Cited on page 36.)

[58] J. Lunze. *Regelungstechnik 1*. Springer, 7. neu bearbeitete Auflage, 2008. (Cited on page 5.)

[59] T. H. Maiman. Stimulated Optical Radiation in Ruby. *Nature*, 187:493–494, 1960. (Cited on page 20.)

[60] A. M. March, A. Stickrath, G. Doumy, E. P. Kanter, B. Krässig, S. H. Southworth, K. Attenkofer, C. A. Kurtz, L. X. Chen, and L. Young. Development of high-repetition-rate laser pump/x-ray probe methodologies for synchrotron facilities. *Review of Scientific Instruments*, 82:073110, 2011. (Cited on page 1.)

[61] V. B. D. Marco and G. G. Bombi. Review mathematical functions for the representation of chromatographic peaks. *Journal of Chromatography A*, 931:1–30, 2001. (Cited on page 119.)

[62] E. M. McMillan. The synchrotron - a proposed high energy particle accelerator. *Phys. Rev. 68*, pages 143–144, 1945. (Cited on page 31.)

[63] D. Meschede and H. Vogel. *Gerthsen Physik*. Springer, 21 edition, 2001. (Cited on page 31.)

[64] D. M. Mills, J. R. Helliwell, A. Kvick, T. Ohta, I. A. Robinson, and A. Authier. Report of the Working Group on Synchrotron Radiation Nomenclature - brightness, spectral brightness or brilliance? *Journal of Synchrotron Radiation*, 12:385, 2005. (Cited on page 32.)

[65] K. Miyata, N. Umemura, and K. Kato. Phase-matched pure $\chi^{(3)}$ third-harmonic generation in noncentrosymmetric bib_3o_6. *Optics Letters*, Vol. 34(Issue 4):500 – 502, 2009. (Cited on page 29.)

[66] R. Muijlwijk. Update of the Edlén Formulae for the Refractive Index of Air. *Metrologia*, 25(3):189, 1988. (Cited on page 22.)

[67] E. W. Otten. *Repetitorium Experimentalphysik für Vordiplom und Zwischenprüfung*. Springer, 1998. (Cited on page 28.)

[68] L. Partanen, R. Sankari, S. Osmekhin, Z. F. Hu, E. Kukk, and H. Aksela. Multiple ionization of Xe-comparison of de-excitation pathways following 3d5/2 ionization and 3d5/2 ->6p resonance excitation. *J. Phys. B: At. Mol. Opt. Phys.*, 38:1881–1893, 2005. (Cited on pages 90 and 91.)

[69] M. Pope and C. E. Swenberg. *Electronic Processes in Organic Crystals and Polymers*. Oxford Science Publications, 2 edition, 1999. (Cited on pages 36 and 37.)

[70] P. Radcliffe, S. Düsterer, A. Azima, W. Li, E. Plönjes, H. Redlin, J. Feldhaus, P. Nicolosi, L. Poletto, J. Dardis, J. Gutierrez, P. Hough, K. Kavanagh, E. Kennedy, H. Luna, P. Yeates, J. Costello, A. Delyseries, C. Lewis, D. Glijer, D. Cubaynes, and M. Meyer. An experiment for two-color photoionization using high intensity extreme-uv free electron and near-ir laser pulses. *Nuclear Instruments and Methods in Physics Research Section A: Accelerators, Spectrometers, Detectors and Associated Equipment*, 583(2-3):516–525, December 2007. (Cited on page 86.)

[71] J. J. Rehr and R. C. Albers. Theoretical approaches to x-ray absorption fine structure. *Reviews of Modern Physics*, 72:621 – 654, 2000. (Cited on pages 36 and 164.)

[72] G. A. Reider. *Photonik: Eine Einführung in die Grundlagen*, volume 2. Springer, 2004. (Cited on pages 23 and 26.)

[73] C. Rullière. *Femtosecond Laser Pulses: Principles and Experiments*. Springer, 2 edition, 2004. (Cited on pages 20, 23, 26, and 30.)

[74] A. L. Schawlow and C. H. Townes. Infrared and Optical Masers. *Phys. Rev.*, 112:1940–1949, 1958. (Cited on page 20.)

[75] R. W. Schoenlein, S. Chattopadhyay, H. H. W. Chong, T. E. Glover, P. A. Heimann, C. V. Shank, A. A. Zholents, and M. S. Zolotorev. Generation of Femtosecond Pulses of Synchrotron Radiation. *Science*, 287:2237–2240, 24 March 2000. (Cited on page 1.)

[76] S. Schulz. *Implementation of the Laser-Based Femtosecond Precision Synchronization System at FLASH*. PhD thesis, Universität Hamburg, 2011. (Cited on pages 79, 81, and 137.)

[77] A. Snigirev, V. Kohn, I. Snigireva, and B. Lengeler. A compound refractive lens for focusing high-energy X-rays. *Nature*, 384:49–51, 1996. (Cited on page 95.)

[78] A. Snigirev, V. Kohn, I. Snigireva, A. Souvorov, and B. Lengeler. Focusing high-energy x rays by compound refractive lenses. *Applied Optics*, 37:653–662, 1998. (Cited on page 95.)

[79] D. Strickland and G. Mourou. Compression of amplified chirped optical pulses. *Optics Communications*, Volume 56:219–221, 1985. (Cited on page 25.)

[80] A. Tramer, C. Jungen, and F. Lahmani. *Energy Dissipation in Molecular Systems*. Springer, 2005. (Cited on page 37.)

[81] J. Viefhaus, F. Scholz, S. Deinert, L. Glaser, M. Ilchen, J. Seltmann, P. Walter, and F. Siewert. The Variable Polarization XUV Beamline P04 at PETRA III: Optics, Mechanics and their Performance. *Nuclear Instruments and Methods In Physics Research A*, 710:151 – 154, 2012. (Cited on pages 46 and 164.)

[82] P. Wessels. *to be published*. PhD thesis, Universität Hamburg, 201x. (Cited on page 2.)

[83] H. Wiedemann. *Particle Accelerator Physics I*. Springer, 2 edition, 1999. (Cited on pages 31 and 32.)

[84] M. Wieland. Kryogene Flüssigkeitsstrahlen als Target einer laserinduzierten Plasmaquelle. Master's thesis, Institut für Röntgenphysik der Georg-August-Universität Göttingen, 1999. (Cited on page 93.)

[85] T. Williams and C. Kelley. *gnuplot 4.6 An Interactive Plotting Program*, version 4.6 edition, 2012. (Cited on page 112.)

[86] A. Winter. Bunch length measurements using electro-optical sampling at the sls linac. Master's thesis, RWTH Aachen / Deutschen Elektronen-Synchrotron (DESY) Hamburg, 2004. (Cited on page 23.)

[87] F. J. Wuilleumier and M. Meyer. Pump-probe experiments in atoms involving laser and synchrotron radiation: an overview. *Journal of Physics B: Atomic, Molecular and Optical Physics*, 39:R425–R77, 2006. (Cited on pages 1 and 86.)

[88] Y. Yacoby and E. A. Stern. Achievements and Prospects in X-ray Absorption Spectroscopy. In R. Johnson, H. Schmidt-Böcking, and B. Sonntag, editors, *X-ray and Inner Shell Processes - 17th International Conference*, AIP Conference Proceedings 389, pages 535 – 555. American Institute of Physics, AIP Press, September 1996. (Cited on page 39.)

[89] A. A. Zholents and M. S. Zolotorev. Femtosecond X-Ray Pulses of Synchrotron Radiation. *Phys. Rev. Lett.*, 76(6):912–915, Feb 1996. (Cited on page 1.)

List of Figures

List of Tables

Selbständigkeitserklärung

Ich erkläre, dass ich die vorliegende Arbeit selbständig und nur unter Verwendung der angegebenen Quellen angefertigt habe.

Hamburg, im Juli 2013 Moritz Schlie

Danksagung

Für Unterstützung bei der Erstellung dieser Arbeit möchte ich mich bedanken bei:

- Prof. Dr. Markus Drescher für die Betreuung der Arbeit, die Aufnahme in seine Arbeitsgruppe und die verlässliche Unterstützung beim Lösen von fachlichen und organisatorischen Problemen
- Dr. Marek Wieland, der als Herz und Seele der Arbeitsgruppe DynamiX auch mich mit unzähligen Tipps und einem immer offenen Ohr zu allen Tages- und Nachtzeiten unterstützte und darüber hinaus hilfreiche Korrekturvorschläge unterbreitete
- Dr. Jens Viefhaus für das beeindruckende Vorbild als enthusiastischer Vollblutwissenschaftler bei der umfangreichen Unterstützung am Synchrotron zu wirklich jeder (möglichen und unmöglichen) Zeit sowie für die Bereitschaft als Zweitgutachter zu fungieren
- Dr. Alke Meents für die intensive und flexible Unterstützung am Synchrotron und die inspirierenden Kontakte ans PSI
- Dr. Armin Azima für umfangreiche Unterstützung bei Fragen rund um Laser- und Regelungstechnik sowie für wichtige Korrekturvorschläge
- meinen „Leidensgenossen“ unzähliger Synchrotron-Strahlzeiten Dr. Sascha Deinert, Benjamin Dicke und Dennis Göries für angenehme Kooperation trotz mitunter widriger Umstände (Joey's liefert nur bis 23 Uhr ...)
- Philipp Wessels für die unkomplizierte Zusammenarbeit bei der Lasernutzung sowie die Unterstützung als erster Testkandidat für die Synchronisations-Beschreibung und die daraus resultierenden Korrekturvorschläge
- Anja Niedermeier und Dr. Jens Salomon für Korrekturvorschläge und Erfahrungsaustausch über die Fachgrenzen hinweg
- allen Gutachtern und dem Prüfungsausschussvorsitzenden für das große Entgegenkommen und die Flexibilität bei der Terminkoordinierung
- allen derzeitigen und ehemaligen Kollegen der Arbeitsgruppe DynamiX für die freundlich-kollegiale Arbeitsatmosphäre
- den Kollegen am DESY, welche aufgrund der offenen Türen und des kollegialen Umgangs mitunter schneller mit hilfreichen Tipps waren als mit der Nennung des eigenen Namens; insbesondere bei den Arbeitsgruppen an P04 und P11 für

die Unterstützung vor, während und nach den Messzeiten; weiterhin bei Sebastian Schulz für die Unterstützung bei den SSA-Messungen sowie bei Jens Klute und Hans-Thomas Duhme für Hilfe im Umgang mit den Referenzsignalen und der Bunch-Uhr

- Oliver Becker sowie den Kollegen in Werkstätten und Verwaltung von Universität und DESY für praktische Unterstützung bei experimentellen und organisatorischen Herausforderungen
- Dr. Peter Gürtler stellvertretend für das HASYLAB, welches mich ein halbes Jahr als DESYaner aufgenommen hat und auch die Veröffentlichung dieser Arbeit durch das DESY ermöglicht
- meinem privatem Umfeld, insbesondere meinen Eltern und meiner Schwester, für das durch mich stark und mitunter auch überbeanspruchte Verständnis sowie jegliche Unterstützung

Danke.